THE UNIVERSITY OF QUEENSLAND

AUSTRALIA

Intelligent Condition Monitoring and Diagnosis of a Power Transformer: On-Load Tap Changer (OLTC) and Main Winding

Junhyuck Seo

MPhil (Electric Eng.), B.E (Electronic Eng.)

A thesis submitted for the degree of Doctor of Philosophy at

The University of Queensland in 2019

School of Information Technology and Electrical Engineering

Abstract

A power transformer is one of the most important assets in a power system. Failure of a power transformer can cause disastrous effects and it can cost a tremendous amount for recovery. Many industry surveys have revealed that the transformer's On-Load Tap Changer (OLTC), the main winding and the bushing are the most common components responsible for a considerable portion of power transformer failures.

For the last couple of decades, many techniques have been developed to evaluate the condition of these transformer components. However, it is still a challenging task to establish a reliable condition monitoring system that provides high visibility of a transformer's condition to make an informed condition assessment. This thesis develops novel and field applicable online condition monitoring systems and advanced signal processing algorithms to pave the way to evaluate the mechanical condition of the OLTC and the insulation condition of the main winding of a power transformer.

This thesis comprises two parts: the mechanical condition monitoring of the OLTC and the condition monitoring of the main winding insulation. In the first part, vibration signal measurement based on OLTC's mechanical condition monitoring techniques is investigated. A number of novel methods are developed for effective application of the vibration signal measurement-based techniques. They are: (1) a vibration signal interpretation method using a novel joint vibration and arcing signal measurement; (2) an advanced vibration and arcing signal extraction and processing method by implementing Savitzky-Golay filters; and (3) a vibration signal comparison method based on waveform simplification, alignment and correlation comparison. In the second part, Partial Discharge (PD) measurement based on winding insulation condition monitoring techniques is investigated. A number of innovative techniques are proposed and implemented. They are: (1) PD signal extraction using the signal's transient strength; (2) PD signal analysis using the Sequential Propagating PD (SPPD) method; and (3) PD source localisation based on a three-dimensional (3D) intersectional spatial visualisation method.

The OLTC is designed to regulate the output voltage of a power transformer through a series of complicated mechanical operations. After a relatively long period of service, the OLTC may experience mechanical condition deterioration and defects such as coking on switches and contacts, misalignments on contacts, spring looseness, motor drive system's malfunction and defects in gears and cams, etc. Such incipient mechanical issues can lead to damage of the OLTC and even failure, and in turn can impair the reliability of a transformer.

In this thesis the vibration signal measurement is adopted to evaluate the mechanical condition of an OLTC since it is performed online and is capable of monitoring a number of different mechanical

components. Vibration signal measurement presents good visibility in detecting a mechanical condition change of an OLTC at different stages of the OLTC's service life. Any changes in an OLTC's mechanical condition can be reflected by the transition of the magnitude and time-of-occurrence of the vibration signal acquired during the OLTC's operation.

However, there are still a number of important tasks that need to be accomplished before the vibration signal measurement can become a ready-to-use tool for OLTC condition monitoring. These tasks are: (1) correlation of vibration signals to corresponding mechanical operations of the OLTC; (2) extraction of features (representative characteristics) of the vibration signals; and (3) evaluation of mechanical condition changes in the OLTC.

Firstly, there is a lack of an effective method for vibration signal interpretation, which can effectively correlate the measured vibration signals to the mechanical events generated during an OLTC operation. Such interpretation method enables the identification of a faulty component of the OLTC. Given the complicated configuration, various control mechanisms and operating conditions of OLTCs, it is almost impossible to directly correlate the measured vibration signals to the mechanical condition of the corresponding OLTC. Therefore, it is necessary to develop an advanced vibration signal interpretation scheme for vibration signal measurement based on OLTC condition monitoring.

This thesis proposes a vibration signal interpretation scheme by incorporating arcing signal into vibration signals and develops a joint vibration and arcing signal measurement system. During an OLTC operation, arcing is provoked when a switching contact is closed to a tap position. The arcing causes an electromagnetic signal, which can flow to a grounding cable through the transformer windings. By effectively integrating vibration and arcing signals, important mechanical events during an OLTC operation can be captured and the corresponding source of the vibration signals can be identified. The proposed joint vibration signal and arcing signal measurement method is performed online and without disturbing the OLTC and transformer operation.

For an effective interpretation of the vibration signal and arcing signals, a special algorithm is developed using a Savitzky-Golay filter. An arcing signal induced by an OLTC switch's closure normally exists at high frequencies reflecting a transient and impulsive nature of an arcing event. In contrast, vibration signals appear at low frequencies. The proposed algorithm can effectively remove noise signals and extract useful information from the measured vibration and arcing signals without causing any distortion. Time alignment between the arcing signal and the vibration signal is a critical requirement in the interpretation process. A time discrepancy between the two signals can cause misinterpretation due to improperly correlated two signals. However, the proposed algorithm is capable of processing the signals without causing a time delay at any degree of filtration.

A correlation coefficient-based vibration signal's waveform comparison method is developed to automatically evaluate a mechanical condition change of an OLTC at different stages. The important features of vibration signals (amplitude, number of peaks and event occurrence time) are used to evaluate the mechanical condition change of an OLTC. However, these features are not able to be compared directly due to the complex nature of the vibration signal. To deal with this difficulty, an improved comparison process of vibration signal is proposed. It uses a waveform-based vibration signal comparison integrated with a Savitzky-Golay filter for waveform extraction and a correlation coefficient for assessing a mechanical condition change. The proposed method is proven effective and sensitive in evaluating the mechanical condition change of an OLTC.

To prove the applicability of the developed signal processing methods and the joint vibration and arcing signal measurement system, online and offline measurements are collected on different types of OLTCs and the results are presented throughout this thesis.

In the second part of this thesis, various techniques for improving PD measurement based transformer winding insulation condition monitoring are proposed. Failure of the main winding insulation system can cause catastrophic consequences. Thus, it is critically important to monitor and diagnose the condition of the main winding insulation systems for a sustainable and reliable operation of a power transformer. For the purpose, many techniques have been developed in the past. Among them, a High Frequency Current Transducer (HFCT) based on inductive PD measurement has been adopted since it provides online condition monitoring, easy installation and no service interruption to the transformer. The sensor only needs to be clamped onto the grounding cable of the transformer. For a successful PD signal measurement, PD signals should be properly acquired, extracted from noise and analysed to identify the types of PD source and the severity of the insulation defects. Finally, the location of the insulation defect is located for repair work. A series of signal processing methods for each of the above tasks are developed thoroughly.

Firstly, a novel differential signal extraction method is developed for PD signal extraction. The method targets the PD signal's impulse caused by discharging the accumulated energy across an insulation defect for a very short time. To extract such transient impulses of PD signals, a transient strength-based PD signal extraction algorithm is developed. Its implementation is straightforward because any complicated transition and process are removed, which benefits online PD measurement of a power transformer.

After PD signal extraction, the source of the PD is required to be investigated to identify the types and severity of insulation defects in the main winding. In PD signal analysis, a phase-resolved PD (PRPD) diagram has been adopted to characterise PD activity and identify the types of discharges by overlaying the obtained PD signals over Alternating Current (AC) power cycles. However, the PRPD

diagram may fail to capture some important instantaneous information embedded in each individual PD signal due to its collective method of superimposing all the obtained signals onto an AC cycle. To explore the information from instantaneous activity of PD signals, a SPPD signal analysis method is developed. It observes the instant behaviour of the PD and investigates the sequential propagation pattern and occurrence features of the PD at each AC power cycle. SPPD is capable of presenting an intuitive way of separating and recognising sparking or corona type of PD signals as well as a phase-based analysis approach that PRPD shows.

Finally, to localise PD sources in a power transformer tank, an acoustic vibration sensor is adopted and visualisation of the insulation defect's location is implemented using the spatial intersectional method. Additionally, the method investigates the effects of multiple propagation paths of acoustic signals (induced by PD activity) in deciding Time of Arrivals (TOA) at each sensor. The obtained vibration signal is processed by the optimised Savitzky-Golay filter for TOA determination.

The suite of methods developed in this thesis is capable of providing an improved means for OLTC and main winding condition monitoring. Ultimately, this thesis deals with comprehensive technical methods to implement online condition monitoring of the OLTC and the main winding using a vibration sensor and HFCT.

Declaration by author

This thesis is composed of my original work, and contains no material previously published or written by another person except where due reference has been made in the text. I have clearly stated the contribution by others to jointly-authored works that I have included in my thesis.

I have clearly stated the contribution of others to my thesis as a whole, including statistical assistance, survey design, data analysis, significant technical procedures, professional editorial advice, financial support and any other original research work used or reported in my thesis. The content of my thesis is the result of work I have carried out since the commencement of my higher degree by research candidature and does not include a substantial part of work that has been submitted to qualify for the award of any other degree or diploma in any university or other tertiary institution. I have clearly stated which parts of my thesis, if any, have been submitted to qualify for another award.

I acknowledge that an electronic copy of my thesis must be lodged with the University Library and, subject to the policy and procedures of The University of Queensland, the thesis be made available for research and study in accordance with the Copyright Act 1968 unless a period of embargo has been approved by the Dean of the Graduate School.

I acknowledge that copyright of all material contained in my thesis resides with the copyright holder(s) of that material. Where appropriate I have obtained copyright permission from the copyright holder to reproduce material in this thesis and have sought permission from co-authors for any jointly authored works included in the thesis.

Publications included in this thesis

1. Junhyuck Seo, Hui Ma and Tapan K. Saha, “A Joint Vibration and Arcing Measurement System for Online Condition Monitoring of On-Load Tap Changer of Power Transformer,” IEEE Transactions on Power Delivery, vol. 32, Issue 2, pp. 1031 – 1038, 2017.

- Incorporated as sections in Chapter 3

Contributor	Statement of contribution
Junhyuck Seo (Candidate)	Laboratory Measurements (90 %) Result interpretation and discussion (80 %) Wrote the paper (85 %)
Hui Ma	Laboratory Measurements (10 %) Discussion on Results (10 %) Wrote and edited paper (15 %)
Tapan K. Saha	Discussion on Results (10 %)

2. Junhyuck Seo, Hui Ma and Tapan K. Saha, "On Savitzky-Golay Filtering for Online Condition Monitoring of Transformer On-Load Tap Changer," in IEEE Transactions on Power Delivery, vol. 33, no. 4, pp. 1689-1698, August 2018.

- Incorporated as sections in Chapter 4

Contributor	Statement of contribution
Junhyuck Seo (Candidate)	Programming, simulation and visualisation (100 %) Laboratory Measurements (90 %) Result interpretation and discussion (80 %) Wrote the paper (85 %)
Hui Ma	Laboratory Measurements (10 %) Wrote and edited paper (15 %) Discussion on Results (10 %)
Tapan K. Saha	Discussion on Results (10 %)

3. Junhyuck Seo, Hui Ma and Tapan K. Saha, “Analysis of Vibration Signal for Power Transformer On-Load Tap Changer (OLTC) Condition Monitoring,” IEEE Power and Energy Society 2018 General Meeting, Portland, US, August 2018.

- Incorporated as sections in Chapter 5

Contributor	**Statement of contribution**
Junhyuck Seo (Candidate)	Programming, simulation and visualisation (100 %) Laboratory Measurements (90 %) Result interpretation and discussion (80 %) Wrote the paper (85 %)
Hui Ma	Laboratory Measurements (10 %) Wrote and edited paper (15 %) Discussion on Results (10 %)
Tapan K. Saha	Discussion on Results (10 %)

4. Junhyuck Seo, Hui Ma and Tapan K. Saha, “A Novel Signal Extraction Technique for Online Partial Discharge (PD) Measurement of Transformers," Int. Trans. Electr. Energ. Syst., 26 (5) 1032-1048, 2016.

- Incorporated as sections in Chapter 6

Contributor	**Statement of contribution**
Junhyuck Seo (Candidate)	Programming, simulation and visualisation (100 %) Laboratory Measurements (90 %) Result interpretation and discussion (80 %) Wrote the paper (85 %)
Hui Ma	Laboratory Measurements (10 %) Wrote and edited paper (15 %) Discussion on Results (10 %)
Tapan K. Saha	Discussion on Results (10 %)

5. Junhyuck Seo, Hui Ma and Tapan K. Saha, “An Improved Spatial Intersectional Method for Partial Discharge (PD) Source Localisation in Power Transformer,” 12th International Conference on the Properties and Applications of Dielectric Materials (ICPADM), Xi’an, China, 2018.

- Incorporated as sections in Chapter 8

Contributor	Statement of contribution
Junhyuck Seo (Candidate)	Programming, simulation and visualisation (100 %) Laboratory Measurements (90 %) Result interpretation and discussion (80 %) Wrote the paper (85 %)
Hui Ma	Laboratory Measurements (10 %) Wrote and edited paper (15 %) Discussion on Results (10 %)
Tapan K. Saha	Discussion on Results (10 %)

Submitted manuscripts included in this thesis

1. Junhyuck Seo, Hui Ma and Tapan K. Saha, "Using Sequential Propagating Characteristics of Partial Discharge (PD) Signal for Condition Monitoring of Power Transformer," submitted to IET Science, Measurement & Technology.

- Incorporated as sections in Chapter 7

Contributor	Statement of contribution
Junhyuck Seo (Candidate)	Programming, simulation and visualisation (100 %) Laboratory Measurements (90 %) Result interpretation and discussion (80 %) Wrote the paper (85 %)
Hui Ma	Laboratory Measurements (10 %) Wrote and edited paper (15 %) Discussion on Results (10 %)
Tapan K. Saha	Discussion on Results (10 %)

Other publications during candidature

1. Junhyuck Seo, "A Practical Scheme for Vibration Signal Measurement-Based Power Transformer On-Load Tap Changer Condition Monitoring," Accepted by *International Conference on Condition Monitoring and Diagnosis (CMD)*, Perth, Australia, 23-26 September 2018.

2. Junhyuck Seo, Hui Ma and Tapan K. Saha, "Analysis of Vibration Signal for Power Transformer On-Load Tap Changer (OLTC) Condition Monitoring," *IEEE Power and Energy Society 2018 General Meeting*, Portland, US, August 2018.

Contributor	**Statement of contribution**
Junhyuck Seo (Candidate)	Programming, simulation and visualisation (100 %) Laboratory Measurements (90 %) Result interpretation and discussion (80 %) Wrote the paper (85 %)
Hui Ma	Laboratory Measurements (10 %) Wrote and edited paper (15 %) Discussion on Results (10 %)
Tapan K. Saha	Discussion on Results (10 %)

3. Junhyuck Seo, Hui Ma and Tapan K. Saha, "Sinusoidal noise suppression technique for partial discharge measurement of transformers,". *2015 IEEE Power and Energy Society General Meeting, PESGM 2015*, Denver, CO, United States, 26-30 July 2015.

Contributor	**Statement of contribution**
Junhyuck Seo (Candidate)	Programming, simulation and visualisation (100 %) Laboratory Measurements (90 %) Result interpretation and discussion (80 %) Wrote the paper (85 %)
Hui Ma	Laboratory Measurements (10 %) Wrote and edited paper (15 %) Discussion on Results (10 %)
Tapan K. Saha	Discussion on Results (10 %)

Contributions by others to the thesis

No contributions by others.

Statement of parts of the thesis submitted to qualify for the award of another degree

No works submitted towards another degree have been included in this thesis.

Research Involving Human or Animal Subjects

No animal or human subjects were involved in this research

Acknowledgements

I would like to express my sincere gratitude to those who helped and supported me during my PhD candidature. Without their helps, expertise and wisdom, I could not have completed the long journey. I will never forget their grateful support.

Firstly, I want to express my sincere gratitude to my supervisors, Prof. Tapan K. Saha and Dr. Hui Ma. In particular, Prof. Saha accepted me to join this exciting research project and supervised me to be successful with his incomparable experience and insight. His invaluable knowledge and advice were shared throughout my thesis. Additionally, his financial support to my academic trips gave me a wonderful chance to broaden human network and excavate new technologies.

A special thank goes to Dr. Hui Ma for his great efforts to guide my PhD candidature. His exceptional advice and supports to my research works had never been compromised regardless of day and night. His enthusiasm encouraged me to keep exploring and working hard for the best achievements. He also supported me to implement all the necessary on-site tests with industries. Without his great support, the invaluable data could hardly be obtained and proper result would not be attained.

I also would like to express my gratitude to Dr. Chandima Ekanayake and Dr. Daniel Martin for their technical advice about transformer insulation system and various test methods. Mr. Steve Wright helped me to implement laboratory test safely and securely. Especially, my colleagues, Dr. Yi Cui, Dr. Lakshitha Naranpanwe, Mr. Muhammad Abdul Hafeez Ansari and Mr. Sameera Samarasinghe were the very persons who helped me with on-site and laboratory tests. Ms. Mandeep Waraich was always supportive officer to solve many difficult situations. I will always remember all these kind, generous and supportive nature from all my colleagues and friends.

I also acknowledge Australian Research Council (ARC) and industry partners of powerlink Queensland, AusGrid, Wilson transformer and Energex for the financial support, on-site tests and technical advice. Especially, I appreciate Gary Russell, Bekker Rikus and Ray Holzheimer in Powerlink and Srinivasan (Steve) Chinnarajan in Energex for supporting on-site tests.

I cannot but acknowledge all others who are too important to be named here. Each moment and their value will not be faded forever.

At last, I would like to hand over all my achievement to my lovely families, Grace, Catherine and Jessica who are always patient, lovely, thoughtful and supportive to me throughout my PhD candidature.

THANK YOU ALL!

Financial support

No financial support was provided to fund this research

Keywords

acoustic emission, condition monitoring, high frequency current transducer (HFCT), insulation system, on-load tap changer (OLTC), partial discharge, Savitzky-Golay filter, power transformer, vibration signal

Australian and New Zealand Standard Research Classifications (ANZSRC)

ANZSRC code: 090607, Power and Energy Systems Engineering (excl. Renewable Power), 50 %
ANZSRC code: 090609, Signal Processing, 30 %
ANZSRC code: 080110, Simulation and Modelling, 20 %

Fields of Research (FoR) Classification

FoR code: 0906, Electrical and Electronic Engineering, 100 %

Table of Contents

List of Figures

List of Tables

List of Abbreviations and Symbols

Abbreviations

3D	Three-Dimensional
AC	Alternating Current
AE	Acoustic Emission
CT	Current Transducer
DC	Direct Current
DGA	Dissolved Gas Analysis
DP	Degree of Polymerisation
DRM	Dynamic Resistance Measurement
DSI	Discrete Spectral Interference
DWT	Discrete Wavelet Transform
FDS	Frequency Domain Spectroscopy
FFT	Fast Fourier Transform
FIR	Finite Impulse Response
HFCT	High Frequency Current Transducer
HPLC	High Performance Liquid Chromatography
IEC	International Electrotechnical Commission
IEEE	Institute of Electrical and Electronics Engineers
LPF	Low Pass Filter
mJ	Milli Joule
ms	Milli Second
MV	Moving Average
OLTC	On-Load Tap Changer
pC	Pico Coulomb
PD	Partial Discharge
PDC	Polarisation and Depolarisation Current
PPM	Parts per Million
PRPD	Phase-Resolved Partial Discharge
PSNR	Peak Signal to Noise Ratio
RMS	Root Mean Square
SNR	Signal to Noise Ratio
SPPD	Sequential Propagation Partial Discharge
SRM	Static Resistance Measurement
STFT	Short Time Fourier Transform
SVM	Support Vector Machine

TOA	Time of Arrival
TTS	Transition Switch
TTV	Transition Switch's Vacuum Interrupter
UHF	Ultra-High Frequency
WCO	Water Content in Oil

Symbols

A	Area
C	Capacitance
C_h	Capacitance of the Defect
C_m	Measured Capacitance
C_s	Remaining Capacitance Except the Capacitance of the Defect
C_0	Geometrical Capacitance
$C(x,t)$	Moisture Concentration at Location x and Time t
$C'(\omega)$	Real Part of Complex Capacitance
$C''(\omega)$	Imaginary Part of Complex Capacitance
d	Gap
D	Diffusion Coefficient
F	2-Furaldehyde
f_m	Mid-Band Frequency
f_1	Lower Frequency Limit
f_2	Higher Frequency Limit
i_p	Polarisation Current
I_C	Capacitive Current
I_R	Resistive Current
Q	Magnitude of Apparent Discharge
R	Resistance
s	Second
T	Temperature
T	Time
$\tan\delta(\omega)$	Loss Factor
U_L	Extinction Voltage
U_z	Inception Voltage
$U_t(t)$	Voltage Across the Defect

U_0	Step DC Voltage
$U_1(t)$	Applied High Voltage Across the Insulation
ε	Permittivity
ε_r	Relative Permittivity
ε_0	Permittivity of Free Space
$\varepsilon'(\omega)$	Real Part of Complex Permittivity
$\varepsilon''(\omega)$	Imaginary Part of Complex Permittivity
σ	Average Conductivity
Ψ	Mother Wavelet
Δf	Frequency Width

Explicit comments on this thesis:

Junhyuck Seo contributed to develop an intelligent condition monitoring and diagnosis system for a power transformer. Especially, the most vulnerable and important parts of a power transformer were investigated. This thesis consists of two major sections. The first section evaluates the mechanical condition of an OLTC using vibration signal measurement as described in Chapters 3, 4 and 5 while the second section comprises high voltage insulation system condition monitoring measured using PD as described in Chapters 6, 7 and 8.

Thus, the sequence of chapters in this thesis are based on the categories of the contents rather than the chronological sequence of the publications.

Chap 1. Introduction

1.1 Background and Problem Statement

A power transformer is one of the most important assets in a power system. Failure of a power transformer can cause disastrous effects and it can cost a tremendous amount for recovery. Many surveys on the causes of power transformer failure have revealed that the transformer's winding, bushing and On-Load Tap Changer (OLTC) are the most common components responsible for transformer failure [1 - 5]. Many techniques have been developed for monitoring and diagnosing the condition of the components. However, it is still challenging to develop, implement and deploy a reliable condition monitoring system (both hardware and software), which can provide high visibility of the transformer's condition and make an informed condition assessment on its winding and OLTC.

An OLTC works to regulate the output voltage of a power transformer through a series of complicated mechanical operations. Other than the cooling fan and pump, the OLTC is the only moving component inside a transformer. After a relatively long period of service, the OLTC may experience various mechanical problems such as misalignments on contacts, spring looseness, defects in gears and cams and malfunction in the motor drive system. Ultimately, these mechanical problems can lead to malfunction of the OLTC and even its failure, and in turn, this can impair the reliability of a transformer. Therefore, it is necessary to develop a mechanical condition monitoring and diagnosis system for the OLTC.

Among current available techniques for OLTC condition assessment, vibration signal measurement provides an online means for continuously monitoring of the mechanical condition of an OLTC without disturbing its operation. The measured vibration signal can reflect the mechanical condition change of an OLTC at different stages of its service life. The information of these changes are embedded in the transition of the magnitude and time-of-occurrence of the vibration signal acquired when an OLTC is activated and in operation.

Given the complicated configuration, control mechanisms and operating conditions of different types of OLTCs, the correlations between the characteristics of the measured vibration signals and the mechanical condition of the corresponding OLTC is not well understood. Moreover, the vibration signal generated from OLTC's operation has a complex nature due to its multiple propagation paths, reflection, refraction, diffraction and noisy environment. Thus, it is an essential task to extract informative characteristics of vibration signals, correlate these characteristics to actual events of OLTC operation, and subsequently evaluate the mechanical condition change of the OLTC.

The interpretation of vibration signals and the subsequent diagnosis requires historic measurement data, previous mechanical condition records and other relevant information for the OLTC of interest. However, for many transformers and their OLTCs, such information may not be recorded or available. To establish an effective scheme for condition assessment of an OLTC, other signals originating from an OLTC may also need to be measured to complement the vibration signal measurement.

During OLTC operation, arcing is provoked when a switching contact is being closed to a tap position. It causes electromagnetic signals flowing to ground through the transformer's windings. A High Frequency Current Transducer (HFCT) clamped on the transformer's grounding cable can be used to capture arcing signals. Such a joint vibration and arcing signal measurement system can provide a means of interpreting vibration signals and can correlate each vibration signal to a corresponding OLTC's mechanical operation.

In the joint vibration and arcing signal measurement system, it is important to properly deal with the two different types of signals having different characteristics simultaneously. Since the arcing signal is caused by the switch's closure to a tap position, the signal is transient and impulsive in nature and occurs at high frequencies. In contrast, the vibration signal is at low frequencies. Thus, a suitable signal processing method needs to be developed for removing noise and extracting useful information from the measured arcing and vibration signals. Especially, a latency caused by the signal extraction process should be avoided as it can cause inappropriate interpretation of the signals.

To further identify the mechanical condition changes of an OLTC from the measured vibration signal, a suite of algorithms also need to be developed. These algorithms are tasked to (1) extract informative characteristics of vibration signals, (2) correlate these characteristics to actual events of OLTC operations, and (3) subsequently to evaluate mechanical change in the OLTC's condition.

The insulation systems of a transformer's main winding are subjected to continuous electrical, thermal and mechanical stresses. These stresses can cause insulation ageing and even lead to transformer insulation system failure. The insulation system failure of a transformer's winding can cause catastrophic consequences. It is thus critically important to monitor and diagnose the condition of insulation systems of the winding. Over the past two decades, many condition monitoring and diagnosis techniques have been developed for that purpose. Among these techniques, Partial Discharge (PD) measurement has been increasingly adopted by utilities for diagnosing the condition of the insulation system of a transformer's main winding. However, there are still challenges in PD signal acquisition, processing and interpretation.

For a successful online PD measurement of a transformer, PD signals must be properly acquired, extracted from noise, and analysed to identify the types of PD source and the severity of the

corresponding insulation defects. A series of signal processing techniques will be developed for each of these tasks.

In PD signal analysis, a Phase-Resolved PD (PRPD) diagram has been generally adopted to characterise PD activity and identify the types of PD source. The PRPD diagram is constructed by projecting PD signals acquired over a sufficient number of alternating current (AC) power cycles onto a single cycle of phase angles. However, the PRPD diagram may fail to capture some important information embedded in each individual PD signal since it only reflects the collective scope of PD signals superimposed onto the phase angles. It is therefore necessary to develop a new scheme to characterise the type and feature of PD activity.

Another major task of PD measurement is to localise the PD source using Acoustic Emission (AE) sensors. It needs to investigate the possible propagation paths of acoustic signals (induced by PD activity) and the Time-of-Arrival (TOA) of acoustic signals travelling along different paths before they reach AE sensors.

1.2 Objectives and Contributions of the Thesis

The overall aim of this thesis is to develop novel and field applicable techniques including both a measurement system and signal and data processing algorithms for assessment of a transformer's main winding insulation as well as monitoring OLTC mechanical condition and diagnosis of potential problems. The objectives include:

1. To develop a comprehensive online condition monitoring system for evaluating the mechanical condition of an OLTC and the insulation condition of the main winding using non-intrusive sensors.
2. To design a novel joint vibration and arcing signal measurement system for improving the visibility of OLTC operation and the interpretation of vibration signals.
3. To develop advanced digital signal processing techniques for processing the measured vibration and arcing signals, removing noise and extracting critical information related to the events generated during OLTC operations without introducing any time delay in processing the vibration and arcing signals.
4. To develop a waveform-based vibration signal comparison scheme, which can be used to identify a mechanical condition change of OLTC to pave the way for mechanical condition assessment of the OLTC.
5. To develop an effective and straightforward PD signal extraction algorithm based on the transient characteristics of PD signals acquired from online PD measurement of a transformer's main winding insulation.
6. To investigate the sequential propagating properties of PD impulses, which can complement the conventional collective PD analysis method (i.e., PRPD), for identifying and separating PD signals from different PD sources and types.
7. To investigate PD signal propagation paths inside a transformer and implement a PD source localisation scheme with necessary signal processing algorithms and visualisation.

To achieve the above objectives, the following tasks have been accomplished in the thesis.

1. The current state-of-the-art condition monitoring and diagnosis methods regarding the mechanical condition of the OLTC and the insulation condition of the main winding have been investigated through an extensive literature review. Feasible and non-interruptive online condition monitoring methods using a vibration sensor and high frequency current transducer (HFCT) have been proposed, developed and deployed for a transformer's OLTC and main winding condition assessment.
2. The characteristics of vibration signals and arcing signals corresponding to OLTC operation

have been investigated and subsequently a joint vibration and arcing signal measurement system has been developed and verified.

3. Savitzky-Golay filter-based signal processing techniques have been developed to effectively extract vibration and arcing signals from noise without causing a time delay and losing information embedded in the original signals measured.
4. A waveform-based vibration signal comparison method has been developed to improve the existing methods, which are based solely on direct extraction of the amplitude and event time of vibration signals.
5. A transient strength-based PD signal extraction method using its natural properties has been developed to extract PD signals from noise. The method showed a substantially positive performance of extracting small amplitude PD signals, which could not have been achieved by existing amplitude-based PD signal extraction methods.
6. A PD signal analysing method using a sequential propagating property of PD pulses has been developed. It has demonstrated the sequential propagating features of PD signals can be used as a complementary method to the PRPD method for classifying and separating PD signals from different types of insulation defects.
7. The signal processing technique has been developed to identify the possible propagation paths and corresponding TOAs for a vibration signal travelling from a PD source inside a transformer tank to a sensor attached to the outside of transformer tank wall. A spatial intersectional method also has been developed to visualise and identify the location of the PD source.

1.3 Thesis Outline

The thesis consists of nine chapters. The contents of Chapters 2 to Chapter 9 are highlighted as below.

Chapter 2 provides a literature review on a variety of techniques for monitoring and diagnosis of potential failures in power transformers. Various research works related to the OLTC's mechanical condition and main winding insulation's condition monitoring and diagnosis are discussed in this chapter. Key challenges of applying vibration signal measurement and PD measurement to online condition monitoring and assessment of power transformers are also addressed.

Chapter 3 discusses the necessities of developing a new vibration signal interpretation scheme for OLTCs given that they have complicated configurations, there are different types and models, and they normally lack historic measurement data. It then presents a novel joint vibration and arcing signal measurement system for interpretation of OLTC's vibration signals.

Chapter 4 presents a Savitzky-Golay filter-based signal processing method, which can extract information from both vibration and arcing signals without causing any time delay in signal processing. The advantages of this method enable the extracted signals to be further evaluated for interpreting vibration signals and revealing the mechanical condition change of the OLTC. The comparative results of signal processing are presented to prove its applicability over a number of conventional signal processing methods.

Chapter 5 develops an effective vibration signal comparison scheme to identify a mechanical condition change of OLTCs. This scheme consists of an Savitzky-Golay filter for signal pre-processing and correlation coefficient computation for evaluating the OLTC's mechanical condition change.

Chapter 6 details a HFCT-based PD measurement system for main winding insulation quality monitoring and diagnosis. A PD signal extraction method based on the transient strength of PD signals is developed to extract PD signal from noise.

Chapter 7 proposes a sequential propagating PD (SPPD) signal analysis method. It considers the behaviour of PD activity at each individual AC power cycle, which complements the conventional PRPD method by analysing a PD signal's instantaneous propagating activity.

Chapter 8 develops an improved spatial intersectional PD source localisation method. To understand the impacts of multiple possible propagation paths of acoustic signals (induced by PD activity) for PD source localisation, the TOAs of acoustic signals travelling along different paths inside a transformer tank are investigated. Especially, the Savitzky-Golay filter is implemented to effectively determine the TOAs.

Chapter 9 draws the conclusions with emphasis on a comprehensive strategy for condition monitoring and diagnosis of a power transformer's OLTC and main winding. It also recommends a number of directions for future research work.

Chap 2. Literature Review

2.1 Power Transformer Failure Statistics

A power transformer is one of the most important and expensive assets in a power system. The reliable operation of a power transformer has a significant impact on the availability of electricity supply to customers. A power transformer has a number of subsystems including winding, OLTC, bushing, cooling systems and other peripherals. The integrity of these subsystems must be continuously monitored for appropriate operational decisions and maintenance schedules. Effective methodologies and innovative techniques need to be developed to pave the way for comprehensive condition monitoring and diagnosis of a power transformer.

A number of industry surveys have been conducted to understand various failure modes and root causes of the failures of power transformers [1 - 5]. In a survey of power transformers in Australia and New Zealand [1], it was found that many transformers experienced damage resulting in expensive repair or replacement. Another Australian transformer failure survey listed responsible components for the failures where OLTC accounted for 25 % of transformer failures followed by main winding (16 %) and bushing (16 %) [5].

A CIGRE (International Council for Large Electric Systems was a French but now international organisation) working group in France conducted a failure survey on power transformers with voltage levels equal to or greater than 69 kV between 1996 and 2010. Figure 2.1 shows the results of the survey. It can be seen that the predominant responsible components for transformer failures are OLTC (31.16 %), winding (19.40 %) and bushings (13.99 %) [3].

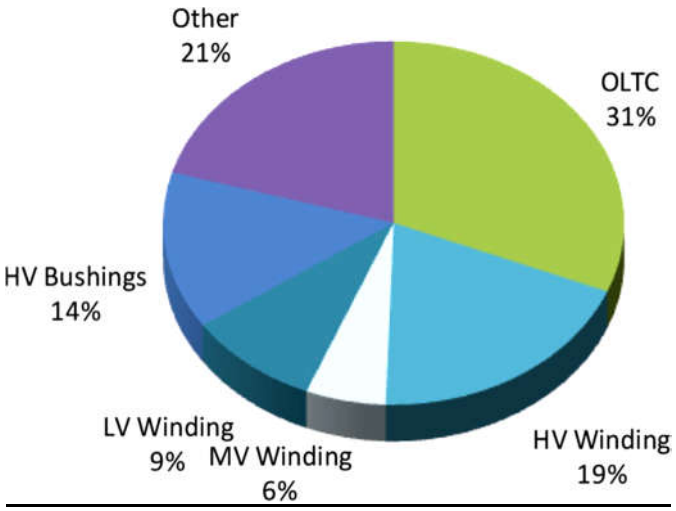

Figure 2.1 Failure cause analysis of substation transformers based on CIGRE [3].

A survey conducted in South Africa showed that the overall annual failure rate of power transformers is at most 0.1 % until the transformers reach 30 years of operation, when the failure rate begins to increase. For high voltage-rated power transformers, OLTCs, bushing and protection equipment (switchgear) are the main causes of the transformer failures. For low voltage-rated power transformers, winding and bushing are the main causes of the failures [4].

The above transformer failure surveys demonstrate that OLTCs, winding and bushing are the most vulnerable subsystem in a power transformer and the failure of a subsystem may lead to a total failure of a transformer. Among them, this thesis focuses on OLTCs and main winding to develop effective and field applicable condition monitoring and diagnosis techniques for sustainable and reliable operation of a power transformer.

In the following sections, a comprehensive literature review is conducted on state-of-the-art techniques regarding condition monitoring and diagnosis of OLTCs and main winding. The review covers necessary background knowledge such as construction, operation and failure modes of OLTCs and main winding.

2.2 Condition Monitoring of On-load Tap Changer (OLTC)

2.2.1 OLTC's Construction and Operations

A tap changer is used to regulate the output voltage of a transformer to respond to load condition changes. Especially, the OLTC is designed to alter the turns ratio of a transformer's winding without service interruption. It changes the tap positions connected to different percentages of a transformer's winding by a mechanical operation completed in a few hundred milliseconds. An OLTC consists of a number of mechanical and electrical components to change tap positions. The switching process of an OLTC requires a complicated and automated mechanical manipulation. Therefore, it is essential to understand the hardware construction and operational sequence of an OLTC for successful condition monitoring.

An OLTC has a variety of design parameters including construction, control scheme, placement location, tap changing mechanism, electrical connection, switching cycle pattern, switching contact material, number of tap positions, transition impedance type, cooling oil sharing type and switch type [6]. The different combinations of the above parameters can lead to different switching operations and events in OLTCs. An OLTC is normally installed in either (1) an independent compartment, i.e., installed in a separate enclosure and then attached onto the side of a transformer's main tank (Figure 2.2, called a compartment type OLTC) or (2) in-tank, i.e., placed inside a transformer's main tank

(Figure 2.3, called a column type OLTC). For a large power transformer, a column type OLTC is normally preferred owing to its easier connection to the transformer's tap windings.

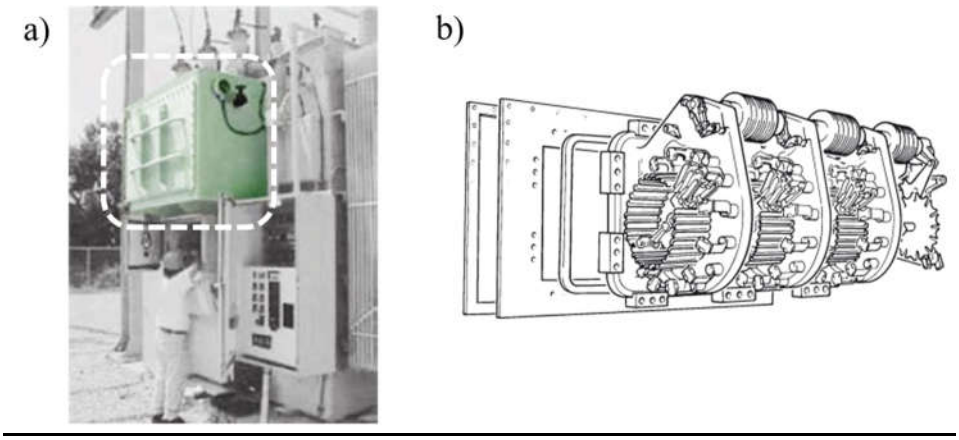

Figure 2.2 Compartment type OLTC (a) compartment type OLTC attached onto a transformer's main tank [7]; (b) internal structure of compartment type OLTC (three phases) [8].

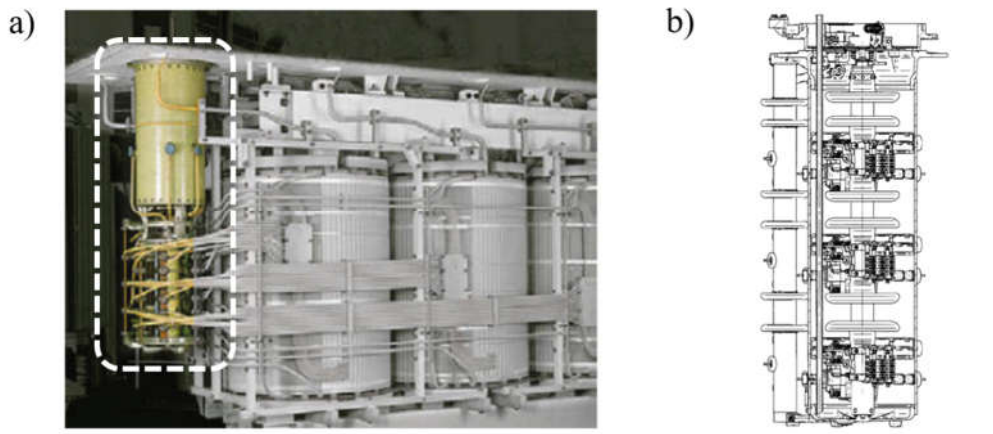

Figure 2.3 Column type OLTC (a) column type OLTC installed vertically inside a transformer [7]; (b) internal structure of column type OLTC (three phases) [9].

Changing the turns ratio of a transformer can be implemented at either its primary side or its secondary side. Thus, OLTC can be connected to either a low voltage side (popular in North America) or to a high voltage side (popular in Europe and Australia) of the transformer's main windings. The OLTC's connection location affects the insulation system design. For instance, an OLTC connected to a high voltage side may experience comparatively low load current but it would have more chance of experiencing arcing or discharge activities compared to an OLTC connected to a low voltage side. Instead of having low voltage to the OLTC, its insulation may be subject to high load current.

An OLTC should have a desirable withstanding capability over electrical stress especially when it changes its tap positions under load current. Also, the switching operation should not interrupt load current. Accordingly, it is important that an OLTC keeps its load current flowing while it switches

between tap positions. The current load is maintained by arcing formed between a selecting switch and a tap position's contact. The arcing can be induced especially when a mechanical gap is formed between them. The ongoing load current can be sustained by the electrical current channel formed by the arcing. If the arcing activity diminishes earlier than the completion of OLTC's switching operation, the load current will be interrupted due to the loss of the current flowing path. Thus, such early arcing quench can cause a transformer's service interruption though it is for a very short time. On the other hand, if the arcing does not diminish even after the completion of OLTC's switching, a short circuit path can be formed between tap windings. This may cause damage to the windings due to the closed loop of the above short circuit.

To avoid the load current interruption and limit the circulating current between tap windings during the OLTC's operation, transition impedance can be added to the path of the transition switch. Transition impedance can prevent the above winding damage due to a short circuit even when a tap selector is connected across two tap positions simultaneously. Depending on the type of transition impedance, it can be classified as a reactor type (popular in the US) or a resistor type (popular in Europe) [10].

According to the method of tap switching, there are two switching cycle modes, i.e., flag cycle and pennant cycle as shown in Figure 2.4. In a flag cycle switching mode, the main current is diverted from the main switch before the circulating current is formed during a tap changing operation as shown in Figure 2.4(a) and 2.4(b) [11]. The pennant cycle mode can be further classified into two types, i.e., symmetrical and asymmetrical pennant cycles. Figure 2.4(c) shows an asymmetrical pennant cycle, which has two different current flows depending on the direction of switch movement. Figure 2.4(d) shows a symmetrical pennant cycle. Regardless of the switch movement direction, a circulating current is made before the main current is diverted from the main contacts [11]

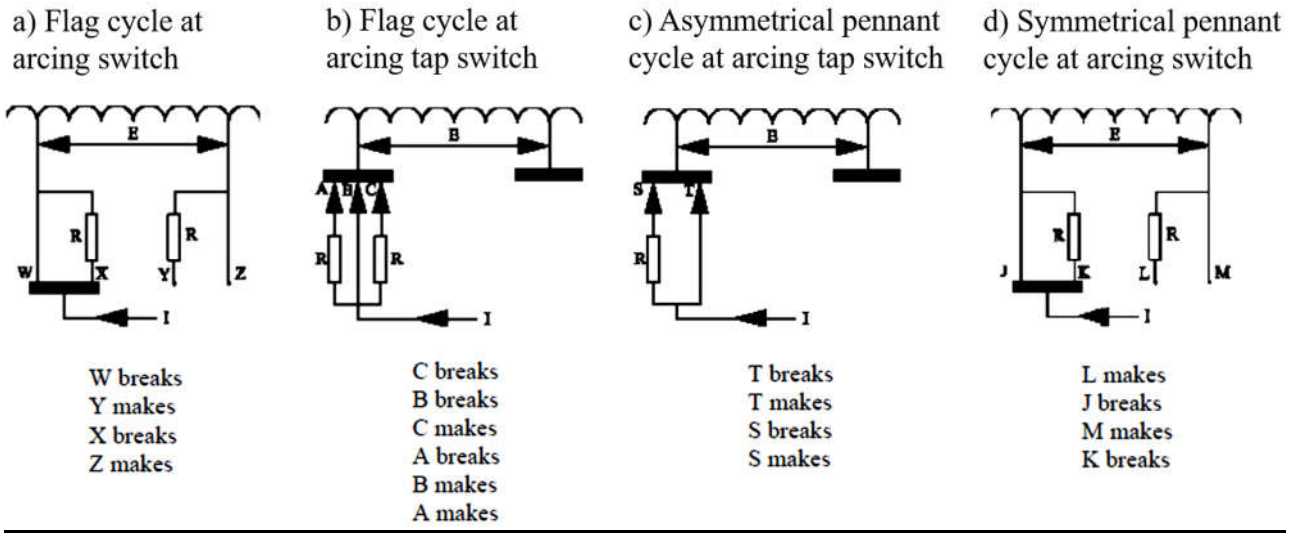

Figure 2.4 Contact operating sequence of different types of switch [11].

An OLTC's switches may experience excessive electrical and thermal stresses when arcing is generated in the course of the switches' making and breaking operations. The mitigation measure of arcing can be the insulation medium, i.e., mineral oil (oil type interrupter) or vacuum (vacuum type interrupter) to suppress or extinguish the discharge exertion. Mineral oil is essentially used in OLTCs for the purpose of insulation, cooling and arcing suppression. The oil can be shared with the transformer's main tank or used exclusively only for OLTC depending on the power rating of the transformer and operational considerations. The quality of the oil in an OLTC can be compromised due to the aforementioned arcing activities. Thus, the OLTC's oil filter needs to be cleaned or exchanged regularly to prevent a reverse effect caused by contaminated oil.

Another way, using a vacuum type interrupter, provides a reliable and effective arcing suppression environment. Arcing can be quenched by the enclosed vacuum interrupter isolated from the oil. By using a vacuum type interrupter, oil is less affected and contaminated by the OLTC's switching operations. Figure 2.5 shows an OLTC equipped with a vacuum interrupter and the surface condition of its switch after 1.8 million operations.

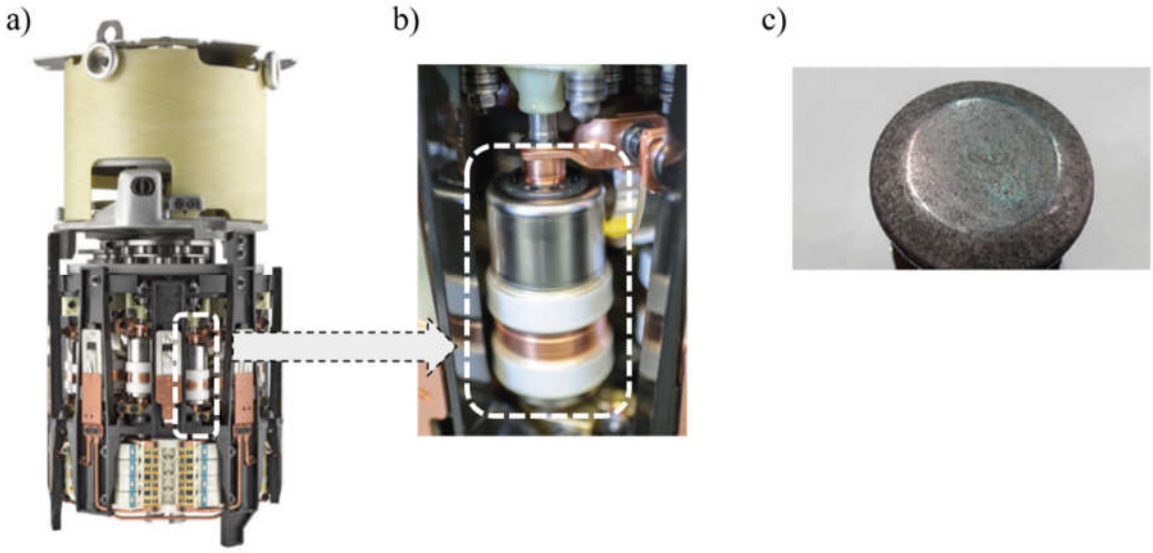

Figure 2.5 (a) OLTC equipped with vacuum interrupter; (b) vacuum interrupter; and (c) vacuum interrupter contact after 1.8 million times of electric arc furnace operations [7].

According to the tap position selection (switch moving mechanism) method, an OLTC can be classified into a diverter switch type in Figure 2.6(a) or a selector switch type as shown in Figure 2.6(b). The diverter and selector switches are required to carry the rated current of the power transformer during events of 'make' and 'break' [12].

In a diverter switch type OLTC with two tap selectors, one tap selector switches to the next tap position while the other tap selector stays at the current tap position. Then the two tap selectors make connections with the current and the next tap position, respectively. After the completion of the tap

selection, a diverter switch is then activated to switch over between the two tap selectors having two sets of contacts (i.e., main and transition contacts). Each set of contacts is connected to either the current tap position or the next tap position.

In a selector switch type OLTC as shown in Figure 2.6(b), a tap position is selected by moving a tap selector consisting of a main switch and two transition switches. To move the main switch from a current tap position to a next tap position, both sides of the transition switches help a smooth switch-over between them. Additionally, a coarse change-over selector is used when a large voltage change is required.

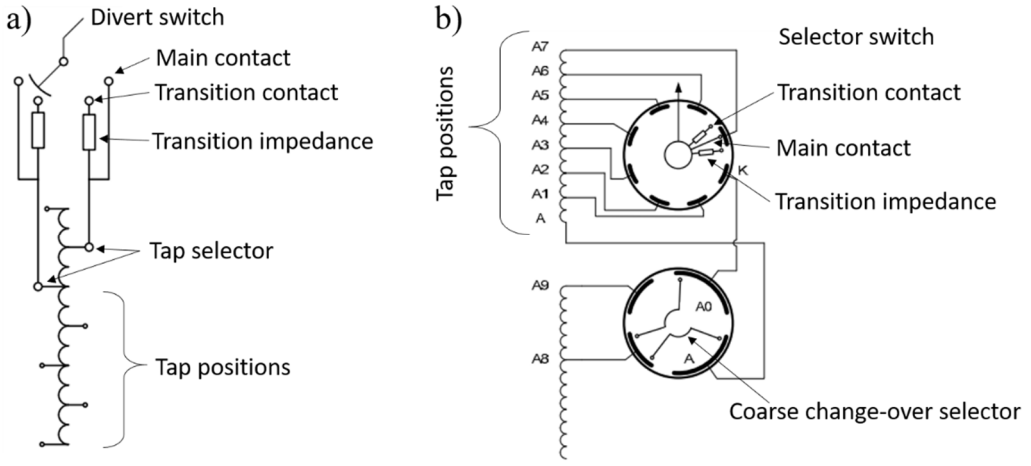

Figure 2.6 OLTC categorisation according to the tap position selection method (a) diverter switch type OLTC; (b) selector switch type OLTC.

2.2.2 Defects and Failure Mode of OLTC

An OLTC's switching operation may cause excessive mechanical stress to its components such as springs, braided contact leads, screw connections and energy accumulators. Over a long period of time, such mechanical stress may cause a malfunction or damage to the components and even lead to failure of the OLTC. For example, mechanical malfunction may hinder moving components of an OLTC during its operation, which can lead to an incomplete switch connection finally causing a short circuit or an open circuit.

The whole operational procedure of an OLTC is mechanically interlocked. Thus, it is important to make sure that all of the motor drive system, drive shaft and switches work in their designed sequence and time frame. Otherwise, the OLTC's operation can be disrupted, which may cause severe damage to an OLTC or even the whole unit of a transformer.

The causes of OLTC failures can be classified into three types: mechanical defects, electrical contact defects and dielectric defects [3]. Mechanical defects can be due to the degradation and failure of mechanical components such as bearings, switches, energy storage system, drive shaft and motor

drive system [13]. Such degradation and failure may be caused by: (1) a damaged or broken shaft, which disturbs synchronisation between moving parts, selector switch and change-over selector; (2) sluggish operation or interruption by abrasion, poor lubrication or degraded energy storage system, which can damage a transition impedance; (3) a shortage of contact pressure from wear, a degraded energy storage system or carbon sediment between contacts; (4) a failure of the braking mechanism of the Geneva wheel or locking system; (5) excessive shaking or vibration after losing tension on a joint or degraded moving components in a drive system; and (6) degraded performance of energy storage system. The aforementioned mechanical defects may not cause an immediate reverse effect on the function of OLTC at an early stage. However, an abrupt service interruption or failure of OLTC can occur unless suitable action is taken in time.

Inside an OLTC, a chemical reaction on the contact surface of an OLTC's switch can considerably damage the electrical properties of the contact. The chemical reaction with oil can promote the ageing process of the contact surface causing filming, coking and carbon formation. At an early stage of the chemical reaction, the contact surface of an OLTC's switch may experience a slightly increased contact resistance. Eventually, the contacts' resistance increases significantly due to contaminating layers forming a thin film on the surface of the contact [14]. The increased resistance between contacts may further lead to a temperature increase of the surrounding area of the contacts [15]. At some stage, coking development can be accelerated and consequently the conductive characteristics of the contacts can be compromised.

The condition degradation of OLTC's contacts can also be expedited by a number of factors: (1) infrequent operation of some tap positions over a long period of time, which leads to the formation of a contaminant layer on the contact's surface [16]; (2) high demanding load condition (peak current), which can cause further damage to the contact surface of switches; (3) low contact pressure, which is not good for removing the contaminated layer on the surface of the switch contact; (4) being exposed to high temperatures, which may accelerate harmful chemical reactions; and (5) using copper or brass-based material for switches, which presents a higher possibility of a surface film forming than for silver [17]. However, silver sulphide, a by-product from the silver coating, has been reported to be a potential damaging factor to a transformer [18].

Coking especially shows a negative effect on the electrical characteristics of a contact surface. Coking is a formation of pyrolytic carbon occurring at temperatures over 300°C [19]. Coking can be formed on the contact surface of stators, rotors and other moving parts of an OLTC. Additionally, the surface of contacts can be worn off. Furthermore, arcing, high energy discharge and high temperatures inside an OLTC can lead to deterioration of mineral oil and generate by-products in the OLTC. The

dielectric property of the oil inside an OLTC can be evaluated by a Dissolved Gas Analysis (DGA) method.

2.2.3 OLTC Condition Monitoring Methods

Several international standards [6, 20 - 25] have been developed to identify the aforementioned OLTC faults and assess the condition of an OLTC. However, there is still a lack of information regarding the implementation of OLTC condition monitoring and diagnosis, i.e., sensor selection (type and specification), sensor installation, measurement setup, data collection and data processing. Especially, it is hard to find a guideline on how to interpret the obtained data and subsequently evaluate the actual condition of an OLTC. This section presents a review of available OLTC condition monitoring methods and also identifies a gap in the methods of condition monitoring for OLTCs.

2.2.3.1 Offline Condition Monitoring Methods for OLTC

Offline OLTC condition monitoring methods are based on resistance measurement. It can evaluate the surface condition of the OLTC switch's contact. However, the transformer is required to be removed from service during the resistance measurement. The measurement requires a constant Direct Current (DC) voltage to measure the corresponding current [26 - 27]. The current is varied depending on the surface condition of the OLTC switches' contact. There are two types of resistance measurement: static or dynamic resistance measurement.

a. Static Resistance Measurement (SRM)

Static Resistance Measurement (SRM) evaluates the contact resistance of an OLTC especially when the OLTC is at a stationary condition [28]. The contact resistance measured by this method can indicate possible thin film formation, coking and other condition changes on the contact surface of the OTLC's switches. The measured resistance normally includes the impedance of transformer winding and bushing. The corresponding resting time prior to resistance measurement is required to mitigate the effect of reactance induced by winding. Moreover, the transformer under test should be demagnetised to remove residual effects. To obtain further condition information of the switches, Dynamic Resistance Measurement (DRM) can be adopted.

b. Dynamic Resistance Measurement (DRM)

DRM is performed when the OLTC switches are moving. Since it can measure both transitional and stationery resistance when tap positions are changing, the DRM method can measure all relevant resistance of switches (including diverter switch contact, tap selector contact, main switch, and transition switch) and transition impedances [10, 29 - 30].

While implementing a DRM, all the tap positions of an OLTC are swept thoroughly. However, since the tap positions are switched every few seconds, the interval time between steps may not be long enough for current to stabilise due to the existence of the inductance (e.g. transformer winding). Due to the lack of resting time between operational steps, DRM can be relatively less accurate than SRM. However, though DRM has this drawback, it is often adopted owing to its versatility in OLTC condition monitoring. It can provide a resistance profile over all steps for representing the condition of contacts. Additionally, it also can detect a switching time deviation between operational sequences caused by mechanical defects [28].

However, both DRM and SRM measurements are vulnerable to temperature change and also greatly affected by the condition of the transformer's winding. Compensations for temperature and transformer condition should be made.

Extensive caution should be taken when applying DC voltage to a transformer since high DC voltage can damage a transformer's winding and affect the condition of the surface of the OLTC contacts. To improve sensitivity of the resistance measurement, a lower DC voltage can be applied to contact defects [29]. However, it may impose another difficulty in interpreting the test results due to signal fluctuations by the low DC input voltage. Also, the low DC voltage sometimes can be disrupted or discontinued by other major components such as winding and joints [29]. Moreover, due to the different reaction of contacts to voltage changes, resistance measurement at different voltage levels may produce different results. Thus, the voltage level should be maintained to avoid an error between measurements.

2.2.3.2 Online Condition Monitoring Methods for OLTC

Online condition monitoring methods for OLTCs present enormous benefits in terms of versatility and applicability. Such methods include DGA, temperature measurement, shaft angle measurement, motor power measurement and vibration signal measurement. This section will introduce these methods.

a. Dissolved Gas Analysis (DGA)

DGA has been recognised as a reliable condition monitoring and diagnosis method for an oil-filled power transformer. It can recognise inception faults due to PD, arcing, high energy discharge and high temperatures. DGA interpretation schemes for an oil-filled OLTC are provided in several publications [31 - 33].

Figure 2.7 presents Duval's triangles for interpreting dissolved gases collected from a transformer's main tank and its OLTC, respectively. DGA for OLTC has six zones, which can be used to identify normal operation (N), thermal fault and coking (T2, T3, X3), abnormal arcing (D1)

and initial thermal fault (X1). Severe thermal faults can be further indicated by T2 (300 < T < 700°C) and T3 (T > 700°C). X3 is an indication of light coking, an early stage of thermal fault. T2 and T3 can indicate a progress of coking in the OLTC.

DGA Interpretation for Transformer		DGA Interpretation for OLTC	
Zone	**Identification**	**Zone**	**Identification**
PD	Partial discharges	N	Normal operation
D1	Discharges of low energy	T3	Severe thermal fault T3 (T>700°C), coking
D2	Discharges of high energy	T2	Severe thermal fault T2 (300<T<700°C), coking
T1	Thermal faults of temp. < 300 °C	X3	Fault T3 or T2 in progress (mostly) with light coking or increased resistance of contacts
T2	Thermal faults of temp. 300 °C < T < 700 °C		
T3	Thermal faults of temp. > 700°C	D1	Abnormal arcing D1 (outside of zone N)
DT	Mixtures of electrical and thermal faults	X1	Thermal fault in progress

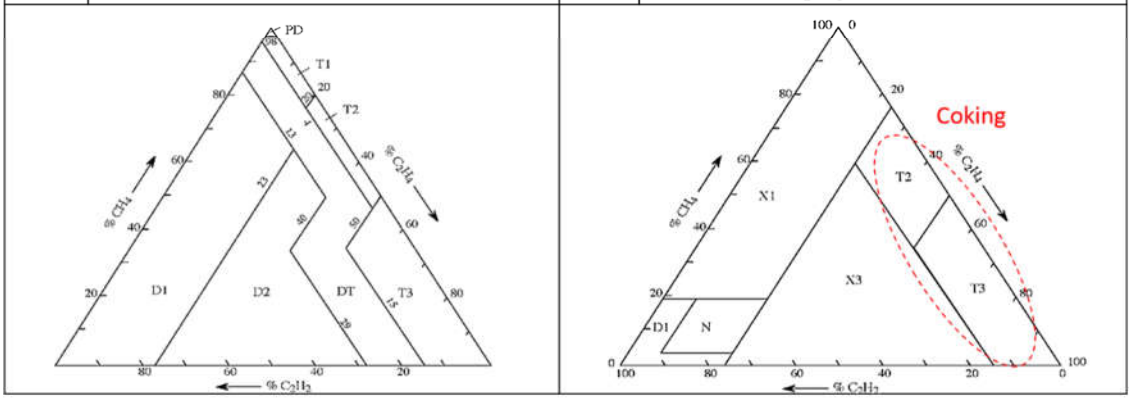

Figure 2.7 Duval's Triangles for DGA interpretation for transformer's main tank and OLTC [33 - 34].

However, the sensitivity of DGA is relatively low since a considerable change in the volume of a particular gas needs to indicate dielectric faults. For example, 10 mJ of PD activity (equivalent to 1,000,000 pC) is considered as a very serious discharge and can cause damage to insulation [35 - 38]. However, 100 mJ of PD activity is required to generate 0.1 ppm of gas to meet the minimum analytical gas detection limit for DGA. If a decision is made based on DGA results, there may not be sufficient time to remedy the fault to prevent a potential failure in the OLTC. Thus, solely using DGA may not be effective for OLTC condition assessment.

b. Temperature Measurement

An abnormal discharge or high temperature can be detected by temperature measurement. For an effective temperature measurement, sensors must be installed inside the OLTC compartment or transformer tank. However, it is not an easy task to install a temperature sensor to an in-service transformer. Moreover, the interpretation of the test result is not a trivial task since the measurement is easily affected by various measurement conditions.

c. Motor Power Measurement

Increased motor power indicates extra power consumption caused by additional friction in the motor drive system and moving parts of the OLTC. Thus, motor power measurement has been adopted to diagnose excessive friction and faults in the motor drive system of an OLTC [9]. As shown in Figure 2.8, a deviation (compared to the normal condition) in the envelope curve of the motor current reveals a high friction issue in the OLTC.

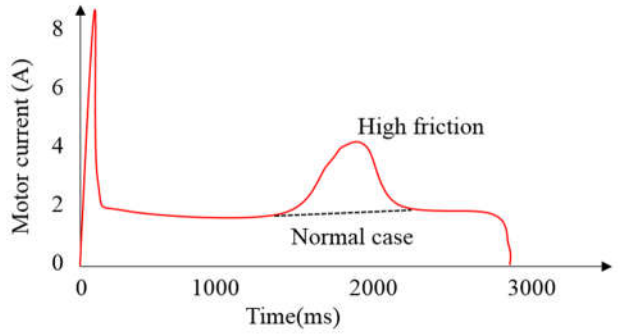

Figure 2.8 Motor current measurement (in normal condition and high friction conditions) [13].

If an OLTC's drive shaft becomes loose, the required initial torque can also be changed. As a consequence, the initial motor driving current may be lower than that of normal condition (Figure 2.9).

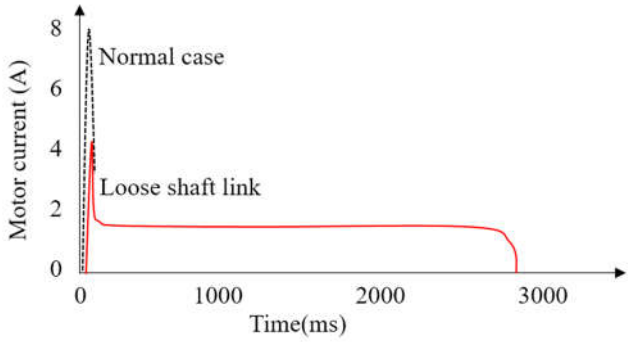

Figure 2.9 Motor current at an initial stage of operation (normal and loose connection in motor drive system) [13].

d. Vibration Signal Measurement

Vibration signal measurement can detect a wide range of OLTC failures when a transformer's OLTC in operation. A number of vibration sensors are mounted on the outside wall of an OLTC to acquire vibration signals generated by the OLTC's operation. The acquired vibration signal is then processed and its characteristics such as amplitude, the number of peaks and event time intervals are used to infer the mechanical condition of the OLTC [13, 39 - 44].

Each OLTC has its own unique vibration signal signature, which can be used as a fingerprint of the OLTC's condition. By comparing these signatures from the same (type) OLTC over a period of

time, a mechanical condition change of the OLTC can be tracked. However, there are still some challenges in using the vibration signal measurement, such as: (1) effective signal acquisition in a substation environment; (2) important parameter extraction from a noise corrupted signal; and (3) data interpretation for an ultimate condition assessment.

Vibration signals consist of a series of bursts and peaks generated by OLTC's mechanical operations. The main idea of using vibration signals is to analyse the time stamps of each peak and to compare the amplitudes of each peak based on a 'before and after' comparison method [13]. However, extracting exact event time stamps of the peaks is not a trivial task. Difficulties arise from (1) the oscillatory nature of vibration signal; (2) the complex reflections of vibration signals; (3) the different propagation paths of vibration signals; and (4) the very short duration of time of OLTC's switching operation (a few hundred milliseconds). Considering the short switching time of an OLTC, an inaccurate event time extraction can lead to an inappropriate assessment on the OLTC's mechanical condition.

For processing the vibration signals, a number of signal processing techniques have been applied such as wavelet transform, Hilbert transform and envelope curve extraction method, etc. [13, 39 - 44]. After signal processing, the resultant data are compared with those obtained from the previous measurements to evaluate a mechanical condition change of the OLTC. However, existing signal processing techniques provoke an unwanted time shift from the original time information. The time error can result in difficulties in comparing with previous results. To tackle the issue, this thesis has developed advanced signal processing techniques to effectively process the measured vibration signal and subsequently correlate the result to the OLTC's mechanical condition [45 - 46].

Another important issue in interpreting vibration signals is how to correlate each peak of the measured vibration signals with the actual mechanical operation of an OLTC. Vibration signals generated by mechanical events involved in an OLTC's operation vary in amplitude and waveform shape. Identifying the event source of the measured vibration signal can be difficult since the signal may originate from different types of components or different operation cycles. Moreover, each OLTC manufacturer may have its own unique or various operational sequences of OLTCs. The various ranges of OLTCs may also pose challenges in processing and interpreting vibration signals.

To deal with the above issues, this thesis has developed a novel joint vibration and arcing signal measurement system to interpret vibration signals and correlate them with the corresponding mechanical operation of OLTCs [47].

2.2.3.3 Summary of OLTC Condition Monitoring Methods

A summary of OLTC condition monitoring methods is presented in Table 2.1. Temperature measurement, shaft angle measurement, motor power measurement, DGA and vibration signal measurement are online techniques enabling measurement during continuous operation of a power transformer.

For evaluating the condition of OLTC's dielectric and electrical contact defects, there are well developed methods and products like DGA and resistance measurements (DRM, SRM). However, it is still challenging to apply vibration signal measurement to OLTC's mechanical condition monitoring though it can provide many benefits. Given the complicated and various configurations, control mechanisms and operating conditions of OLTCs, the correlations between vibration signals and mechanical events are not well understood. Moreover, vibration signals induced by OLTC's operation is hard to process due to its complicated nature caused by complex propagation paths and noisy environment.

Thus, there are essential research and development tasks for properly utilising vibration signal measurement for OLTC's mechanical condition monitoring. They are: (1) extracting informative characteristics of vibration signals; (2) correlating these characteristics to actual events of OLTC operations; and (3) subsequently evaluating the mechanical condition change of an OLTC. Therefore, this thesis is aimed at investigating and further developing vibration signal measurement method for expediting mechanical condition monitoring of an OLTC.

Table 2.1 Summary of OLTC condition monitoring methods.

Test locations / Methods	Diagnosis					Operation	
	Motor drive		Electrical contacts		Dielectric	Online test [Reference]	Sensor installation
	Up to springs	Behind springs	Arcing switch	Tap selector			
Visual inspection	Wear and defects		WD + misalign	Not applicable	Arcing S/W	X	Oil removal
Static resistance measurements	Not applicable		Coking, wear, misalignment		Not effective	X [29]	Moderate
Dynamic resistance measurements	Not applicable	Defects	Coking, wear, misalignment		Not effective	X [15,30,31]	Moderate
Temperature	Not applicable		Coking and overheated		Not effective	O [16-19]	Difficult
Shaft angular position	Not effective	FW, Synch.	Friction	Not effective	Not applicable	O	Moderate
Motor power Measurement	FW	Not effective		FW	Not applicable	O	Easy
DGA	Not applicable		Coking, wear, discharges, overheat		Surface discharge	O [32-34]	Not required
Acoustic vibration	MD		MD + excessive arcing and friction		Not applicable	O [10-11]	Easy

DGA = dissolved gas analysis; FW = friction and wear; WD = wear and defects; MD = mechanical defects; S/W = switch

2.3 Condition Monitoring of Insulation System of a Transformer

As mentioned in Section 2.1, the insulation systems of a transformer's main winding can eventually deteriorate and further development may lead to transformer failure. In this section, the construction and failure mechanisms of a transformer's main winding are reviewed. It is followed by condition monitoring methods of a transformer's insulation systems.

The transformer's insulation system is constantly exposed to severe thermal, electrical and mechanical stresses. Silk, cotton and asbestos were used in the early power transformer's insulation system without any other insulation medium. Then, resin paper impregnated with shellac was adopted to effectively withstand such stresses. After that, oil impregnated Kraft paper has been widely used. Kraft paper demonstrates a greatly improved insulation performance especially when it works together with oil, i.e., in oil-filled power transformers. In modern transformers, oil has become the essential working medium as it is both an insulating liquid and a coolant.

2.3.1 Solid Insulation System

Owing to the desirable mechanical and dielectric properties of paper and pressboard, solid insulation has become the most widely used insulation material. Additionally, the insulation property of Kraft paper and pressboard greatly improves when they are immersed in oil [48 - 49]. In a power

transformer, insulation paper is used where flexibility is required such as insulating wires, windings, small components and metal parts. Pressboard is applied where more mechanical strength is demanded such as in a support structure, bed and space block. Figure 2.10 illustrates insulation paper and pressboard inside a transformer.

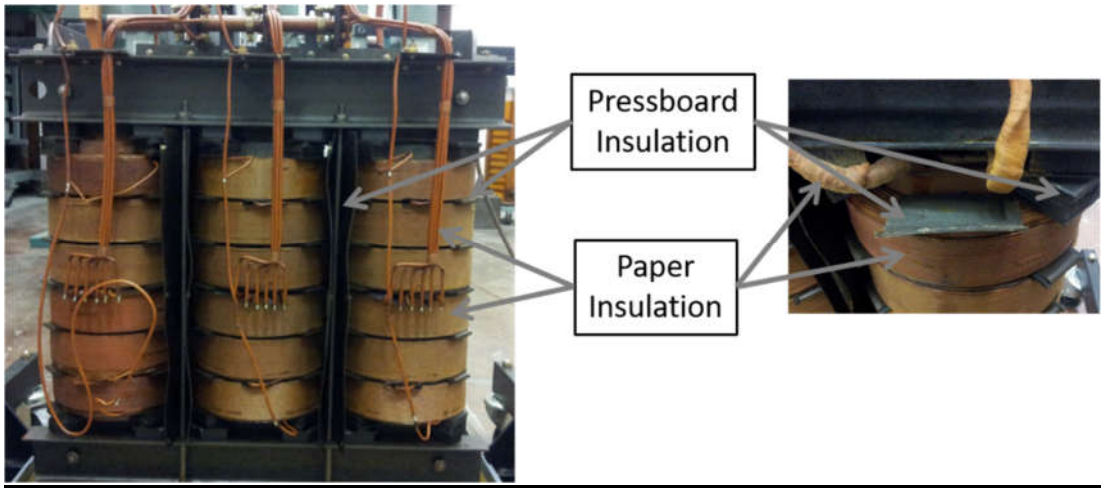

Figure 2.10 Solid insulation (paper and pressboard) used inside a transformer.

The original material of paper and pressboard is wood, which is composed of 40–50 % cellulose fibre, 10–30 % hemi-cellulose, and 20–30 % lignin and waxes. Among the composites, lignin has a hydrophobic nature good for preventing moisture ingression, although, it can cause paper to be brittle losing mechanical strength. Hemi-cellulose can significantly affect the insulation condition of paper as it is hygroscopic and can absorb water easily.

The Kraft process was adopted to treat raw material (i.e., wood) to make insulating paper suitable for insulating a transformer. The Kraft process is depicted in Figure 2.11. It can effectively reduce the amount of lignin and hemi-cellulose but still maintain the cellulose fibre [50]. During the Kraft process, chipped wood is processed with a mixture of sodium hydroxide or sodium sulphide in aqueous solution at a high temperature. Then it is washed, cooked, dried and processed to produce insulation paper or pressboard. Kraft processed insulation paper has an improved composite ratio of 75–90 % cellulose, 10–15 % hemi-cellulose, 0–5 % lignin and 0.2–0.8 % mineral substances [51]. Normally, new Kraft paper has a Degree of Polymerisation (DP) value of 1000–1300 compared to 2000 for the original wood. Though the DP value drops after the Kraft process, the obtained Kraft paper (cellulose) shows a significant improvement in both mechanical and electrical strength.

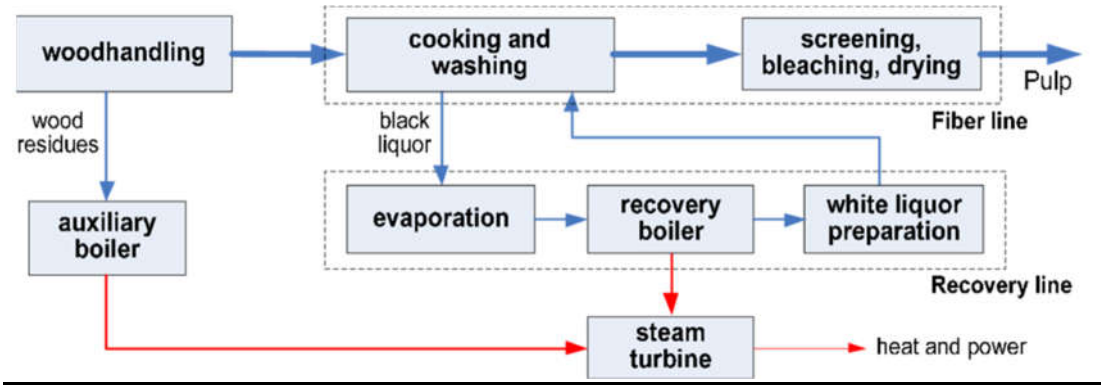

Figure 2.11 Kraft process [52].

Figure 2.12 shows the structure of cellulose (solid insulation). The significant improvement of its mechanical strength comes from its microcrystalline structure and molecule chain alignment.

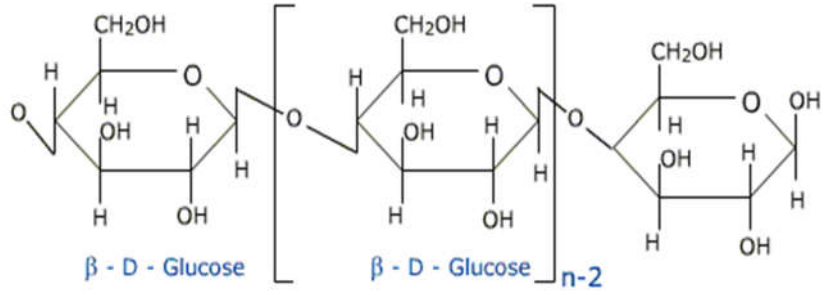

Figure 2.12 Cellulose (solid insulation) structure [52].

2.3.2 Transformer Oil

Transformer insulating oil has two important roles: cooling and improving dielectric strength. It also enhances the properties of insulation paper and pressboard insulation. Transformer oil should have the following properties: (1) high dielectric strength; (2) low dielectric losses; (3) good thermal conductivity; (4) low viscosity; (5) high oxidation resistance; and (6) low volatility and high flash point.

2.3.3 The Ageing of a Transformer's Insulation System

The ageing of a transformer's insulation paper is a process of losing bonds between the cellulose fibres due to the breakdown of glucose bonds and inter/intra-molecular bonds. Hydrolytic, thermal and oxidative reactions can accelerate the ageing of a transformer's insulation paper. Various ageing by-products like water, hydrocarbon gases, furan composite, carbon dioxide and carbon monoxide can be produced and resolved into the transformer's oil.

Major contributors to hydrolytic degradation in insulation paper are water and acids which can lead to the breakdown of glucose bonds. The disconnected glucose units or short chain glucose units can form degradation by-products such as furans, levulinic acids and formic acids [53 - 54]. Levulinic

acid can be further degraded into an acidic compound. Formic acid may generate carbon monoxide and water.

Oxidation is affected by the nature of an oxidising agent and the formation of a hydroxyl group. Oxidation in oil may affect the process of oxidation in insulation paper. The oxidation of oil produces several acids which are absorbed by the insulation paper. The acid absorption accelerates the oxidation process in insulation paper.

Temperature has a significant impact on hydrolytic and oxidative degradation process. At high temperature, thermal energy contributes to break glycosidic bonds.

2.3.4 Condition Monitoring and Diagnosis Methods for Transformer's Main Winding

Over past decades, various insulation condition monitoring and diagnosis methods have been developed for a transformer's insulation system. They can be categorised into two groups as follows:

1. Chemical test methods – DGA, oil test and furan analysis.
2. Electrical test methods – Polarisation and Depolarisation Current (PDC), Frequency Domain Spectroscopy (FDS) and PD measurement.

The chemical test methods are widely used to evaluate the condition of the oil-insulation paper system including the transformer's main winding. In addition, moisture measurements have been conducted for the oil-insulation paper system. This is because water can accelerate insulation paper ageing, which reduces both its dielectric and mechanical strength insulation paper.

The following sections provide a review on chemical and electrical diagnosis methods targeting the winding insulation system of a transformer.

2.3.4.1 Chemical Test Methods for Oil-impregnated Insulation System

a. Dissolved Gas Analysis (DGA)

In the degradation process of an oil immersed insulation system of a transformer, various chemical reactions generate certain gases. A considerable amount of these gases dissolve into the oil [55 - 56]. Electrical and thermal faults inside the oil-insulation paper system of a transformer can be revealed by DGA measurement conducted on an oil sample collected from a transformer. A number of DGA interpretation schemes have been developed by organisations such as, the Institute of Electrical and Electronics Engineers (IEEE) C57.104-2008 [55], International Electrotechnical Commission (IEC) 60559 [57], CIGRE TF 15.01.01 [58] and IEC Publication 61464 [59]. A brief review of these schemes are provided as follows.

b. Key Gas Method

The key gas method examines the relative concentrations of six gases: hydrogen (H_2), methane (CH_4), ethane (C_2H_6), ethylene (C_2H_4), acetylene (C_2H_2) and carbon monoxide (CO). It can diagnose four types of incipient faults including arcing, PD, overheating in oil and overheating in solid insulation. However, the accuracy of the key gas method is not high enough for accurate diagnosis [60 - 61].

c. Doernenburg Ratio Method

Four gas ratios,C_2H_2/C_2H_4, C_2H_2/CH_4, CH_4/H_2 and C_2H_6/C_2H_2, are used in this method [55, 62]. The predefined interpretation criteria of the four ratios are shown in Table 2.2 [55]. To apply the Doernenburg method for diagnosing a transformer's insulation faults, the minimum amount of gas concentration is required to have a reliable result. Therefore, the obtained gas concentration level should be two times higher than the threshold concentration level as shown in Table 2.3.

Table 2.2 Doernenburg ratio method [55].

Fault identification	CH_4/H_2	C_2H_2/C_2H_4	C_2H_2/CH_4	C_2H_6/C_2H_2
Thermal decomposition	>1	<0.75	<0.3	>0.4
Partial discharge	<0.1	Not significant	<0.3	>0.4
Arcing	>0.1 to <1	>0.75	>0.3	<0.4

Table 2.3 Threshold of gas concentration in the Doernenburg ratio method [55].

Dissolved gas	Minimum concentrations (ppm)
H_2	100
CH_4	120
CO	350
C_2H_2	35
C_2H_4	50
C_2H_6	65

d. Rogers Ratio Method

The Rogers ratio method is similar to the Doernenburg ratio method. However, it can be used even when the obtained gas concentrations are below the minimum thresholds in Table 2.3 [55].

The Rogers ratio method can detect twelve incipient faulty symptoms using four gas concentration ratios of C_2H_4/C_2H_6, CH_4/H_2, C_2H_2/C_2H_4 and C_2H_6/CH_4 [63]. Among the four ratios, it was found that C_2H_6/CH_4 does not show high correlations with particular faults [60, 62]. Thus, that gas ratio is not used in the updated Rogers ratio method. As such, the updated Rogers ratio method only identifies six faults as shown in Table 2.4 [55]. The diagnosing accuracy of Rogers ratio method is not very high [64].

Table 2.4 Updated Rogers ratio method [55].

Fault identification	C_2H_2/C_2H_4	CH_4/H_2	C_2H_4/C_2H_6
Unit normal	<0.1	>0.1 to <1	<1
Partial discharge	<0.1	<0.1	<1
Arcing	0.1 to 3.0	0.1to 1	>3
Low temperature	<0.1	>0.1to <1	1 to 3
Thermal <700º C	<0.1	>1	1 to 3
Thermal > 700 ºC	<0.1	>1	> 3

e. IEC Ratio Method

The IEC ratio method uses three gas ratios, C_2H_2/C_2H_4, CH_4/H_2 and C_2H_4/C_2H_6, as shown in Table 2.5 [34]. The criteria for fault classification of the IEC ratio method is different from those of the Rogers ratio method. The IEC ratio method can attain higher accuracy than the Rogers method in finding a transformer's insulation faults [65].

Table 2.5 IEC codes and associated fault types [34].

Fault identification	C_2H_2/C_2H_4	CH_4/H_2	C_2H_4/C_2H_6
Partial discharge	NS	< 0.1	< 0.2
Discharge of low energy	> 1	0.1 – 0.5	> 1
Discharge of high energy	0.6 – 2.5	0.1 – 1	> 2
Thermal < 300 °C	NS	> 1 but NS	< 1
Thermal: 300 °C < T < 700 °C	< 0.1	> 1	1 – 4
Thermal > 700 °C	< 0.2	> 1	> 4

NS = not significant

f. Duval Triangle Method

Duval triangle is a graphical presentation method as shown in Figure 2.13 [34]. It is built upon the relative portions of three gas concentrations, namely $\%C_2H_2 = x / (x + y + z)$, $\%C_2H_4 = y / (x + y + z)$ and $\%CH_4 = z / (x + y + z)$, in which x, y and z denote the concentrations of C_2H_2, C_2H_4 and CH_4, respectively. The triangle consists of seven fault zones including partial discharge, arcing and thermal faults at different temperature levels (below 300℃, 300℃ to 700℃ and over 700℃). The Duval triangle method has the advantages of high diagnostic accuracy and consistency [62, 64, 66]. However, the Duval triangle does not have a fault-free zone and thus it may not be able to readily recognise the normal condition of a transformer (Figure 2.13) [67].

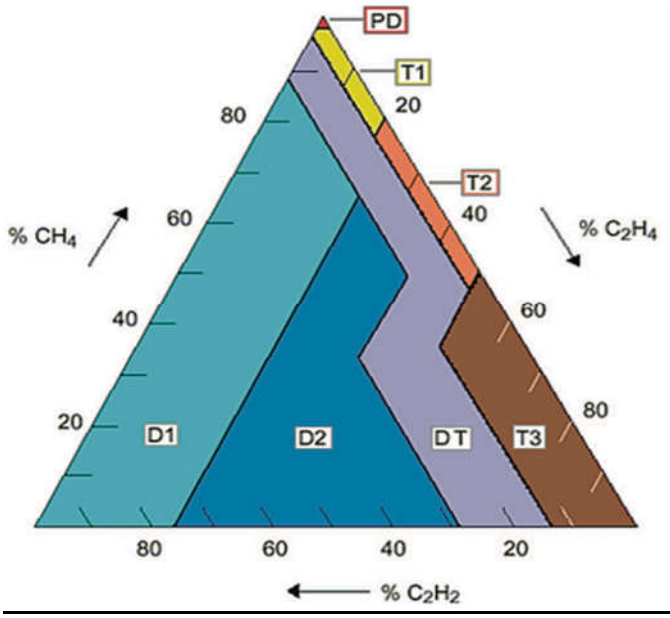

PD	Partial Discharge
D1	Discharges of low energy
D2	Discharges of high energy
DT	Combination of thermal faults and discharges
T1	Thermal faults not exceeding 300°C
T2	Thermal faults exceeding 300°C but not exceeding 700°C
T3	Thermal faults exceeding 700°C

Figure 2.13 Duval triangle method and its interpretation for an oil-filled transformer [67].

g. Duval Pentagon Method

An improved DGA interpretation scheme have been developed as a complementary tool to the Duval triangle [68]. The Duval pentagon scheme coordinates five axes with each axis corresponding to a concentration ratio of the five dissolved gases (H_2, CH_4, C_2H_6, C_2H_4 and C_2H_2). It can identify seven types of faults as summarised in Table 2.6.

Table 2.6 Comparison of fault types between two types of Duval pentagon [68].

Duval pentagon I	Duval pentagon II
PD: corona partial discharges	PD: corona partial discharges
D1: low energy discharges	D1: low energy discharges
D2: high energy discharges	D2: high energy discharges
T3: thermal faults > 700°C	T3-H: thermal faults T3-H in oil only
T2: thermal faults of 300-700°C	C: thermal faults T3-C, T2-C, and T1-C with carbonization of paper
T1: thermal faults <300°C	O: overheating T1-O < 250°C
S: stray gassing S of mineral oil at 120°C and 200°C	S: stray gassing S of mineral oil at 120°C and 200°C

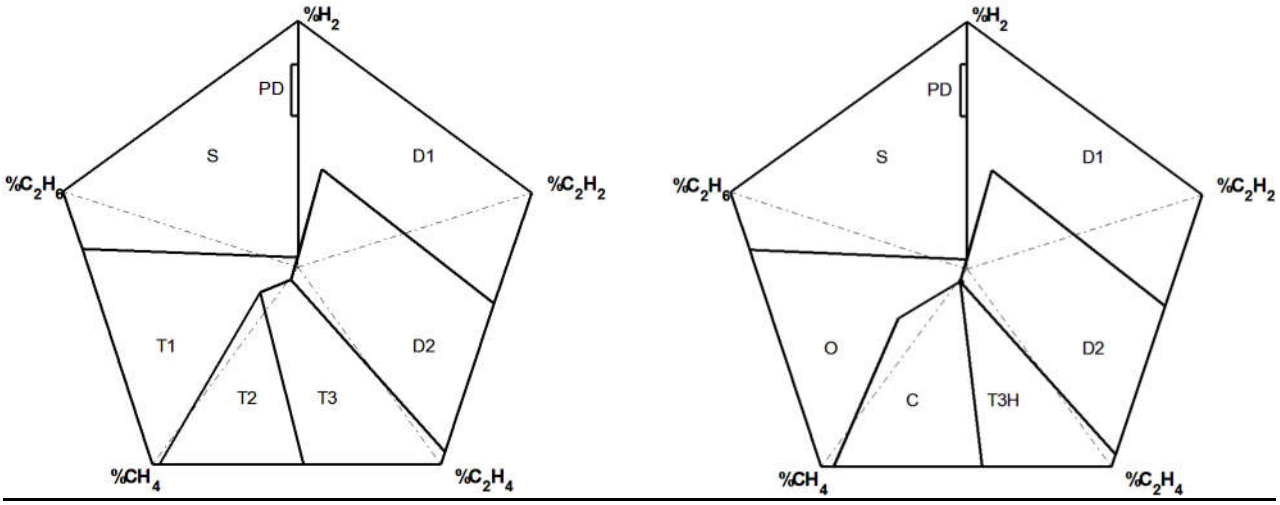

a) b)

Figure 2.14 Coordinates and fault boundaries of the Duval pentagon method (a) Duval pentagon type I; (b) Duval pentagon type II [68].

h. Oil Acidity Test

Acids are produced by oxidation of oil and hydrolysis of the insulation paper [69 - 71]. Most acids have low molecular weight and properties of volatile, low boiling point and high polarity. The oil acidity is measured by determining the amount of alcoholic potassium hydroxide required for neutralising the acids using the pH level of the solution [69].

i. Oil Resistivity Test and Oil Breakdown Voltage Test

A high oil resistivity implies a low amount of free ions, contaminants and conductive particles in the oil [72]. The dielectric strength of oil can be evaluated by measuring the oil breakdown voltage [73]. Breakdown voltage measurement is sensitive to oil quality since it is highly affected by contaminated particles, moisture content and other produced dissolved gases.

j. Moisture Measurement

Moisture in oil-insulation paper can reduce both breakdown strength and PD inception voltage. It can also accelerate the ageing rate of transform insulation. For a heavily loaded transformer, increased moisture can increase the possibility of generating a bubble, which weakens insulation strength and may result in PD [74]. The moisture content in oil-insulation paper can be estimated through moisture diffusion modelling, cellulose adsorption isotherms and dielectric response measurement. Recently, moisture content in oil can be obtained directly by measuring water activity (or relative humidity) and temperature using water solubility of oil [75 - 77], which enables to monitor water content in transformer in real-time.

In a moisture diffusion model, moisture migration can be modelled based on moisture concentration equalisation. Water molecules in a high moisture concentration region tend to move to a lower moisture

concentration region [78]. The macroscopic moisture migration can be modelled by Fick's equation [79]:

$$\frac{\partial C(x,t)}{\partial t} = \frac{\partial}{\partial x}\left(D\frac{\partial C(x,t)}{\partial x}\right) \tag{2.1}$$

where $C(x,t)$ denotes the moisture concentration at location x (assuming moisture migration in one dimension) and time t, D is the diffusion coefficient which varies and is defined as

$$D = D_0 e^{\left[kx_c + E_a\left(\frac{1}{T_0}-\frac{1}{T}\right)\right]} \tag{2.2}$$

To evaluate moisture concentration in insulation paper, moisture absorption isotherms have been used. Especially, the measurement can be made practical by using a water activity sensor. Water Content in Paper (WCP, Figure 12.15(a)) and Water Content in Oil (WCO, Figure 12.15(b)) can be estimated by using a moisture (relative humidity) sensor [80 - 82]. For an accurate moisture content estimation, oil temperature and the condition of oil (new or aged) are required.

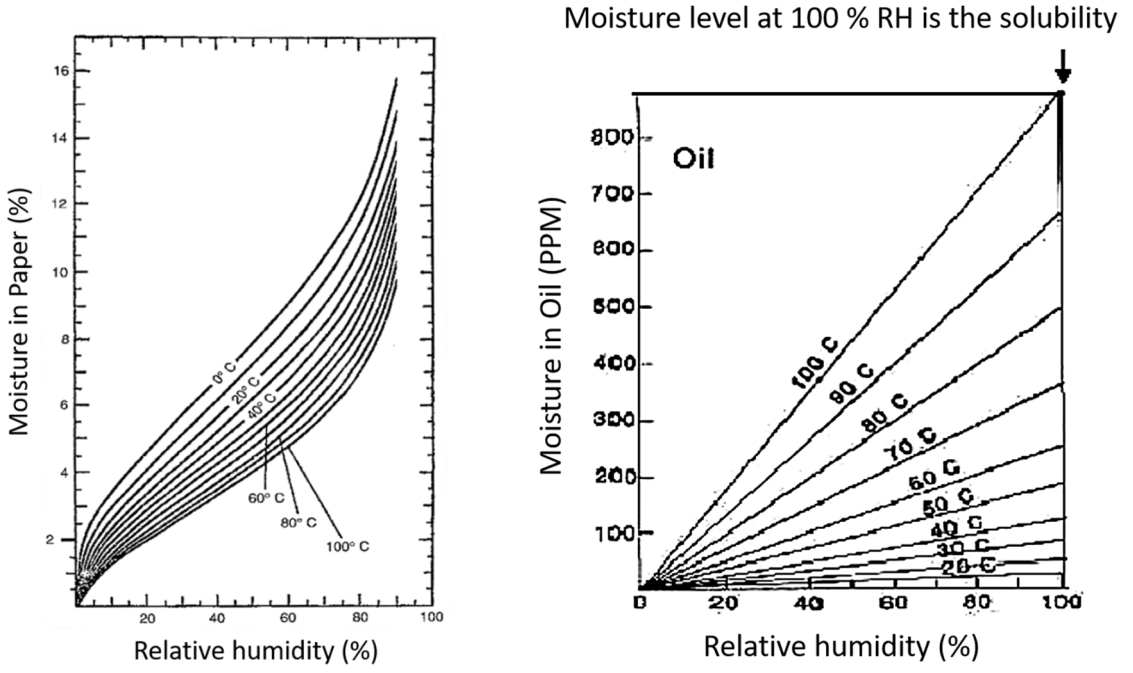

a) b)

Figure 2.15 (a) Relations of relative humidity and water content in paper (WCP) [83]; (b) Relation of relative humidity and absolute water content in oil (WCO) [84].

Oommen's curves shown in Figure 2.16 [80] depict equilibrium isotherms between new oil and solid insulation at different temperatures. The curves are derived from relations between the moisture concentration in the paper and the relative water content of the oil [85, 86]. To apply Oommen's curves, it is essential that an equilibrium condition of moisture between oil and solid insulation (paper and pressboard) has been established and maintained. At low temperature and low moisture content level, the diffusion process takes a longer time. In some cases it may require more than three weeks

to reach a reasonable equilibrium condition [86 - 87].

Therefore, for attaining a stable equilibrium between oil and solid insulation material, a sufficiently long time period is required without a condition change. However, this may not be a practical method for an in-service transformer due to its varying load and environmental condition changes.

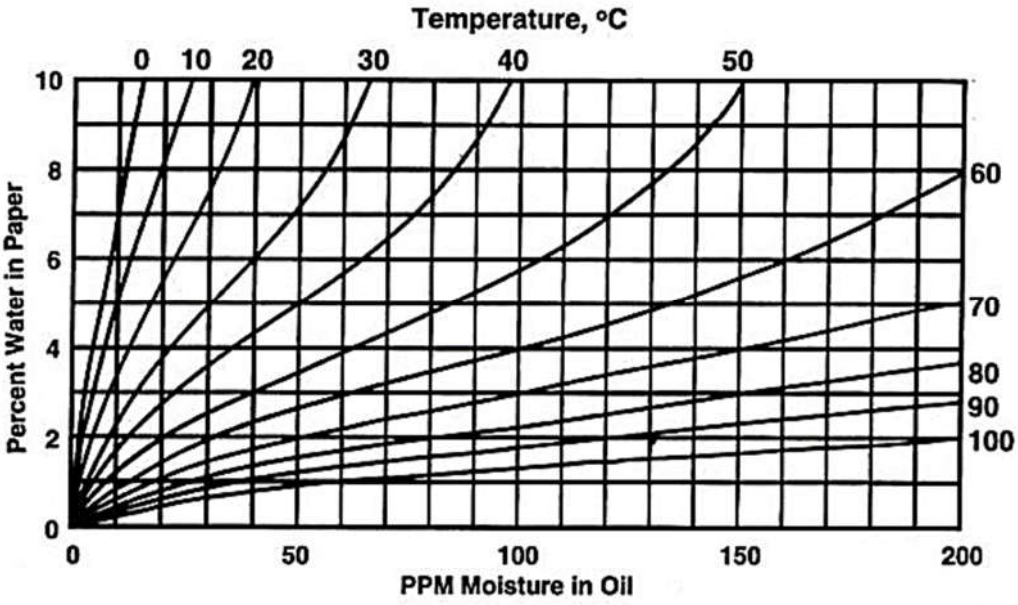

Figure 2.16 Oommen's water content equilibrium curves between new oil and paper [80].

k. Degree of Polymerisation (DP) Measurement

The ageing condition of insulation paper can be determined by the DP, which equates to the average number of cellulose molecules. Cellulose is a linear polymer combining glucose units connected to each other by a glucosidal bond at the first and the fourth carbon atoms as shown in Figure 2.17 [88].

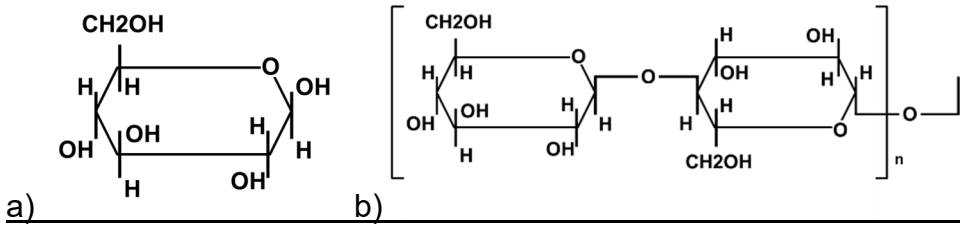

Figure 2.17 Structures of glucose and cellulose (a) Glucose unit ;(b) cellulose chain [88].

The mechanical strength of insulation paper can be determined by measuring the DP using a viscometrical method. The DP value of new insulation paper ranges from 1000 to 1500 whereas it drops to 200 to 250 at the end-of-life [88 – 89]. As the DP decreases, insulation paper becomes brittle and its tensile strength drops. Also, the DP decreases at a faster rate if insulation paper is exposed to

increased temperature and moisture level. For example, if the moisture content increases by 1 % or temperature increases by 6^0C, the life time of the insulation paper can be halved [90].

To measure the DP of insulation paper, a paper sample needs to be collected from the transformer, which is not a practical method. Thus, some utilities adopt dummy paper samples installed inside a transformer's tank [77]. However, the measured DP of the dummy sample may not reflect the overall condition of the insulation paper around the winding, i.e., a hot spot area.

l. Furan Analysis Method

Furan compounds are generated and dissolved in oil when the insulation paper ages [91]. A furan compound is normally not evenly distributed in transformer oil. Most furan compounds reside close to the solid insulation [92]. The concentration of furans in oil is measured using High Performance Liquid Chromatography (HPLC) [93]. The concentration of 2-furaldehyde is the most significant compound to evaluate the condition of insulation paper. The DP can be obtained using 2-Furaldehyde concentration, as seen in the following equations [94 - 102].

$$\mathrm{DP} = \frac{1.51 - \log F}{0.0035} \quad by\ Chendong \tag{2.3}$$

$$\mathrm{DP} = \frac{1.71 - \log F}{0.00288} \quad by\ Scholnik\ et\ al \tag{2.4}$$

$$\mathrm{DP} = \frac{800}{(0.186 \times F) + 1} \quad by\ Pahlavanpour \tag{2.5}$$

$$\mathrm{DP} = \frac{7100}{8.88 + F} \quad by\ DePablo \tag{2.6}$$

where F is 2-furaldehyde concentration in ppm.

2.3.4.2 Electrical Insulation System Test Methods

a. Polarisation and Depolarisation Current (PDC) Measurement

PDC method evaluates the dielectric response of an insulation system. When an external DC source is applied to an insulation system, randomly diverted dipoles inside the insulation system are redirected to be aligned with the applied electric field. During the realignment of dipoles, a polarisation current flows in the insulation system. The oriented dipoles return to their original directions when the external DC source is removed. The relaxation stage results in a depolarisation current flowing in the insulation system. Thus the polarisation and depolarisation current can provide information regarding the condition of insulation system. Figure 2.18 shows the schematic diagram of PDC measurement and the current profiles obtained from the PDC method.

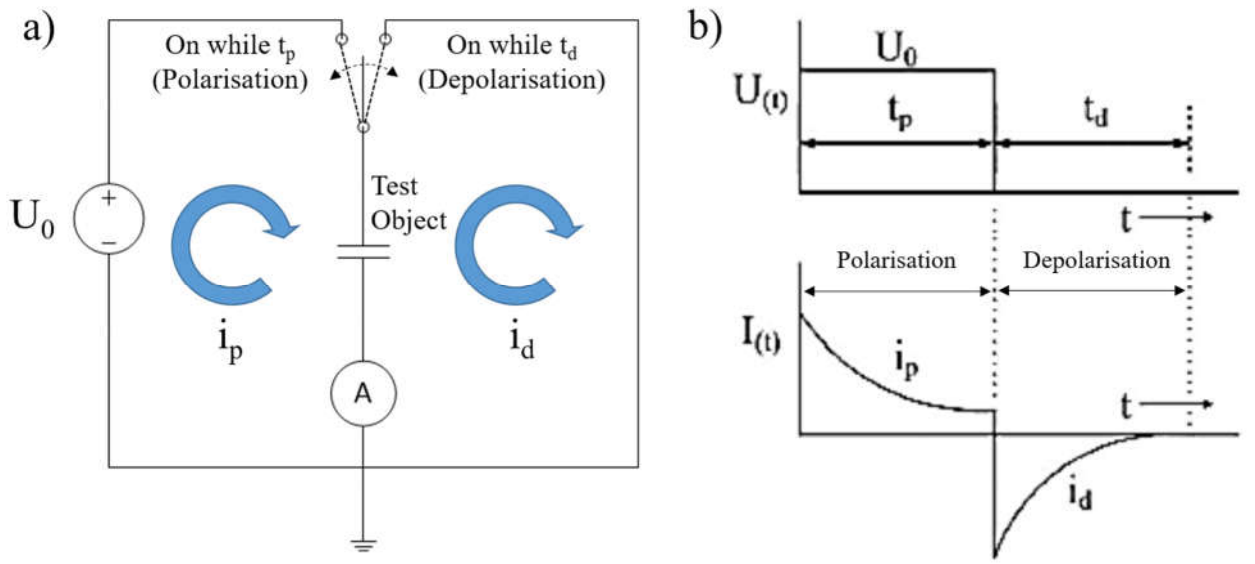

Figure 2.18 PDC measurement (a) PDC test circuit diagram; (b) example of voltage and current profile of PDC [94].

During the polarisation stage, a DC voltage across an insulation system is applied for about 5,000 to 10,000 seconds and the corresponding polarisation current is measured. It is followed by a depolarisation stage, in which the DC source is removed and the insulation system is short-circuited for discharging. The depolarisation current is measured for about 5,000 to 10,000 seconds.

At the polarisation stage, the polarisation current, i_p is affected by the two processes of conduction and slow polarisation. It can be written as:

$$I_p(t) = \left\{\frac{\sigma}{\varepsilon_0} + f(t)\right\} C_0 U_0, \quad 0 < t < t_p \tag{2.7}$$

where $C_0 = \frac{C_m}{\varepsilon_r}$ denotes the insulation system's geometrical capacitance (C_m is obtained from a capacitance measurement), ε_r denotes the insulation's relative permittivity at power frequency, σ is the insulation system's average conductivity and ε_0 is free space's permittivity. The function of $f(t)$ decreases with respect to time, which is termed the dielectric response function.

The depolarization current, i_d can be expressed as:

$$I_d(t) = -\{f(t) - f(t + t_p)\} C_0 U_0, \; t_p < t < t_d \tag{2.8}$$

The effect of $f(t + t_p)$ on Equation 2.8 can be neglected if the insulation system is charged over a sufficiently long period of time, t_p [94]. Therefore, Equation 2.8 can be simplified as:

$$I_d(t) \approx -f(t) \times C_0 U_0 \tag{2.9}$$

Generally, the obtained polarisation and depolarisation currents are affected by conductivity, moisture content and ageing of the oil and insulation paper. The early part of polarisation and depolarisation currents are affected by the condition of oil whereas the final part of the currents are decided by the condition of the paper and pressboard insulation. The PDC measurement can evaluate the condition of both oil and insulation paper and can be used to address the ageing condition of the transformer insulation system [94]. However, it needs to interrupt the transformer service while the test is run.

b. Frequency Domain Spectroscopy (FDS)

The frequency domain spectroscopy (FDS) measurement uses a sinusoidal voltage source with varied frequencies to evaluate the condition of an insulation system [103]. Figure 2.19 depicts the FDS measurement system. A voltage source and voltmeter are connected to an insulation system (sample) in parallel. The corresponding current is measured. The resultant current at a particular frequency of the applied voltage can be written as:

$$I^*(\omega) = j\omega\left\{C^{'}(\omega) - jC^{''}(\omega)\right\} U^*(\omega) = j\omega C_0\left\{\varepsilon^{'}(\omega) - j\varepsilon^{''}(\omega)\right\}U^*(\omega) \qquad (2.10)$$

where $C'(\omega)$ and $C''(\omega)$ denote the real and imaginary parts of complex capacitance $C^*(\omega)$. $\varepsilon'(\omega)$ and $\varepsilon''(\omega)$ denote the real and imaginary part of permittivity, respectively. If the geometrical capacitance of C_0 is not known, the condition of the insulation system can be evaluated by the frequency dependent loss factor: $\tan\delta(\omega) = C^{''}(\omega)/C^{'}(\omega)$ [104]. The frequency dependent loss factor can reflect an insulation condition change without obtaining absolute dielectric loss and relative permittivity of the insulation system.

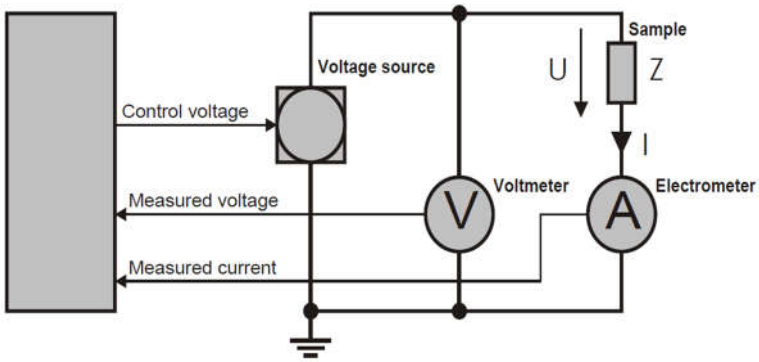

Figure 2.19 FDS measurement system [105].

The frequency dependent loss factor, $\tan\delta(\omega)$ can be used to investigate a change in moisture content, oil conductivity and geometry. The obtained curve of FDS at low frequencies can provide moisture content related information. The conductivity of oil can be evaluated from the result of FDS

at mid-range of the frequencies. Figure 2.20 shows the resultant curve obtained from FDS measurement.

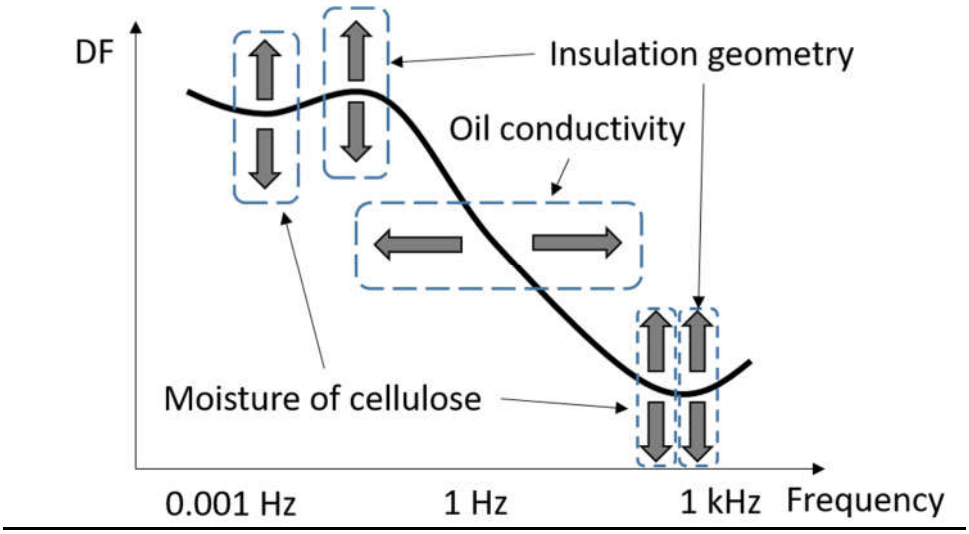

Figure 2.20 The resultant curve by FDS measurement showing trends in moisture content, oil conductivity and geometry condition change [106].

2.3.4.3 Online PD Measurement for Transformer Insulation Condition Monitoring

This section reviews various aspects of PD measurement including PD signal generation mechanism, PD signal measurement systems, PD signal extraction, PD signal analysis and PD source localisation [107 - 113].

a. PD Mechanism

PD is defined in IEC 60270, a partial discharge measurement standard, as "localised electrical discharge that only partially bridges the insulation between conductors and which can or cannot occur adjacent to a conductor" [114]. The PD signal can be classified into internal discharge, surface discharge, corona, electrical treeing and floating discharge depending on the discharge mechanism, medium type, and construction of the insulation system [115].

The PD phenomena can be explained using an equivalent circuit as shown in Figure 2.21. In the figure, C_0 denotes the capacitance of a complete (original) insulation system, C_h denotes the capacitance of defected parts, and Cs denotes the capacitance of the remainder.

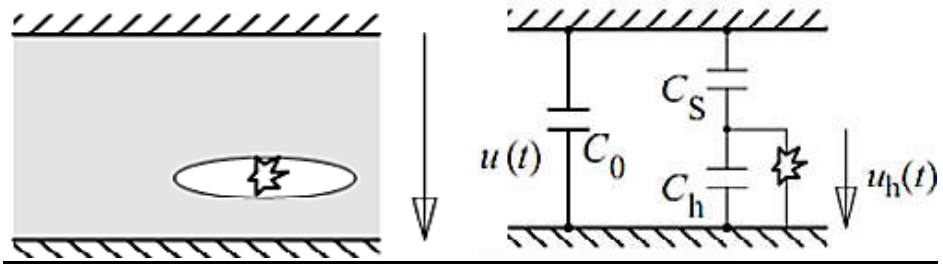

Figure 2.21 Equivalent circuit model of a defected insulation system [115].

The charge (q) due to PD at a defect location can be obtained by the multiplication of capacitance (C_h) and voltage (ΔV_h) as:

$$q = C_h \Delta V_h \tag{2.11}$$

The capacitance C_h of the defect can be calculated from permittivity (ε) and the geometry information of area (A) and gap (d) as:

$$C_h = \varepsilon \frac{A}{d} \tag{2.12}$$

As shown in Figure 2.22, at positive power cycle, discharge may occur when a voltage, $U_1(t)$, across the insulation defect of a test object (insulation system) exceeds inception voltage, U_z. A discharge is generated normally for a very short time of less than 1 μs [114 - 115]. The discharge lasts until the voltage $U_1(t)$ drops below an extinction voltage, U_L. The discharge in negative AC power cycle occurs similarly except it comes with a minus polarity.

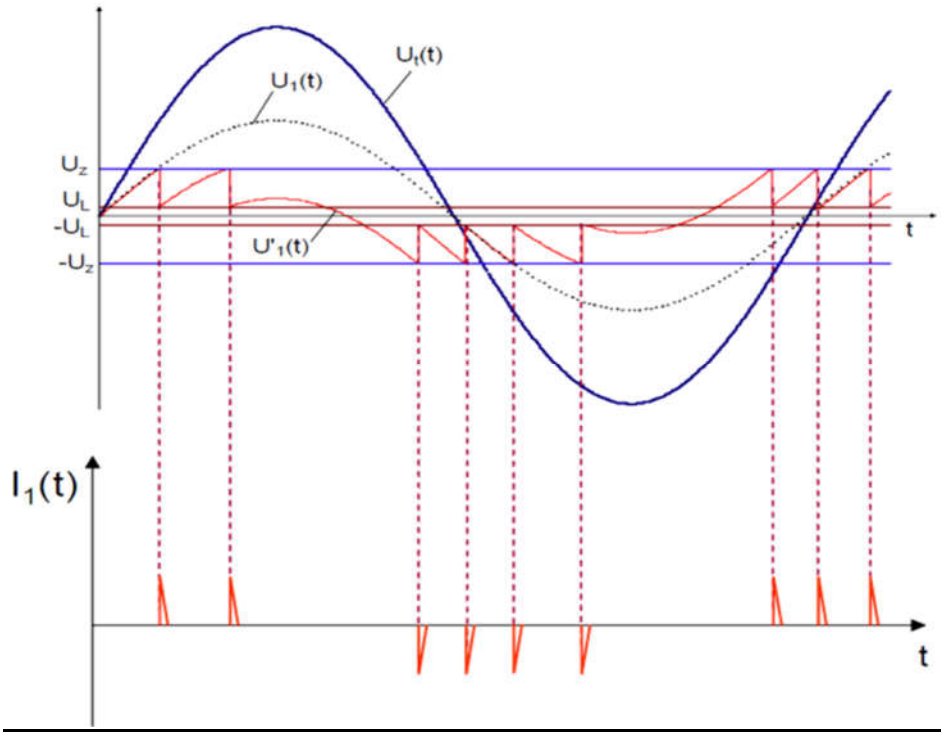

Figure 2.22 Partial discharge mechanism [114 - 115]. $U_t(t)$ = the applied voltage across a test object (insulation system), $U_1(t)$ = the corresponding voltage across the test object, U_z = inception voltage, U_L = extinction voltage.

b. PD Measurement System

The PD occurrence often comes with light, heat, sound emission, a chemical reaction with oil and electrical eruption. Thus, PD can be detected by many different methods like temperature, AE, Ultra-

High Frequency (UHF) antenna, DGA and electrical measurements. Among the above methods, electrical PD measurement is widely adopted because of its high sensitivity.

There are two representative types of electrical PD measurement systems: (1) a capacitive type PD measurement system comprising a coupling capacitance [114 - 115]; and (2) an inductive type PD measurement system comprising an inductive sensor [88, 97]. The capacitive PD measurement system is well described in IEC 60270 [114]. It has good sensitivity for detecting PD signals compared to the inductive method. However, the capacitive PD measurement method requires a coupling capacitor connected in parallel or in series with a transformer of interest and an external voltage source to energise the transformer. The transformer of interest should also be disconnected from the power grid during the implementation of the capacitive PD measurement.

In contrast, for an inductive PD measurement, the transformer does not need to be disconnected from the power grid or interrupted from its service while setup and PD signal measurement is made. The inductive PD sensor, a Current Transducer (CT), can be installed on the grounding cable of a transformer. Also, it can be performed at normal operating conditions without an external power source.

However, there are some issues in an inductive PD measurement system such as PD measurement sensitivity and signal saturation on a CT sensor. They may pose some difficulties in adopting the inductive PD measurement system. The following sections address both capacitive and inductive PD measurement systems to understand the important features of them.

c. Capacitive PD Measurement System

IEC 60270 provides detailed information regarding capacitive PD measurement systems [114]. One of the most important features affecting the sensitivity of PD signal measurement is how to employ a coupling circuit over a test object. There are two types of coupling (or detection) circuits, i.e., a serial detection circuit (Figure 2.23) and a balanced detection circuit (Figure 2.24) [114 - 115].

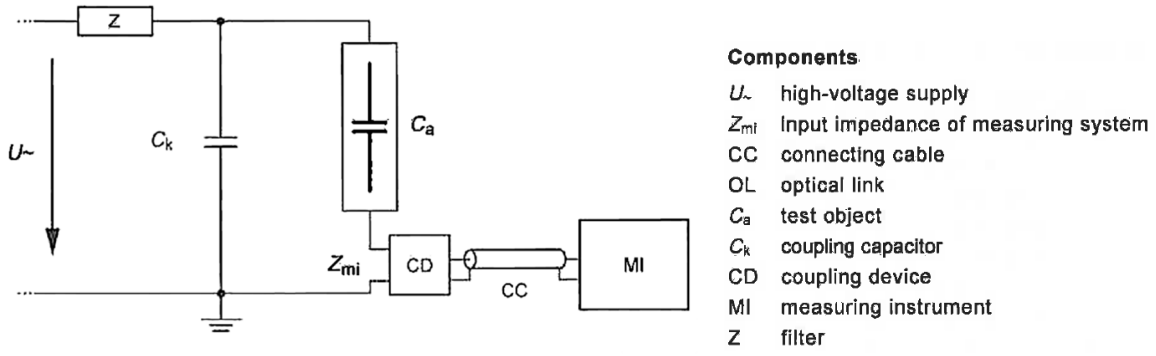

Figure 2.23 Straight PD detection circuit (capacitive PD measurement) [114 - 115].

In particular, the balanced coupling circuit has the benefit of rejecting external disturbances [114 - 115].

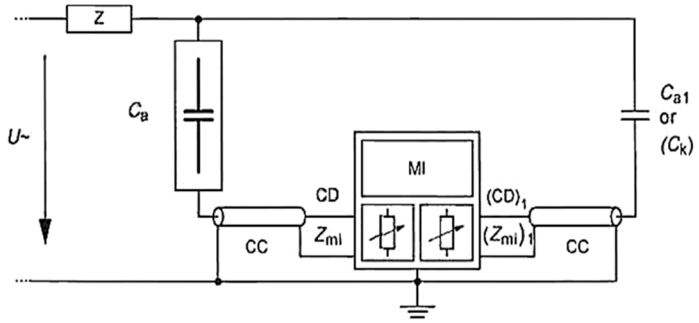

Figure 2.24 Balanced PD detection circuit (capacitive PD measurement) [114 - 115].

Instead of installing an external coupling capacitor, the transformer's bushing can be an alternative. By using a busing tap, bushing capacitance C1 can be used as a coupling device as shown in Figure 2.25 [114].

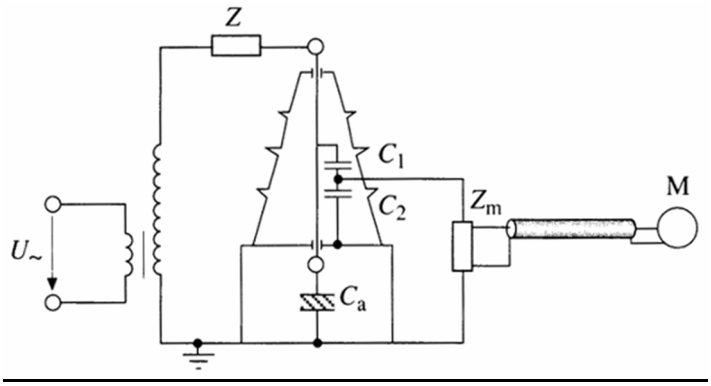

Figure 2.25 An alternative coupling device using a bushing capacitance *C1* [114].

The obtained PD signals vary according to the values of capacitance and resistance of the measurement impedance. The magnitude of PD signals at the output of the measurement impedance can be calculated as [115]:

$$\mathrm{V} = \frac{q}{a+C\left(1+\frac{a}{k}\right)} \times e^{-t/Rm} \tag{2.13}$$

where a is the coupling capacitance and k is the capacitance of a test object, C and R are the capacitance and resistance of measurement impedance, respectively, t is time, q is the magnitude of apparent discharge and m can be calculated as follows:

$$\mathrm{m} = \frac{ak}{a+k} + C \tag{2.14}$$

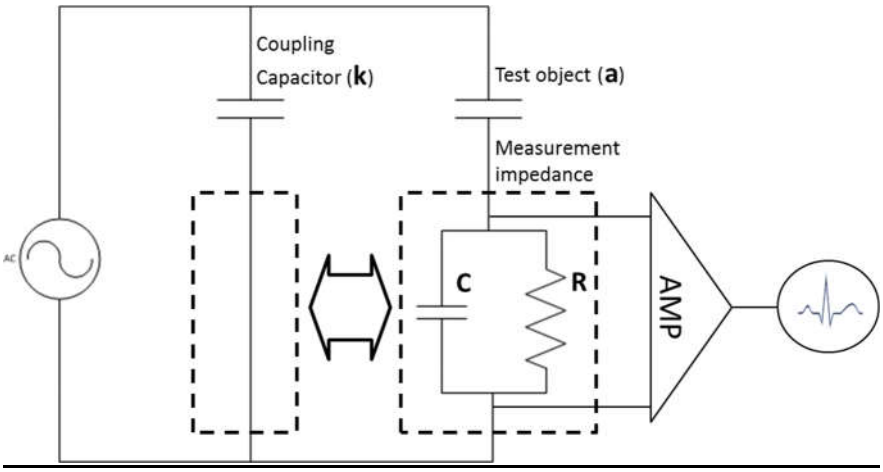

Figure 2.26 Capacitive PD measurement with measurement impedance [114 - 115].

The magnitude of the PD impulse is directly proportional to the apparent charge q. The shape of the PD impulse at measurement impedance is significantly affected by m and R as shown in the above equations. However, these two parameters do not affect the amplitude of PD signals. Thus, if R or m is too small, the PD impulse at measurement impedance will be too steep to be properly captured. If a very small coupling capacitor, k, is adopted, the amplitude of PD signals will be very small because of the increased C/k ratio.

In PD measurement, the frequency band of a system should be considered since it affects PD signal analysis and interpretation. IEC 60270 proposes two types of PD signal measurement frequency bands:

1) Wide band PD measurement frequency

$$30\ \text{kHz} \leq f_1 \leq 100\ \text{kHz}$$

$$f_2 \leq 500\ \text{kHz}$$

$$100\ \text{kHz} \leq \Delta f \leq 400\ \text{kHz}$$

2) Narrow band PD measurement frequency

$$9\ \text{kHz} \leq \Delta f \leq 30\ \text{kHz}$$

$$50\ \text{kHz} \leq f_m \leq 1\ \text{MHz}$$

where f_1 is the lower frequency limit, f_2 is the higher frequency limit, f_m is the mid-band frequency and Δf is the frequency width.

The amplitude of PD signals need to be calibrated before a test. The calibration process is implemented by injecting the already known impulse signals U_o into the test object C_0 with a pulse generator. The measured magnitude of the impulse q_0 can be written as:

$$q_0 = U_0 C_0 \tag{2.17}$$

Figure 2.27 shows a circuit diagram for a PD signal calibration.

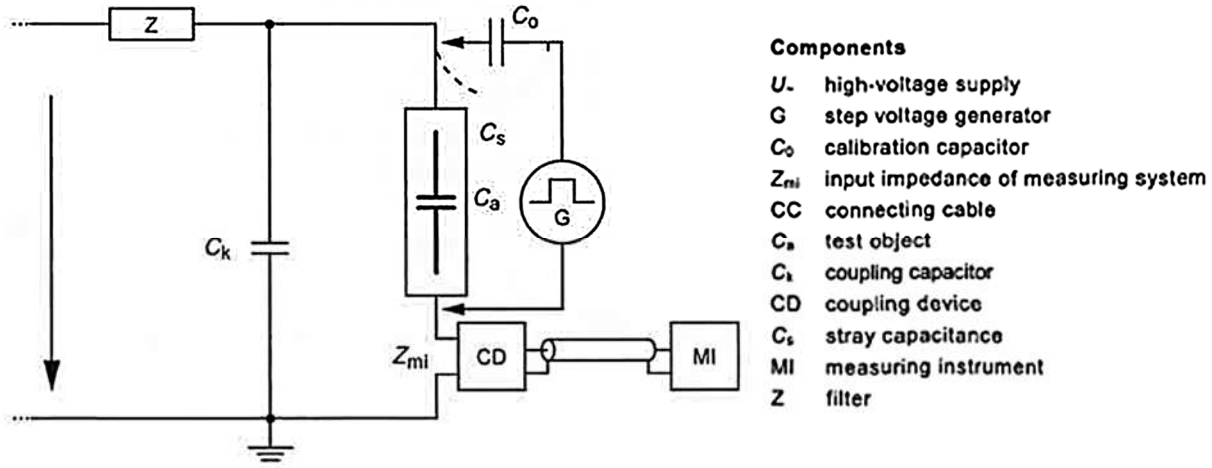

Figure 2.27 PD signal calibration [114].

However, the actual amplitude of a PD impulse at its discharge location (inside the transformer) can hardly be obtained even through the calibration is executed. This is because the PD impulse would experience attenuation and distortion when it propagates from its discharge location to a PD sensor [116]. Thus, the PD signals obtained from an onsite test object may only provide qualitative indication of PD activity rather than actual apparent charge from a PD source. This needs to be taken into account for interpreting PD measurement data properly especially when information regarding geometric and design parameters of a test object (i.e., transformer) are not known [116].

d. Inductive PD Measurement System

An inductive PD measurement system uses a HFCT, which has a broad frequency band from several hundred kHz to several GHz [117 - 119]. The sensor installation and inductive PD measurement system diagram is shown in Figure 2.28.

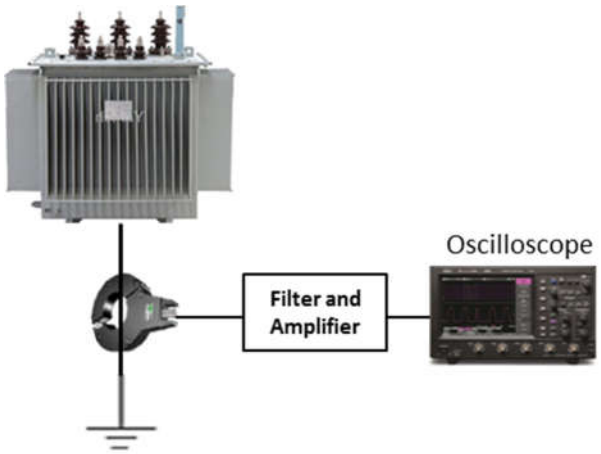

Figure 2.28 Inductive PD measurement system.

Before conducting a PD measurement, the HFCT needs to be calibrated by adjusting the number of coils and air gap of the sensor [120]. For example, increasing the number of winding turns of the sensor at a constant coupling resistance will lead to decrease a cut-off frequency. This can reduce the overall sensitivity of the sensor in capturing components of PD signals at high frequency. On the other hand, if coupling resistance increases while the number of winding turns of the sensor remains the same, its sensitivity will increase as cut-off frequency increases [120].

Additionally, the HFCT could be vulnerable to core saturation if high current flows through it. Such core saturation can be prevented by adjusting the air gap of the core of the HFCT though this may slightly compromise the sensitivity of the sensor [120].

e. UHF Antenna based PD Measurement System

UHF antenna can be inserted into a transformer's oil drain valve to capture electromagnetic waves generated by PD activities inside a transformer. Generally, an UHF sensor has a frequency range from 300 MHz up to 3 GHz for PD signal measurement. It has a good sensitivity with high Signal to Noise Ratio (SNR). However, the performance of a UHF based PD measurement system can degrade if a PD source is located away from the location of an UHF antenna.

f. PD Signal Extraction and De-noising Techniques

One of the most important tasks for a successful PD measurement is PD signal extraction from noise and interferences. The noise and interferences include Discrete Spectral Interference (DSI) from neighbouring communication systems emitting radio frequencies, repetitive impulses by power electronics, random impulses by infrequent switching operations or lightning and other ambient and environmental noise.

The effect of interferences and noise signals can be mitigated by applying an analogue filter to the measured PD signals. For an effective noise suppression, proper frequency range of filters should be decided. However, it is hard to know the types and characteristics of noise prior to PD measurement. Therefore, adaptive digital signal processing techniques are necessary. A number of representative PD signal processing techniques are briefly discussed as follows.

In a time-domain based analysis, a non-recursive Finite Impulse Response (FIR) filter or a recursive Infinite Impulse Response (IIR) filter can be applied to remove noise. However, there may be some limitations if noise signals exhibit similar waveforms to the PD signals [121] or the amplitude of the PD signals is relatively lower than noise signals. In a frequency domain-based analysis, Fourier transform, Short Time Fourier Transform (STFT) and wavelet transform have been applied for PD signal extraction.

Fourier transform transforms the acquired signals from time domain to frequency domain. Then, a notch filter can be designed to extract PD signals while rejecting noise signals. However, the extracted signal can be distorted and attenuated since PD signals have a broad frequency spectrum. Moreover, PD activity is a stochastic phenomenon in nature and highly time varying. Thus, it is not an easy task to design a suitable filter for extracting PD signals [122]. Therefore, Fourier transform may not be effective for PD signal extraction in practical PD measurement.

STFT can be used to process stochastic features of PD signals [122 - 124]. STFT processes originally measured a signal by dividing a raw signal into many fixed time slots and the signal in each time slot is processed by Fourier transform as:

$$STFT\{x(t)\}(\tau,\omega) \equiv X(\tau,\omega) = \int_{-\infty}^{\infty} x(t)\omega(t-\tau)e^{-j\omega t}\,dt \tag{2.16}$$

where $x(t)$ denotes an originally measured signal in a time domain, $\omega(t)$ denotes a window function, τ denotes time, ω denotes frequency and $X(\tau, \omega)$ denotes Fourier transform of $x(t)\omega(t-\tau)$. STFT can compensate the disadvantage of the original Fourier transform in dealing with time-varying PD signals. Though STFT brings some improvement over Fourier transform, it still does not achieve a desirable performance due to its fixed resolution in time and frequency. Such fixed resolution causes difficulties in analysing time-varying PD signals across wide frequency bands.

Wavelet transform provides a superior benefit of using multi-resolution of time and frequency. The multi-resolution scheme provides an optimal configuration like shorter length of time at higher frequencies and longer length of time at lower frequencies. Wavelet transform can be expressed as:

$$WT(a,b) = \frac{1}{\sqrt{a}}\int_{-\infty}^{\infty} x(t)\,\psi\left(\frac{t-b}{a}\right)dt \tag{2.17}$$

where a denotes a scaling factor, b denotes a time shifting factor, $x(t)$ denotes an original signal and $\psi(t)$ denotes a wavelet filter (or mother wavelet). Wavelet transform decomposes an input signal (i.e., noise corrupted PD signal) into multiple wavelet coefficients at each decomposition level related to corresponding frequency bands. Each decomposed wavelet coefficient has a unique window size of different time length and frequency.

Discrete Wavelet Transform (DWT) decomposes an input signal into dyadic components of approximation and detail coefficients [122]. DWT is defined as:

$$W_{j,k} = \sum_{n \in Z} X(n)2^{(-j/2)}\psi(2^{-j}n - k) \tag{2.18}$$

where $W_{j,k}$ denotes transformed output by DWT, $x(t)$ denotes an original signal and $\psi(t)$ denotes a wavelet filter (or mother wavelet).

$$
\begin{aligned}
x(t) &= A_1(t) + D_1(t) \\
&= \sum_k cA_2(k)\phi_{j-2,k}(t) + \sum_k cD_2(k)w_{j-2,k}(t) + \sum_k cD_1(k)w_{j-1,k}(t) \\
&= A_2(t) + D_2(t) + D_1(t) \\
&= A_3(t) + D_3(t) + D_2(t) + D_1(t) \\
&= \sum_k cA_3(k)\phi_{j-3,k}(t) + \sum_k cD_3(k)w_{j-3,k}(t) + \sum_k cD_2(k)w_{j-2,k}(t) + \sum_k cD_1(k)w_{j-1,k}(t)
\end{aligned}
$$

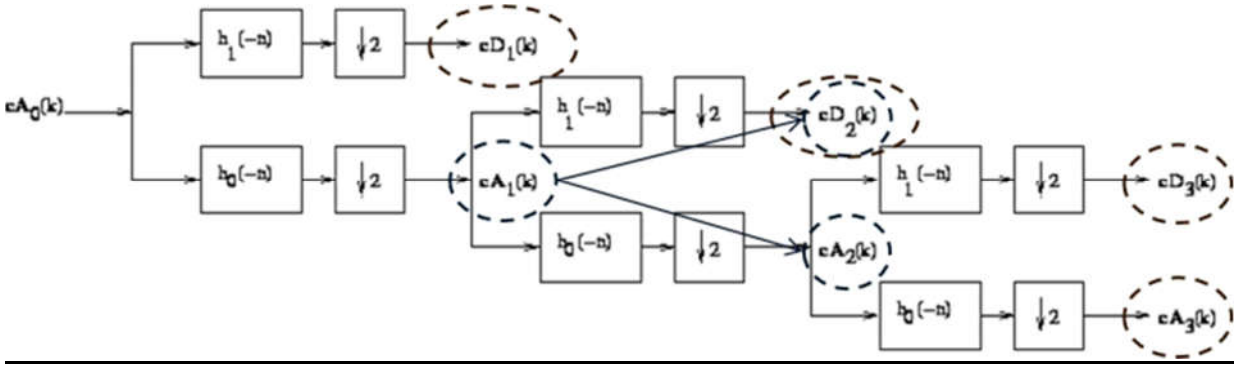

Figure 2.29 Decomposition of an input signal by Discrete Wavelet Transform [122].

Owing to the multi-resolution of wavelet transform, non-stationary and time varying PD signals can be effectively extracted [124 - 127]. However, wavelet transform requires complex processes of selecting a mother wavelet and decomposition level and deciding a threshold. This is not a trivial task and difficulties may be encountered in online condition monitoring of a transformer's insulation system.

g. PD Signal Analysis

After successful PD signal extraction, the PD signal needs to be analysed to identify the types of PD sources and to evaluate the severity of PD activity inside a transformer. The most frequently adopted method is a PRPD diagram to reveal the types of PD source. According to the type of PD source, a PD signal exhibits different phase location, polarity, amplitude and distribution along a phase axis. The different appearances of the feature of PD signals work as a kind of finger print on each type of PD source.

To analyse PD signals, extensive work has been conducted from PRPD to machine learning using such features of PD signals. However, there are still difficulties in precisely identifying the PD source type and condition of the insulation system.

For a separation and classification method towards stochastic PD activity, machine learning techniques have been adopted and developed to improve their practicability and accuracy. However,

there is still a gap for achieving an automatic PD source separation and classification. One of the difficulties is that the PD signal is varied, attenuated and distorted depending on the PD signal's propagation paths, internal structure of the transformer, the location of the PD source and the PD signal measurement system. Thus, many statistical parameters representing PD signals can scarcely be applied to different PD signal measurement conditions and test objects. Especially, a database constructed from an experimental condition has limitations in order to be used for an in-service transformer and test objects.

However, many experts and researchers still rely on the PRPD method to identify the PD source and the type of insulation defects. By overlaying PD signals measured over a minute of PD signal measurement, the overall features of a PD signal source can be evaluated, such as, internal discharge, floating discharge, corona and surface discharge. However, the way of overlaying PD signals on a single phase axis may miss some of the important information about the PD source. Additionally, the method is vulnerable to small amplitude PD signals since they are easily disregarded by higher amplitude PD signals in the overlaying process. Thus, there is a necessity to develop a complementary PD signal analysis method to be able to look at the features of a PD signal within a small time frame.

h. PD Source Localisation

The last step of PD measurement is to locate the PD source. Multiple AE sensors installed on the tank of a transformer can detect ultrasonic waves generated by a PD source. The distance from PD source to each sensor can be calculated by identifying the travel time of an ultrasonic wave, which is the elapsed travel time of the ultrasonic wave from a PD source to a sensor. The time is called the TOA. Thus, the distance from a PD source to an AE sensor can be calculated as:

$$distance(m) = velocity(m/s) \times travel\ time(s) \tag{2.19}$$

The propagating velocity of an ultrasonic wave is calculated according to the types of propagating medium of the wave-like oil or transformer tank. By using three AE sensors, the location of a PD source can be determined by the following Equation 2.20 [128].

$$\begin{aligned}
(\mathrm{x} - x_1)^2 + (\mathrm{y} - y_1)^2 + (\mathrm{z} - z_1)^2 &= (\mathrm{v} \cdot T_1)^2 \\
(\mathrm{x} - x_2)^2 + (\mathrm{y} - y_2)^2 + (\mathrm{z} - z_2)^2 &= (\mathrm{v} \cdot T_2)^2 \\
(\mathrm{x} - x_3)^2 + (\mathrm{y} - y_3)^2 + (\mathrm{z} - z_3)^2 &= (\mathrm{v} \cdot T_3)^2
\end{aligned} \tag{2.20}$$

where x_i, y_i, z_i (i = 1, 2, 3) denote locations of AE sensors, v denotes propagating velocity of an ultrasonic wave, and T_i (i = 1, 2, 3) denotes TOAs on each AE sensor. For an accurate TOA

measurement, a trigger signal is essential to activate the three AE sensors and to record the PD event. The initial time stamp of the PD event can be obtained from an electrical PD signal measurement.

According to the ultrasonic pressure wave propagation direction, there are two types of wave forms: longitudinal and transversal. The longitudinal wave propagates via either liquid-like insulation oil; or solid materials like steel construction and paper and pressboard insulation materials. However, a transversal wave can transverse only through solid material, not through liquid medium [128 - 129]. Various possible propagation paths of an ultrasonic wave pose difficulties in deciding accurate TOA to AE sensors [128]. Additionally, the propagation velocity of an ultrasonic wave varies depending on the type and condition of the medium through which it is passing; viscosity and temperature of oil, type of gas filled in air pockets, wave signal frequency and transformer construction [130].

Chap 3. Development of an Online On-Load Tap Changer Condition Monitoring System

Contribution of the Chapter

Vibration signal measurement has been adopted for online condition monitoring of a power transformer's On-Load Tap Changer (OLTC). By comparing vibration signals measured at different stages, it might be possible to assess the mechanical condition of an OLTC. However, there are still considerable difficulties in correlating vibration signals to the corresponding mechanical events of an OLTC's operation, which may compromise the capability of vibration signal measurement for the condition monitoring of an OLTC. Therefore, an arcing signal measurement is considered to interpret OLTC's vibration signal in this chapter. An arcing signal is provoked at the moment when the OLTC's switching contact is closed at a tap position which can lead to electromagnetic signals flowing through the transformer windings and finally reaching the grounding cable of a transformer. The arcing signal measurement is achieved using a High Frequency Current Transducer (HFCT) clamped onto a transformer's grounding cable. The joint vibration and arcing measurement can provide an ultimate means of interpreting vibration signals involved in the OLTC's mechanical operation and facilitating an improved OLTC condition monitoring. Field measurements on two different types of OLTCs are performed using the proposed joint vibration and arcing measurement system to validate the proposed methodology.

This chapter has been reproduced from the following paper: J. Seo, H. Ma and Tapan K. Saha, "**A Joint Vibration and Arcing Measurement System for Online Condition Monitoring of On-load Tap Changer of the Power Transformer**," in IEEE Transactions on Power Delivery, vol. 32, no. 2, pp. 1031-1038, April 2017.

3.1 Introduction

Over the last decades, a number of OLTC condition monitoring techniques have been developed (please refer to Chapter 2). Recently, utilities have paid more attention to vibration signal measurement for OLTC's mechanical condition monitoring [131 - 134]. By detecting a change in the magnitude and number of peaks as well as the event time of a vibration signal obtained from OLTC's operation, it is possible to infer the mechanical condition of an OLTC at some extent. However, it is still not an easy task to reveal the mechanical source of each vibration signal, which hinders from correlating the vibration signals to OLTC's operation and subsequently evaluating its condition. The major difficulties include: (1) vibration signals generated by OLTC's operation do not always exhibit a consistent pattern (in amplitude and pattern of waveforms). Additionally, it is difficult to fully and accurately interpret each vibration signal with OLTC's mechanical operation by using only the vibration signal; more than that (2) different types of OLTCs exhibit different control mechanisms and configurations of switching contacts and different (vacuum) interrupters. Thus, it is almost impossible to develop a generalised vibration signal interpretation scheme. The above difficulties impair the capability of online vibration signal measurement for OLTC's condition monitoring.

Other than vibration signals, arcing signals are also generated during OLTC's operation. When a switching contact leaves one tap position to approach a next tap position, an arcing event is provoked due to a voltage difference between the two tap positions. The arcing event can cause electromagnetic signals to flow into a grounding cable through the transformer's windings. In this thesis, a joint vibration signal and arcing signal measurement method is proposed to capture both signals for an improved vibration signal interpretation in order to assess the mechanical condition of an OLTC. In the method, an arcing signal is captured by a split core HFCT clamped onto the grounding cable of a transformer. While vibration signal measurement responds to all mechanical events of the OLTC's operation, arcing measurement responds only to closing events of switches (refer to Section 3.3.2). Owing to the unique response feature of an arcing signal measured during OLTC's operation, arcing measurement can complement vibration signal measurement to investigate OLTC's operation. Moreover, switching events with different combinations of OLTC components (i.e., main contact, transition contact with resistor and vacuum interrupters) result in different amplitudes of arcing signals. This also can be exploited to facilitate interpreting vibration signals and inferring the condition of OLTC's contacts.

An arcing signal measurement system is developed by using HFCT complying with online measurement and it is successfully integrated with a vibration signal measurement system in this chapter. However, the arcing signal measurement can be compromised by induced extensive noise into

HFCT during field measurements. To effectively extract the arcing signals of interest from the noise corrupted signals, a probabilistic wavelet transform is applied [135].

This chapter is organised as follows. A review on operational mechanisms of two typical types of OLTCs (selector switch type and diverter switch type) is provided in Section 3.2. A discussion on the arcing mechanism involved in OLTC's operation and its implications on developing arcing signal measurement for OLTC is presented in Section 3.3. The key aspects of the joint vibration and arcing signal measurement method are also presented. A wavelet transform-based signal processing technique to extract the arcing signal from noise is presented in Section 3.4. To verify the proposed joint measurement system, case studies of field measurements on two different types of in-service OLTCs are provided in Section 3.5. This chapter is concluded in Section 3.6.

3.2 Operational Mechanisms of Two Major Types of OLTCs

Two different types OLTCs, namely selector switch (bolt-on) type OLTC and diverter switch (column) type OLTC with vacuum interrupters, are investigated in this thesis. Extensive vibration and arcing measurements have been performed on the two types of OLTCs and the results are used to verify the applicability of the proposed joint vibration and arcing signal measurement method. The operational mechanisms of the two types of OLTCs are reviewed briefly in this section. The understanding of the mechanisms is helpful in interpreting OLTC's operation and justifying the proposed joint measurement method.

3.2.1 Selector Switch (compartment or bolt-on) Type OLTC

The bolt-on type OLTC contains all components in a single compartment, which is mounted on the outside of a transformer's tank. Normally, the bolt-on type OLTC has a selector switch consisting of a main contact and two transition contacts each equipped with resistive or reactive impedance. The switching sequence of the bolt-on type OLTC is presented in Figure 3.1 [136].

During OLTC's operation, the main switch 'H' initially carries the load current solely and two transition switches 'M1' and 'M2' are open as shown in Figure 3.1(b). To change tap positions from '1' to '2', the main switch 'H' is firstly disconnected from tap position '1' and a transition switch 'M2' is connected to tap position '1' as shown in Figure 3.1(c). Then the transition switch 'M1' is connected to tap position '2' while the transition switch 'M2' remains at tap position '1' as shown in Figure 3.1(d). This makes a closed-loop circuit and the current in the circuit is limited by the two impedances in the branches of transition switches 'M1' and 'M2'. After that, 'M2' is disconnected from tap position '1' and only 'M1' is still connected to tap position '2' as shown in Figure 3.1(e). Finally, 'M1'

is disconnected from tap position ‘2’ and the main switch ‘H’ is connected to tap position ‘2’ as shown in Figure 3.1(f).

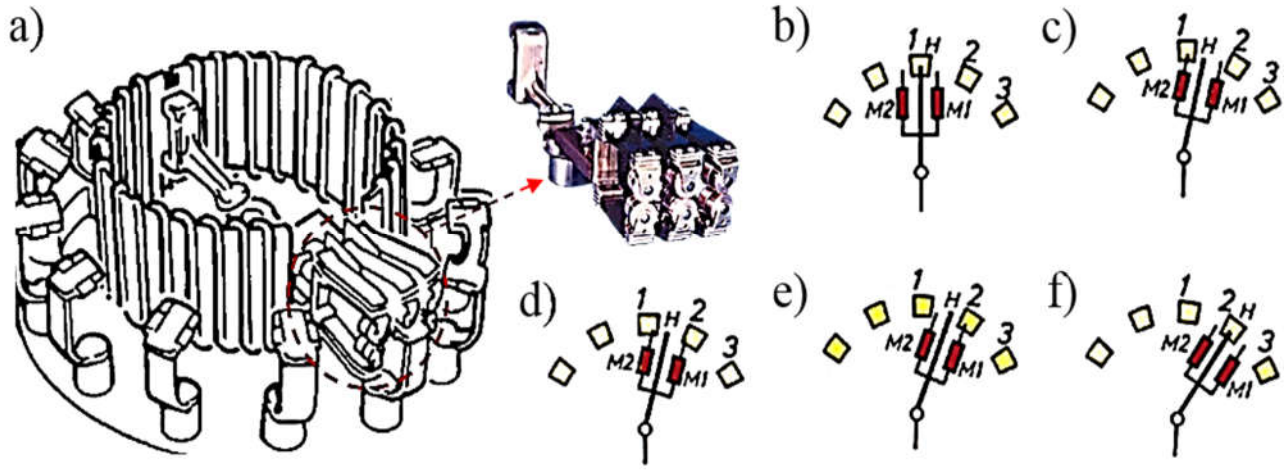

Figure 3.1 The switching sequence of a selector switch (bolt-on) type OLTC (a) one phase of an on-load tap changer and moving contact system and tap positions; (b) main switch ‘H’ is conducting load current to tap position ‘1’; (c) main switch ‘H’ is disconnected from tap position ‘1’ and transition switch ‘M2’ is connected to tap position ‘1’; (d) transition switch ‘M1’ is connected to tap position ‘2’; (e) transition switch ‘M2’ is disconnected from tap position ‘1’; and (f) transition switch ‘M1’ is disconnected from tap position ‘2’ and main switch ‘H’ is connected to tap position ‘2’ [136].

3.3.2 Diverter Switch (Column) Type OLTC with Vacuum Interrupters

The column type OLTC is housed directly inside a transformer’s tank. The studied column type OLTC has a diverter switch consisting of one main switch and one transition switch. Each contact is equipped with a vacuum interrupter. The vacuum interrupter helps prevent electrical discharge from damaging contacts and contaminating insulation oil, which extends the overall life of the OLTC. The switching sequence of the OLTC’s diverter switch is depicted in Figure 3.2 [137].

As shown in Figure 3.2, to change tap positions from ‘*n*’ to ‘*n+1*’, a transition switch (TTS) is disconnected from tap position ‘*n*’ as shown in Figure 3.2(b) and the transition switch’s vacuum interrupter (TTV) is opened as shown in Figure 3.2(c). After the connection of the TTS to the tap position ‘*n+1*’ as shown in Figure 3.2(d), the TTV is closed as shown in Figure 3.2(e). At this step, a closed-loop current flows through from tap position ‘*n*’ to ‘*n+1*’. This current is restricted by a transition impedance ‘R’ installed on the transition switch’s arm. The main switch, i.e., tap selector switch (MTS) changes its tap positions as the transition switch (TTS) does as shown in Figure 3.2(g) - Figure 3.2(i). A timing diagram of the diverter switch of OLTC’s operation is shown in Figure 3.2(j).

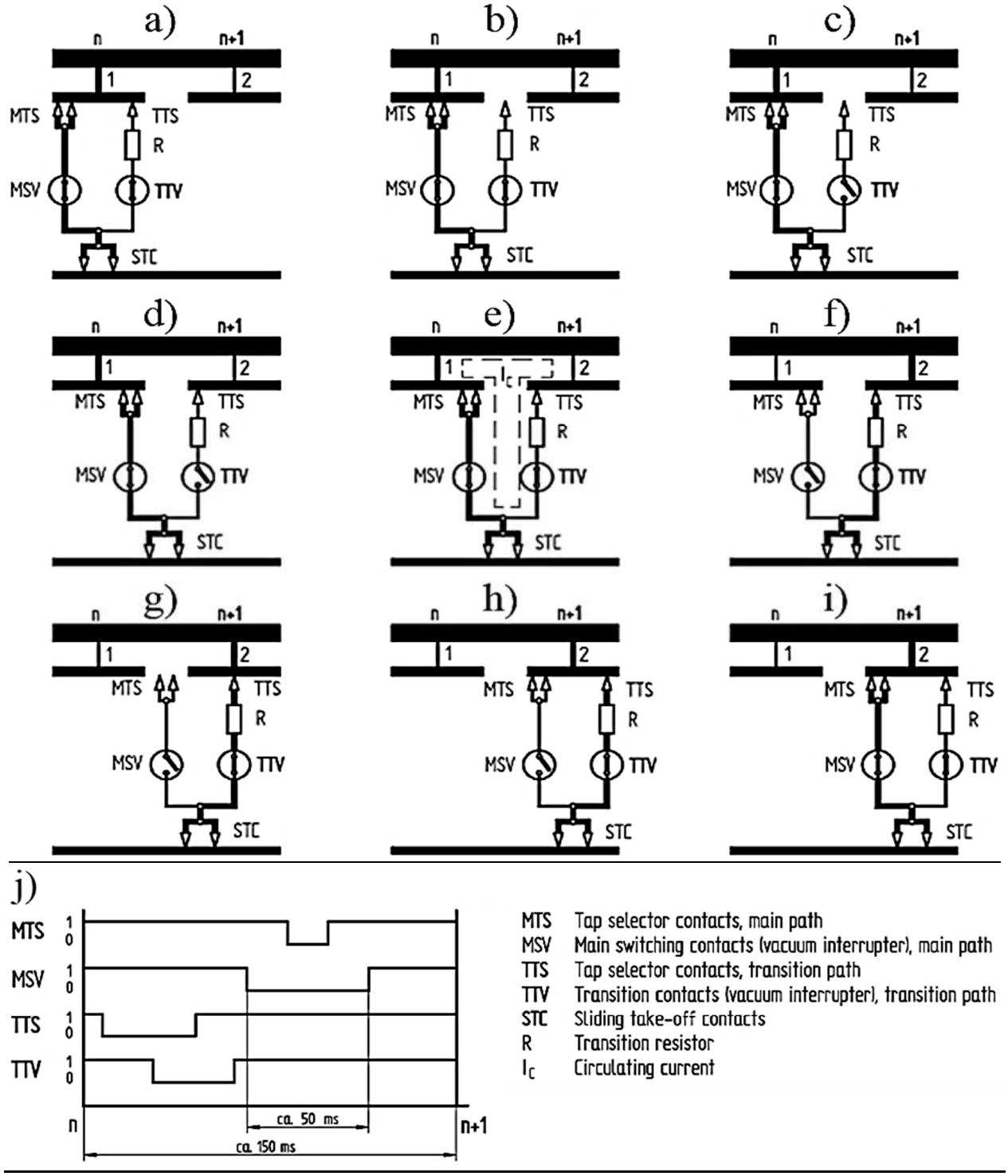

Figure 3.2 The switching sequence of a diverter (column) type OLTC with vacuum switches (a) before starting to change tap positions at 'n'; (b) transition switch (TTS) left from tap position 'n'; (c) transition switch's vacuum interrupter (TTV) is opened; d) TTS is connected to a tap position at 'n+1'; (e) closed loop current is made between tap positions of 'n' and 'n+1'; (f) main switch's vacuum interrupter (MSV) is opened; (g) main switch (MTS) is opened from a tap position 'n'; (h) MTS is connected to a tap position 'n+1'; (i) MSV is closed and completes tap position changing from 'n' to 'n+1'; and (j) a timing diagram of OLTC's operation [137].

3.3 A Joint Vibration and Arcing Signal Measurement Method for Vibration Signal Interpretation in OLTC's Condition Monitoring

3.3.1 Vibration Signal Measurement

As presented in Section 3.2, a series of mechanical events occur during an OLTC's operation. The most significant events are when (1) the OLTC's motor system starts and stops; (2) the Geneva gear is activated or inactivated; and (3) the switches are operating. Vibration signal measurement is employed to capture the acoustic waves induced by the above events.

The existing method of using vibration signal measurement for an OLTC's condition monitoring compares the amplitudes and number of peaks and event times of bursts in vibration signals obtained from the most recent measurement with the previous measurement (so called "before-and-after" comparison method) [39 - 40]. The time intervals between the bursts are greatly influenced by the condition of the OLTC's components including spring, switching contacts and Geneva gears. For example, weakened springs can cause a switch to leave a current tap position earlier and to reach a next tap position later than scheduled. Accordingly, switching transition time increases. Similarly, the wornness and misalignment of switches can also be evaluated by using the "before-and-after" approach.

However, the characteristics of vibration signals, such as amplitude, event time and number of peaks, are significantly affected by the types and models of OLTCs. Especially, time intervals between mechanical events are also decided by properties of switch types and operating mechanisms. The above "before-and-after" approach cannot readily correlate a burst of vibration signals to corresponding mechanical events of an OLTC's operations. Figure 3.3 shows vibration signals measured from an OLTC. It can be observed that it is difficult to infer a specific mechanical operation of an OLTC from the measured vibration signals.

Therefore, this chapter focuses on the interpretation of vibration signals generated by the movement of switches as well as the correlation of each vibration event to relevant mechanical operation of an OLTC. Since it is impossible to achieve this task with only vibration, arcing measurement is proposed for marking important signatures on vibration signals, which is discussed in the following section.

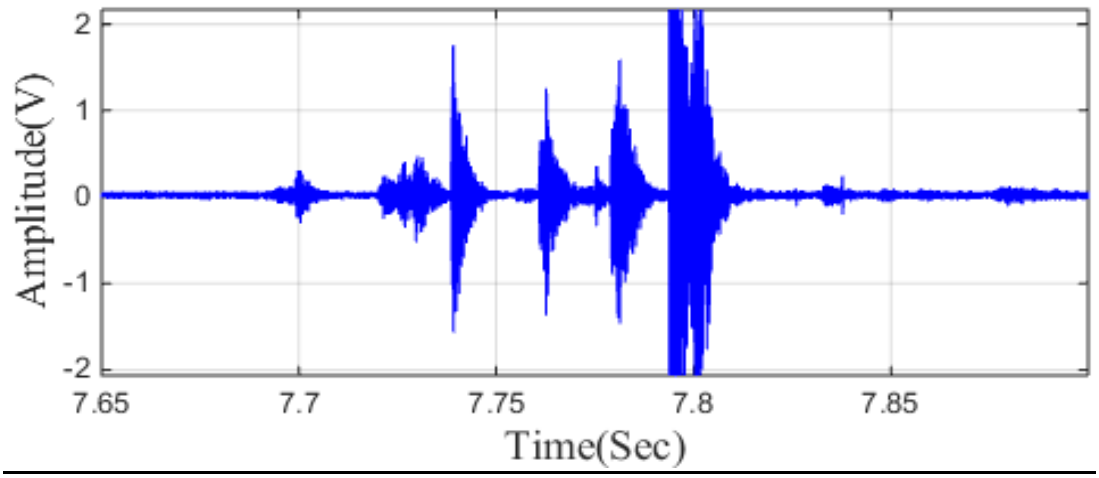

Figure 3.3 Vibration signal measured from an OLTC [47].

3.3.2 Arcing Signal Measurement

As mentioned in the previous sections (refer to Figure 3.1 and Figure 3.2), arcing is also generated during the course of switch operation from one tap position to another tap position. The arcing occurs at the moment when switches are closed at a tap position. This is due to a voltage difference between switches and tap positions. By referring to Figure 3.4, the voltage difference (ΔU) can be derived as follows:

$$V_{1\ at\ tap\ (n)} = \frac{N_{1\ at\ tap\ (n)}}{N_2} V_2 \tag{3.1}$$

$$N_{1\ at\ tap\ (n+1)} = N_{1\ at\ tap\ (n)} \pm \Delta N_{per\ tap} \tag{3.2}$$

$$V_{1\ at\ tap\ (n+1)} = \frac{N_{1\ at\ tap\ (n+1)}}{N_2} V_2 \tag{3.3}$$

$$\Delta U = \left| V_{1\ at\ tap\ (n)} - V_{1\ at\ tap\ (n+1)} \right| \tag{3.4}$$

where $V_{1\ at\ tap\ (n)}$ is a voltage at a tap position 'n', V_2 is a voltage at the secondary side, $N_{1\ at\ tap\ (n)}$ is the number of winding turns at a tap position 'n' of the primary side, N_2 is the number of winding turns at the secondary side and $\Delta N_{per\ tap}$ is the difference between the number of winding turns between two tap positions.

The tested OLTCs were installed on a transformer's high voltage side. In the United States, most OLTC selector switches are installed on the low voltage side. However, with some modifications in Figure 3.4 (i.e., changing OLTC's location to the secondary winding), a voltage difference between a selector switch and a tap position can also be derived for the OLTC installed on the high voltage side as well.

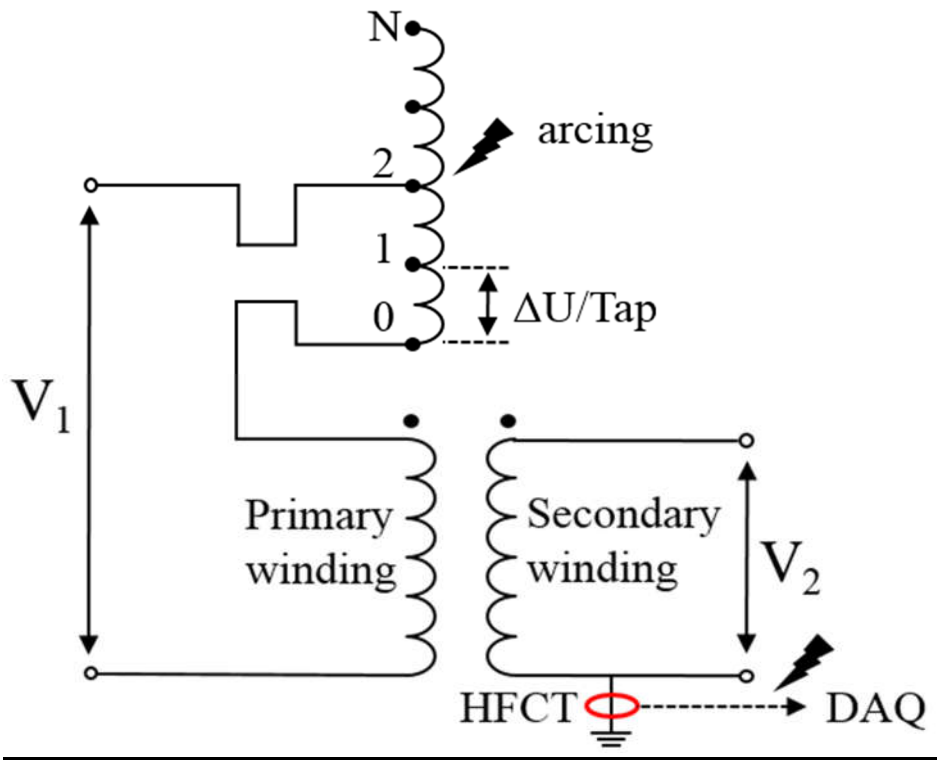

Figure 3.4 Arcing signal generation and measurement in OLTC [47].

When an arcing signal occurs, corresponding electromagnetic signals flow through the primary side of the coil and are then induced to the secondary side of coil and finally to ground through the transformer's grounding cable. Such electromagnetic signals due to arcing can be captured by a HFCT clamped onto the transformer's grounding cable. The configuration of an arcing measurement system is the same as that of an inductive PD measurement system for a transformer. Separating arcing signals (due to OLTC's operation) from PD signals (due to transformer insulation defects) is discussed in Section 3.4.

The arcing signal measured by HFCT is a type of electromagnetic signal having a short decay time compared to a vibration signal. It propagates through an electrical path (transformer's winding) in a transformer. Moreover, it exhibits a consistent characteristic over various environmental conditions such as temperature and structure of OLTC. On the contrary, vibration signal is vulnerable to propagation medium (air or oil), temperature and structure of an OLTC [109, 130]. As such, the obtained arcing signals are suitable to identify the event time of an OLTC's mechanical operation.

Figure 3.5 presents vibration and arcing signals measured simultaneously when a three-phase OLTC is in operation. It can be observed that the measured arcing signal occurs 300 μs earlier than the vibration signal. This is due to different propagation velocities of the two types of signals as discussed above. Moreover, the operational time difference between the three phases of the OLTC can also be identified from the measured arcing signals (red impulses in Figure 3.5), which is distinctive and cannot be accomplished by using the measured vibration signals. The time difference found among

the arcing signals in the three phases may be mainly due to the different signal propagation paths on each phase or mechanical synchronous error between the three phases.

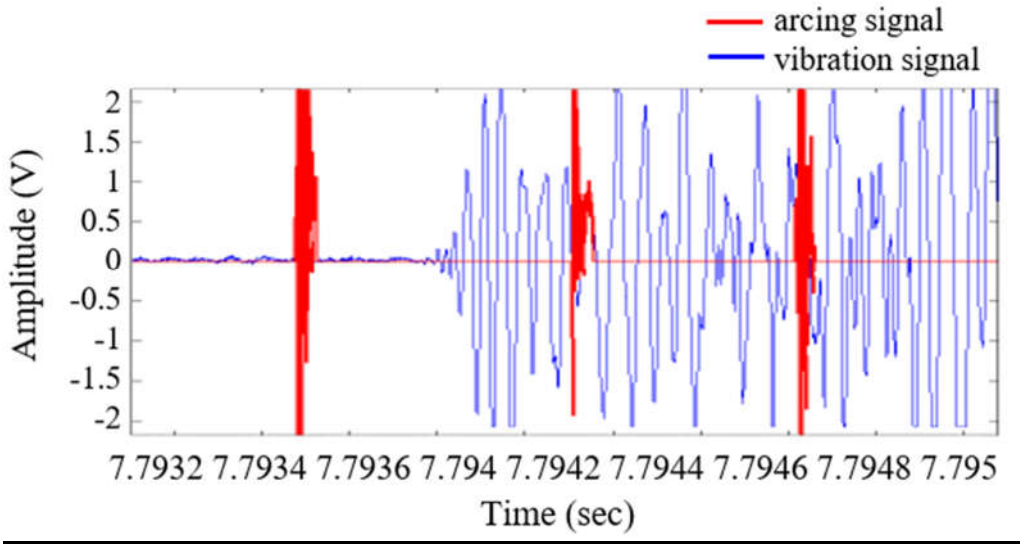

Figure 3.5 Vibration and arcing signals measured from a three phase OLTC [47].

3.3.3 Implementation of a Joint Vibration and Arcing Signal Measurement System

The joint vibration and arcing signal measurement system developed in this thesis is shown in Figure 3.6. It consists of a number of components: (1) a vibration sensor in the frequency range of 50 - 400 kHz; (2) a pre-amplifier to amplify vibration signals to 60 dB; (3) a HFCT for measuring arcing signals with its - 3 dB frequency band of 350 kHz to 35 MHz; (4) a current transformer for measuring OLTC's motor drive current; and (5) a high speed data acquisition system with the sampling rate of one Mega sample per second. In one acquisition, 50 seconds of signals were recorded to capture all signals generated for four consecutive OLTC operations.

A vibration sensor was installed on the tank of a bolt-on type OLTC or on the transformer's tank close to installed column type OLTC. The clamping type HFCT was installed on the grounding cable of a transformer to capture arcing signals. Motor current was measured to obtain the information of OLTC's motor drive system. The motor current measurement can also help analyse the sources of impulses, i.e., establishing whether these impulses are generated by arcing or power electronics (due to motor's stops or starts, refer to Figure 3.10).

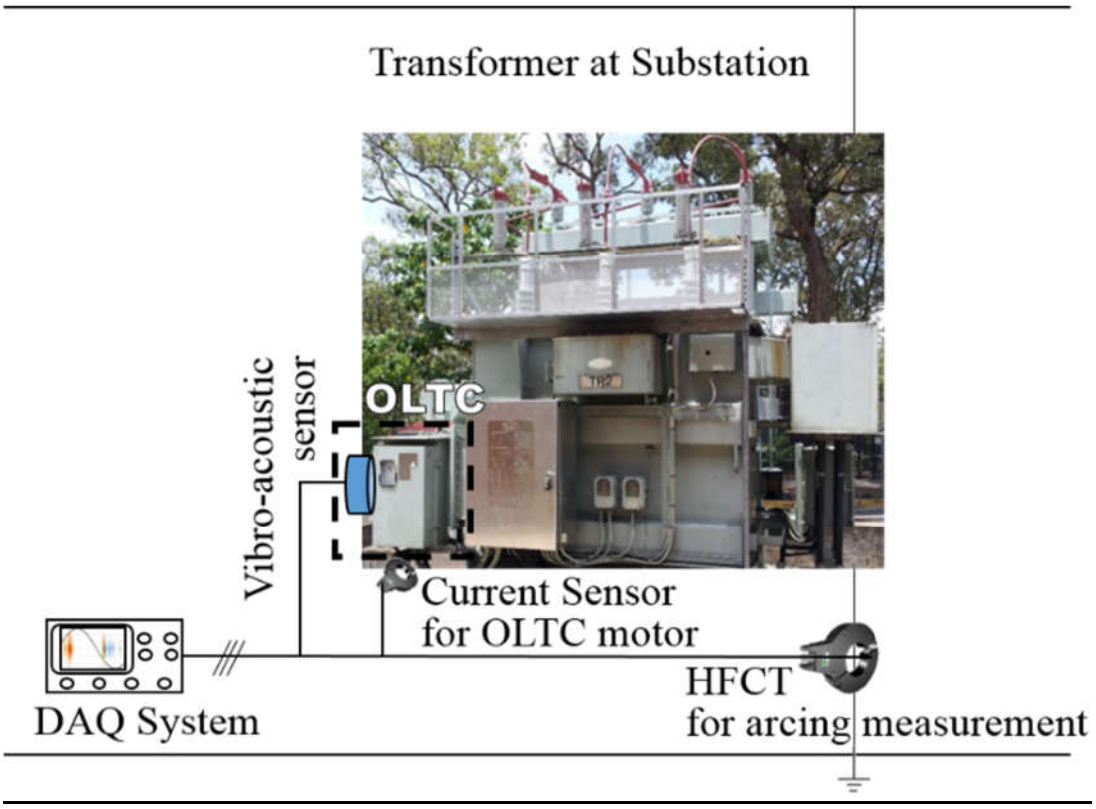

Figure 3.6 Joint vibration and arcing measurement system for vibration signal interpretation in OLTC condition monitoring [47].

3.4 Probabilistic Wavelet Transform for Extracting Arcing Signal from HFCT Measurement

During online condition monitoring of OLTC at a substation environment, arcing signals acquired by HFCT can be highly coupled with noise signals. It is therefore necessary to apply appropriate signal processing techniques to extract arcing signals of interest from the measured signals. In this chapter a probabilistic wavelet transform technique is adopted. This technique was initially developed by the author of this thesis [135]. It has been extended and applied for extracting arcing signals obtained from the joint vibration and arcing signal measurement system. Instead of using a single threshold to make a decision on whether the measured signals are from arcing signals or noise, the adopted probabilistic wavelet transform provides probability indices for measured signals by using multiple thresholds. Thus, the result presents the likelihood of the measured signals as being arcing signals.

Wavelet transform has been widely adopted to extract signals of interest, similar to a mother wavelet but being distinguishable from other (noise) signals [39 – 40, 134]. In a wavelet transform, a wavelet function decomposes the originally measured signals with a pre-selected mother wavelet into a series of wavelet coefficients at different decomposition levels, which correspond to frequency bands. Then a single threshold is imposed onto the obtained wavelet coefficients to extract interested signals (i.e., arcing) and remove the remainder. Only those coefficients largely correlated with the selected mother

wavelet and remaining after applying a threshold are regarded as the arcing signals of interest. Those extracted coefficients are used for reconstructing original signal.

However, in online arcing signal measurement for OLTC, excessive noise might exist and wavelet coefficients related to noise may have higher correlation than those of arcing activity. Thus, it might be scarcely possible to find a single threshold that can extract only arcing signals without including a significant amount of noise signals having higher amplitude than arcing signals. As such, signals from the above single threshold cannot be assured always as being arcing signals.

The adopted probabilistic wavelet transform adopts a quantile based multi-scale thresholding method. An ordered dataset needs to be split into *N* subsets with an equal probability interval. For the purpose of the segmentation, quantile values are used to define the boundaries of consecutive data subsets. A comparison between a quantile-based segmentation method and an amplitude-based segmentation method is presented in Figure 3.7 [135].

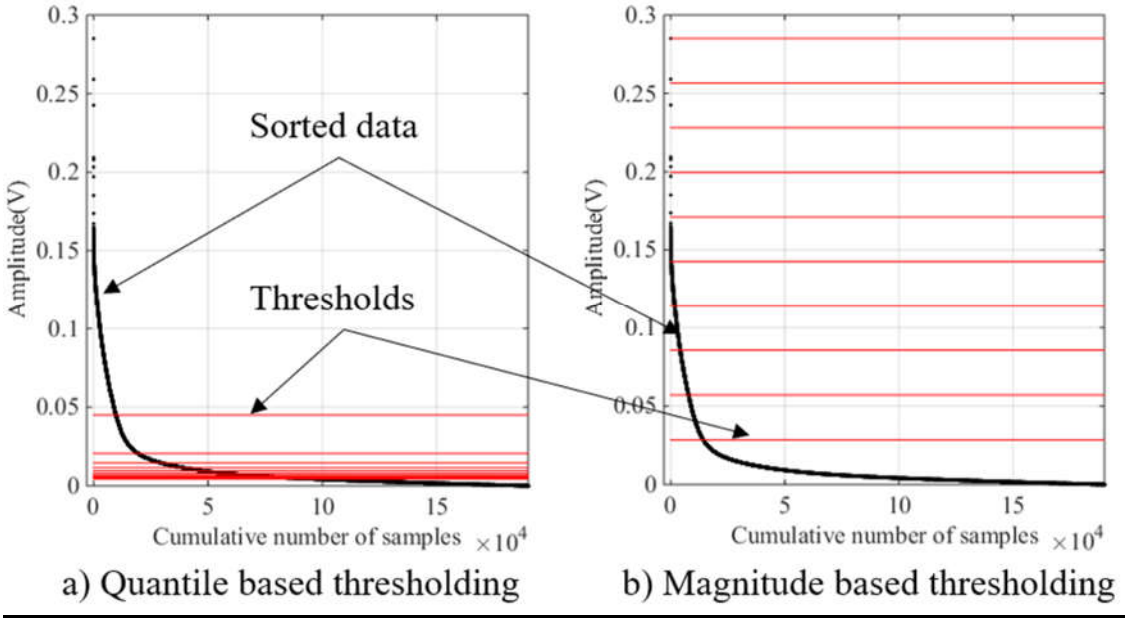

Figure 3.7 Data segmentation approaches (a) quantile-based; and (b) magnitude-based. Data points (samples) are in blue, boundary lines are in red, horizontal axis shows the data sample number and vertical axis shows the signal amplitude (measured by inductive measurement system, in V) [135].

It can be seen from the figure that quantile-based segmentation is based on a signal's occurrence rate and it can provide a probability means for differentiating arcing signal from noise. In contrast, the single amplitude-based segmentation method adopts a fixed interval between data samples. Thus, the amplitude-based method may not be effective for establishing a multi-level threshold targeting a probability-based wavelet transform.

The quantile-based data segmentation method is adopted for constructing a multi-scale thresholding in probabilistic wavelet transform. In the multi-scale thresholding, a baseline threshold (the lowest one in multi-scale thresholds) is firstly determined as:

$$\sum \left| \frac{X_i}{\max(X_i)} \right| / \#\ (X_i) \tag{3.5}$$

where max(X_i) is the largest magnitude of wavelet coefficients of extracted signals and # (X_i) is the number of wavelet coefficients at the i-th decomposition level. The quantile-based segmentation as shown in Figure 3.7a is then applied to determine the multi-scale thresholds. Figure 3.8 presents the whole procedure of the probabilistic wavelet transform [135].

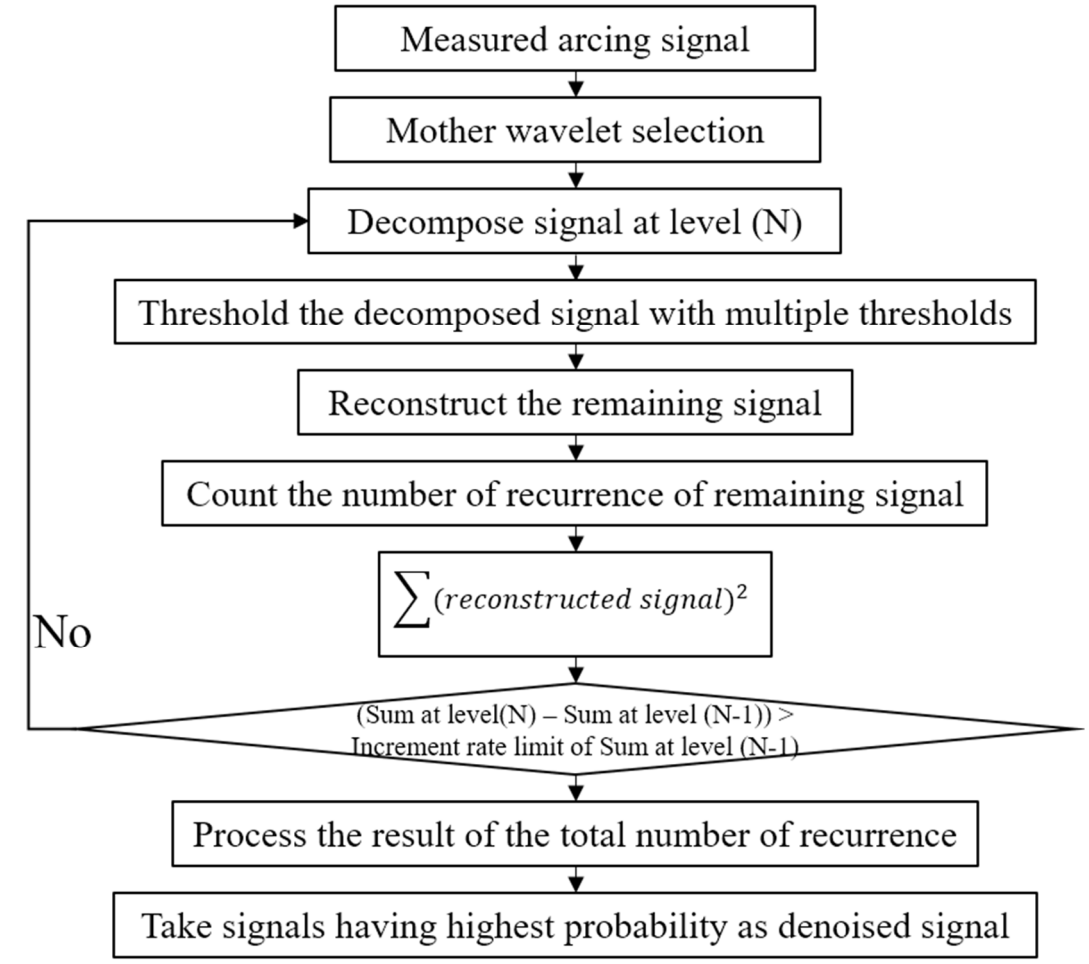

Figure 3.8 Implementation of the probability based wavelet transform [135].

In the probability based wavelet transform, the optimal mother wavelet (or wavelet function) is selected based on the normalised correlative energy by:

$$E_N = \sum \left\{ \frac{R_N(i)}{\max[R_N(i)]} \right\}^2 \tag{3.6}$$

where N is the N-th decomposition level, $R_N(i)$ denotes the i-th reconstruction signal after applying thresholds at the N-th decomposition level and $\max[R_N(i)]$ denotes the largest magnitude of the reconstructed signals at the N-th decomposition level. A mother wavelet having the highest normalised correlative energy is finally selected for decomposing measured signals in probability-based wavelet transform.

In the probability-based wavelet transform, a decomposition level is decided by evaluating the normalised energy of reconstructed signals after multi-scale thresholding. If the difference between the normalised energy of a current decomposition level and that of a previous decomposition level becomes within a very small range, then the previous decomposition level becomes the final decomposition level.

Finally, a probability index is calculated to indicate the possibility of the extracted signal being an arcing signal as:

$$Prob(i) = \frac{\sum_{k=1}^{N_{decmp}} \sum_{j=1}^{N_{sub}} Ps(i)_{k,j}}{N_{decmp} \times N_{sub}} \times 100(\%) \tag{3.7}$$

where *Prob(i)* denotes the probability index for the i-th extracted signal, N_{decmp} is the number of decomposition levels, N_{sub} denotes multi-scale thresholds at each decomposition levels and $Ps(i)_{k,j}$ can be zero or one to indicate whether there is a wavelet coefficient associated to the i-th extracted signal at the j-th level threshold of the k-th decomposition level.

Figure 3.9 provides an example of arcing signal extraction by the probability-based wavelet transform. Figure 3.9(a) is the original signal obtained from HFCT measurement. According to the above quantile-based thresholding, mother wavelet selection and decomposition level determination, the baseline threshold is calculated as 99.99 %, the optimal wavelet function is 'db20' and the number of decomposition levels is six.

The probability indices of measured signals are presented in Figure 3.9(b). In the figure, the originally measured signals are depicted in grey, signals in other colours are extracted signals and their probability indices are represented using a colour bar. The signals' probabilities of being generated by arcing events are magnified in Figure 3.9(c). The final extracted arcing signals are shown in Figure 3.9(d). In Section 3.5, these extracted arcing signals will be further investigated together with vibration signals.

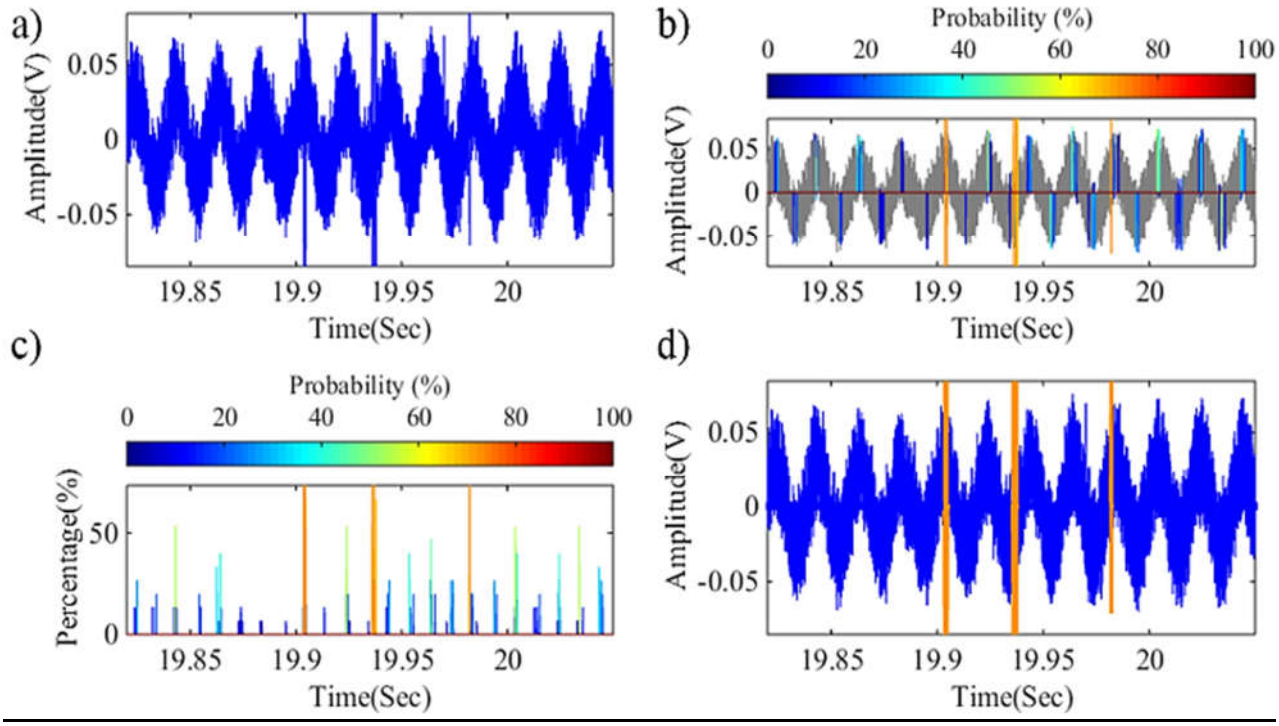

Figure 3.9 Arcing signal extraction results (a) data measured by a HFCT; (b) processed arcing signal by the probability-based wavelet transform; (c) results of probability indices; and (d) initial signal (blue) and extracted arcing signal (orange) [47].

During online measurements, the above probability-based wavelet transform is firstly performed offline. By using the arcing signals measured by a HFCT sensor, calculations are conducted to determine mother wavelet, thresholds and the number of decomposition levels. Once the above three parameters are determined, the wavelet transform can be performed online along with the acquisition of vibration, HFCT and motor current data using the joint measurement system.

3.5 Case Studies

The joint vibration and arcing measurement system was employed for online condition monitoring of two different types of OLTCs at a substation of a local distribution authority. The two types of OLTCs are: a selector (bolt-on or compartment) switch type OLTC for a 15 MVA (33/11 kV) transformer installed in 1990; and a diverter switch (column) type OLTC equipped with vacuum interrupters for a 25 MVA (33/11 kV) transformer installed in 2002. During the measurement, OLTC's tap positions were changed by manual operation with a sequence of one step-up, two step-downs and one step-up. The online joint vibration and arcing measurements followed the setup depicted in Figure 3.6.

3.5.1 Results and Analysis

Figure 3.10 presents the test results of the selector switch type OLTC, including measured signals and the extracted arcing signals by the probability-based wavelet transform. Figure 3.10(a) shows the

timing diagram of the tested OLTC's operation and Figure 3.10(b) presents the measured vibration signals showing five significant mechanical events of the OLTC. Figure 3.10(c) depicts the noise immersed original arcing signals (in blue) and the extracted arcing signals (in red) obtained by the adopted probability-based wavelet transform. The extracted arcing signals are related to the closing events of OLTC's switches; or the motor drive system of the OLTC (i.e. stop and/or start).

Among the five extracted arcing signals found in Figure 3.10(c), the first arcing signal (located at around 24.15 second) was provoked when the transition switch 'M2' was connected to tap position '1' as shown in Figure 3.10(a). The second arcing signal was caused by the transition switch 'M1' moving to tap position '2'. When the main switch 'H' was connected to its target tap position (tap position '2'), the third arcing signal was invoked. Amongst the three arcing signals, the second arcing signal has the largest amplitude. The reason is due to the voltage difference between the transition switch 'M1' and tap position '2' as derived from Equation 3.4. On the other hand, the first arcing signal shows the lowest amplitude since the moving switch 'M2' is energised with a similar voltage to tap position '1'. The third arcing signal shows a smaller amplitude than that of the second signal. The voltage level of main switch 'H' is lower than that of the transition switch 'M1' and the same as a voltage drop across the transition resistor of 'M1'. Main switch's voltage (V_H) can be represented as:

$$V_H = V_{M1} - R_{M1} I_{Circulating} \tag{3.8}$$

where V_H is a voltage at the main switch 'H', V_{M1} is a voltage at the transition switch 'M1', R_{M1}denotes transition resistance on the transition switch 'M1' and $I_{Circulating}$ is the circuit current between the main switch 'H' and the transition switch 'M1'.

The last two impulses in Figure 3.10(c) are caused by power electronics, especially when an OLTC's motor stops. This is verified by the measured motor current on OLTC as shown in Figure 3.10(d). With reference to the above analysis of arcing signal, it is possible to further analyse vibration signals shown in Figure 3.10(b). By comparing signals in Figure 3.10(b) and 3.10(c), it can be shown that vibration signals 'a' and 'c' were due to the closing and opening events of the transition switch 'M2'; vibration signals 'b' and 'e' were due to the closing and opening events of the transition switch 'M1'; and vibration signal 'd' was due to the closing event of the main switch 'H'.

Figure 3.11 presents the results of the diverter type (column) OLTC with the measured vibration and arcing signals. It is followed by the extracted arcing signals calculated by the probability-based wavelet transform. Figure 3.11(a) shows the timing diagram of the switching operations of the OLTC. It can be seen that the diverter type OLTC shows more operational steps than for the selector switch type OLTC. The additional sequences are required for the equipped vacuum interrupters as well as main and transition switches.

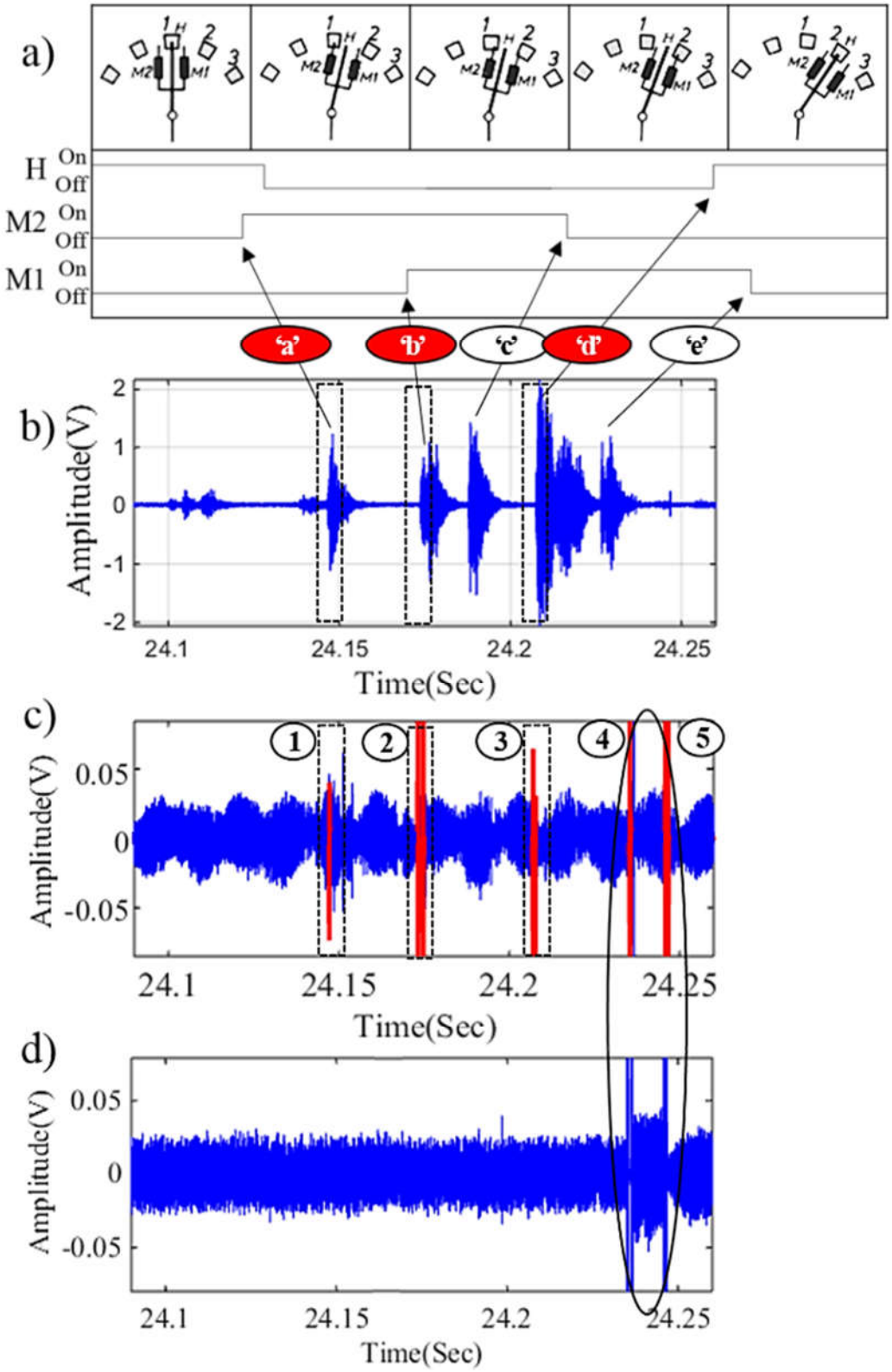

Figure 3.10 Selector switch (bolt-on or compartment) type and the OLTC's operation analysis (a) timing diagram of OLTC's operation; (b) measured vibration signals; (c) measured and extracted arcing signals; and (d) measured OLTC motor current [47].

Figure 3.11(b) shows the measured vibration signals. It can be seen that there are eight vibration signals corresponding to each switches' operation to complete a cycle of changing tap positions.

However, it is impossible to explain the source vibration signals with each step of OLTC's operations, i.e., specifying which vibration signal is generated by which switch's events.

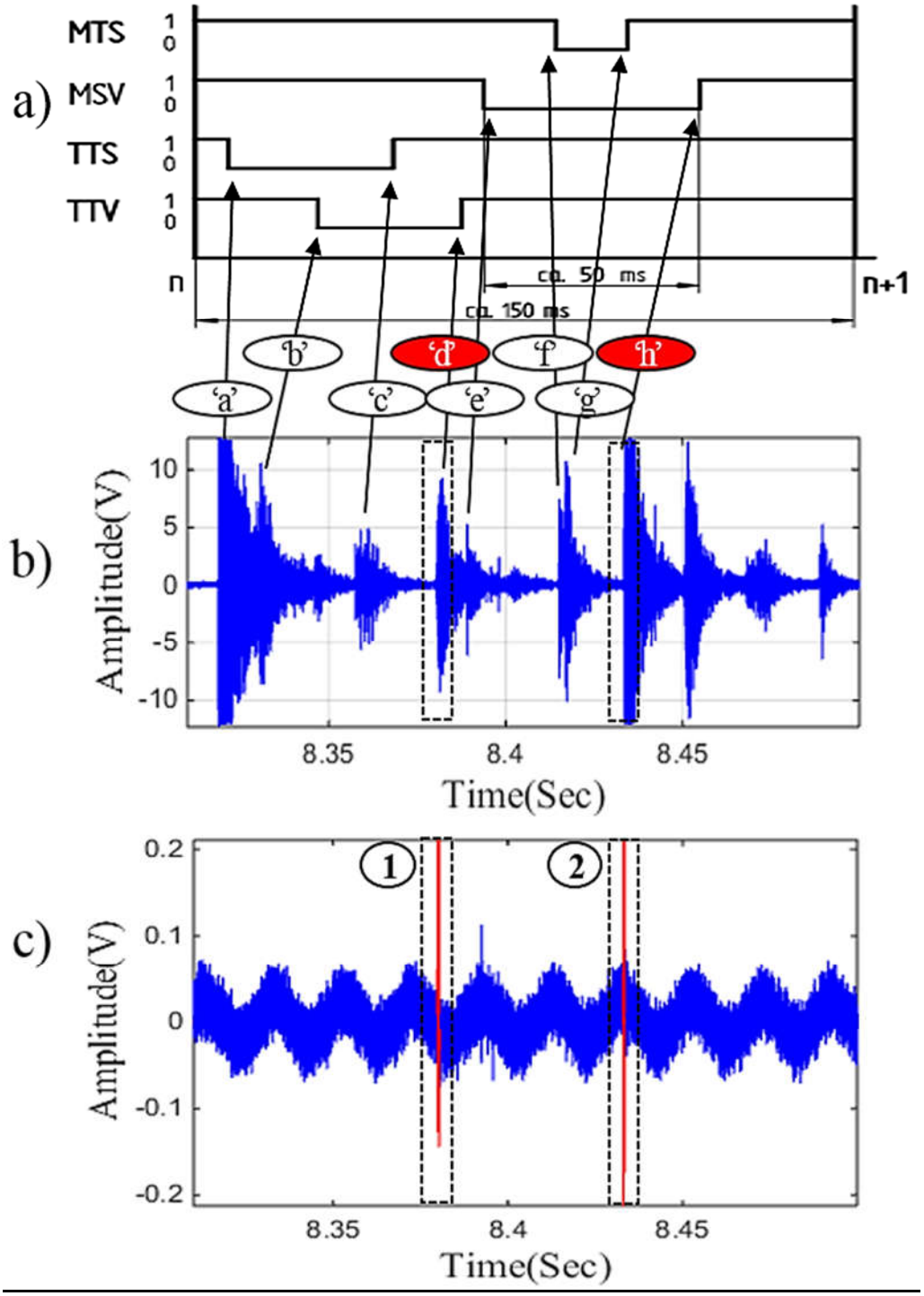

Figure 3.11 The analysis of diverter switching (or Column) type OLTC with vacuum interrupters (a) timing diagram of OLTC's operation; (b) measured vibration signals; and (c) measured and extracted arcing signals [47].

Figure 3.11(c) presents the originally measured signals by HFCT (in blue) and extracted arcing signals (in red). With reference to the diagram of the operational sequence of the column type OLTC (refer to Figure 3.2), it can be seen that the first arcing signal was generated when the transition

switch's vacuum interrupter was closed at its target tap position as shown in Figure 3.2(e), while the second arcing signal was generated when the main switch's vacuum interrupter was closed at its target tap position as shown in Figure 3.2(i). For the two arcing signals, the second signal caused by the closing event of the main switch's vacuum interrupter has a higher amplitude compared to the first signal caused by the closing event of the transition switch's vacuum interrupter. The difference is due to the resistor installed in the transition switch.

With reference to Figure 3.11(c), it is possible to further analyse the eight vibration signals shown in Figure 3.11(b). By considering the signals' occurrence in Figure 3.11(b) and Figure 3.11(c), it can be concluded that vibration signal 'd' was due to the closing event of the transition switch's vacuum interrupter as shown in Figure 3.2(e), while vibration signal 'h' was due to the closing event of the main switch's vacuum interrupter as shown in Figure 3.2(i). For the other six vibration signals shown in Figure 3.11(b), there are no corresponding arcing signals found in Figure 3.11(c). This is because vacuum interrupters were opened during the operation of the main and transition switches. This can prevent the main and transition switches from being exposed directly to arcing events, which prolongs the life of the switch contacts.

3.5.2 Discussion

From the above two case studies, it can be seen that arcing signals are generated at the moment of a switch's closing event. Measuring the arcing signals can be used to identify the source of the switches' closing events in a series of vibration signals. Vibration signals synchronised with the arcing signals in time can be taken as the corresponding OLTC's operations. Therefore, arcing measurement can be used to interpret vibration signals to reveal a corresponding OLTC operation.

Thus, the proposed joint vibration and arcing signal measurement helps provide a clear interpretation of vibration signals regarding OLTC's mechanical operation, especially for closing and opening events of switches. Such interpretation will pave the way for a better understanding about vibration signals from OLTC operations.

Additionally, HFCT for capturing the OLTC's arcing events can also detect PD signals induced by PD activity inside a transformer. However, the arcing signals by OLTC's switching events are more evident in amplitude and the occurrence time of the arcing events by an OLTC is strictly limited for the time of OLTC's operation, a couple of hundred milliseconds. By looking at the vibration signals from OLTC's mechanical events, the obtained arcing signals can be confirmed properly.

The joint vibration and arcing measurement system developed in this chapter can be used to capture vibration signals, arcing signals and motor current of OLTC operation. A database consisting of characteristic signatures of the vibration signals can then be established for automated analysis for

ongoing OLTC condition monitoring. Then based on the developed database, pattern recognition algorithms can indicate a corresponding fault diagnosis by analysing vibration signals on the OLTC of interest.

3.6 Summary

This chapter demonstrated a proof-of-concept on the joint vibration and arcing measurement method for online mechanical condition monitoring of an OLTC. By innovatively integrating arcing measurement with vibration measurement, the joint measurement method clearly identified the opening and closing events of OLTC switches and subsequently revealed the event sequences in OLTC's operations. The implementation of this method is straightforward without disturbing a normal operation of a transformer. It can pave the way for an online OLTC's mechanical condition assessment.

To jointly analyse the measured vibration and arcing signals and correlate the two different types of signals to corresponding mechanical events of an OLTC, it is critical to extract information from both vibration and arcing signals in a synchronised manner without distortion. For the purpose of not inducing any time gap between the two signals, a suitable signal processing method has been developed and it will be discussed in the next chapter.

Chap 4. Online On-Load Tap Changer Condition Monitoring System Development

Contribution of the Chapter

In the previous chapter, a joint vibration signal and arcing signal measurement method was presented. It correlated the measured vibration signals to mechanical events of OLTC's operation. However, there are still considerable difficulties in processing vibration signals and arcing signals in a synchronised manner without any distortion. In this Chapter, a Savitzky-Golay filter is proposed to process the two different types of signals acquired from the joint vibration and arcing measurement system installed on in-service OLTCs. It is found that the Savitzky-Golay filter has the potential to process both vibration and arcing signals induced from OLTC's operations to extract essential information from both types of signals without any time delay. Moreover, the Savitzky-Golay filter also is capable of retrieving voltage phase information from the measured arcing signal. The methodologies presented in this chapter can significantly improve the visibility of OLTC's mechanical operation for effective online OLTC's condition monitoring.

This chapter has been reproduced from the following paper: J. Seo, H. Ma and Tapan K. Saha, "**On Savitzky-Golay Filtering for Online Condition Monitoring of Transformer On-Load Tap Changer**," in IEEE Transactions on Power Delivery, vol. 33, no. 4, pp. 1689-1698, August 2018.

4.1 Introduction

A change in an OLTC's mechanical condition can be reflected in the transition of the magnitude and time of occurrence of vibration signals obtained while OLTC is in operation [13, 39 - 40, 43, 138]. However, considerable difficulties still exist in identifying the precise time stamps (time of occurrences) of peaks of the vibration signals due to the complex nature of vibration signals and the very short time of an OLTC's operation, about 10 milliseconds. An error in capturing the event time of peaks can cause misinterpretation in correlating vibration signals to the corresponding mechanical events of OLTC [40]. This may impair the effectiveness of the joint vibration and arcing measurement proposed in Chapter 3 for OLTC's condition monitoring [47].

A number of signal processing techniques have been applied to analyse OLTC's vibration signal [39 - 40, 43, 138]. Several researchers adopted wavelet transform [39, 138]. Instead of directly dealing with the originally measured signal to decide the amplitude and time stamp of vibration signal, they attempted to smooth vibration signals to produce a simplified waveform using a wavelet's approximation. The smoothed (simplified) waveforms were then used to investigate any condition change of OLTC. However, in the wavelet's approximation approach, it is not a trivial task to decide important parameters of wavelet transform such as a mother wavelet (wavelet filter) and decomposition levels to obtain a satisfactory approximation result. Moving Average (MA) filter and Low Pass Filter (LPF) have also been used to simplify vibration signals.

However, wavelet's approximation, MA filter and LPF can cause a time shift in outputs compared to the original signal. Such time difference can cause an issue in signal analysis, in which signal matching and alignment are essential. In the joint vibration and arcing signal measurement system, signal processing algorithms for vibration signal and arcing signal need different parameters since they exist in different frequencies. The different parameters of the signal processing methods cause an undesirable time gap of different extents between the signals.

In the joint vibration signal and arcing signal measurement method presented in the previous chapter, the time alignment of the two types of signals is a critical requirement in analysing them. A time discrepancy between the two signals can cause a misinterpretation of the correlation between vibration signals and seeking the source of mechanical events. It is challenging to process vibration and arcing signals simultaneously, especially with a requirement to maintain the event time information of two different types of signals without causing any time discrepancy.

This chapter demonstrates the application of Savitzky-Golay filter for the first time to process both vibration and arcing signals for facilitating the joint measurement system for OLTC's condition monitoring. The Savitzky-Golay filter processes a signal without causing a time delay regardless of

the degree of filtration while it extracts necessary profiles and information from the signals. This is because it computes at each individual data point by using a local least mean squared error based polynomial approximation of an input signal. After investigating a proper selection of the filter's parameters for each vibration and arcing signal from the OLTC's operations, optimal Savitzky-Golay filters are designed accordingly. The designed filters are then used to process vibration and arcing signals acquired from the joint measurement system installed on two different types of in-service OLTCs. It will be demonstrated that Savitzky-Golay filter can acquire an ideally simplified waveform of vibration signals and extract an arcing signal of interest from noise without disturbing the original time information. Additionally, the method can identify AC phase information with a signal captured by HFCT for the purpose of arcing signal measurement. The result can be used to support the interpretation of OLTC's operational sequence in online condition monitoring.

This Chapter is organised as follows. The mathematical formulation and implementation of the Savitzky-Golay filter are discussed in Section 4.2. Three major applications of the Savitzky-Golay filter to analyse vibration signal and arcing signal are presented in Section 4.3 to 4.5, respectively. To verify the applicability of the proposed Savitzky-Golay filter, case studies using the field measurements of two different types of in-service OLTCs are provided in Section 4.6. Section 4.7 concludes this Chapter.

4.2 The Fundamentals of the Savitzky-Golay Filter [140 – 141]

Figure 4.1 shows the measured vibration signal and arcing signals from an OLTC. It can be seen that necessary signal processing needs to be performed on the measured signals for inferring the mechanical events involved in OLTC's operation. In [47], a LPF was applied to smooth the vibration signal while a probabilistic wavelet transform algorithm was applied to extract the arcing signal from noise and harmonics. However, such arrangements may still have two issues: (1) time delay can exist between the originally measured signal and the smoothed/extracted signal, which leads to an inappropriate alignment between the vibration signal and arcing signal; and (2) the probabilistic wavelet transform algorithm adopted in Chapter 3 can be time-consuming in extracting an arcing signal.

This chapter addresses the above two issues by applying the Savitzky-Golay filter to capture the profile of vibration signal and extract the arcing signal of interest from the measured signal corrupted with noise and harmonics. The Savitzky-Golay filter does not cause any time gap in processing and thus it maintains the original synchronisation between vibration and arcing signal. A brief review of the fundamentals of Savitzky-Golay filter is provided as follows.

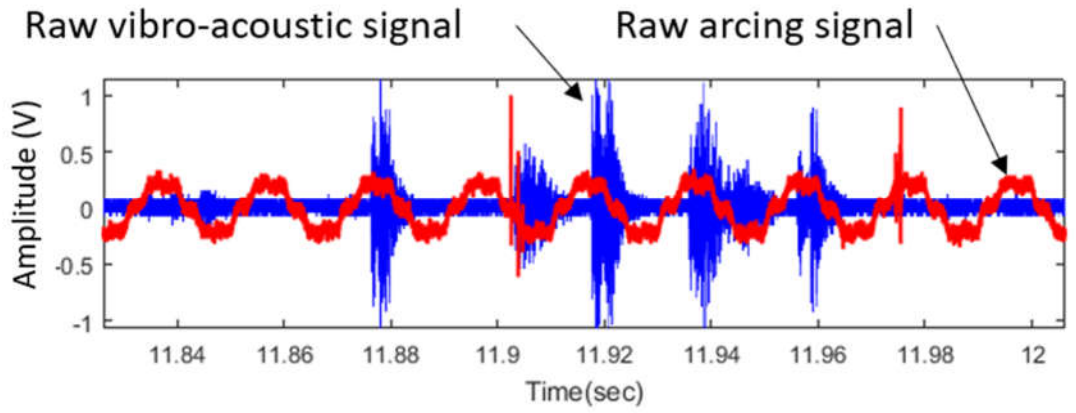

Figure 4.1 Vibration and arcing signals from an OLTC at field [139].

The Savitzky-Golay filter uses a local least-squared polynomial approximation method. By controlling the parameters of the degree of polynomial and data size of a frame, noise can be removed at some frequencies and also a simplified envelope curve (profile) of the input signal can be generated. Moreover, it has the advantages of preserving the peaks and widths of the original signal while discarding components at unwanted frequencies. Such properties have considerable merits in processing OLTC's vibration and arcing signals [140 - 142]. Figure 4.2 illustrates the idea behind the Savitzky-Golay filter.

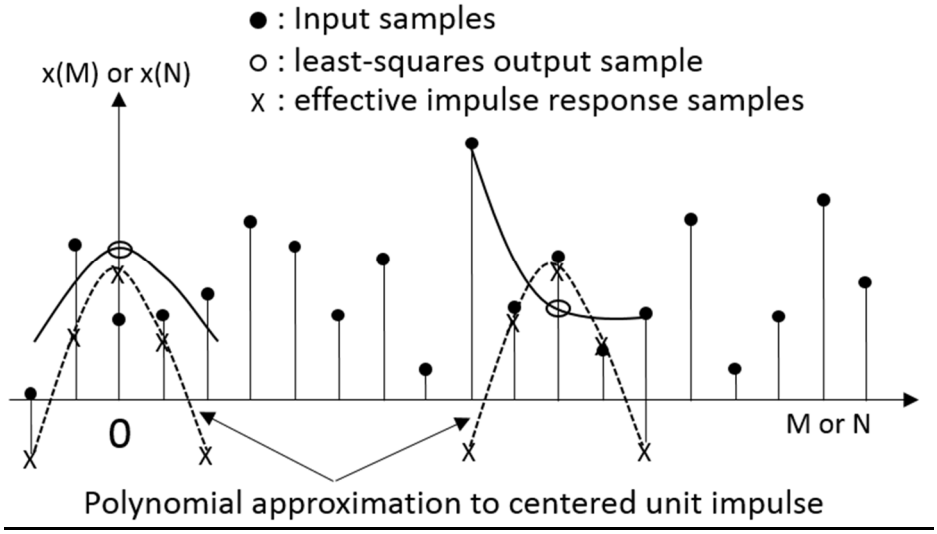

Figure 4.2 Illustration of the Savitzky-Golay filter [141].

If $x[n]$ denotes a series of samples of a signal by picking $2M + 1$ samples centred at $n = 0$, one can find a series of coefficients of a polynomial [141]:

$$p(n) = \sum_{k=0}^{N} a_k n^k \tag{4.1}$$

which minimises a mean squared error ϵ_N as

$$\sum_{n=-M}^{M} (p(n) - x[n])^2 = \sum_{n=-M}^{M} (\sum_{k=0}^{N} a_k n^k - x[n])^2 \tag{4.2}$$

As an example, in Figure 4.2 (left hand side of the graph), $p(n)$ is evaluated at an approximation interval of $[-2, 2]$ and the smoothed output is obtained at the centre of this interval. The output $y[0] = p(0) = a_0$ is equal to the 0-*th* polynomial coefficient. In practice, the approximation interval may not necessarily be symmetric with respect to the evaluation point. The whole process of the Savitzky-Golay filtering is:

1) Right shifting the interval by one sample.
2) Making the position of the middle sample of total $2M + 1$ samples as the new origin.
3) Performing the polynomial fitting and evaluation at the new origin. This process is repeated until the last sample of total $2M + 1$ samples.

To find the optimal coefficients for the polynomial in (4.1), one can differentiate ϵ_N for $i = 0, 1, \dots, N$ (total $N + 1$ unknown coefficients) and then set the corresponding derivative equal to zero as:

$$\frac{\partial \epsilon_N}{\partial a_i} = \sum_{n=-M}^{M} 2n^i \left(\sum_{k=0}^{N} a_k n^k - x[n]\right) = 0 \tag{4.3}$$

By interchanging the order of the summations, one can have $N + 1$ equations with $N + 1$ unknowns [4.9]:

$$\sum_{n=0}^{N}\left(\sum_{n=-M}^{M} n^{i+k}\right) a_k = \sum_{n=-M}^{M} n^i x[n], i = 0, 1, \dots, N \tag{4.4}$$

The Equation 4.4 is the normal equation for the least-squared approximation problem. It is worth mentioning that solving Equation 4.4 requires $2M \geq N$samples. If the order of the polynomial N is too large, the approximation problem can be badly conditioned to be close to $x[n]$.

An appropriately designed Savitzky-Golay filter can preserve the waveform of interest but remove noise-corrupted signals. Such performance of the Savitzky-Golay filter is more obvious from the frequency domain, in which the filter's output is extremely flat in their passbands with modest attenuation in their stopbands [141]. Since the symmetric Savitzky-Golay filter has zero phase, it does not introduce any feature shift with respect to the original signal.

4.3 Application of Savitzky-Golay Filter to Analyse Vibration Signal of OLTC

This section presents the extraction of the envelope curve from OLTC's vibration signal using Savitzky-Golay filter with properly selected parameters (order of polynomial and data size of a frame). It also provides a comparison of signal processing performance among Savitzky-Golay filter, LPF and wavelet's approximation in processing OLTC's vibration signal.

4.3.1 Vibration Signal's Pre-processing

As shown in Figure 4.1, the measured OLTC vibration signal exhibits a fast commutation between positive and negative polarities. Before Savitzky-Golay filtering, it needs to determine which form of vibration signal to be fed into the filter as the input. Three possible inputs of the filter are:

1) The spline curve using peaks in positive polarity.
2) The spline curve using peaks in both positive and negative polarities (negative polarity is reverted in the spline curve).
3) The absolute value of the original signal.

Figure 4.3 presents the above first two spline curves. It can be seen that the spline curve using peaks in positive polarity (black dotted line) is smoother than the spline curve using peaks in both positive and negative polarities (red dotted line). The third type of input for the filter takes the absolute value of the measured vibration signal instead of using any spline curve of the signal.

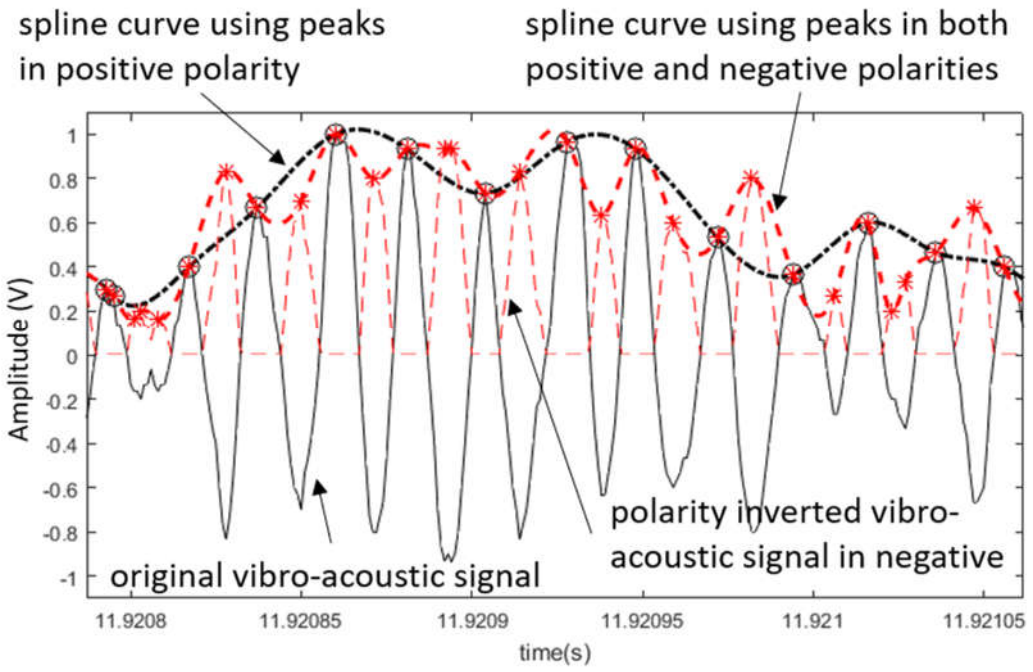

Figure 4.3 (1) Spline curve using peaks in positive polarity (black dotted line); and (2) spline curve using peaks in both positive and negative polarities (red dotted line) [139].

Using the above three inputs, three Savitzky-Golay filters are implemented with the same parameters of frame size and polynomial order. Figure 4.4 presents the results of the Savitzky-Golay filters. It can be seen that the Savitzky-Golay filter using the spline curve with peaks in both positive and negative polarities (red dotted line in Figure 4.4) generates more fluctuated waveform compared to the other two filters. This is because the signal's peaks in the positive and negative polarities are not strictly symmetric with respect to the 'X' axis as shown in Figure 4.3.

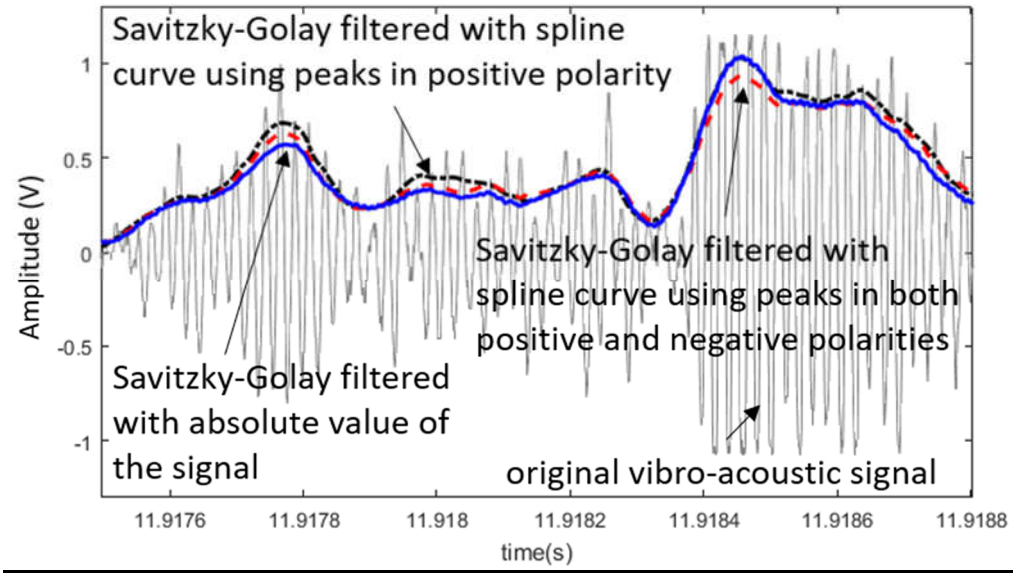

Figure 4.4 Results of Savitzky-Golay filters with three different inputs as described in Figure 4.4 (1) signal components with positive polarity (black dotted line); (2) signal components with both positive and negative polarities (red dotted line); and (3) the absolute value of the vibration signal (blue line) [139].

Figure 4.5 shows the results of Savitzky-Golay filter on the vibration signal obtained from a full cycle of OLTC's operation (i.e., changing one tap position). As shown in the figure, though the filter using the spline curve of peaks in positive polarity can achieve an approximation of the vibration signal around its peaks, some components of it slip into the negative side in amplitude (highlighted with black circles). A filter not being able to keep consistency is unfavourable for an output.

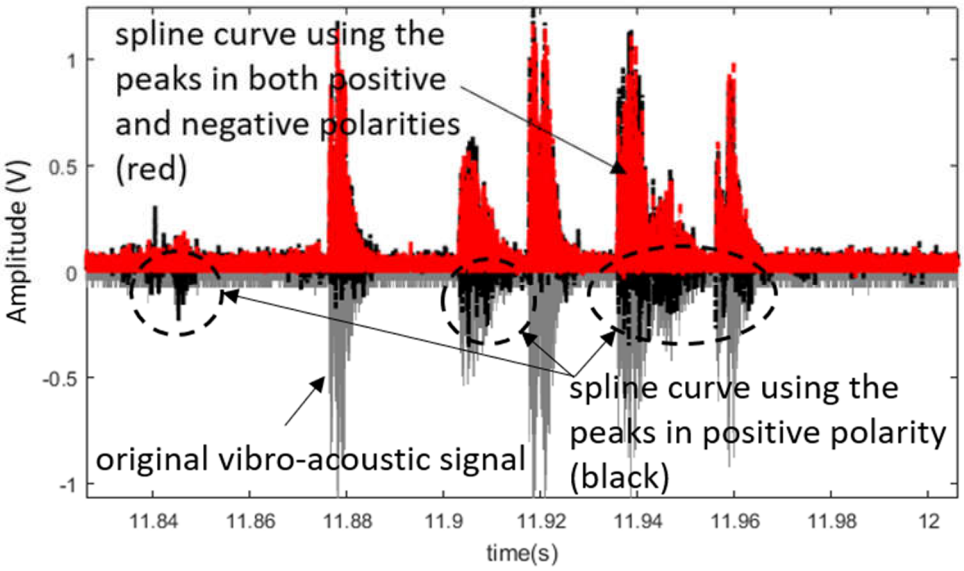

Figure 4.5 Results of Savitzky-Golay filtering on the vibration signal obtained from a full cycle of OLTC's operation (i.e., changing one tap position) using (1) spline curve of peaks in positive polarity (in black); and (2) spline curve of peaks in both positive and negative polarities (in red). The signal components highlighted in the black circles are denoted as those leaked to the negative magnitude [139].

As shown in Figure 4.4, the Savitzky-Golay filter using the absolute value of the original vibration signal exhibits a smoothed approximation of the measured vibration signal without compromising its consistency. Also, this filter does not exhibit the signal component leakage problem as mentioned in Figure 4.4. Therefore, in this Chapter, the absolute value of vibration signals other than spline curve of its peaks is fed into the Savitzky-Golay filter as inputs.

4.3.2 Savitzky-Golay Filter Parameter Selections

4.3.2.1 Selecting the Degree of Polynomial (N)

It can be seen from Equations 4.1 and 4.2 that with the increase in the degree of polynomial, the polynomial curve fits the original signal better and the mean squared approximation error becomes smaller. However, adopting an excessive polynomial degree may lead to no solution in the signal waveform smoothing and simplification.

Figure 4.6 compares the results of five Savitzky-Golay filters, which have the same data frame size ($M = 150$) but different orders of polynomial (from the first to the ninth order). It can be seen that the resultant curve using the Savitzky-Golay filter with the first order of polynomial is over-smoothed (i.e., too simplified). It fails to capture the necessary profile of the original signal. On the contrary, the filters with the seventh and the ninth order of polynomial lead to a better fitted curve, which tracks the changing trend of the original vibration signal. The Savitzky-Golay filter with the fifth order of polynomial shows a balanced performance in simplifying and tracking the changes of the original vibration signal.

The frequency spectrums of the outputs of the above filters are plotted in Figure 4.7. As the order of polynomial curve decreases, signal components at high frequencies diminish accordingly. Compared to the output by the fifth order of polynomial, the outputs of the first and the third order of polynomials are significantly compromised at 2.5 kHz, which is the frequency of interest corresponding to the mechanical operation of OLTC from an observation.

Considering a trade-off between the traceability and the simplification of the signal's waveform, the fifth order for configuring Savitzky-Golay filter is adopted to process OLTC's vibration signal.

It is worth mentioning that regardless of the order (N) of polynomial, the output of a Savitzky-Golay filter does not cause a time shift with respect to the input signal. This is a significant advantage when the filter is used for processing multiple types of signals (e.g., vibration and arcing signals in the joint OLTC condition monitoring system).

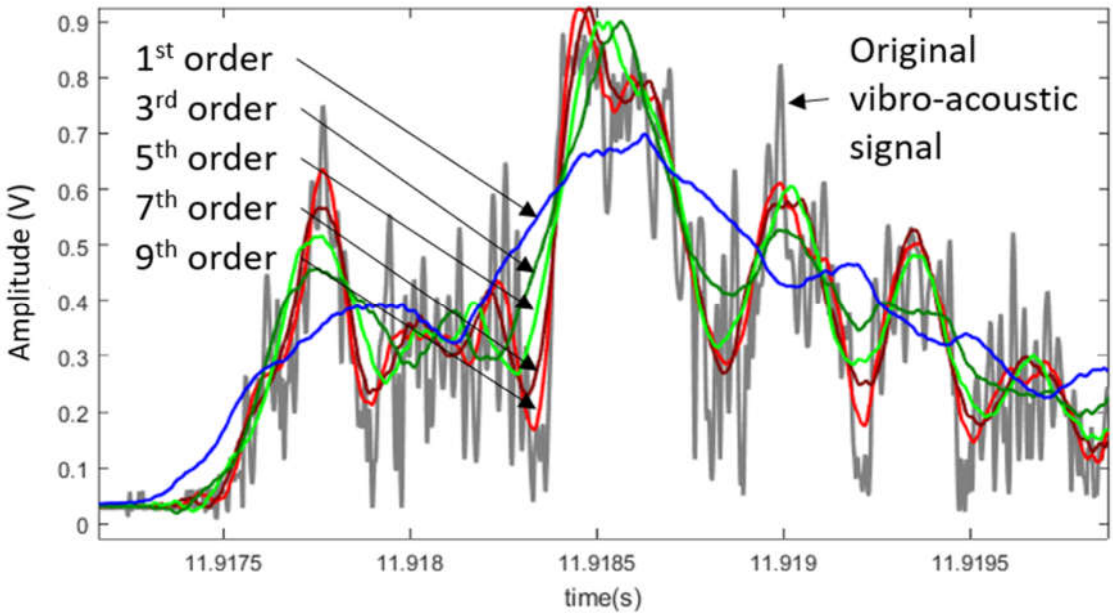

Figure 4.6 Results of Savitzky-Golay filters with different orders of polynomials (*N* = 1, 3, 5, 7, 9) but the same data frame size ($M = 150$)[139].

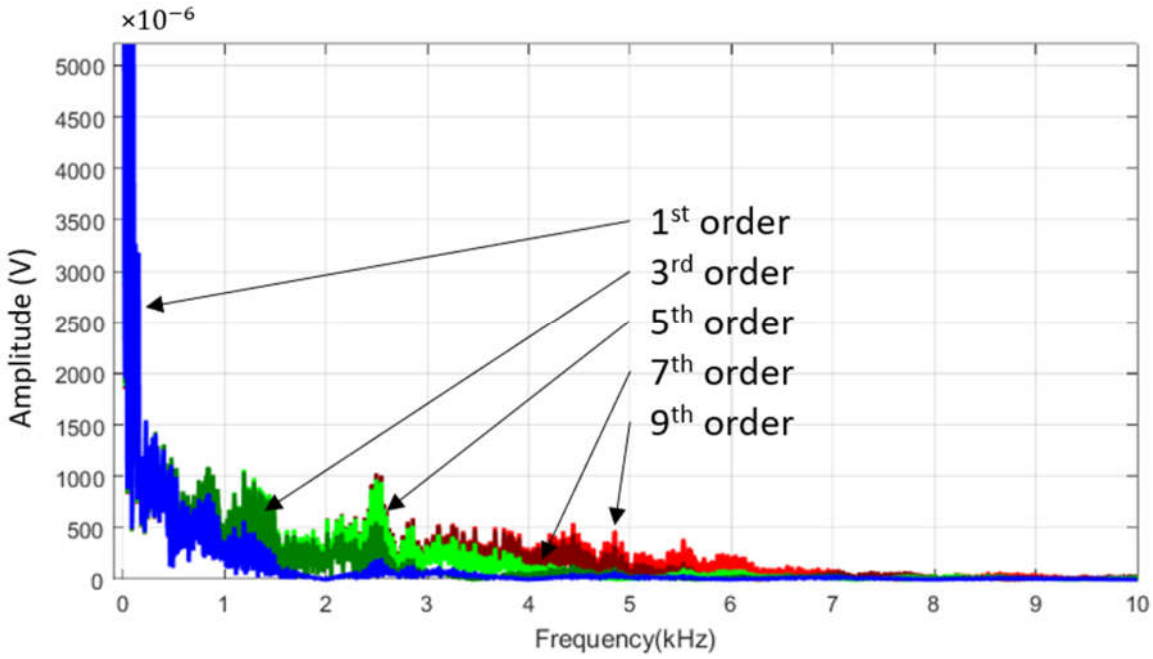

Figure 4.7 Frequency spectrum of the outputs of Savitzky-Golay filters with different orders of polynomials from the first to the ninth order (*N* = 1, 3, 5, 7, 9) but the same data frame size ($M = 150$) [139].

4.3.2.2 Selecting the Data Frame Size ($2M + 1$)

Along with the degree of polynomial, the data frame size ($2M + 1$) also affects the output of a Savitzky-Golay filter. Figure 4.8 shows the results of five Savitzky-Golay filters with different data frame sizes (*M* = 50, 200, 350, 500, 650) but the same order of polynomial (the fifth order). Figure 4.9 presents the frequency spectrum of the outputs of the filters.

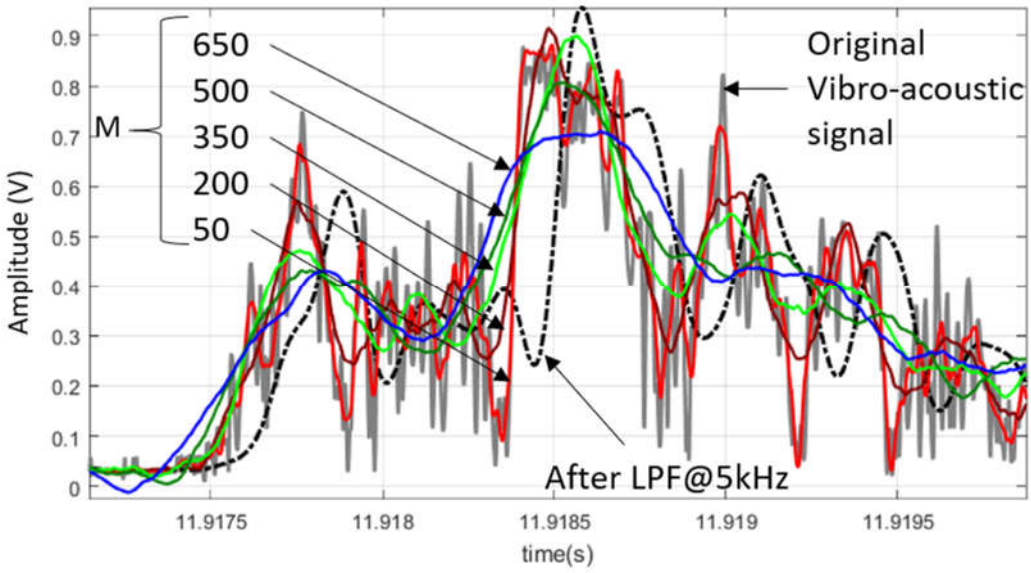

Figure 4.8 Outputs of Savitzky-Golay filters with different frame sizes (M = 50, 200, 350, 500, 650) but the same order of polynomial (N = 5) [139].

It can be seen from Figure 4.8 that the variation of the data frame sizes of a Savitzky-Golay filter affects the smoothness of the filter's output. With the increase of the data frame size (keeping the same polynomial order), the filter can produce more smoothed (simplified) curve over the original signal. This is because more data samples for a data frame of a polynomial results in smoother outputs under the same order (N) of a polynomial. The effect of increasing data frame size is similar to reducing a lower cut-off frequency of the LPF.

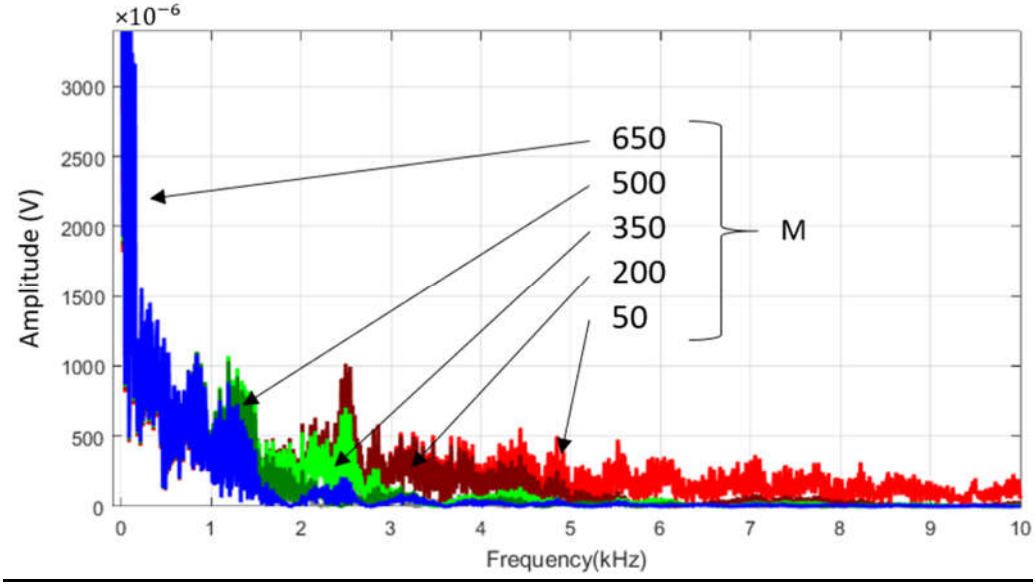

Figure 4.9 Frequency spectrum of the outputs of Savitzky-Golay filters with different data frame sizes (M = 50, 200, 350, 500, 650) and the same order of polynomial (N = 5) [139].

As shown in Figure 4.8, the Savitzky-Golay filter with a frame size of 1301 (M = 650, blue line) has the most smoothed result. However, it cannot properly track the changes in the original signal (i.e., over-smoothed). Moreover, as shown in Figure 4.9, its frequency component at 2.5 kHz is significantly

reduced compared to the other filters. From Figure 4.8 and Figure 4.9, it can be observed that the filter with a data frame size of 701 (M = 350) presents desirable smoothing performance as well as a good traceability of the changes of the original vibration signal. The frequency component of the filter at 2.5 kHz is also retained. As such, the fifth polynomial order and a frame size of 701 (M = 350) is chosen for the Savitzky-Golay filter for processing OLTC's vibration signal.

4.3.3 Comparison of Different Filters (Savitzky-Golay Filter, Low-Pass Filter and Wavelet's Approximation) for OLTC's Vibration Signals

As illustrated in Figure 4.6 and Figure 4.8, the output of a Savitzky-Golay filter always maintains time alignment with the original signal regardless of the output's smoothness. On the contrary, the outputs of wavelet's approximation and LPF failed to keep time alignment with the original signal. The time delay in the output of an LPF depends on the output's smoothness, i.e., its cut-off frequency. The time shift in the output of a wavelet's approximation is mainly determined by the types of mother wavelet, the number of decomposition levels and the approximation level, of which the signals are reconstructed [122].

Figure 4.10 presents the results of applying a Savitzky-Golay filter (N = 5 and M = 350), a wavelet's approximation algorithm and two LPFs (cut-off frequencies of 3 kHz and 5 kHz, respectively) to process OLTC's vibration signal. The vibration signal is acquired from an in-operation OLTC at the sampling rate of 1 MHz. It can be seen that the Savitzky-Golay filter well preserves the profile of the original signal without any time gap.

On the contrary, the two LPFs produce time delays of 0.13 and 0.27 ms with respect to the original signal, respectively. The time delay between the outputs of a LPF and the original signal varies according to the LPF's cut-off frequency. Thus, when there is a change in the cut-off frequency, the time delay will also be changed. This can pose significant difficulties in analysing differently featured signals like arcing and vibration signals. Factors such as the resonant frequency of OLTC's construction, the sensor type and the configurations of the measurement system and the environmental conditions can affect the frequency spectrum of a vibration signal. These factors may require a frequent adjustment of a LPF's cut-off frequency, which in turn causes a change in time delay between the output of a LPF and the original signal.

It also can be observed in Figure 4.10, at the time of 1.8003 and 1.8021 second, there are large gaps between the output curve of the wavelet's approximation and the original signal. In these time instances, wavelet's approximation (black cross marked line) lacks supporting data points and generates a shift to the left side along the time axis (highlighted in a blue box in the figure). As such, the wavelet's approximation fails to track the changes in the original OLTC's vibration signal.

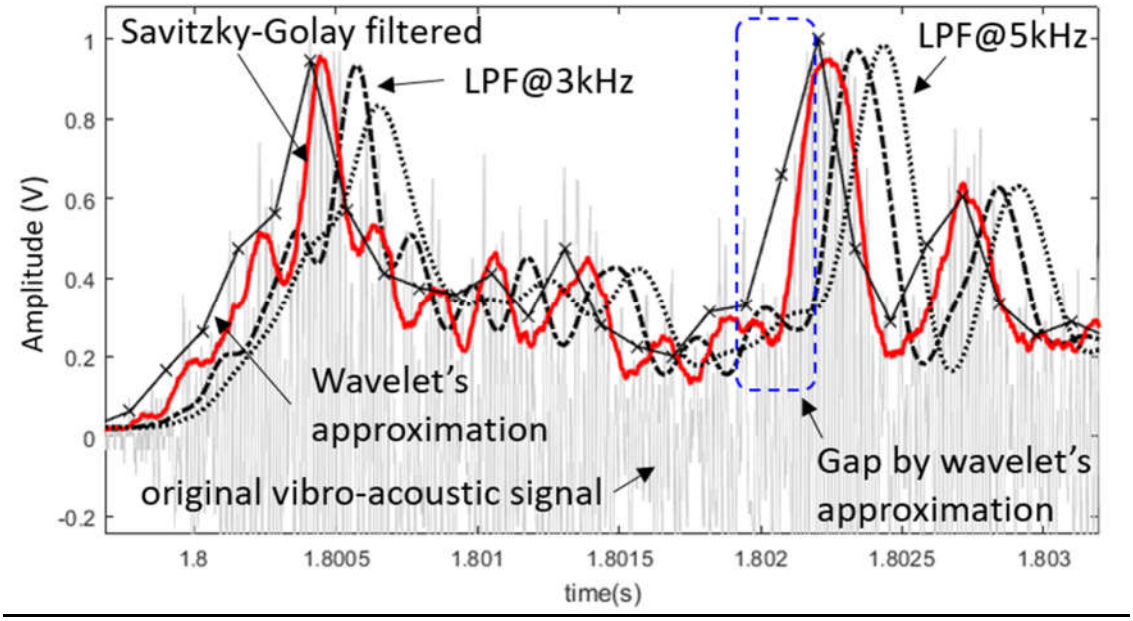

Figure 4.10 Comparison of the time shifts in outputs of Savitzky-Golay filter, wavelet's approximation and low-pass filter [139].

In an OLTC's condition assessment using joint vibration and arcing signal measurement, it is critical to have a time difference induced when using wavelet approximation and LPF. This is because differently featured signals of arcing and vibration signals can hardly be aligned together. Such misalignment has reverse impacts on the sequence analysis of OLTC's mechanical operation and ultimately can lead to an inappropriate condition assessment of OLTC.

4.4 Application of Savitzky-Golay Filter to Arcing Signal

In Section 4.3, Savitzky-Golay filtering was reviewed to obtain a simplified waveform of the vibration signal. This section investigates the applicability of Savitzky-Golay filter to extract arcing signal from noise.

In a joint vibration and arcing signal measurement system, the arcing signal is generated by the closing events of OLTC's switches. The signal can be obtained by measuring the electromagnetic signal flowing through a transformer's grounding cable or phase cables using HFCTs. The sensor collects not only arcing signals, but another mixture of noise signals, load current, harmonic and various interferences. Figure 4.11 shows the originally captured arcing signals on two types of OLTCs (i.e., selector switch and diverter switch type) [136 - 137].

As discussed earlier in Section 4.3.2, by tuning the parameters (N and M) of a Savitzky-Golay filter, the smoothness of its output waveform can be controlled without causing any time delay. This property can also be utilised to extract arcing signals of interest at high frequencies and to remove noise signals, i.e., load current, harmonics and environmental noise normally found at low frequencies.

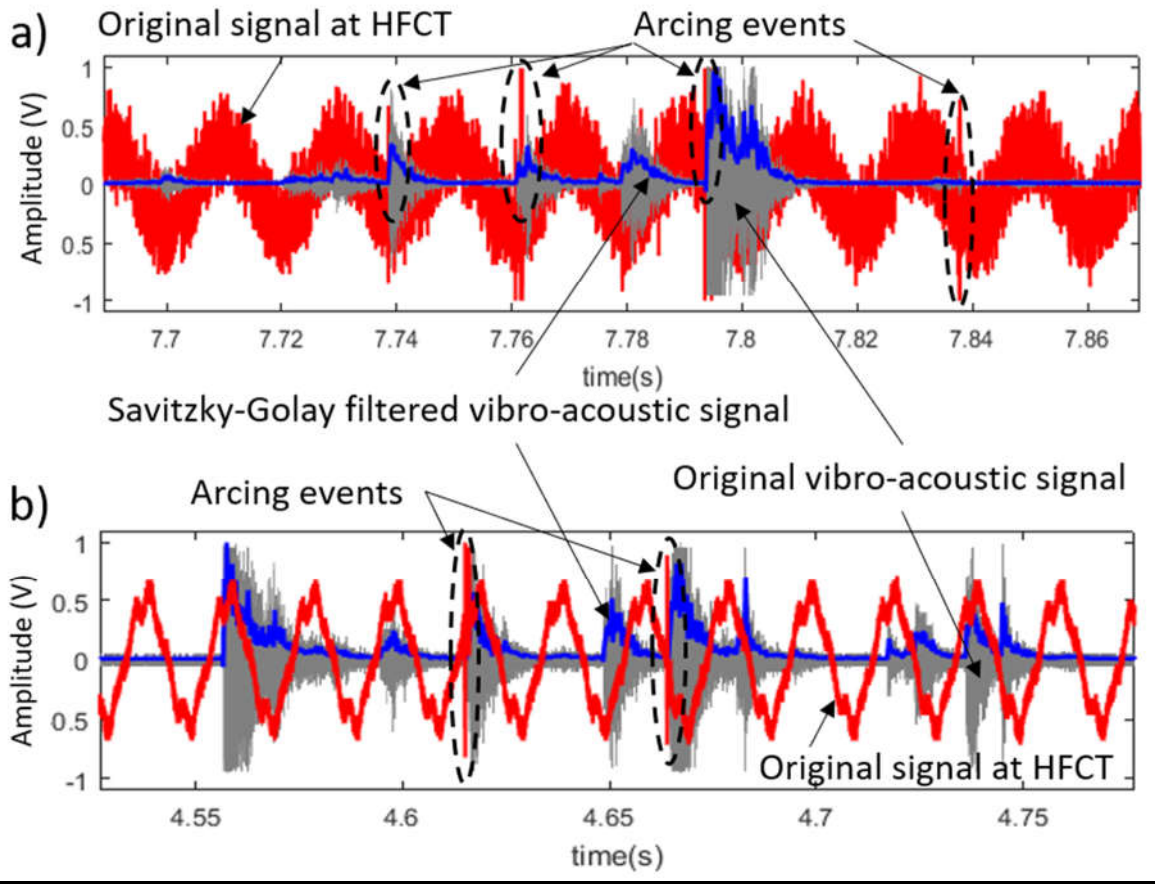

Figure 4.11 Arcing signals (in red) acquired by HFCTs from (a) selector switch type OLTC; and (b) diverter switch type OLTC [139].

For the purpose of extracting arcing signals, two Savitzky-Golay filters are required. One is to extract high frequency components but to remove low frequency components. The other filter is designed for the opposite purpose of the first filter. The first filter has the parameters of nine polynomial order and a data frame size of 101 ($M = 50$) while the second filter is with zero polynomial order and a data frame size of 1301 ($M = 650$). The results of the two filters are drawn in Figure 4.12. In the figure, the signal plotted in black is the output of the first Savitzky-Golay filter (the filter keeps high frequency components) and the signal plotted in green is the output of the second filter (the filter keeps low frequency components). Since the Savitzky-Golay filter does not cause any time difference regardless of the parameters, the outputs of both differently designed filters in Figure 4.12 are well synchronised.

The low frequency components (related to load current, harmonics and noise) embedded in the measured arcing signal can be removed by subtracting the output of the second filter from that of the first filter. Through the subtraction, only high frequency components are left, whereas low frequency components are removed (as shown in Figure 4.13). Then a threshold is applied to the remaining high frequency components in Figure 4.13 to extract a pure arcing signal to reflect the closing event of the OLTC switches. The results are shown in Figure 4.14.

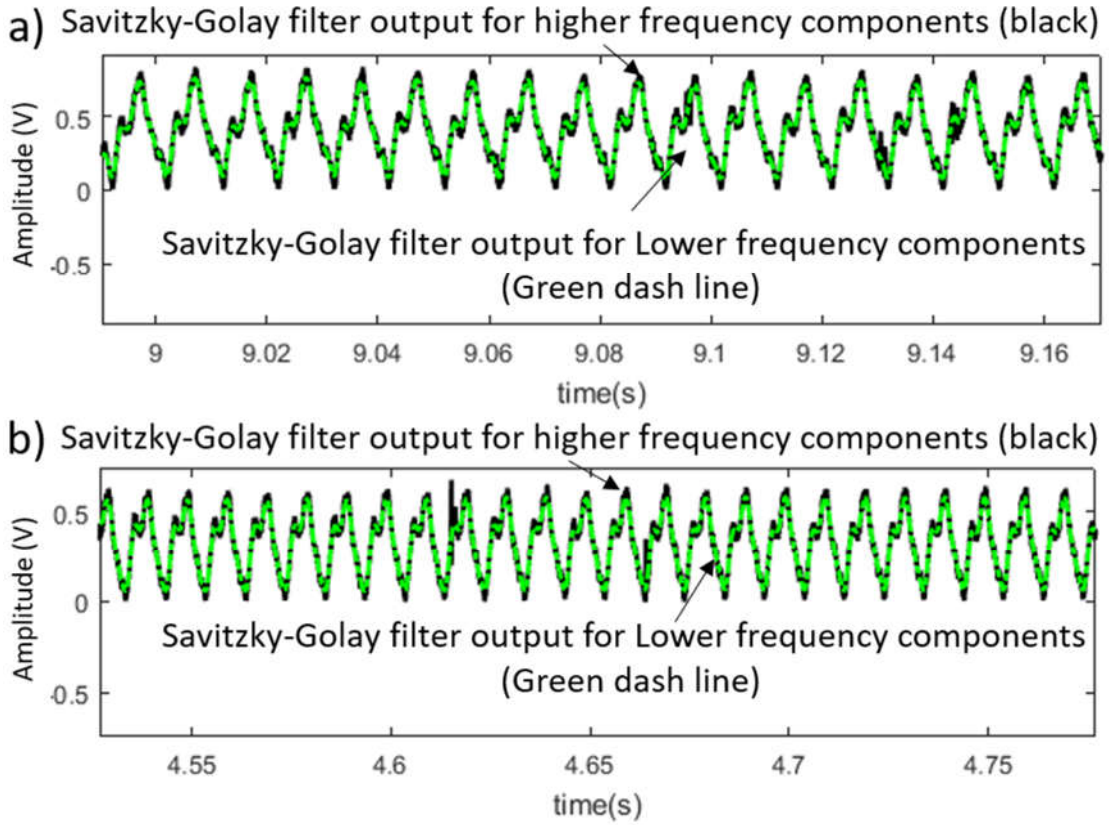

Figure 4.12 Results of two Savitzky-Golay filters (black signal is the output of the filter to keep high frequency components; green signal is the output of the filter to keep low frequency components) of (a) selector switch type OLTC; and (b) diverter switch type OLTC [139].

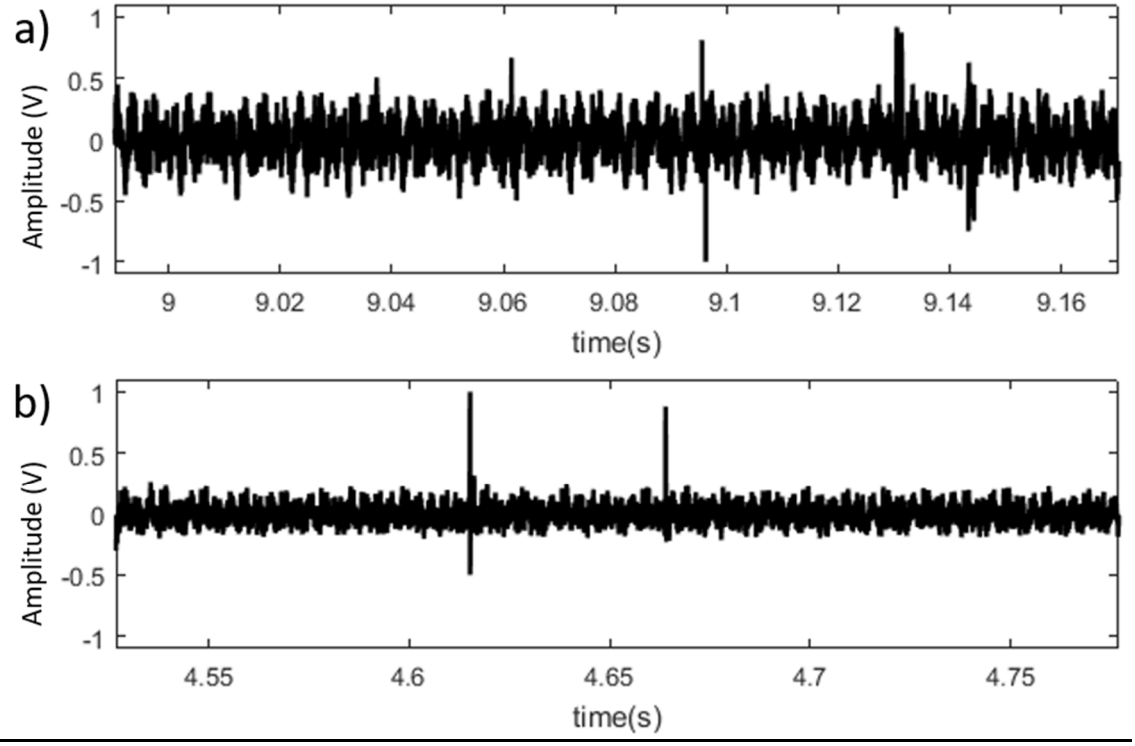

Figure 4.13 Extracted arcing signals (a) selector switch type OLTC; and (b) diverter switch type OLTC [139].

It is worth mentioning that in the field environment, arcing signals may also be corrupted by other types of complex noise signals. The noise signals can be removed by using other digital signal processing techniques, for example, the probability based wavelet transform [135]. However, as shown above, the Savitzky-Golay filter can separate successfully an arcing signal from noise signals at power frequency and harmonics.

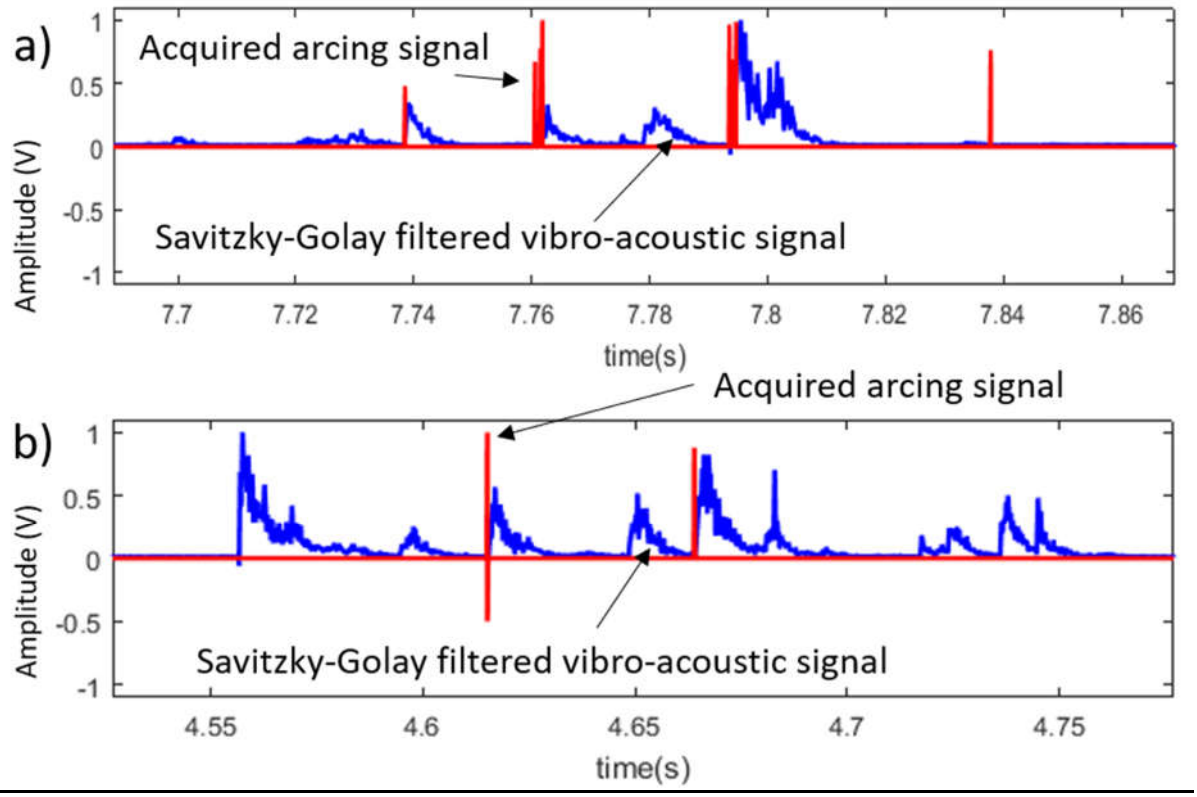

Figure 4.14 Processed vibration signal (blue) and arcing signal (red) by Savitzky-Golay filter (a) selector switch type OLTC; and (b) diverter switch type OLTC [139].

4.5 Application of Savitzky-Golay Filter to Extract Phase Information from Arcing Signal

In the above discussions about arcing signal extraction, it is implicitly assumed that the arcing signals flowing to the transformer's phase connection cable or grounding cable are solely caused by the closing events of OLTC's switches. However, in reality, other types of discharges caused by the insulation defects inside a transformer can also flow into a transformer's grounding or phase connection cables. The discharge signals can be extracted as an arcing signal. It is therefore necessary to distinguish arcing signals generated by OLTC's operation from other types of discharges generated by transformer insulation defects.

The types of electrical discharge can be identified based on the discharge impulses' phase locations. Thus the phase angle of a transformer's AC voltage needs to be recorded [114 - 115]. The phase angle can be directly measured from AC voltage and requires an additional channel of data acquisition

hardware. The implementation of the joint vibration and arcing measurement system on a three-phase OLTC requires at least one vibration signal measurement and three HFCT measurements on each phase. This section investigates the possibility of applying the Savitzky-Golay filter to extract phase information from the signals measured by the HFCTs.

Figure 4.15(a) shows the AC voltage signal measured from a wall socket in a substation, in which the online condition monitoring of OLTCs was conducted. Figure 4.15(b) and Figure 4.15(c) show the signals measured from HFCTs clamped on a phase cable and a grounding cable, respectively.

It can be seen from Figure 4.15(b) that the measured signal (acquired from a phase connection cable) is a mixture of load current, harmonics and arcing signal generated while the OLTC was in operation. The dominant energy in the frequency spectrum locates at 50 Hz followed by harmonics at 250 Hz and 350 Hz (right side of the graph in Figure 4.15(b)). Since the 50 Hz of load current signal is distorted, it is not an easy task to extract phase information from this signal directly. However, as shown below, the Savitzky-Golay filter can extract phase information from the mixture of signals as shown in Figure 4.15(b).

It can be seen from Figure 4.15(c) (right side of the graph) the measured signal (acquired from the grounding cable) is dominated by DC and 50 Hz and is followed by harmonics at 250 Hz and 350 Hz. It looks impossible to extract phase information from the signal. However, even in this case, the Savitzky-Golay filter can extract phase information from the signal.

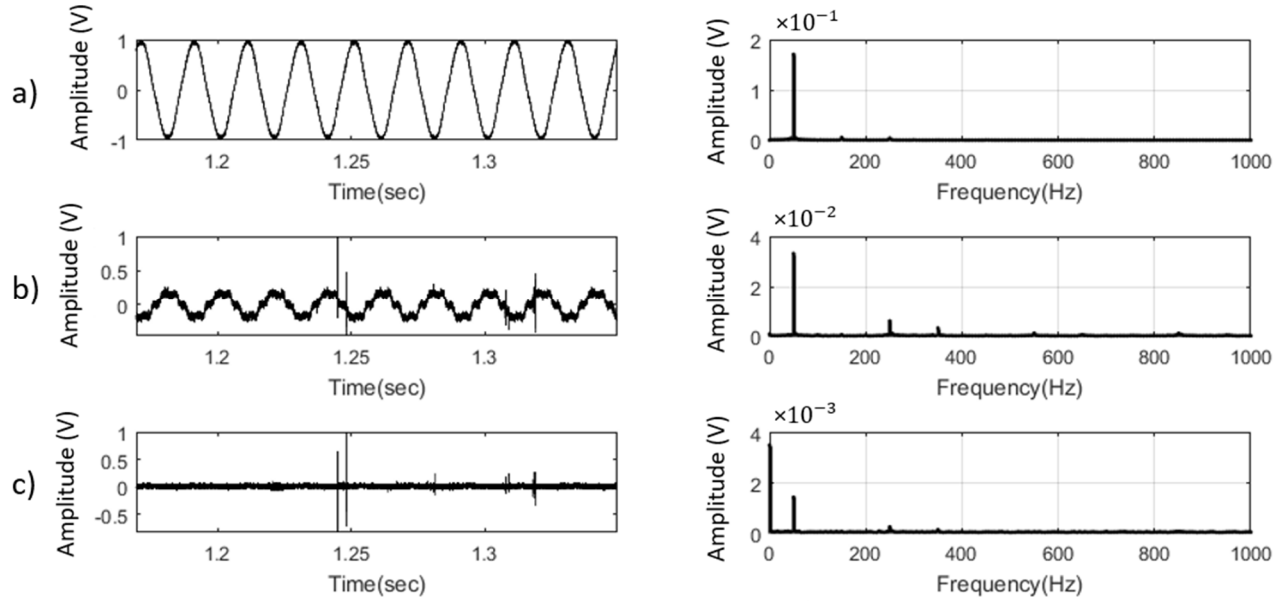

Figure 4.15 Time domain and frequency domain of signals (a) AC signal measured from a wall socket of the transformer under investigation; (b) current signal measured by a HFCT clamped on a phase connection cable; and (c) current signal measured by a HFCT clamped on the ground cable [139].

To retrieve AC phase information from the current signals in Figure 4.15(b) and Figure 4.15(c) using Savitzky-Golay filter, signal components at low frequencies (around AC power frequency) are taken and signal components at high frequencies are discarded. As such, the zero order polynomial and frame size of $M = 650$ are used for the application. After Savitzky-Golay application to the signal, DC offset is removed by subtracting the mean value of the current signal. Finally, only a signal at around AC power frequency is extracted without causing a time delay whereas the harmonics, noise and arcing signal are removed. This signal can be synchronised with the extracted vibration and arcing signals.

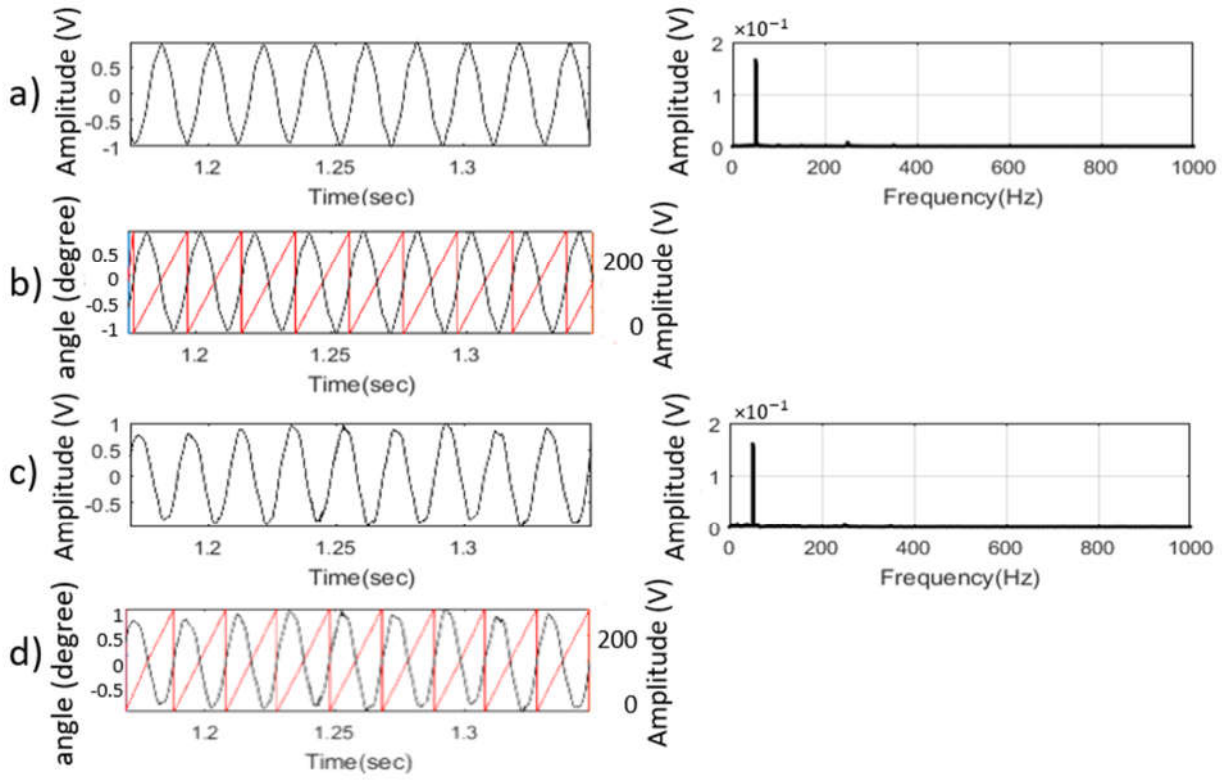

Figure 4.16 (a) Extracted AC cycle and its frequency spectrum from the signal measured at the phase connection cable; (b) phase information obtained from Figure 4.16(a); (c) extracted AC cycle and its frequency spectrum from the signal measured at a grounding cable; and (d) phase information obtained from Figure 4.16(c) [139].

Figure 4.16(a) shows the extracted AC waveform by the Savitzky-Golay filter on the signal measured at a phase. It can be seen that this AC waveform becomes clearer and the phase information can be extracted as shown in Figure 4.16(b). More interestingly, the Savitzky-Golay filter can extract an AC waveform from the signal measured at the ground cable as shown in Figure 4.16(c) and Figure 4.16(d) though the signal is dominated by DC components as shown in Figure 4.15(c).

4.6 Case Studies of Application of Savitzky-Golay Filter to Joint Vibration and Arcing Measurement of OLTC

From Section 4.3 to Section 4.5, a number of important applications of the Savitzky-Golay filter for the joint vibration and arcing measurement system have been investigated to extract a waveform of vibration signal, arcing signal and phase information. This section demonstrates an integration of all the aforementioned applications of Savitzky-Golay filters. The applications of the filters can improve the interpretability on the vibration and arcing signals obtained from the joint measurement system for OLTC condition monitoring.

In Figure 4.17 and Figure 4.18, vibration and arcing signals measured on two different types of OLTC (selector switch type in Figure 4.17 and diverter switch type in Figure 4.18) are processed by Savitzky-Golay filters. Figure 4.17(a) and Figure 4.18(a) show the originally measured vibration and arcing signals. It is apparent that they cannot be used for OLTC condition monitoring. Figure 4.17(b) and Figure 4.18(b) show the timing sequence of OLTC's operation. The results of Savitzky-Golay filters on the signals are plotted in Figure 4.17(c) and Figure 4.18(c) with reference to each OLTC mechanical operation.

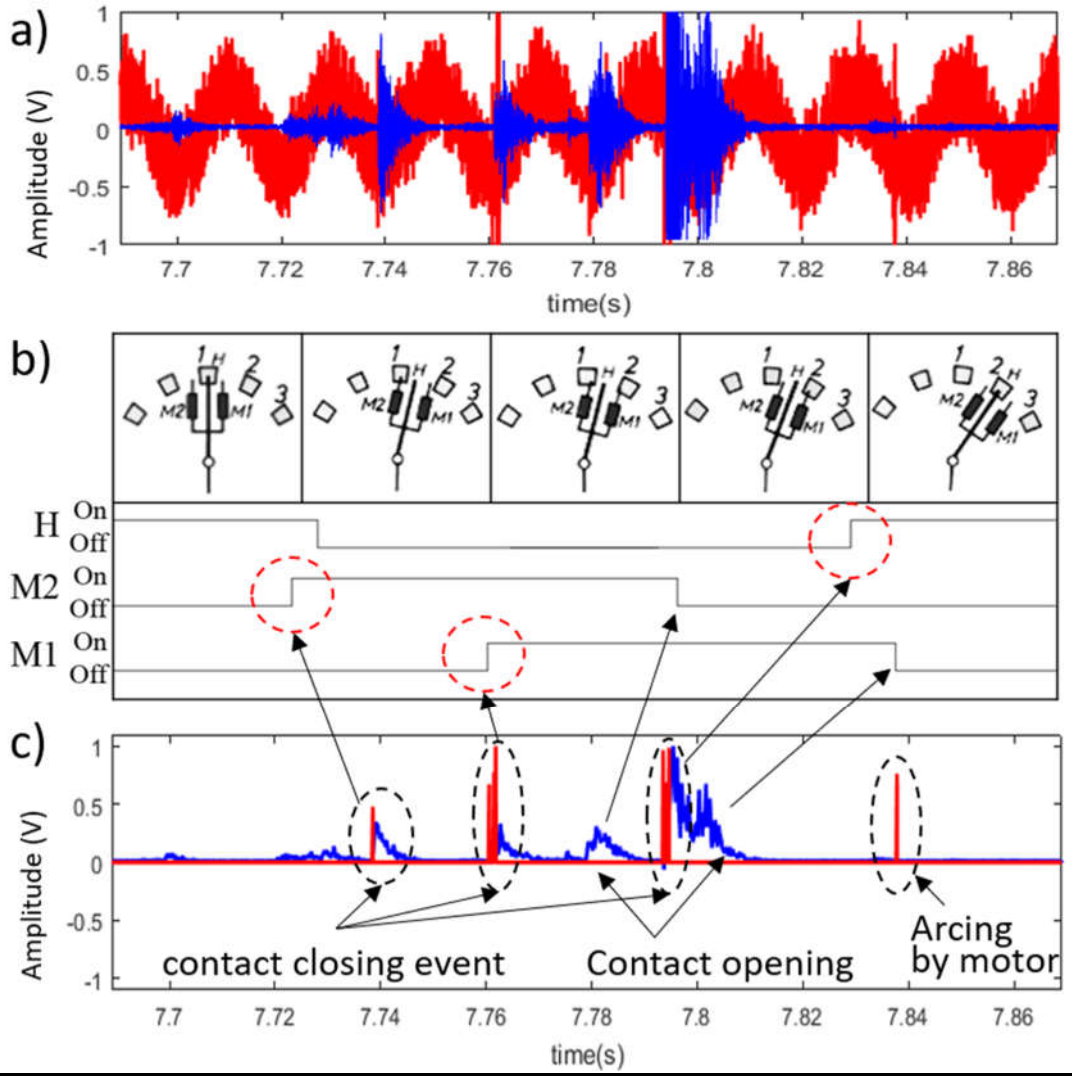

Figure 4.17 (a) Original vibration and arcing signals acquired from a selector switch type on an OLTC; (b) timing diagram of OLTC contacts; and (c) results of Savitzky-Golay filters for processing vibration and arcing signals (red impulses represent the arcing signals extracted and blue represents the signals smoothed by the filters developed in this chapter) [139].

For the selector switch (bolt-on or compartment) type OLTC, arcing signals are generated when a main or two transition switches are in closing operation to tap positions. The signals corresponding to the closing events of the three switches (one main and two transition switches) are successfully extracted by a Savitzky-Golay filter and are clearly identified in Figure 4.17(c) (red impulses). The last arcing event shown in Figure 4.17(c) is caused by stopping the motor, which is also confirmed by additional current measurement on OLTC's motor [47]. Also, as shown in Figure 4.17(c), the vibration signals (blue signals) are simplified by the Savitzky-Golay filter.

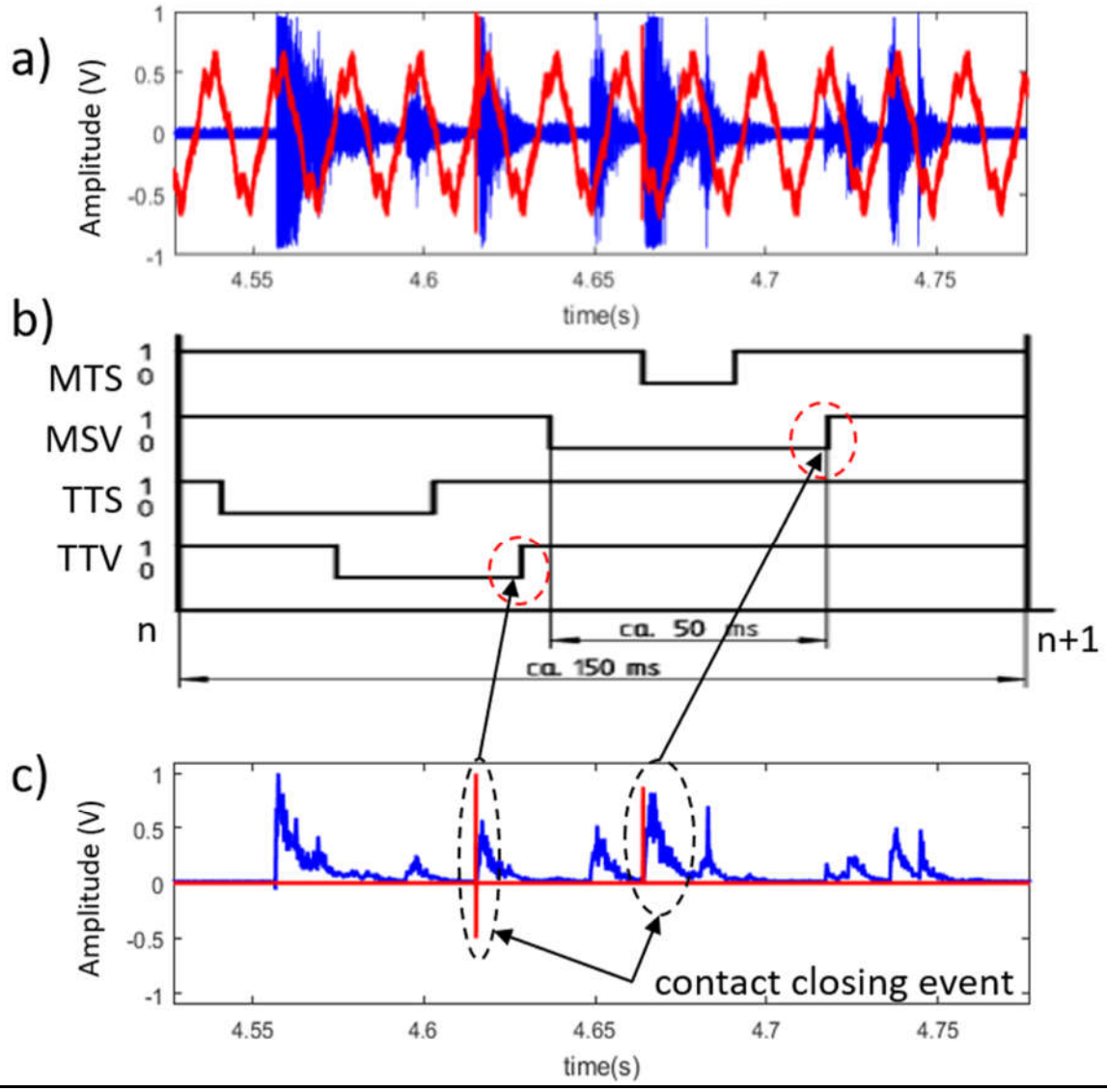

Figure 4.18 (a) Original vibration and arcing signals acquired from a column type OLTC; (b) timing diagram of OLTC contacts; and (c) results of Savitzky-Golay filters for processing vibration and arcing signals (red impulses are the arcing signals extracted and blue represents the signals smoothed by the filters developed in this chapter) [139].

In the case of a diverter switch type OLTC, the closing events of vacuum interrupters on the main and transition switches generate arcing signals. The arcing signals corresponding to the closing events of two switches are successfully extracted by the Savitzky-Golay filter and can be clearly identified in Figure 4.18(c) (red signal). Also, as shown in Figure 4.18(c), the vibration signals (blue signals) are simplified by the Savitzky-Golay filter. With the combination of the extracted arcing signal and filtered vibration signal, it is possible to interpret the sequential operation of OLTC. Any mechanical condition changes can be identified with the vibration signal interpretation scheme.

As seen from Figure 4.17 and Figure 4.18, the smoothed waveform of vibration signal and the extracted arcing signal by the Savitzky-Golay filter are synchronised without any time gap compared

with the original vibration and arcing signals. Additionally, Figure 4.19 shows the results of applying the Savitzky-Golay filter to extract phase information on the above two types of OLTC.

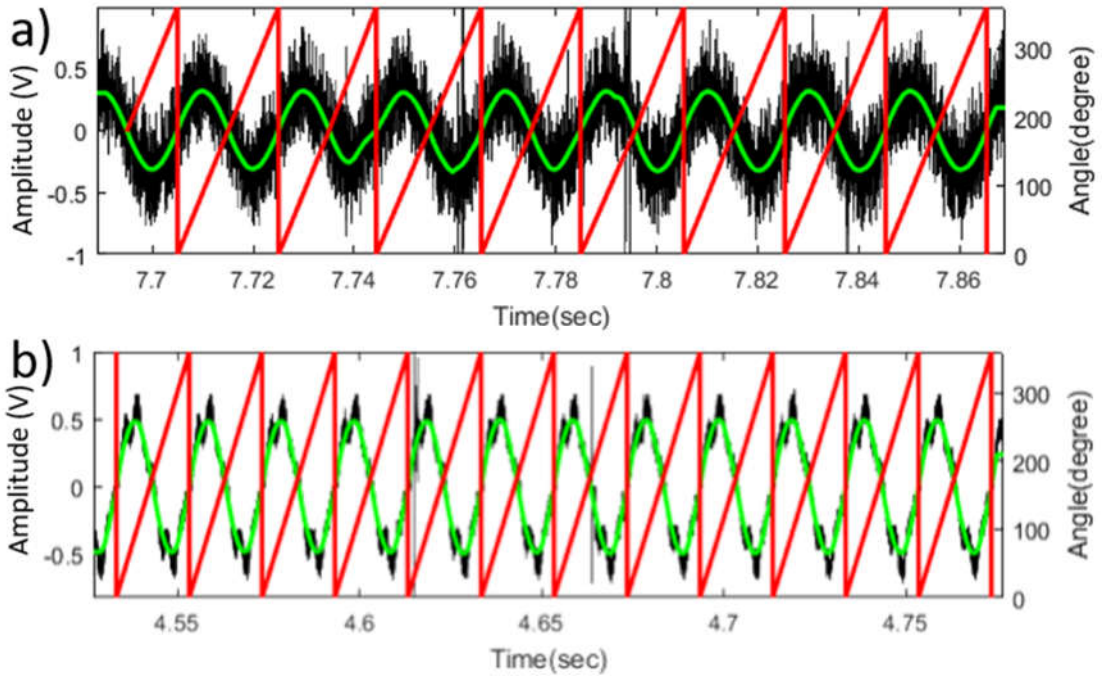

Figure 4.19 Results of phase information from a current signal at a phase connection cable (a) selector switch type OLTC; and (b) diverter switch type OLTC [139].

The above case studies proved that the Savitzky-Golay filters can attain reliable performance of smoothing and filtration for the signals acquired by the joint vibration and arcing measurement system for OLTC condition monitoring. It was achieved owing to the unique benefits of Savitzky-Golay filters, namely not causing a time gap regardless of the level of filtration.

4.7 Summary

This chapter presented the developed Savitzky-Golay filters for processing and analysing vibration and arcing signals acquired from the joint measurement system installed on two different types of OLTCs. With the merits of easy implementation and without causing any distortions in its outputs, it was demonstrated that the proposed Savitzky-Golay filter is capable of extracting:

1) The envelope curve of vibration signals;
2) The arcing signal from noise; and
3) Phase information from the obtained arcing signal.

A long-serviced OLTC may encounter different types of mechanical problems such as spring looseness, coking on switches and contacts, motor drive system's defects and misalignments of switches, etc. These problems can be reflected on the measured vibration signal. After collecting, processing and extracting the vibration signal as discussed in Chapter 3 and this chapter, the next task

is to detect a mechanical condition change of an OLTC by comparing vibration signals. In Chapter 5, a waveform-based vibration signal comparison method is presented to identify a mechanical condition change of an OLTC using a correlation coefficient.

Chap 5. Waveform-based Vibration Signal Comparison Methods for OLTC Condition Monitoring

Contribution of the Chapter

To properly correlate the obtained vibration signal to mechanical events of OLTC's operations, a joint vibration and arcing signal measurement system was introduced in Chapter 3. Then the Savitzky-Golay algorithm was used to process both vibration and arcing signals in Chapter 4. This chapter presents a waveform-based signal comparison method to evaluate the mechanical condition of an OLTC.

The characteristics of an OLTC's vibration signal can be used to assess a condition change in its mechanical energy storage system, switches, contacts and drive shaft system. The mechanical condition changes can be inferred from time stamps and amplitude of vibration signals. However, due to the complex nature of vibration signals, it is not easy to decide the exact time instances of the acquired vibration signals for comparative analysis. Thus, this chapter develops a waveform-based signal comparison method using a Savitzky-Golay filter and correlation coefficient to evaluate the mechanical condition of an OLTC. The waveform comparison method has been applied to identify the mechanical condition of each tap positions of an OLTC. The results demonstrate the waveform-based comparison method can attain a considerable sensitivity on the mechanical condition change of an OLTC.

This chapter has been reproduced from the following paper:

J. Seo, H. Ma and Tapan K. Saha, "**Analysis of Vibration Signal for Power Transformer's On-Load Tap Changer (OLTC) Condition Monitoring**," 2018 IEEE Power & Energy Society General Meeting, Portland, Orland, 2018.

5.1 Introduction

As addressed in Chapters 3 and 4, an in-service OLTC can experience mechanical malfunctions due to switch misalignment, reduced mechanical driving force (spring) and motor drive system's degradation. As such, the mechanical condition of an OLTC needs to be properly assessed [10, 14 ,41-42 ,131 - 133 ,140]. Vibration signal measurement can be used to monitor and diagnose the mechanical condition of an OLTC [13, 40]. However, it is still a challenging task to infer the mechanical condition of an OLTC from the measured vibration signal [39 - 40].

A vibration signal is generated by the instantaneous energy dissipation of the mechanical event in an OLTC. However, identifying the accurate time instances of each mechanical event of an OLTC's operation in vibration signals is not a simple task due to the complex nature of the vibration signal [39 - 40]. In this chapter, a waveform-based comparative analysis method is developed to identify a change in vibration signal to tackle this difficulty.

Firstly, a Savitzky-Golay filter is adopted to extract a simplified envelope curve (waveform) from the originally measured vibration signal [140 - 141]. The obtained envelope curve can still reflect important features of vibration signals, i.e., amplitude and number of peaks and event time of events.

To make a proper alignment amongst different envelope curves of the vibration signals, a proper time shift needs to be performed with respect to a reference waveform (base waveform). The process can minimise the calculation error of the correlation coefficient amongst different waveform envelopes. The base waveform can be an envelope curve showing the highest correlation with all other envelope curves. Then a waveform comparison can be conducted between the base waveform and the other waveforms. Such comparison approach can provide information regarding a mechanical condition change of an OLTC.

The remainder of this chapter is as follows. Section 5.2 details the vibration signal measurement on an OLTC including test setup and vibration signal characteristics. Section 5.3 presents application of the Savitzky-Golay filter to process the measured OLTC's vibration signal. Section 5.4 details the waveform-based signal comparison method. It is followed by the results of applying the waveform comparison method to all tap positions of an OLTC to demonstrate the applicability and sensitivity of the proposed method. The chapter is concluded in Section 5.5.

5.2 Vibration Signal Measurement on an OLTC

Figure 5.1 presents a setup for vibration signal measurement on an OLTC. A vibration sensor was attached (using a magnet) on the outside wall of a selector switch (compartment) type OLTC. The sensor had a frequency range of 50 - 150 kHz. It was connected to a data acquisition system. During

the measurement, the signal sampling rate was set at 1 MHz and each data acquisition was made for a time duration of 200 ms. This allows for completion of one OLTC operational cycle, in which an OLTC's switch moves between tap positions.

The tested transformer, on which the above OLTC was attached, was disconnected from the grid, making it possible to operate the OLTC throughout all its available (10) tap positions without causing any issue in power service. During the measurement, the OLTC's switch was driven from the 1st tap position to the 10th tap position upwards and then it was driven from the 10th tap position back to the 1st tap position downwards. The above operations were repeated 10 times. Thus, vibration signatures at each tap positions were recorded 20 times.

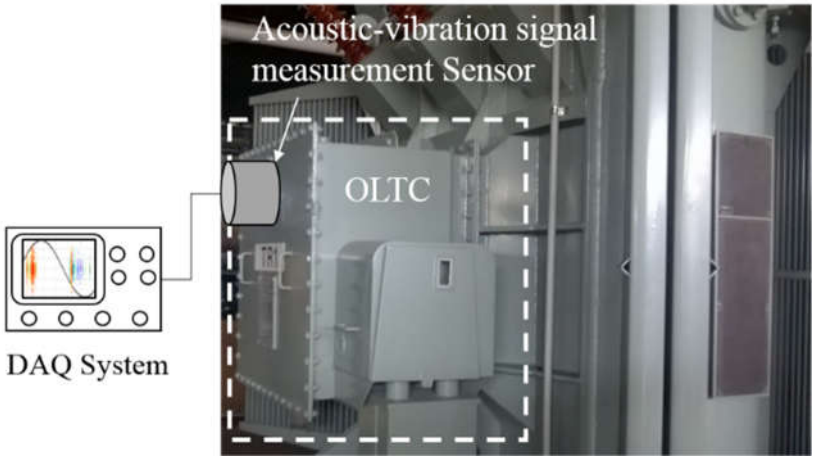

Figure 5.1 OLTC vibration signal measurement setup.

DAQ = Data Acquisition system

Figure 5.2 presents an original vibration signal measured from the aforementioned OLTC. It can be seen that the signal consists of a number of bursts by the OLTC's operation. If the OLTC experienced any mechanical condition change in the condition of contacts, mechanical force storage (spring), rotating components, joints and other auxiliary components, the amplitudes or time intervals between bursts of the vibration signals may change accordingly. Such changes in vibration signal need to be identified as they may be a critical indication for OLTC's condition assessment [13].

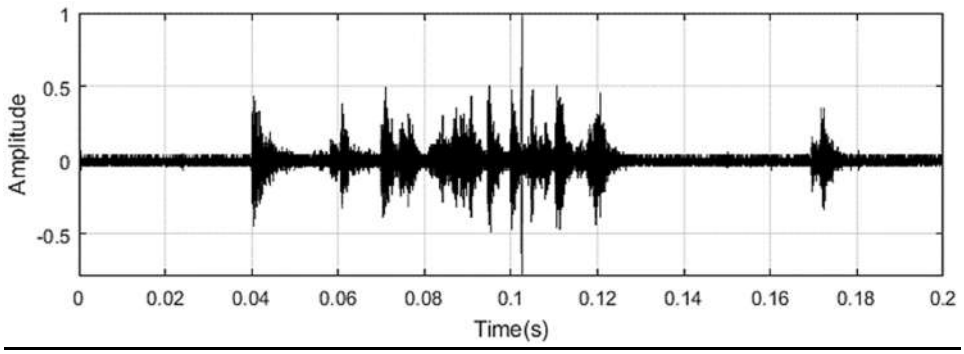

Figure 5.2 An example of the vibration signal measured from an OLTC [45].

To find a mechanical condition change in an OLTC, the "before-and-after" method is normally adopted [13]. In the method, one compares the bursts of vibration signals obtained from the previous measurement with the current measurement. A discrepancy between them can be an indication of a mechanical condition change of an OLTC.

In this chapter, a waveform comparison method is proposed to compare the characteristics of the vibration signals, rather than comparing amplitudes and time intervals between bursts of vibration signals. The proposed method investigates a difference in correlation coefficients among the envelope curves reflecting the characteristics of vibration signals. For an effective waveform comparison, the Savitzky-Golay filter is adopted. Additionally, this chapter will also discuss the effect of a long-time stationary condition of an OLTC by observing vibration signals.

5.3 Application of Savitzky-Golay Filter to Analyse OLTC's Vibration Signal

This section details the application of the Savitzky-Golay filter with properly selected parameters to analyse vibration signals measured from the OLTC shown in Figure 5.1. It also provides a comparison in time latency among MA, LPF, Hilbert transform, wavelet's approximation and the Savitzky-Golay filter in processing the OLTC's vibration signal.

5.3.1 Savitzky-Golay Filter Parameter Design

Two parameters, i.e., the degree of polynomial (N) and the data frame size ($2M + 1$) of the Savitzky-Golay filter need to be determined. Increasing the degree of polynomial (N) in the Savitzky-Golay filter makes the mean squared approximation error smaller, i.e., the polynomial curve of the filter becomes closer to its input signal. The details of determining a set of optimal parameters for the Savitzky-Golay filter have been provided in Chapter 4.

To obtain a desirable waveform of vibration signal, three repetitions of cascaded Savitzky-Golay filters are implemented as shown in Figure 5.3(b). It can be seen that it is capable of capturing the waveform curve (profile) of the original vibration signal.

In this chapter, considering a compromise between the simplification and the traceability of the vibration signal's waveform, all the measured vibration signals are filtered by the cascaded Savitzky-Golay filters and each filter is designed with the order of polynomial as '$N = 0$' and a data frame size of '$M = 350$'.

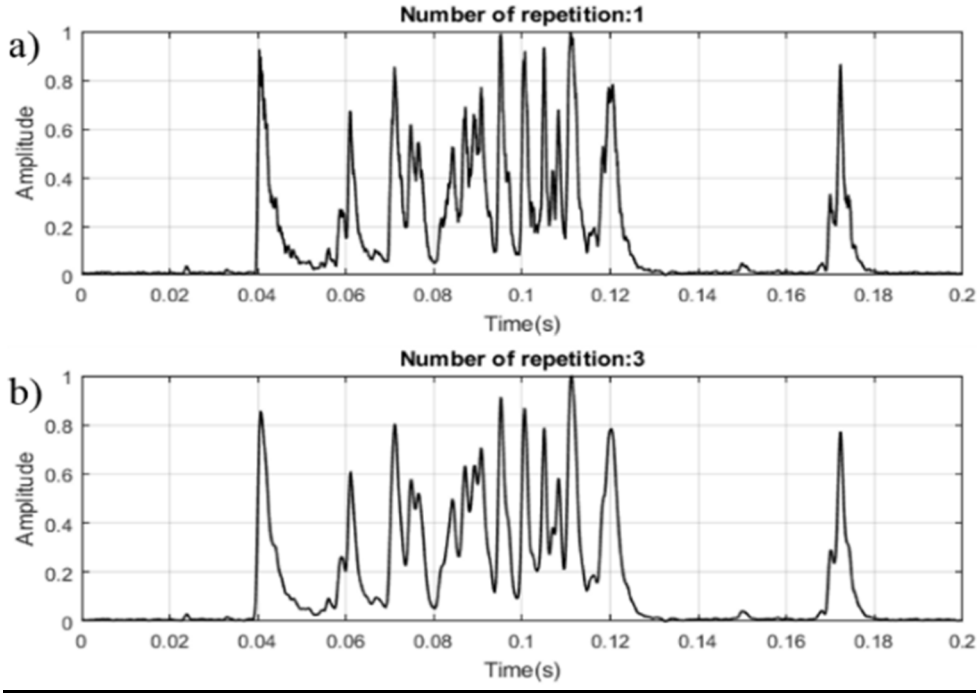

Figure 5.3 The results of applying Savitzky-Golay filter to OLTC's vibration signal. (a) the result of the first Savitzky-Golay filter; (b) the result of the third Savitzky-Golay filter [45].

5.3.2 Comparing Savitzky-Golay Filter with Other Methods

Regardless of the degree of output smoothness, the original signal's time information is not affected by using a Savitzky-Golay filter. Its original time alignment is not compromised. On the contrary, other vibration signal processing methods such as MA, LPF, Hilbert transform and wavelet approximation fail to keep time alignment with the original signal. Those methods resulted in varied time latencies dependent on the parameters and configurations of each method. For example, LPF is affected by its cut-off frequency; MA by the number of data samples averaged; Hilbert transform by its configuration; and wavelet transform by the choice of mother wavelet and the number of decomposition levels.

Figure 5.4 provides the comparison results between the Savitzky-Golay filter and the other methods. In the figure, the grey signal is an original vibration signal (absolute value). In the comparisons, all five methods are properly designed to achieve the corresponding level of smoothness.

As can be seen in Figure 5.4(a) (consisting of signals in full time scale), Hilbert transform (in red) exhibits an inferior traceability of the original signal. MA, LPF and wavelet transform seem to fit the signal well at a distance. However, as shown in Figure 5.4(b) and 5.4(c) (in magnified time scales), the outputs of MA, Hilbert transform and LPF show time delay with respect to the original vibration signal. In the case of wavelet transform approximation (in blue), it cannot provide a desirable data sampling resolution for depicting the original vibration signal. The approximation method fails to trace the original vibration signal with proper resolution in time.

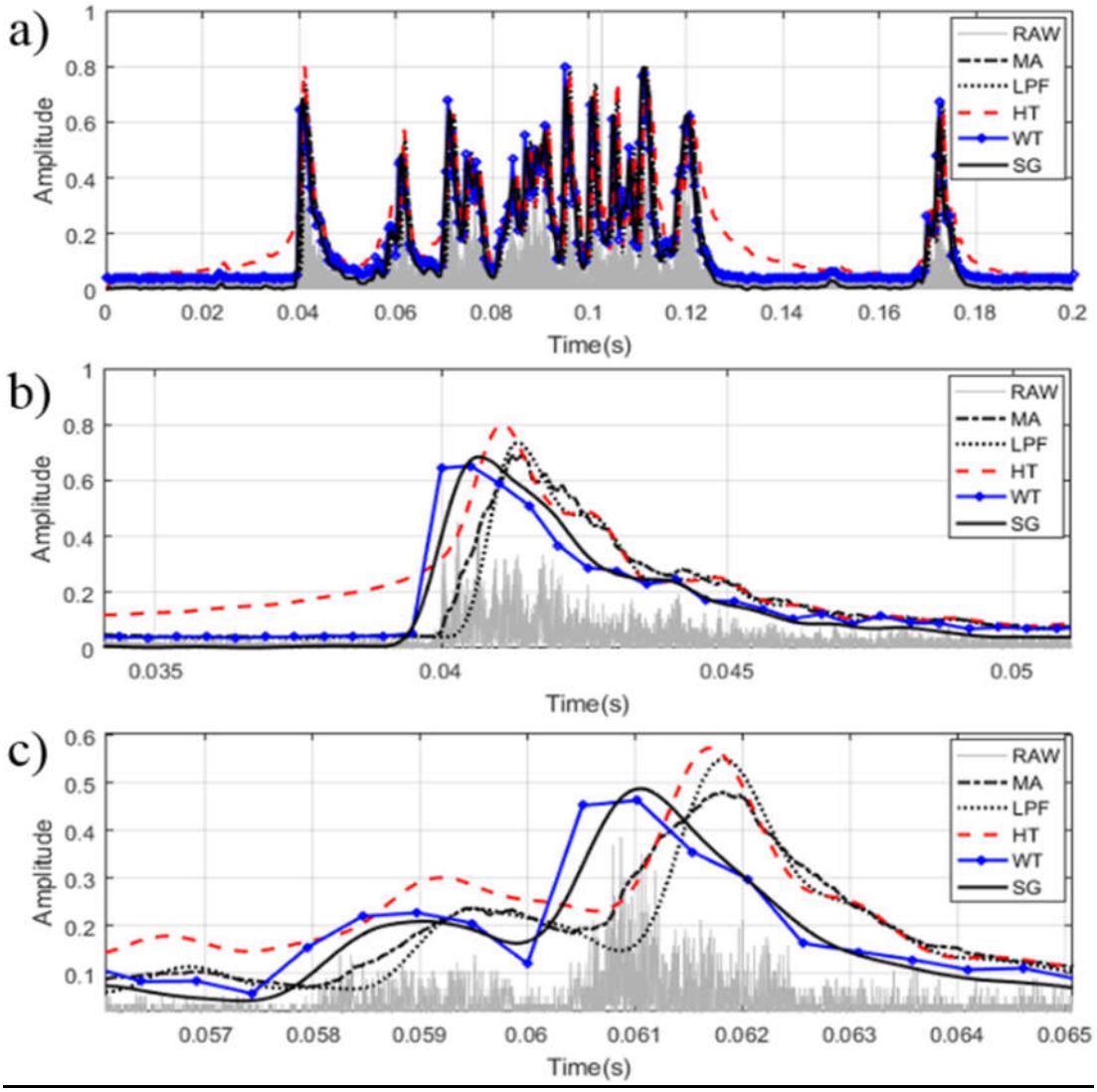

Figure 5.4 Comparison of the time shifts in outputs of Moving Average (MA), Low-Pass Filter (LPF), Hilbert Transform (HT), Wavelet Transform (WT) approximation and Savitzky-Golay filter. (a) vibration signal and output of five methods in full time scale; (b) vibration signal and output of five methods in the magnified time scale from 0.035 s to 0.05 s; (c) vibration signal and output of five methods in the magnified time scale from 0.057 s to 0.065 s [46].

The time delay (latency) of moving average, LPF, Hilbert transform and wavelet transform approximation can be a critical issue when they are applied to measurement data that are configured differently (i.e., sampling rate and environmental conditions) for analysing the OLTC's vibration signal. It can result in an inappropriate condition assessment on an OLTC.

5.4 Waveform-based Signal Comparison Method for OLTC's Condition Assessment

After obtaining simplified waveforms of all the tap positions of the OLTC using the Savitzky-Golay filter, waveform comparisons were made using a correlation coefficient. For the OLTC in Figure 5.1, there is no previous record of vibration signal measurement as a reference for a comparison. Thus, all

the vibration signals on the 10 tap positions were used for a comparative evaluation. The approach can be justified with the assumption that the number of tap positions in normal condition would outnumber the defected conditions. Through the comparison, it was possible to evaluate the relative mechanical condition differences among the tap positions.

To compare the waveforms of all tap positions of the OLTC, a base waveform needs to be selected. The selection is carried out as follows: (1) computing the correlation coefficients of each individual tap position's waveform with respect to other tap positions' waveforms; (2) performing averaging of all the acquired coefficients over other waveforms; and (3) selecting a waveform showing the highest average of correlation coefficients over other waveforms as a base waveform.

In the above base waveform procedure, Spearman's rank Correlation Coefficient (CC) is used

$$CC = \frac{\sum_{i=0}^{N-1}(Y(i)-\overline{Y})(R(i)-\overline{R})}{\sqrt{\sum_{i=0}^{N-1}(Y(i)-\overline{Y})^2 \sum_{i=0}^{N-1}(R(i)-\overline{R})^2}} \tag{5.5}$$

where Y and R are two simplified waveforms (after having been processed by the Savitzky-Golay filter) and $\overline{Y}$ and $\overline{R}$ are the mean of each of these two simplified waveforms (Y and R). Since each signal only has a positive value after taking the absolute value of vibration signal, the result of correlation coefficient is always positive.

As mentioned in Section 5.2, 200 samples of vibration signals were obtained from all the tap positions when the OLTC moves from tap positions upwards and moves back downwards.

The correlation coefficients (Figure 5.5) are plotted in polar diagrams, which describe the similarity amongst the waveforms of the vibration signals. In the polar diagrams (Figure 5.5, Figure 5.7 and Figure 5.8), labels in the theta direction indicate the number of trials and labels in the radial axis are the correlation coefficients. Figure 5.5 shows the polar diagrams for each of the 10 tap positions. Each diagram corresponds to a tap position and the 10 correlation coefficients obtained while switching upwards.

It can be seen from Figure 5.5 that for all the 10 tap positions, most of the coefficients amongst the 10 trials are above 0.8, exhibiting high similarity. At the 4th tap position, coefficients calculated from the first and the second vibration signal measurement (marked with dashed circles) are comparatively small. To further investigate the condition of this tap position, its correlation coefficients over 10 trials are drawn in Figure 5.6. In the figure, the values beside circles are correlation coefficients before the time alignment and the values beside asterisks are correlation coefficients after alignment. As seen from Figure 5.6, the alignment process affects the results significantly. Thus, the alignment process

should be taken prior to the similarity evaluations. It can be observed that after the third trial at the 4th tap position, the level of similarity converges above 0.8.

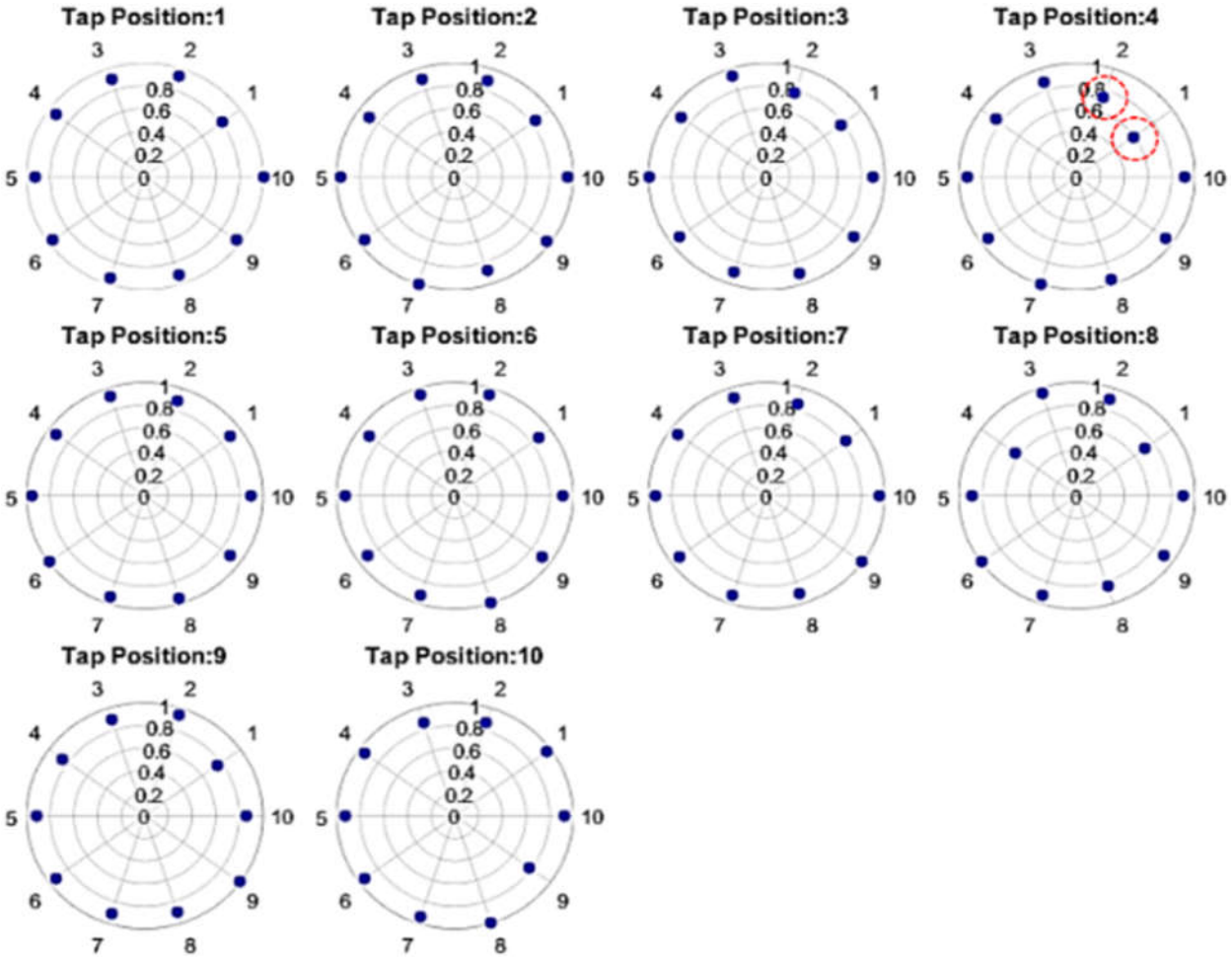

Figure 5.5 Correlation coefficients of 10 trials at each tap positions when the OLTC operates upwards. Labels in the theta direction indicate the number of trials and labels in the radial axis show the correlation coefficient [46].

Such changes in coefficient may be caused by the continuous tap changing operations, which may remove contaminants on the surface of the OLTC's contacts (the OLTC tested is out of service for a quite a long time).

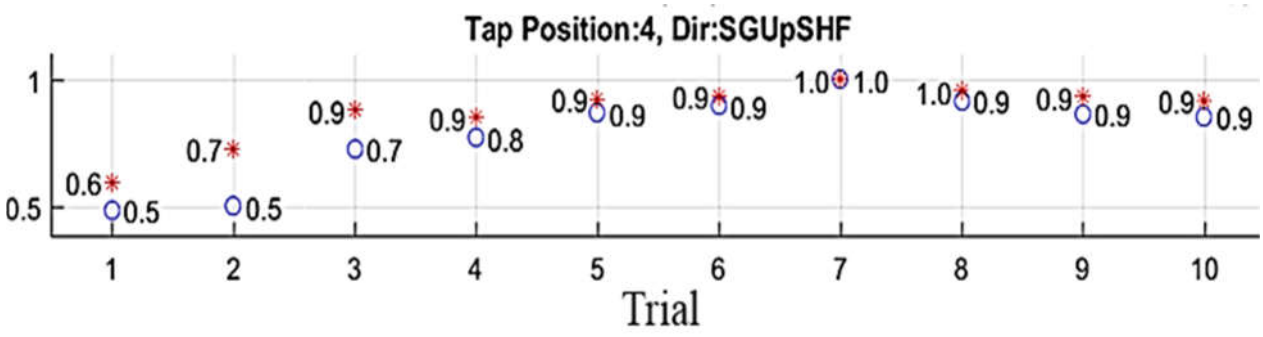

Figure 5.6 Similarity coefficients at the 4th tap position. The value at a circle is a correlation coefficient before waveform alignment and the value at an asterisk shows a coefficient after adjustment [46].

Figure 5.7 shows polar diagrams for each of the 10 tap positions. Each diagram corresponds to each tap position and the correlation coefficients amongst 10 trials (downwards) of this tap position. It can be seen that with the increase of the number of trials, the correlation coefficients become larger and converge. Normally, it is observed that it takes two trials to reach coefficients above 0.8.

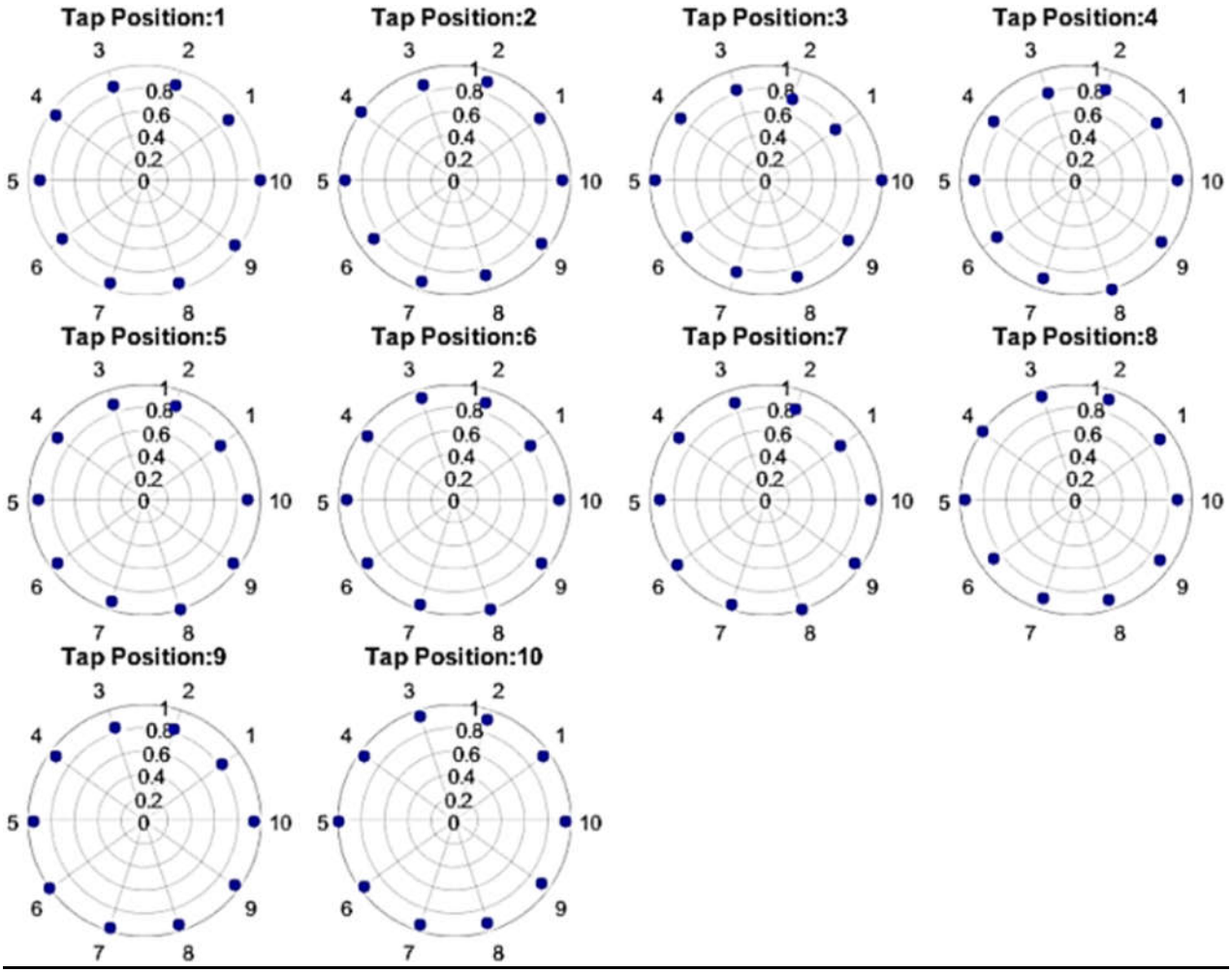

Figure 5.7 Correlation coefficients of 10 trials at each tap positions when the OLTC operates downwards. Labels in the theta direction indicate the number of trials and labels in the radial axis show the correlation coefficients [46].

Figure 5.8 represents correlation coefficients based on the sequence of 10 trials. It can be seen that at the first and second trials, coefficient values are dispersed and not stable compared to the following trials. This is consistent with the results shown in Figure 5.5 and Figure 5.6.

In a vibration signal measurement on an OLTC, random noise signals with small amplitudes may be found. To improve the accuracy of a waveform comparison, a suitable threshold can be applied to remove noise signal more strictly. The amplitude of vibration signals acquired at the same tap position do not always exhibit a constant pattern but vary from trial to trial. However, even though such a

variation in amplitude of signal exists, dominant features of vibration signals are still maintained and can be utilised to evaluate an OLTC's mechanical condition change.

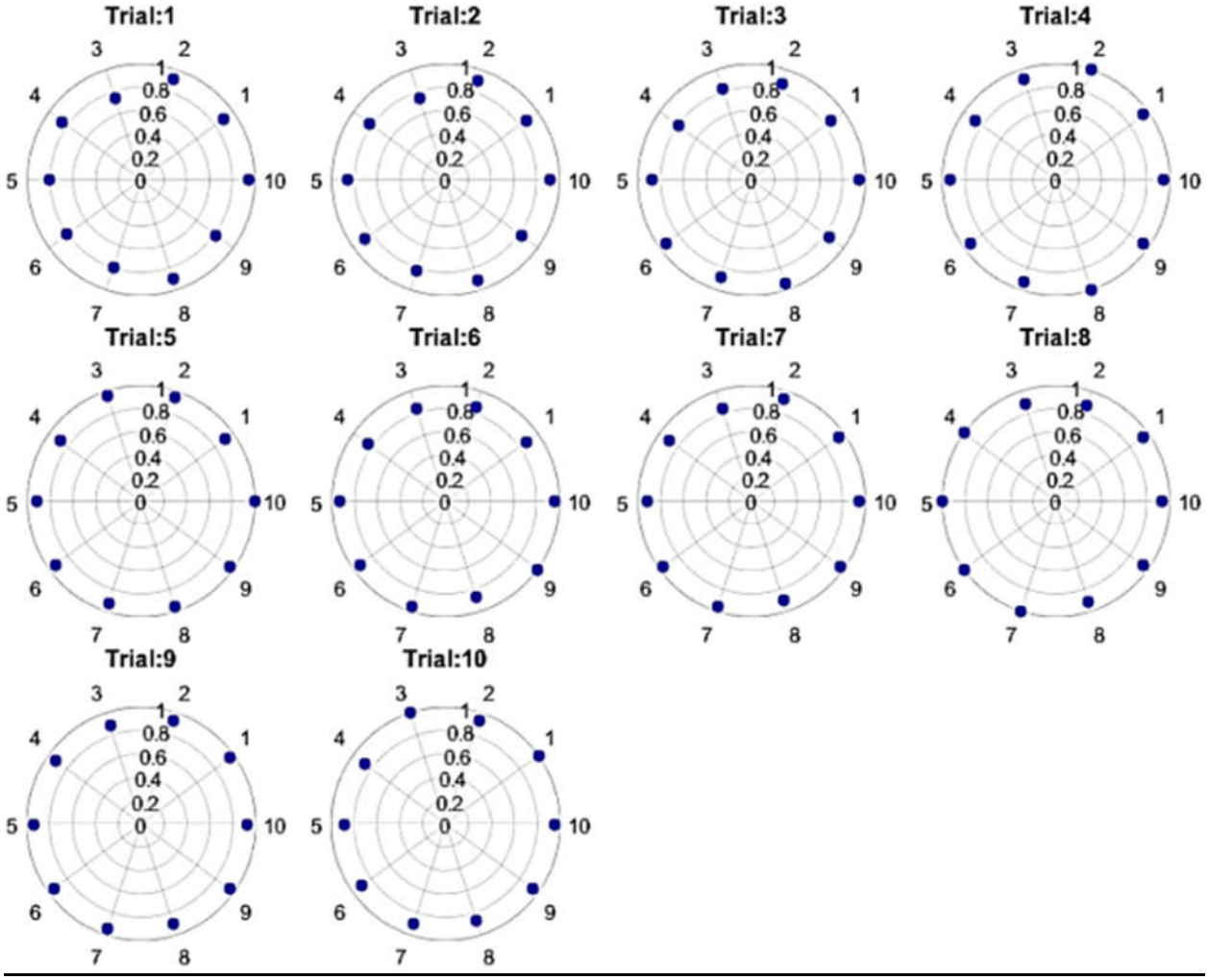

Figure 5.8 Similarity coefficients at each trial operating downwards. Labels in the theta direction indicate the number of trials and labels in the radial axis show the similarity coefficients [46].

Before implementing the above waveform comparison method, the operation and maintenance history of an OLTC should be reviewed. Such information may help avoid a misinterpretation due to the effect of the infrequent use of some tap positions of an OLTC.

5.5 Summary

This chapter demonstrated that a mechanical condition change of an OLTC can be evaluated and quantified by the proposed waveform-based vibration signal comparison method integrated with Savitzky-Golay filter and correlation coefficient. The proposed method shows the capability of identifying OLTC's mechanical condition change with good sensitivity. This can pave the way for online vibration signal measurement and automated evaluation for monitoring an OLTC's mechanical condition.

From Chapter 3 to 5, vibration signal-based method for OLTC's mechanical condition monitoring has been investigated by exploiting vibration signal interpretation methods using a joint arcing and vibration signal measurement system, advanced signal processing techniques for extracting arcing and vibration signals, and a waveform-based vibration signal comparison method.

In the following Chapters 6 and 7, a PD measurement based on a main winding insulation system and a condition monitoring system will be discussed especially for PD signal extraction, PD signal propagating property analysis and PD source.

Chap 6. Transient Strength-based Partial Discharge (PD) Signal Extraction

Contribution of the Chapter

As discussed in Chapters 1 and 2, a PD measurement has been adopted for monitoring and diagnosing the insulation condition of main winding of a power transformer. In PD measurement, there are three major tasks: (1) PD signal extraction; (2) PD signal analysis and classification; and (3) PD source localisation. In this thesis, several novel techniques have been developed to fulfil these three tasks. These techniques are presented in Chapters 6, 7 and 8.

The first task of online PD measurement is an effective PD signal extraction from heavily coupled noise signals. One of the methods, wavelet transform has been widely adopted for PD signal extraction. However, determining an optimal threshold using a wavelet transform is not an easy task. PD signals can be generated by multiple PD sources inside a transformer. Moreover, the measured PDs are dependent on the configuration of an insulation system, a measurement system setup, and environmental conditions such as electrical condition and measurement condition. As such, the amplitudes of PD signals can have a high degree of fluctuation. It is also difficult to select an optimum mother wavelet having high similarity with all PD signals generated by different types of PD sources (insulation faults).

This chapter proposes a differential PD signal extraction method, which considers the transient characteristics of measured signals and uses a quantile-based thresholding method to separate the measured signals from noise. The proposed method makes it possible to extract PD signals generated from various PD sources inside a transformer. The applicability of the proposed method is verified through case studies using datasets obtained from experimental PD test models in the laboratory and from in-service transformers at substations. It demonstrates that the proposed method can be applied to online PD measurement for the insulation system of a transformer.

This chapter has been reproduced from the following paper:

J. Seo, H. Ma and Tapan K. Saha, "**A Novel Signal Extraction Technique for Online Partial Discharge (PD) Measurement of Transformers**," *Int. Trans. Electr. Energ. Syst.*, 26: 1032–1048, 2016.

6.1 Introduction

Effective PD signal extraction remains a challenging task due to a strong coupling of extensive interferences and noise in a substation environment [143 - 144]. Recently, wavelet transform has been adopted as a promising tool to extract PD signals owing to its advantages of analysing signals at multi-resolutions in both time and frequency domains [145 - 150].

Nevertheless, wavelet transform's performance can be compromised unless its mother wavelet, a threshold level and decomposition levels are properly decided [145]. On the other hand, multiple types of PD sources (insulation defects) may co-exist in a transformer. PD signals generated from different types of PD sources exhibit different characteristics, i.e., amplitudes, distribution locations in phase and appearance patterns (sparking type or corona type). A single mother wavelet may not be applicable to all types of PD signals. Therefore, in this chapter a novel PD signal extraction method has been developed. This method evaluates the changing rate of the acquired signal and its performance is found to be not much affected by the amplitudes and shape of waveforms of PD signals. It can be applied in the presence of multiple PD sources in a transformer.

The proposed differential method evaluates a changing rate (termed transient strength) of a signal's amplitude at each sampling interval. By adopting such transient strength criterion and a quantile-based PD signal and noise separation method, the signals with a high likelihood of PD signal can be identified and subsequently extracted. Additionally, the proposed method does not require time consuming processes such as selecting a mother wavelet and decomposition levels as wavelet transform requires. Therefore, the proposed method would be suitable for an online PD measurement in the presence of heavy noise and co-existence of multiple types of insulation defects inside a transformer.

This chapter is organised as follows. Section 6.2 presents an online PD measurement system for the insulation condition monitoring of a transformer. It also briefly discusses the characteristics of major types of noise signals in substation environments and the criteria for differentiating PD signals and noise. The limitations of a wavelet transform-based PD signal extraction technique are also discussed. Section 6.3 details the methodologies of the proposed differential extraction method including signal's transient strength computation, quantile-based PD signal and noise separation method and signals' polarity direction identification. Section 6.4 exemplifies the complete procedure of the proposed method by using simulated PD signals and noise. Section 6.5 presents the results of applying the proposed method to extract PD signals from experimental PD test models and online measurements of in-service transformers at substations. Section 6.6 concludes this chapter.

6.2 Online PD Measurements for Power Transformers

6.2.1 Online PD Measurement System

There are two major types of PD measurement systems for transformers. One type is a capacitive PD monitoring system complying with IEC 60270 and the other type is an inductive PD monitoring system using a HFCT clamped on the transformer's ground cable [114, 117]. This thesis adopts an inductive PD monitoring system (Figure 6.1) owing to the benefits of non-interruption to the service of a power transformer while installing a HFCT sensor and testing a transformer.

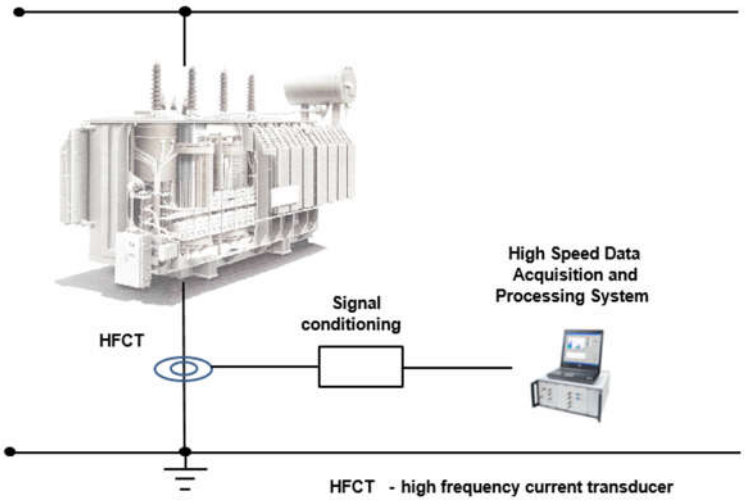

Figure 6.1 Inductive PD measurement system using HFCT [151].

In Figure 6.1, the inductive system consists of (1) a HFCT with -3 dB frequency bandwidth of 360 kHz to 25 MHz to obtain PD signals; and (2) a high speed data acquisition and processing system with a frequency bandwidth of 600 MHz and sampling frequency up to 10 GHz. To capture PD signals, the sampling frequency of an inductive PD measurement system needs to be high enough. On the other hand, the time duration of a PD signal acquisition needs to be long enough to deal with the stochastic feature of PD signals. In this thesis, the time duration of PD measurement is set to be equivalent to 25 AC power cycles. Moreover, the size of the acquired signals should be moderate, not to consume too much computational resources (processing time and data storage). Such measurement configuration is suitable for continuous online condition monitoring of power transformers. Based on the above considerations, the sampling frequency is selected at 25 MHz in this thesis.

6.2.2 Noise Signals in Online PD Measurements

During online PD measurement of a power transformer, four major types of noise signals can interfere with the measured signals [150]. They are: (1) Discrete Spectral Interference (DSI) from communication systems and power electronics; (2) white noise from the measurement system and

ambient environment; (3) repetitive pulses from power electronics or other periodic switching controls; and (4) stochastic impulsive interferences from infrequent switching operations or lighting, arcing and corona from other neighbouring high voltage apparatuses. To separate PD signals from noise, the following criteria can be adopted [152]:

1) Occurrence – time instances of signals, for example, repetitive type noise may only appear at some time instances and can be removed by time domain filtering;
2) Frequency ranges of signals, for example, DSI may only appear at some discrete frequencies and can be removed by discrete Fourier transform or wavelet transform;
3) Time-frequency characteristics of signals, for example, wavelet transform separates PD signals from noise in both time and frequency domains at multi-resolutions;
4) Phase locations of signals, for example, white noise may span a whole AC power cycle while PD signals may only appear at some phase locations of an AC power cycle.

The successful extraction of PD signals from noise largely depends on the differences between PD signals and noise in the above criteria. If a PD signal and a noise signal exhibit the same properties in all of the above criteria, it would be difficult to differentiate the two signals.

6.2.3 The Limitations of Wavelet Transform in PD Signal Extraction

To extract PD signals, wavelet transform firstly decomposes the original signal into a series of wavelet coefficients by using a pre-selected mother wavelet (or wavelet filter). Then it uses a threshold to retain wavelet coefficients associated with PD signals while discarding other coefficients due to noise. Finally, the extracted PD signals are reconstructed using the remaining wavelet coefficients [153 - 154].

In a wavelet transform, if the waveform shape of a mother wavelet is similar to that of PD signal but dissimilar to that of noise, the obtained coefficients can be more closely associated with the PD signal. Subsequently, effective PD signal extraction can be achieved in the wavelet transform. However, in online PD measurement of transformers, the performance of a wavelet transform can be compromised due to the following factors:

1. It is not always possible to find a single mother wavelet showing high similarity with all the types of PD signals. This is because the shapes of PD signals can be affected by various factors, i.e., measurement system, location of PD source and especially the types of insulation defects.
2. Some wavelet coefficients associated with noise signals may have higher amplitudes compared to those of PD signals. Thus, the amplitude-based thresholding method adopted by wavelet transform may not be effective in separating wavelet coefficients associated with PD signals from those associated with noise.

6.3 Differential PD Signal Extraction Method

6.3.1 Differential Method for Extracting PD signals

The proposed method adopts the signal's amplitude changing rate as a criterion for separating PD signals from noise. It computes the gradient of a signal's waveform (transient strength) at each sampling interval:

$$y'(n) = \frac{y(n+1)-y(n)}{t(n+1)-t(n)} \tag{6.1}$$

where n denotes the n-th sampling point, $y(n)$ denotes the amplitude of signal at the n-th sampling point and $t(n)$ refers to time stamp at the n-th sampling point.

The differential method is illustrated in Figure 6.2. In the figure, a signal acquired by a HFCT-based inductive PD measurement system is depicted in blue. The sampling points of the signal are marked as blue dots. For the purpose of comparison, a signal acquired by a capacitive PD measurement system is also plotted (in red) in the figure. It is noted that the signal obtained by an inductive PD measurement system has bidirectional polarities. Thus, in an inductive PD measurement system, inevitably the polarity information of PD signals is lost. This could be a critical drawback in using the inductive PD measurement system. Nevertheless, the proposed differential method can retrieve the PD signal's polarity information by referring to the driving polarity direction of the highly transient PD signals (the dotted blue arrow in Figure 6.2)

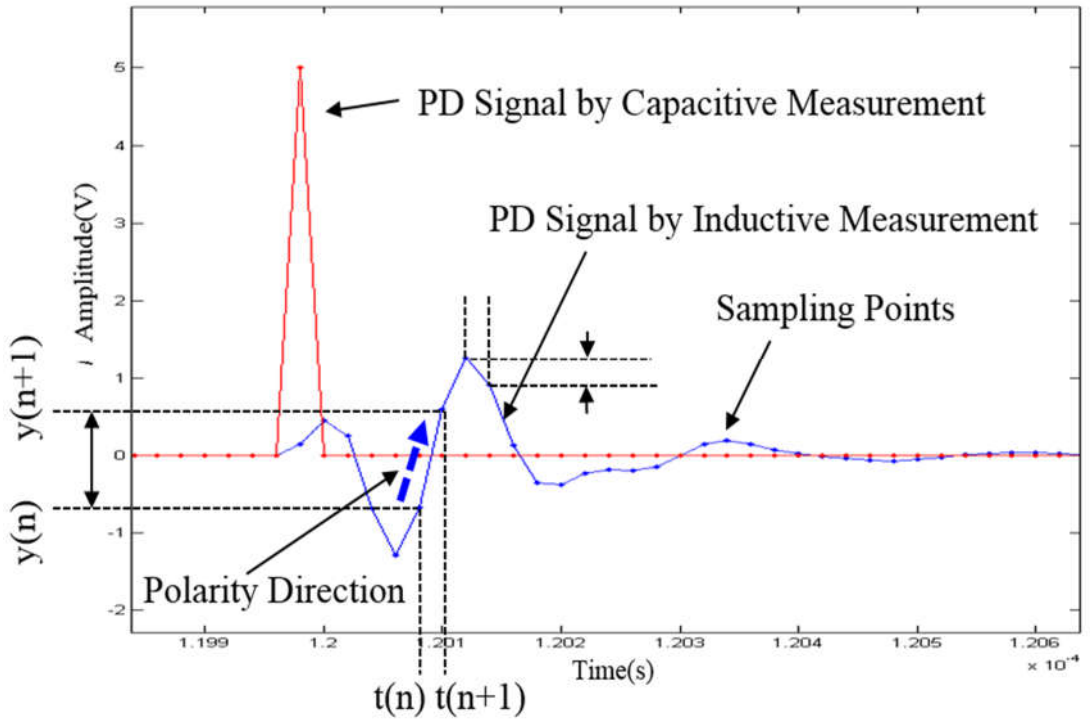

Figure 6.2 Illustration of differential method [151].

The proposed differential method starts with differentiating the original signal as in Equation 6.1. The signs of the differentiated signal are removed to take its absolute value. Then the transient strength (differentiated values) are sorted in descending order. After that, a threshold decided by a quantile-based method is applied to segregate PD signals from noise signals. The quantile-based probabilistic thresholding method is detailed in the next section.

6.3.2 Quantile-based Probabilistic Thresholding Method

After computing the transient strength of an acquired signal, the differentiated values are then segmented by a quantile-based thresholding method [155]. The quantile method segments the ordered transient strength of the data into *N* subsets of equal size. The value of a quantile denotes a boundary line between two consecutive subsets. The *k*-th ($0 < k < N$) of *N*-quantile is the value x satisfying: (1) the probability that the value of data will be less than x is (k/N); and (2) the probability that the value of data will be more than x is $(1 - k/N)$. By using quantile, a probability of the data points above a specific value in their cumulative distribution can be obtained. Accordingly, the transient strength of signals can be segmented based on probability-based intervals. Applying a probability-based thresholding method can provide an improved approach in deciding a threshold for extracting PD signals.

Figure 6.3 compares the results of quantile-based data segmentation (Figure 6.3(a), adopted by the proposed differential extraction method) and fixed amplitude-based data segmentation (Figure 6.3(b), adopted by a conventional method). In Figure 6.3, the horizontal axis is the cumulative number of signals and the vertical axis is the transient strength of the signals in voltage per millisecond. In the figures, a trend curve (blue dots) indicates the distribution pattern of data points. Horizontal lines (red lines) in the figure denote segmentation boundaries for grouping signals at different probabilities as PD signals. On the other hand, it can be seen that amplitude based segmentation as shown in Figure 6.3(b) has a fixed interval between groups of signals. It may not be able to provide a proper segmentation for PD signal extraction since PD activities are stochastic in nature. In contrast, the quantile-based segmentation method divides datasets based on the occurrence rate of signals.

A threshold for separating PD signals from noise signals is decided by the following ratio criterion in the quantile-based data segmentation in Figure 6.3(a):

$$\text{Ratio} \geq \frac{\left[\sum_{quantile(k_{i+1},\ N)}^{quantile(k_{i+2},\ N)} |x'_i|\right] / [n(i+1) - n(i+2) + 1]}{\left[\sum_{quantile(k_i,\ N)}^{quantile(k_{i+1},\ N)} |x'_i|\right] / [n(i) - n(i+1) + 1]} \tag{6.2}$$

where $|x'_i|$ denotes the sorted differentiated data. $Quantile(k_i,\ N)$, $quantile(k_{i+1},\ N)$ and $quantile(k_{i+2},\ N)$ denote the *i*-th, (*i*+1)-th and (*i*+2)-th quantile of total *N* quantiles. The three

quantiles are used to define a boundary for two adjacent data subsets. In Equation 6.2, $[n(i) - n(i+1) + 1]$ and $[n(i+1) - n(i+2) + 1]$ are the numbers of data points in the two adjacent data subsets. A smaller ratio of Equation 6.2 will lead to a higher threshold for discarding noise signals and vice versa.

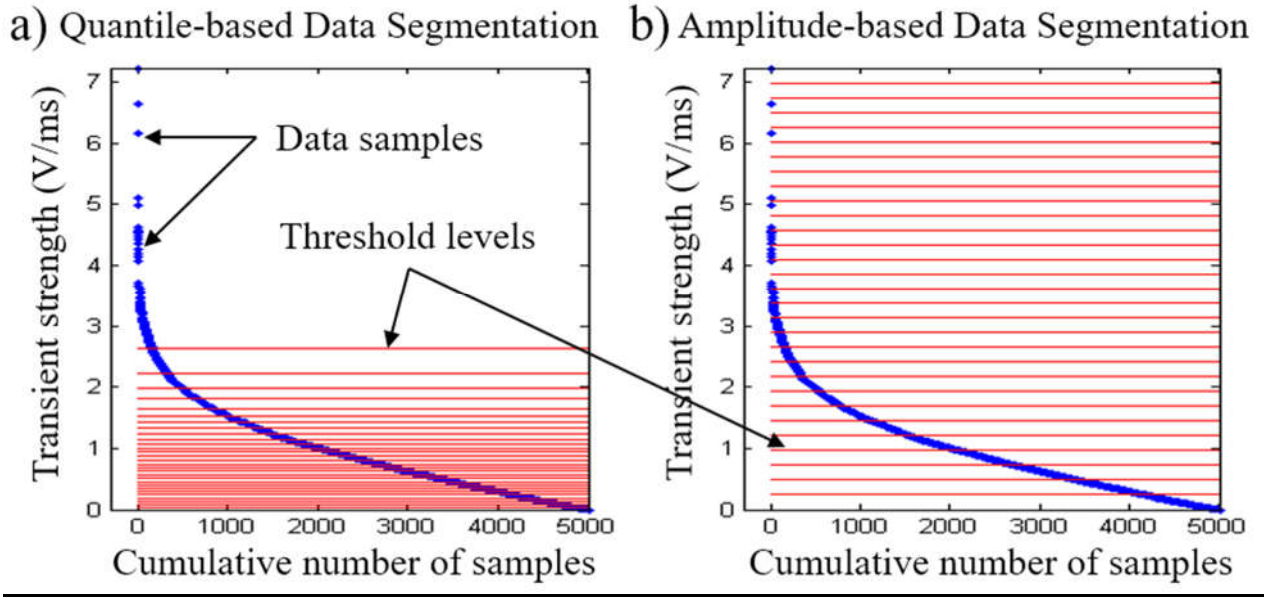

Figure 6.3 PD signals segmentation (a) quantile-based signal segmentation; and (b) amplitude-based signal segmentation [151].

Figure 6.4 exemplifies the above quantile-based thresholding method on the transient strength of PD signals obtained from inductive PD measurements on an experimental PD test model (Figure 6.4(a), refer to Section 6.5.1). Figure 6.4(a) shows the original signals collected from a HFCT for an AC power cycle. Figure 6.4(b) is the corresponding transient strength distribution curve over the accumulated number of data samples in Figure 6.4(a). In Figure 6.4(b), the horizontal lines (in black) are quantile-based boundaries for data segmentation as discussed above.

It can be observed from Figure 6.4(b) that the signals having high transient strength, PD signals, are found in the upper left area while the signals with low transient strength, noise signals, are found in the bottom right area. Accordingly, the difference between consecutive data segments in the average value of the transient strengths becomes narrower and eventually may not be distinctive, i.e., the condensed dark lines in Figure 6.4(b). The signals below the condensed lines are thought to be mainly due to noise. Therefore, the concentrated dark bold line in Figure 6.4(b) can be selected as the overall threshold to distinguish PD signals from noise in the proposed differential method.

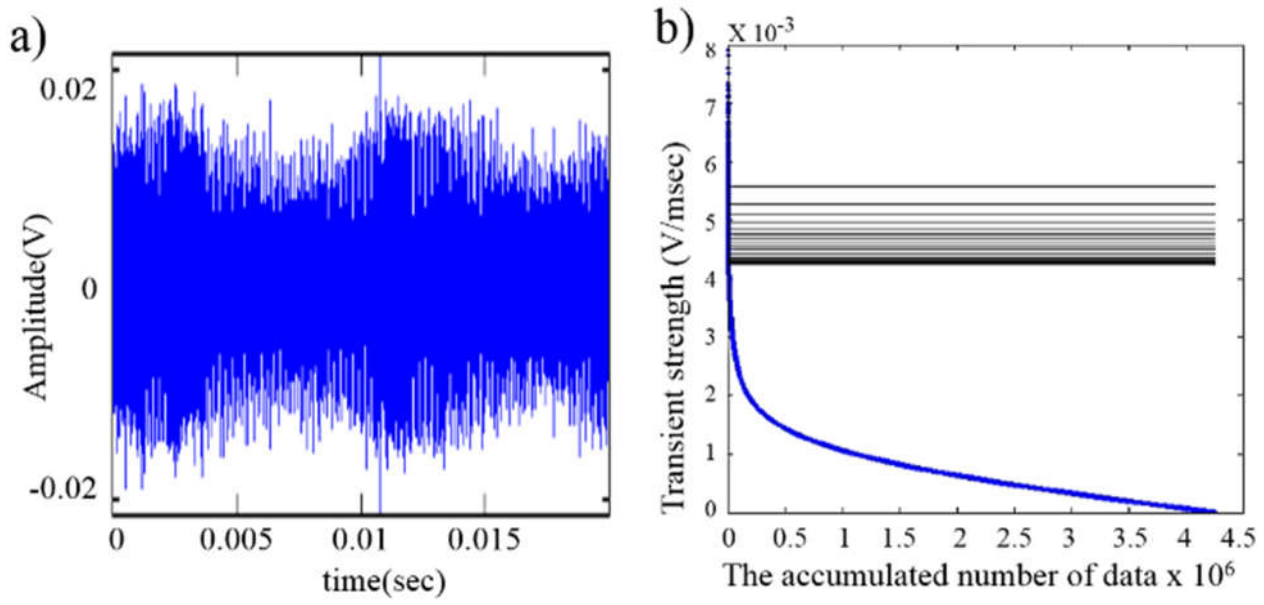

Figure 6.4 Illustration of quantile-based thresholding method: (a) acquired signals from an HFCT for an AC power cycle; and (b) transient strength distribution over the accumulated number of data (quantile) [151].

6.3.3 PD Signals Representation with Transient Strength

The proposed differential PD signal extraction technique can present useful information regarding PD activity using a PRPD diagram [114, 144]. An example of PRPD with the measured PD signals by a HFCT is depicted in Figure 6.5. The original signal represented in PRPD and the extracted PD signals by the proposed method are depicted in Figure 6.5(a) and Figure 6.5(b), respectively. The vertical axis on the left hand side of both figures is the magnitude of the signals in volts. The vertical axis on the right hand side in Figure 6.5(b) shows the transient strength of the signals quantified by a colour bar as voltage per millisecond (V/ms). The dark red signal represents that its transient strength is high, whereas the light blue signal is associated with low transient strength. The result shows that the extracted PD signal does not always exhibit high amplitude of signal. The obtained PD signals having highly transient strength are shown in red at a phase angle of 260°.

In a defected insulation system, a PD event normally occurs as an electrical burst with its accumulated charge for a short time span (microseconds) and subsequently it generates an impulsive PD signal with relatively sharp gradient waveform (e.g., high transient strength). It can be observed from Figure 6.5 that significant PD signals locate at phase angles of around 260° (shown in dark red). On the contrary, signals with high amplitude at around 55° in Figure 6.5(a) are not considered PD signals since they do not have high enough transient strength. This will be further investigated in Section 6.5.3 by frequency domain analysis.

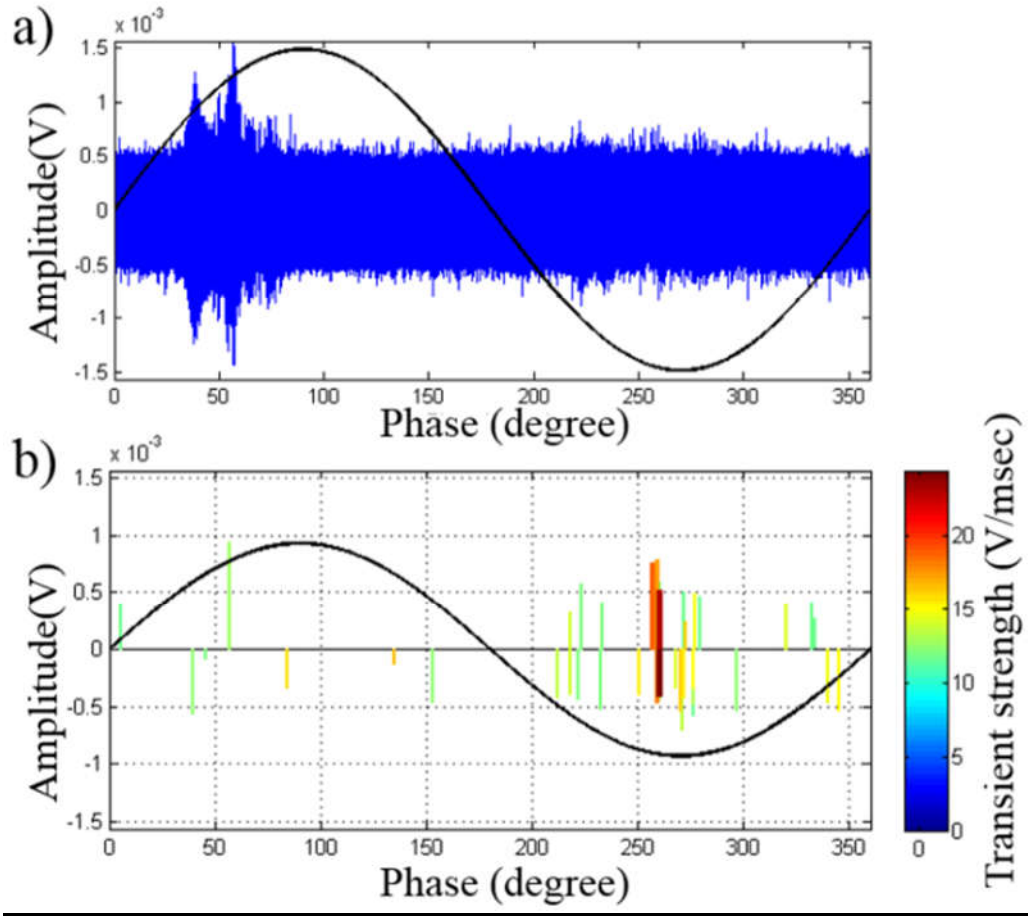

Figure 6.5 Representation of PD signals: (a) originally measured signal; and (b) extracted PD signals by the proposed transient strength method [151].

6.4 Illustration of the Proposed Method

This section explores simulation studies to verify the capability of the proposed method. The obtained PD signals were simulated as if they appeared in an inductive PD measurement system (i.e., bidirectional polarities) as seen in Figure 6.6. It was generated through a process of convolution between an ideal impulse signal and the impulse response of a third order Butterworth filter (*f1* / *f2*: 30 kHz - 10 MHz) for simulating inductive response by a HFCT. White noise and DSI were mixed with the simulated PD signals. White noise has a feature of zero mean and its variation is decided depending on the target SNRs (refer to Table 6.1). DSI was composed from the sinusoidal signals of 10 frequencies of 2, 2.5, 3.3, 3.8, 4.2, 5.4, 7.0, 8.0, 10.0 and 10.5 MHz.

To evaluate the PD signal extraction performance of the proposed transient strength method, SNR and Peak SNR (PSNR) were adopted [156]

$$\mathrm{SNR(dB)} = 20\log\left(\frac{RMS_{PD}}{RMS_{noise}}\right) \tag{6.3}$$

$$\text{PSNR(dB)} = 20\log\left(\frac{Peak_{PD}}{\sqrt{RMS_{noise}}}\right) \tag{6.4}$$

$$\text{RMS(sig)} = \sqrt{\frac{1}{N}\sum_{i=1}^{N}[sig]^2} \tag{6.5}$$

where N is the number of samples, RMS_{PD} and RMS_{noise} are the root mean square of PD signals and noise respectively.

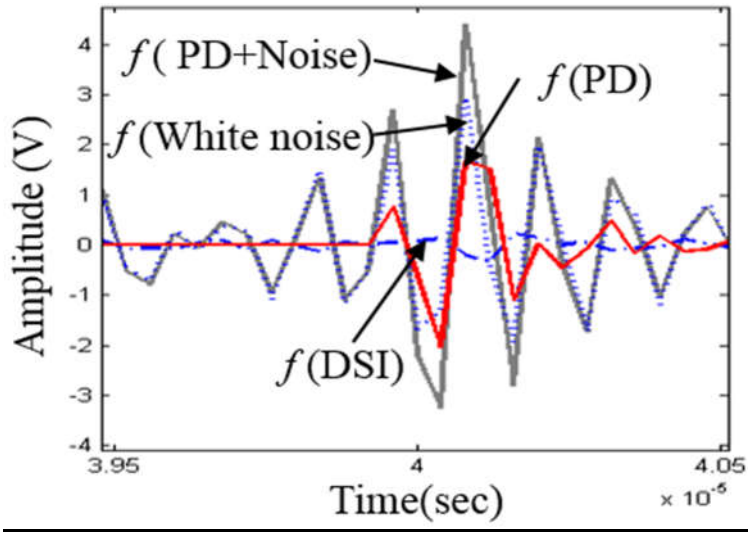

Figure 6.6 PD signal and noise signals simulated for inductive PD measurement system. Red solid line = PD signal, blue dash dot line = DSI, blue dot line = white noise and grey line = superposed signal [151].

Figure 6.7 presents the results of applying the proposed transient strength method to extract four artificially injected PD signals, which were combined with DSI and white noise signals. The characteristics of the employed signals like PD signals, DSI and white noise signals are defined in Figure 6.6. Figure 6.7(a) shows the original signals generated. Figure 6.7(b) depicts the convoluted signals to be measured by an inductive sensor. In the figure, SNR is -19.4 dB and the PSNR is 6.6 dB. Figure 6.7(c) shows the frequency spectrum for the convoluted signals. Figure 6.7(d) shows the cumulative transient strength distribution of the signals. In the figure, the threshold level of 1 % (i.e. signals above 1 % of transient strengths are extracted) is decided based on the method presented in Section 6.3.2.

Figure 6.7(e) shows the PD signal extraction by the proposed transient strength-based PD extraction method. In the figure, the signals with highly transient strength are drawn in black. It can be seen that the four originally injected PD signals have the highest transient strength and have been successfully extracted. Additionally, the original polarity directions of the four PD signals have been successfully reconstructed as those shown in Figure 6.7(a). On the contrary, wavelet transform processed with a

mother wavelet of 'db1' and 10 decomposition levels failed to extract the PD signals and to retrieve their original polarity directions as shown in Figure 6.7(f).

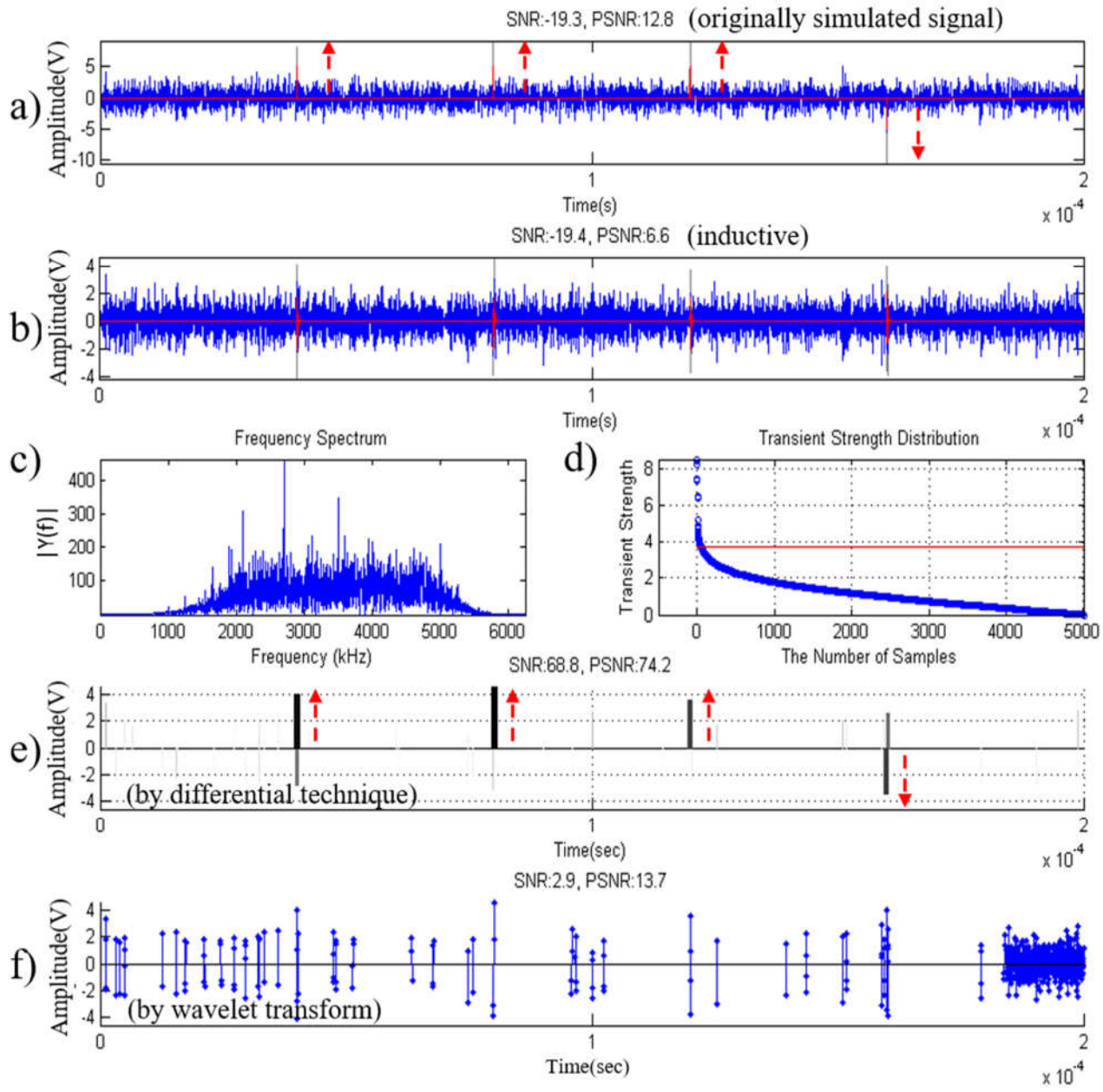

Figure 6.7 Verification results of the proposed transient strength method (a) originally simulated PD signals; (b) convoluted PD signals for simulating inductive PD measurement system; (c) frequency spectrum of the signals in Figure 6.7(b); (d) cumulative transient strength distribution of the convoluted signals and the threshold level selected; (e) the extracted PD signals by the proposed transient strength method; and (f) the results of the wavelet transform with a mother wavelet of 'db1' and 10 decomposition levels [151].

Table 6.1 presents a summary of the simulation results of PD signal extraction at three different SNRs (i.e. -21.3 dB, -20.1 dB and -18.1 dB), which is controlled by a white noise signal [156]:

$$\text{Noise signal} = \text{PD signal} + \text{rand}(N) \times \sqrt{\frac{1}{N-1} \times \left[\sum_{i=1}^{N} [PD\ signal]^2\right]} \times 10^{(-(Target\ SNR)/(10)} \qquad (6.6)$$

For a wavelet transform, it adopts ‘Harr’ mother wavelet with 10 decomposition levels.

Table 6.1 Comparison of the results of differential method and wavelet transform [151]

	SNR (after extraction)	PSNR (after extraction)
-21.3 dB (original signals)		
Differential Method	68.6	73.1
Wavelet Transform	2.9	15.7
-20.1dB (original signals)		
Differential Method	69.9	73.9
Wavelet Transform	2.8	14.9
-18.1 dB (original signals)		
Differential Method	69.4	74.2
Wavelet Transform	8.0	17.0

It can be seen from Table 6.1 that the proposed differential extraction method consistently attains superior performance in noise reduction to the wavelet transform-based PD extraction method.

6.5 Results and Discussions

This section presents the results of the application of the proposed method to extract PD signals from PD measurements performed in laboratory and at substations of local distribution authorities.

6.5.1 Laboratorial PD Measurement Setup

Figure 6.8 presents the PD measurement setup for experimental PD test models in the laboratory. The test configuration consists of HFCT based inductive and IEC standard based capacitive PD measurement systems. These two systems were used to perform PD measurement simultaneously. Such a setup is to verify the polarity directions of PD signals obtained by the differential PD extraction method with reference to those obtained by the capacitive PD measurement.

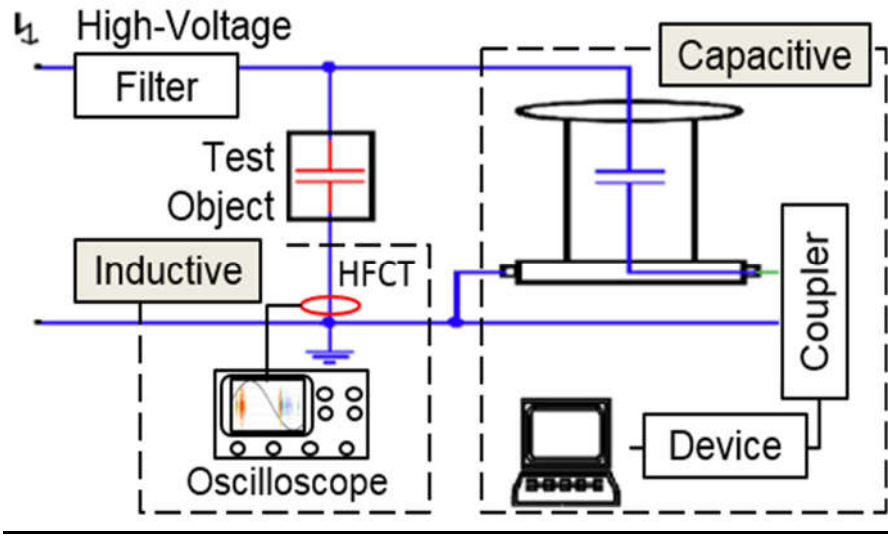

Figure 6.8 Laboratory PD measurement setup (including both inductive and capacitive PD measurement systems) [151].

Three experimental PD test models were constructed to simulate three major types of PD sources in transformers (refer to Figure 6.9). Internal discharges were obtained by placing three pressboards (1 mm in thickness and 45 mm in diameter) between two electrodes. The pressboard in the middle had a cylindrical void of 5 mm in diameter and 1mm in depth. The whole setup of the internal discharge was immersed in mineral oil. Corona discharges were obtained by using a point-to-plane electrode system in air. The high voltage electrode was a steel needle with a tip radius of 3 μm and the grounding electrode was a flat plane with a diameter of 45 mm. The distance between two electrodes was 50 mm. Surface discharges were generated by making the steel needle contact the surface of the pressboard placed on top of the flat electrode. Multiple PD sources were formed by combining the above three experimental PD test models as shown in Figure 6.9(d).

During the laboratory tests, constant AC voltage was applied to the PD models. During PD measurements, a constant voltage higher than inception voltage was applied to each PD model for more than 15 minutes to obtain relatively stable PD activity prior to PD signal recording. During measurement, the PD inception voltage of each model (PD source) was kept at a similar voltage level by adjusting the distances between the electrodes in each model.

6.5.2 Results of Experimental PD Test Models

The PD signal processing results for the experimental PD models are presented in Figure 6.9. The left column of the figure depicts the configuration of the experimental PD test models including internal discharge as shown in Figure 6.9(a), corona as shown in Figure 6.9(b), surface discharge as shown in Figure 6.9(c) and multiple PD sources as shown in Figure 6.9(d). The PRPD diagrams obtained from a capacitive PD measurement system are depicted in the centre column of the figure (Figure 6.9). The vertical axis of the diagram indicates Coulomb (apparent discharge). On the right

column of the figure, the PRPD diagrams obtained by inductive PD measurement system are presented. The vertical axis of the diagram indicates the amplitude of PD signals at the HFCT in volt. The right side of the vertical axis shows the transient strength in V/ms.

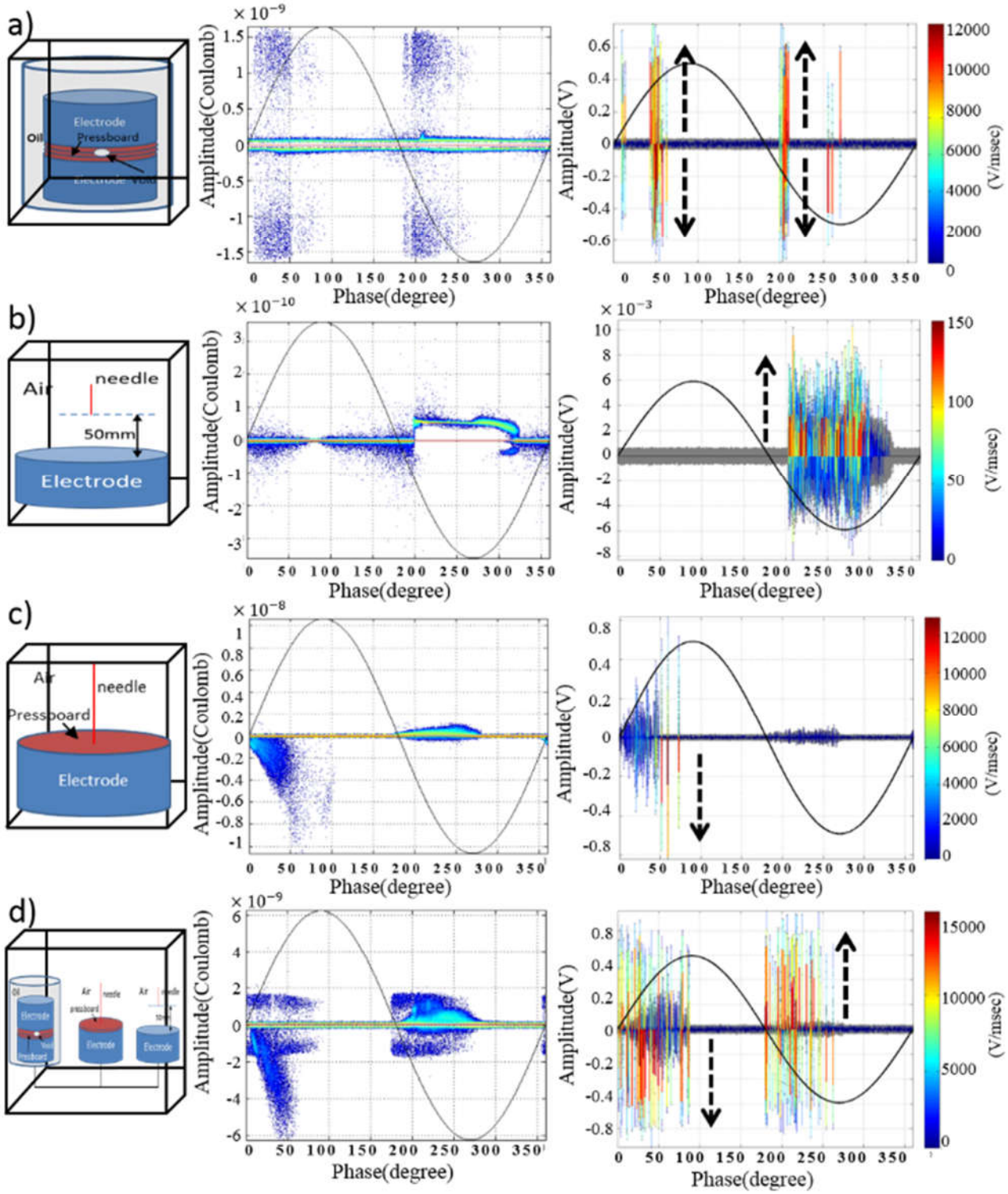

Figure 6.9 Result of experimental PD test models. PD test models configuration (left column); PRPD results obtained from the capacitive PD measurement system (centre column); PRPD results obtained from the inductive PD measurement system (right column). (a) internal discharge; (b) corona; (c) surface discharge; and (d) multi-PD source consisting of internal discharge, corona and surface discharge [151].

Figure 6.9(a) shows the results of internal discharge. From the PRPD diagram of the capacitive PD measurement system, it can be seen that the PD signals with bidirectional polarity are found in both positive and negative cycles. On the other hand, in the case of the inductive PD measurement system, PD signals with highest transient strength (in red) are found at the phase angle of approximately 50° and 200°. The PD signals are found with bidirectional polarity. The two results from the different PD measurement systems demonstrate the same polarity direction and phase angle location of PD signals.

Figure 6.9(b) shows the corona results. In the PRPD diagram constructed from the capacitive PD measurement system, the small amplitude of PD signals are located in the negative AC cycle. For the case of inductive PD measurement system, PD signals with highest transient strength (in red) are found between phase 200° and 250°. The polarity of the PD signals is identified by the proposed transient strength method as shown in Figure 6.9(b).

Figure 6.9(c) shows the surface discharge results. The PRPD diagrams captured from the capacitive PD measurement system shows PD signals have negative polarity direction in the positive AC cycle; and a relatively small amplitude of PD signals in the negative AC cycle. From the results of an inductive PD measurement system, significant PD signals (in red) have negative polarity and are located in the range between 50° and 80°. The proposed method reveals the polarity direction of PD signals in accordance with those obtained by the conductive PD measurement system.

Figure 6.9(d) shows the results from multiple PD sources, which are the combination of the three PD experimental test models. The PD signals from the capacitive PD measurement system are not distinguishable from each other in the PRPD diagram unlike those from the inductive PD measurement system. The PD signals have different transient strength patterns, which enables them to be distinguished among PD signals from different sources.

The above results show that the proposed method can provide distinguishability in separating PD signals and can overcome the inherent drawback of losing polarity direction of PD signals using their transient strength.

6.5.3 Results of Online PD Measurements on In-service Transformers at Substations

This section demonstrates the application of the proposed method to extract PD signals from online PD measurements on three in-service transformers at the substations of local distribution authorities. It can be seen the configuration of an inductive PD measurement system using a HFCT installed on the ground cable of a transformer in Figure 6.1.

Figure 6.10 presents the results of applying the proposed transient strength method to extract PD signals obtained from the online PD measurement system on Transformer ‘T1’, 1 MVA (11 kV/433

V) in-service transformer. Figure 6.10(a) shows the PRPD results of the original signals acquired over 25 AC power cycles. Figure 6.10(b) shows the results of wavelet transform using 'Daubechies 12' as a mother wavelet and 10 decomposition levels. As can be observed from these three graphs, wavelet transform failed to extract PD signals properly as shown in Figure 6.10(b). On the contrary, the proposed transient strength method could effectively extract PD signals and identify significant PD events, which are depicted in red as shown in Figure 6.10(c).

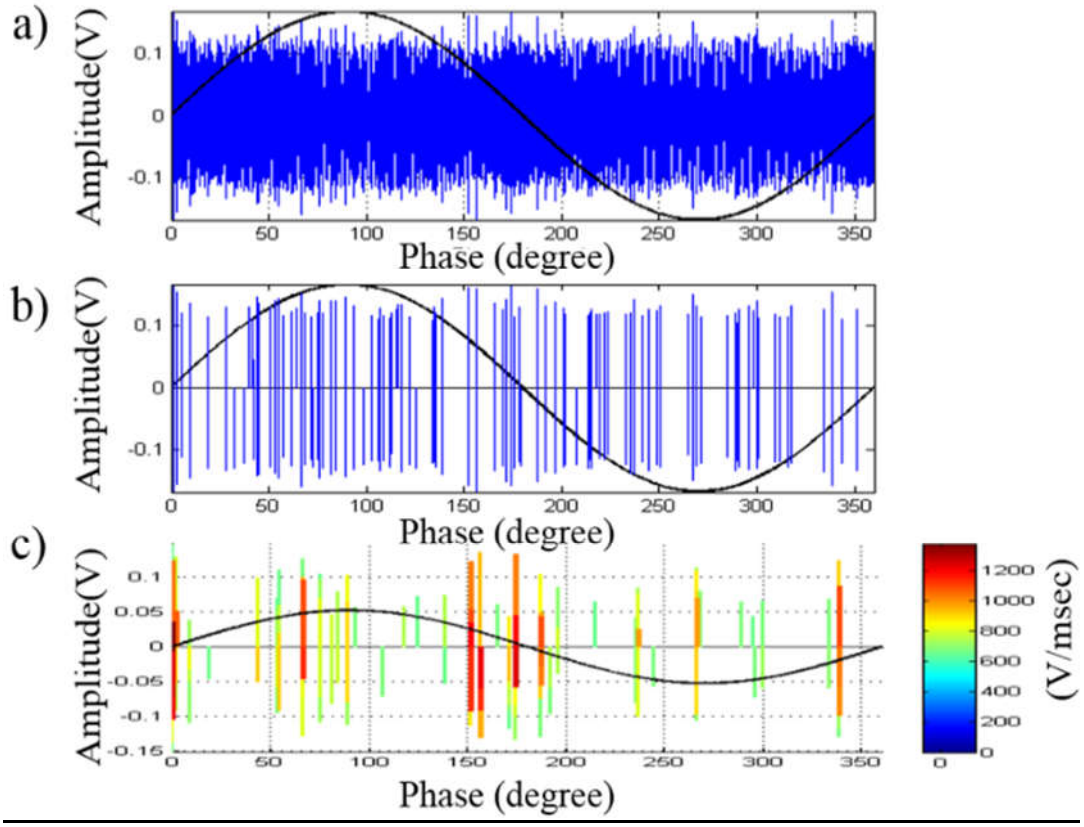

Figure 6.10 PD signal extraction results of transformer 'T1': (a) original signals measured by the inductive PD measurement system; (b) PD signals extracted by a wavelet transform; and (c) PD signals extracted by the proposed transient strength method [151].

Figure 6.11 presents the results of extracting PD signals obtained from online PD measurements on transformer 'T2', 1 MVA (11 kV/433 V). Instead of showing a PRPD result, Figure 6.11 shows the signals in time domain of 10 AC power cycles (200 ms). Figure 6.11(a) shows the originally measured signals and Figure 6.11(b) shows the extracted PD signals by the proposed transient strength method. In Figure 6.11(b), three signals located at 'S1', 'S2' and 'S3' with high transient strength are extracted as significant PD signals. The three signals are chosen for further investigation in Figure 6.12, which presents the three reconstructed signals. It can be observed from the figure that the waveforms of PD signals 'S1' and 'S2' have high similarity compared to the waveform of PD signal 'S3'. This implies that the first two signals ('S1' and 'S2') and the third signal ('S3') may be generated from different

PD sources. This proves that the proposed transient strength method can extract and identify PD signals even when they originate from different PD sources.

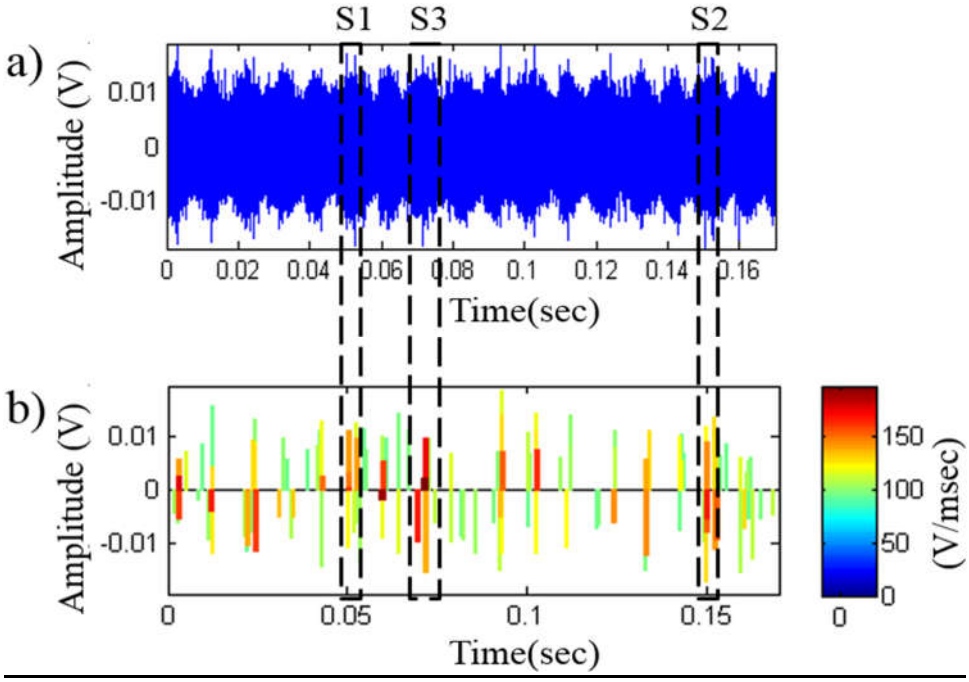

Figure 6.11 PD signals extraction results of transformer 'T2': (a) original signals measured by inductive PD measurement system; (b) PD signals extracted by the proposed differential method [151].

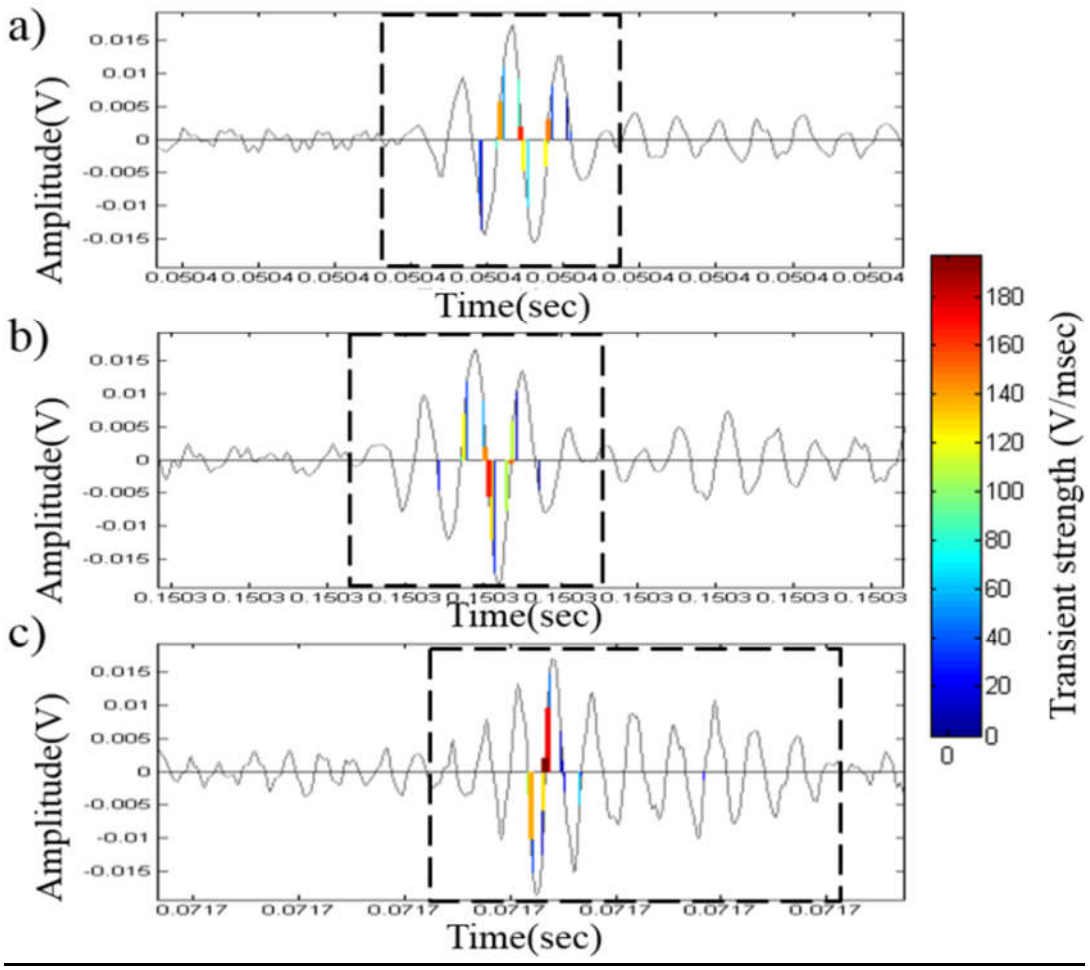

Figure 6.12 Reconstruction of three PD signals from Figure 6.11: (a) reconstructed PD signal of 'S1'; (b) reconstructed PD signal of 'S2'; and (c) reconstructed PD signal of 'S3' [151].

PD measurements were also conducted on transformers 'T3', 10 MVA (33 kV/11 kV). Figure 6.13(a) shows the PRPD diagram of the original signals obtained from the transformer and Figure 6.13(b) shows the signals extracted by the proposed transient strength method. As it can be observed from Figure 6.13, there are two clusters of signals, i.e., cluster 'b' locates at around 50° with high magnitudes and cluster 'a' locates around 250° with high transient strengths. Signals in cluster 'b' have high amplitude as shown in Figure 6.13(a) while signals in cluster 'a' have high transient strength. These two clusters are further investigated in Figure 6.14.

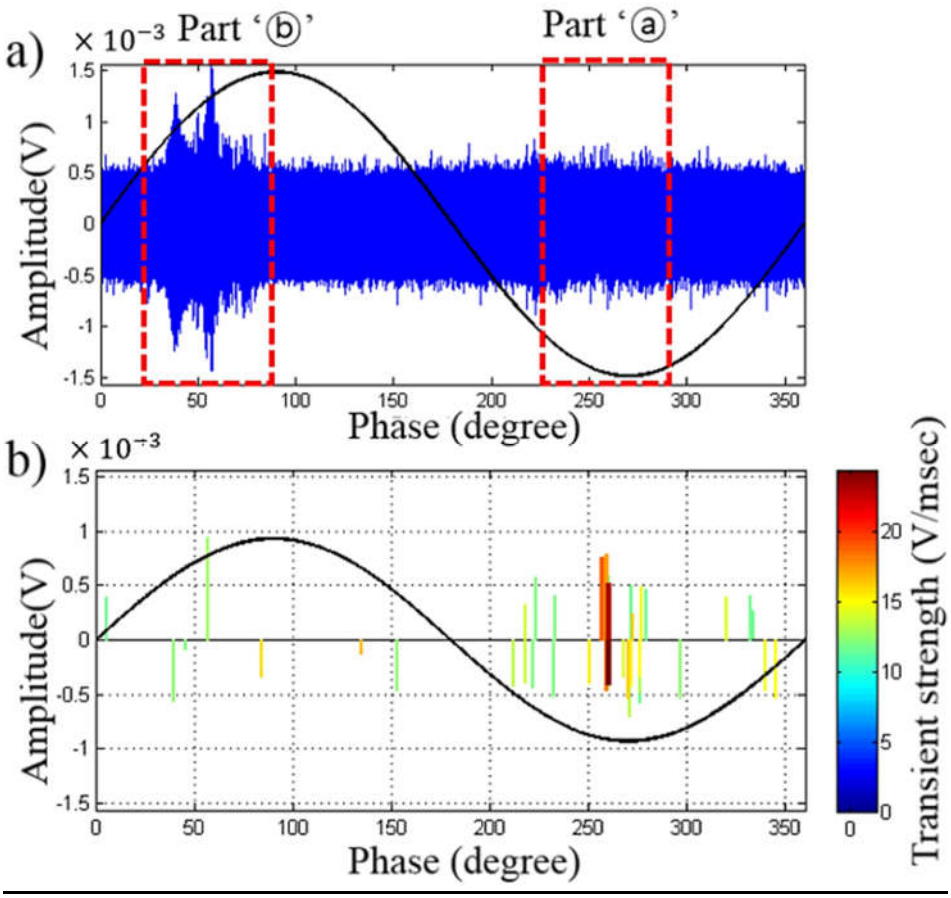

Figure 6.13 PD signals extraction results of transformer 'T3': (a) original signals acquired by an inductive PD measurement system; and (b) PD signals extracted by the proposed differential method [151].

Figure 6.14(a) shows the originally acquired signals in time domain and the corresponding results by Fast Fourier Transform (FFT). Figure 6.14(b) magnifies the signals in cluster 'a' and also presents the corresponding FFT. Figure 6.14(c) magnifies the signals in cluster 'b' and presents the corresponding FFT. The frequency spectrums of the signals in cluster 'a' and 'b' are different. For the signals of cluster 'a', the frequency components at 1000 kHz are slightly suppressed as shown in Figure 6.14(b). Contrarily, for the signals of cluster 'b', the frequency components centred at 1000 kHz are amplified significantly. This indicates the signals in cluster 'a' may be generated by PD events while the signals in cluster 'b' may be induced by a noise source with a narrow frequency band. From the above analysis, it can be seen that signals with high amplitudes are not necessarily PD signals. Signals with small amplitudes but high transient strength have a strong possibility of being PD signals.

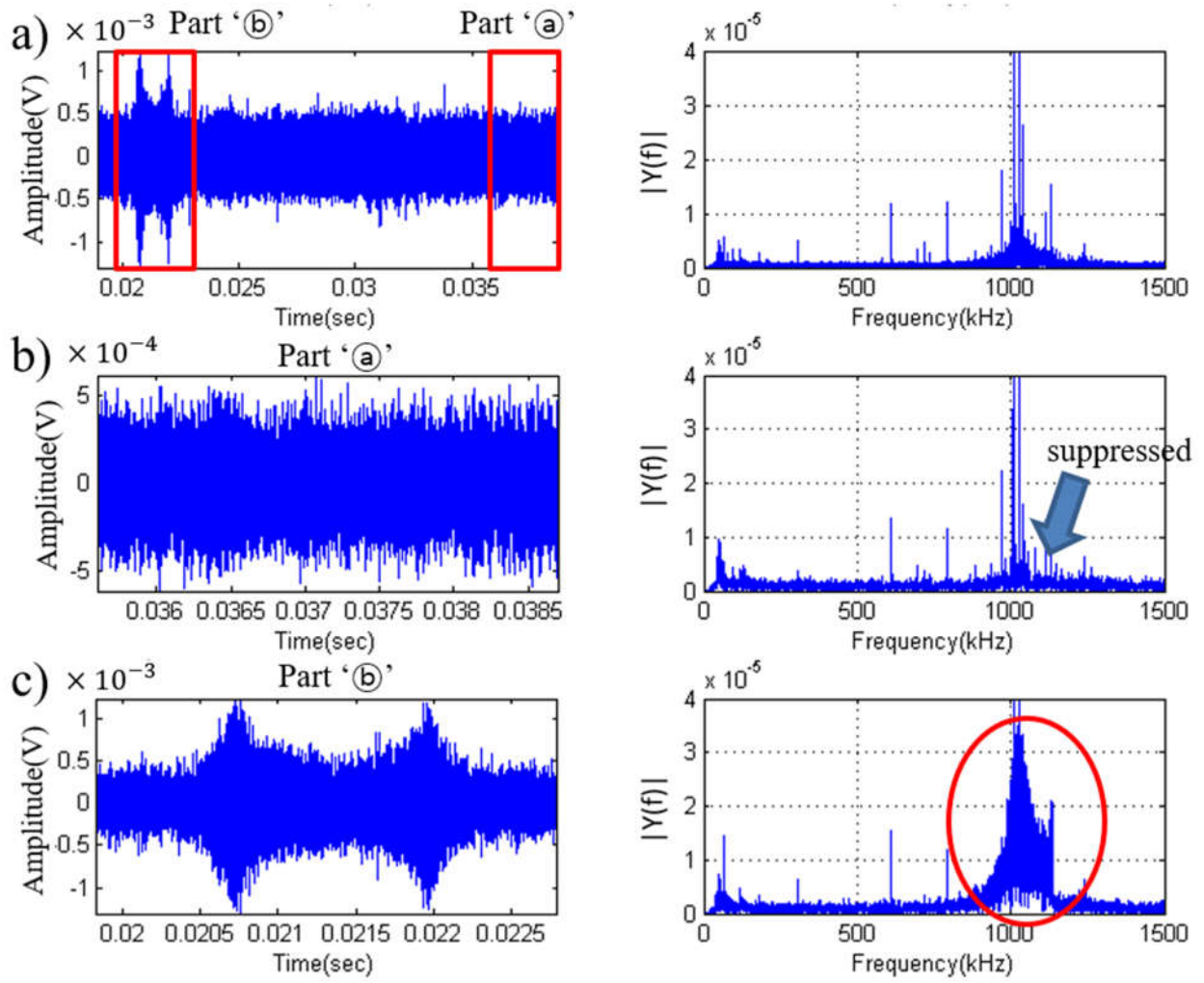

Figure 6.14 Frequency spectrum analysis for transformer 'T3': (a) original signals in one AC power cycle in time domain and corresponding FFT; (b) the scaled up signals of cluster 'Part (a)' and corresponding FFT; and (c) the scaled up signals of cluster 'Part (b)' and corresponding FFT [151].

6.6 Summary

This chapter demonstrated a capability of the proposed differential PD signal extraction method utilising transient characteristic of PD to differentiate PD signals from noise and interference. PD signal extraction was successfully implemented by adopting the transient strength criterion and the probabilistic thresholding method. The case studies demonstrated that the proposed method outperforms a wavelet transform in extracting PD signals with low amplitude and identifying the polarity direction of the PD signal. In particular, the proposed method overcomes the inherent limitations of wavelet transform in mother wavelet selection and the amplitude-based thresholding method by showing the simplicity of implementation and effectiveness of PD signal extraction. It shows a high capability of being applied for continuous online PD monitoring and diagnosis of a transformer at substations.

After PD signal extraction and the removal of noise signals as demonstrated in this chapter, PD source type and pattern are required to be analysed. In the next chapter, a sequential propagation based PD signal analysis method will be discussed. The proposed Sequential Propagation based PD analysis method will show a complementary feature that PRPD analysis method lacks. Especially, it will demonstrate an effective capability of distinguishing different types of insulation defects and sparking type or corona type of PDs.

Chap 7. Sequential Propagation based Partial Discharge (SPPD) Signal Analysis

Contribution of the Chapter

In this chapter, an effective and intuitive Partial Discharge (PD) signal extraction method is developed, which uses the transient strength of PD signals and the quantile-based thresholding method. This chapter investigates a new feature of PD signal and subsequently develops a complementary PD signal analysis method to the Phase Resolved PD (PRPD) method. This will improve the PD analysis process especially in PD source identification and separation.

In PD signal analysis, the PRPD diagram has been commonly used to characterise PD activities and to recognise the types of PD sources (insulation defects) in a power transformer's insulation system. However, the PRPD diagram only reflects a collective behaviour of PD impulses. To construct a PRPD diagram, it is recommended that PD signals are recorded over sufficient numbers of AC power cycles and then all obtained PD impulses are superimposed onto a phase angle axis. This chapter proposes a Sequential Propagating based PD (SPPD) signal analysis method as a complementary method to the PRPD method. The SPPD analysis method explores the sequential propagation and occurrence characteristics of PD impulses by observing instantaneous PD activities. One of the inherent advantages of the proposed SPPD method is the capability of separating and recognising the type of PD source, i.e., sparking or corona type. The applicability of the SPPD analysis method has been verified using data collected from experimental PD test models and from an in-service field transformer.

This chapter has been reproduced from the following paper:

J. Seo, H. Ma and Tapan K. Saha, "Using Sequential Propagating Characteristics of Partial Discharge (PD) Signal for Condition Monitoring of Power Transformer," submitted to IET Science, Measurement & Technology on 27th December, 2018.

7.1 Introduction

During PD measurement on a power transformer, the industry standard recommends recording a series of discharge impulses over a sufficient number of AC power cycles [114 - 115, 117, 157]. The recorded PD impulses are plotted along a phase angle axis to form a PRPD diagram [115, 144, 158, 159]. The PRPD diagram can be used to identify the type of PD source, i.e., establishing whether the discharge is caused by a cavity in the solid insulation or by a protrusion or a floating metal particle inside a transformer tank or a bubble formed in the insulation oil [115].

However, since the PRPD diagram exhibits collective PD activities, small amplitude PD impulses can be disregarded by comparatively large amplitude PD impulses [160]. Especially when multiple PD sources exist in a transformer, the PRPD diagram may further impair the capability of PD source classification since PD impulses generated by different PD sources can be mixed together and are not separable on the PRPD diagram. Therefore, complicated and extensive computational algorithms are required to deal with such multiple PD source classification [161 - 162].

To address the above limitations of the PRPD diagram, this chapter proposes a SPPD signal analysis method. The SPPD analysis method explores the propagating characteristics of PD impulses over a number of AC power cycles. Other than the phase locations and magnitudes used in the PRPD analysis method, the proposed SPPD analysis method can also reveal the propagating direction with respect to phase angle, the population density and the category (sparking type or corona type [157 - 158]) of the PD impulses. Having been applied to a number of experimental PD test models, the SPPD analysis method is found uniquely distinctive for each type of insulation defect and even for the same type of insulation defect but with different geometry (i.e., configuration) and under different test conditions (i.e., applied voltage). Especially, the proposed SPPD analysis method has been successfully implemented on an inductive PD measurement system using a HFCT.

This chapter is organised as follows. Section 7.2 provides a brief review of two major categories of PD phenomena in power transformer and the PD measurement system setup. In Section 7.3, the SPPD analysis method is applied to investigate the properties of PD impulses on different experimental PD test models. The applicability of SPPD analysis method to PD source classification is verified. In Section 7.4, the SPPD analysis method is applied to process PD impulses obtained from PD measurements on a field transformer. Section 7.5 concludes this chapter.

7.2 PD Phenomena in an Oil-Insulation Paper System

The oil-insulation paper system of the main winding in a power transformer is subjected to continuous electrical, thermal and mechanical stresses and eventually the insulation system can deteriorate. This may cause PD activities in a weak part of the insulation system being exposed to an

excessive electrical field concentration. The PD activities can be influenced by the construction of a transformer's insulation system, properties of insulation defects and the types of insulation material [115, 157].

According to the literature, PDs in transformer's oil-insulation paper system can be categorised into two major types, namely sparking type and corona type [34, 157, 163]. Corona is a result of gas ionisation in air or bubbles in insulation oil [7.3]. The corona type PD activity produces hydrogen (H_2) and methane [34]. Sparking type PD can be caused by solid insulation damages such as cracks or cavities (i.e., internal discharge) or small floating metal particles in the insulation oil (discharge due to floating particles). It generates acetylene (C_2H_2) and hydrogen (H_2) [34, 35]. This type of PD can damage solid insulation material (carbonising pinholes and tracking on paper) and deteriorate the quality of oil (oil decomposition and gassing) [157]. By exploiting the sequential propagating characteristics of a series of PD impulses collected over a number of AC power cycles, the proposed SPPD analysis method can classify the type of PD activities into their categories (refer to Section 7.3).

To investigate the sequential propagating characteristics of PD impulses, a number of experimental PD test models have been designed. These models are used to simulate different types of PD sources (insulation defects) in power transformers, including internal discharge, discharge due to metal particles, surface discharge, corona and multiple PD sources (Figure 7.1(b) and Figure 7.9). Details of the PD test configurations can be refer to Section 6.5.1.

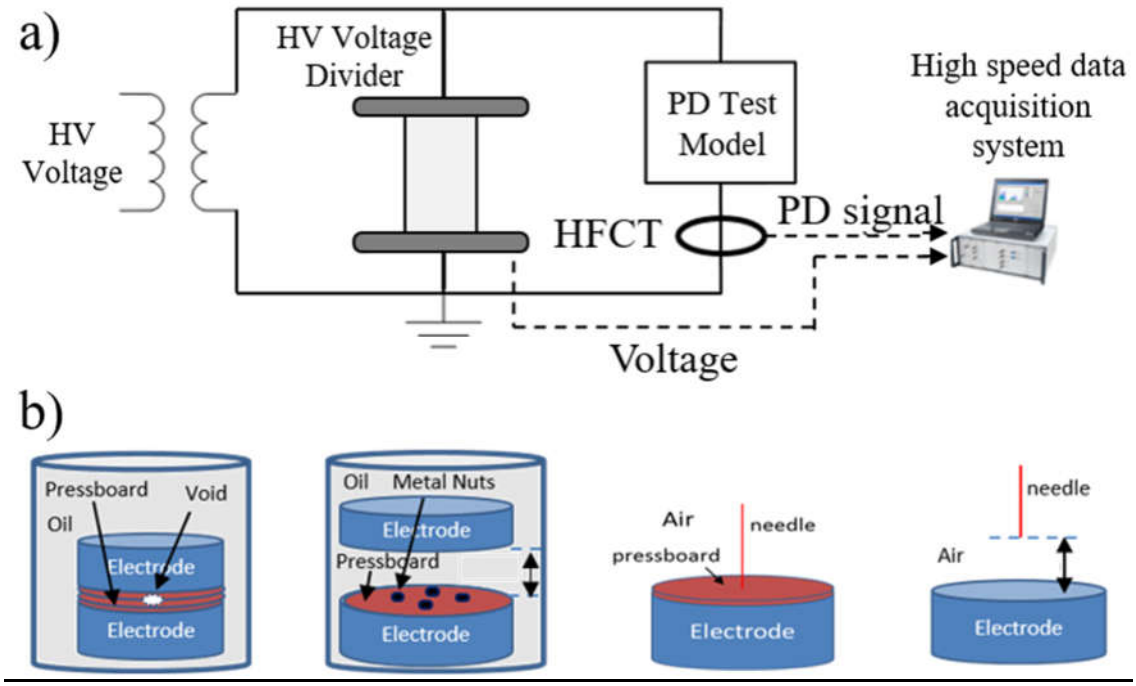

Figure 7.1 Experimental test models: (a) Test setup of HFCT based PD measurement; (b) experimental PD test models for simulating internal discharge, discharge by floating metal particles, surface discharge and corona (from left to right side).

In this thesis, an inductive PD measurement system using a HFCT is adopted for both laboratory and field PD measurements as shown in Figure 7.19(a). The HFCT is clamped onto the ground cable of the PD experimental model or field transformer to capture PD signals [114]. The -3 dB frequency range of the HFCT is from 350 kHz to 35 MHz. The PD signals acquired by the HFCT are fed into a high speed data acquisition system. The sampling rate is 40 mega times per second. In one acquisition, signals for 500 ms (25 AC cycles at 50 Hz) are recorded. During PD measurement on experimental PD test models, the applied voltage level is adjusted until the PD activity becomes stable [115].

7.3 Sequential Propagating based PD (SPPD) Analysis of Experimental PD Test Models

In this section, PD signals acquired from experimental PD test models are analysed to investigate the sequential propagating characteristics of PD activities. Since the PD measurements were conducted in a well-controlled laboratory environment, the noise level is low (less than 10 pC) and PD impulses are significantly comparable to noise signals.

7.3.1 SPPD Analysis of Internal Discharge

Figure 7.2 presents the results of the SPPD analysis on the experimental PD test model of internal discharge. The model consists of three pressboards (the middle pressboard has a small void) between two electrodes. The whole model was immersed in insulation oil (refer to Figure 7.1(b)). During the PD measurement, the test voltage was eventually set to 8 kV and kept at 8 kV for continuous PD activity.

Figure 7.2(a) presents the acquired PD impulses of two AC power cycles out of a total 25 cycles. There are two impulses in each AC cycle. One is found in the positive half of AC cycle (the ‘positive cycle impulse’) and the other is found in the negative half of AC cycle (the ‘negative cycle impulse’). It is noted that the number of impulses can vary depending on the type and condition of the PD source.

To observe and quantify the sequential propagating characteristics of PD impulses, the phase angle difference (the ‘phase angle distance’) between impulses in the above positive and negative AC cycles is calculated. The phase angle distances between PD impulses in all pairs of positive and negative AC cycles over 25 AC power cycles are plotted as shown in Figure 7.2(b). As an example, the phase angle distance between impulses at the first AC cycle is about 200° (marked as ‘a’ in Figure 7.2(b) and Figure 7.2(c)) and the phase angle distance at the last AC cycle is about 150° (marked as ‘b’ in Figure 7.2(b) and Figure 7.2(c)).

In Figure 7.2(c) the PD impulses acquired at different AC cycles are depicted in different colours. For example, the impulses at the first AC cycle are depicted in blue and the impulses at the 25th AC

cycle are in red. Such a colour scheme enhances the visibility of phase angle locations of PD impulses for each AC cycle.

From Figure 7.2(b) and Figure 7.2(c), it can be observed that the phase angle distances between impulses at the positive and negative cycles become smaller with the increase of AC cycles. It can be regarded that impulses in the positive and negative AC cycles eventually move toward each other (as indicated by the two arrows in Figure 7.2(c)) with respect to AC cycles. Though there is a small fluctuation as shown in Figure 7.2(b), the overall sequential propagating trend of impulses at the positive and negative AC cycles is to narrow their spatial distance in phase angle.

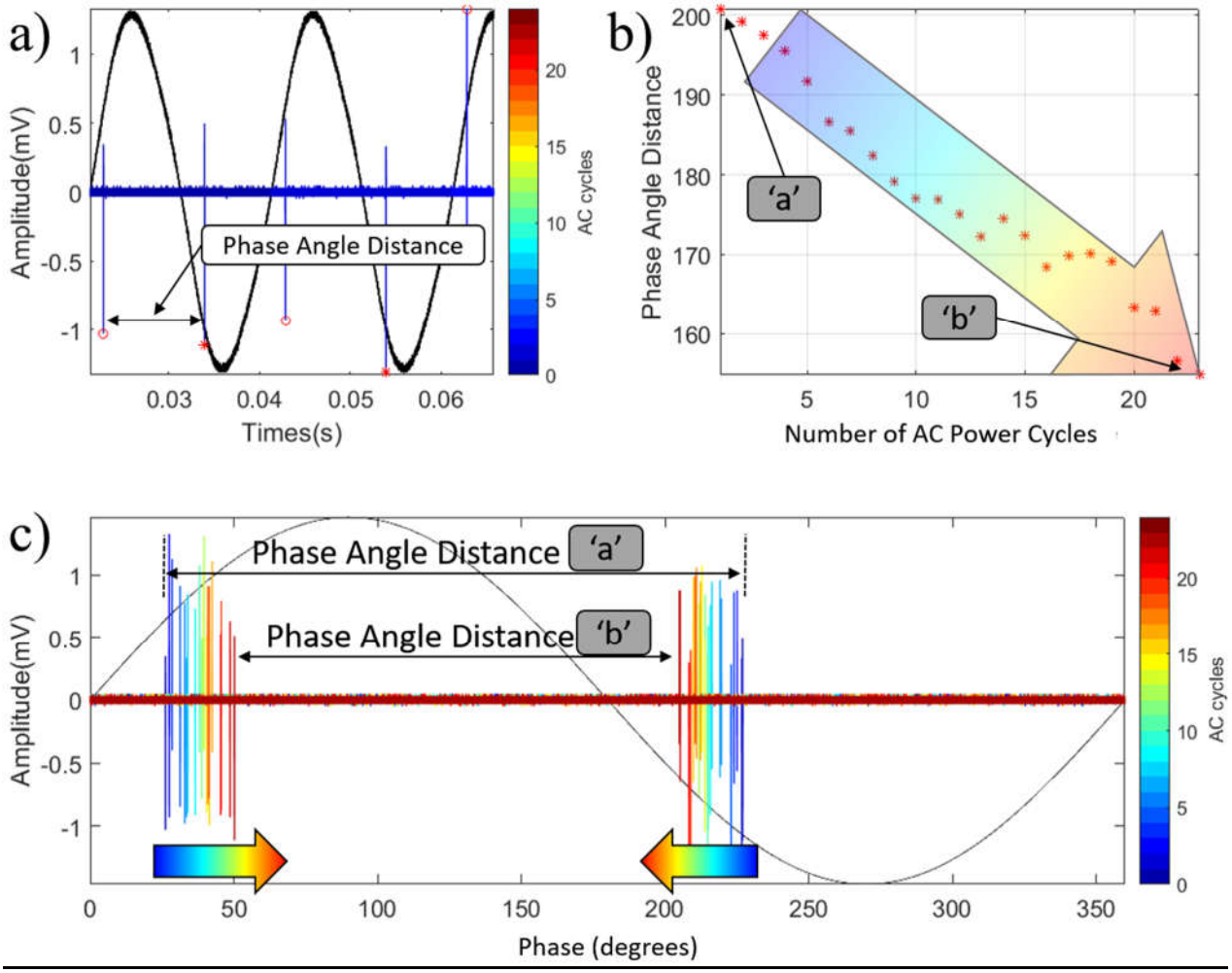

Figure 7.2 Internal discharge at 8 kV test voltage. (a) PD impulses in two AC cycles out of 25 cycles; (b) phase angle distance between two PD impulses in the positive and negative AC cycles; and (c) PD impulses acquired over 25 AC cycles depicted in a colour scheme to show the evolvement of spatial distance between the impulses in the positive and negative AC cycles. Note: in the figures, 'a' refers to the phase angle distance between impulses in the positive and negative cycles during the first AC power cycle, and 'b' refers to phase angle distance between impulses during the positive and negative cycles at the 25th AC power cycle.

The above case study shows that SPPD analysis can complement PRPD in analysing PD activities. The advantages of SPPD in revealing the moving pattern of PD impulses with respect to the phase angle and its application for PD source classification are further demonstrated as follows.

By maintaining the voltage at 8 kV to the above experimental PD test model of internal discharge for another 20 minutes, a second data acquisition was conducted. The corresponding SPPD analysis is presented in Figure 7.3.

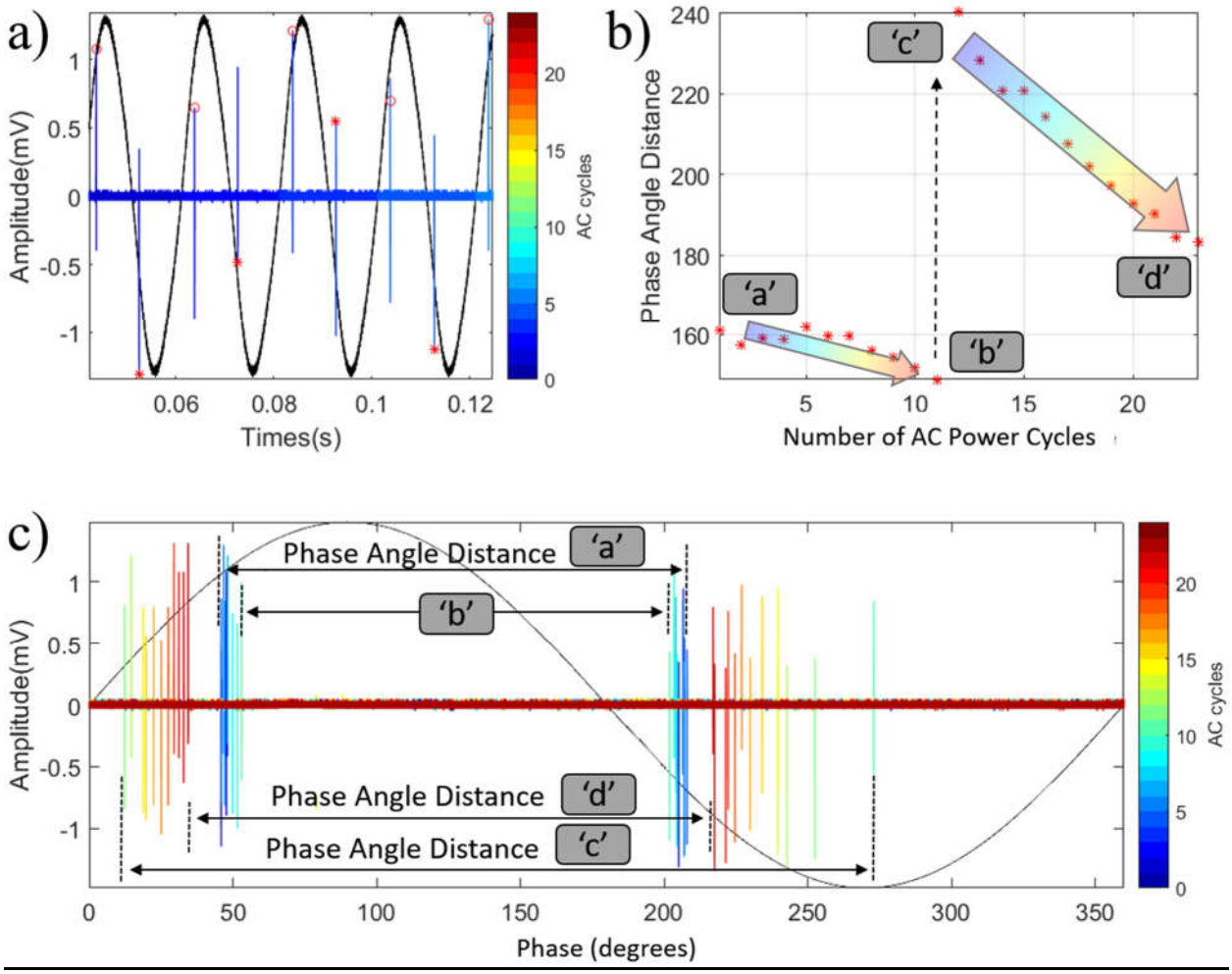

Figure 7.3 Another data acquisition to an internal discharge test model (Figure 7.1(b)) conducted after another 20 minutes of the first data acquisition in Figure 7.2 with the same test condition. (a) PD impulses in four AC cycles out of 25 cycles; (b) phase angle distance between two PD impulses in the positive and negative AC cycles; and (c) PD impulses acquired over 25 cycles depicted in a colour scheme to show the evolvement of spatial distance between the impulses in the positive and negative AC cycles.

As can be seen in Figures 7.3(b) and 7.3(c), the phase angle distance between impulses at the positive and negative AC cycles is 160° (marked as 'a') at the first AC power cycle. It slightly decreases to 140° (marked as 'b') at the 11th AC cycle. Then it changes to 240° (marked as 'c') at the 12th AC cycle and then eventually decreases to 180° (marked as 'd') at the 25th AC cycle. Thus, it can

be seen that impulses at both positive and negative AC cycles are circulating in each positive and negative AC cycle by narrowing the phase angle distance as shown in Figure 7.3(b).

The sequential propagating characteristics of PD impulses in Figure 7.3 is similar to those in Figure 7.2. However, the PD impulse phase distribution range has been extended along with dispersed density compared to that at the first PD data acquisition (Figure 7.2). Such a PD impulse population density change in phase cannot be identified in a PRPD diagram since PDs are overlaid in PRPD. The above change in PD impulse population density may be caused by continuous electrical stress.

7.3.2 SPPD Analysis of Discharge due to Metal Particles

For an in-service transformer, some small metal particles may detach eventually. They can affect the electrical field distribution inside a transformer and contribute to PD activity. The experimental PD test model for this type of PD was configured by placing four metal nuts (2 mm in radius) on top of a pressboard, which in turn was placed on top of a grounding electrode. A high voltage electrode was placed 10 mm above the metal nuts. The whole setup was immersed in insulation oil. The SPPD analysis results are shown in Figure 7.4.

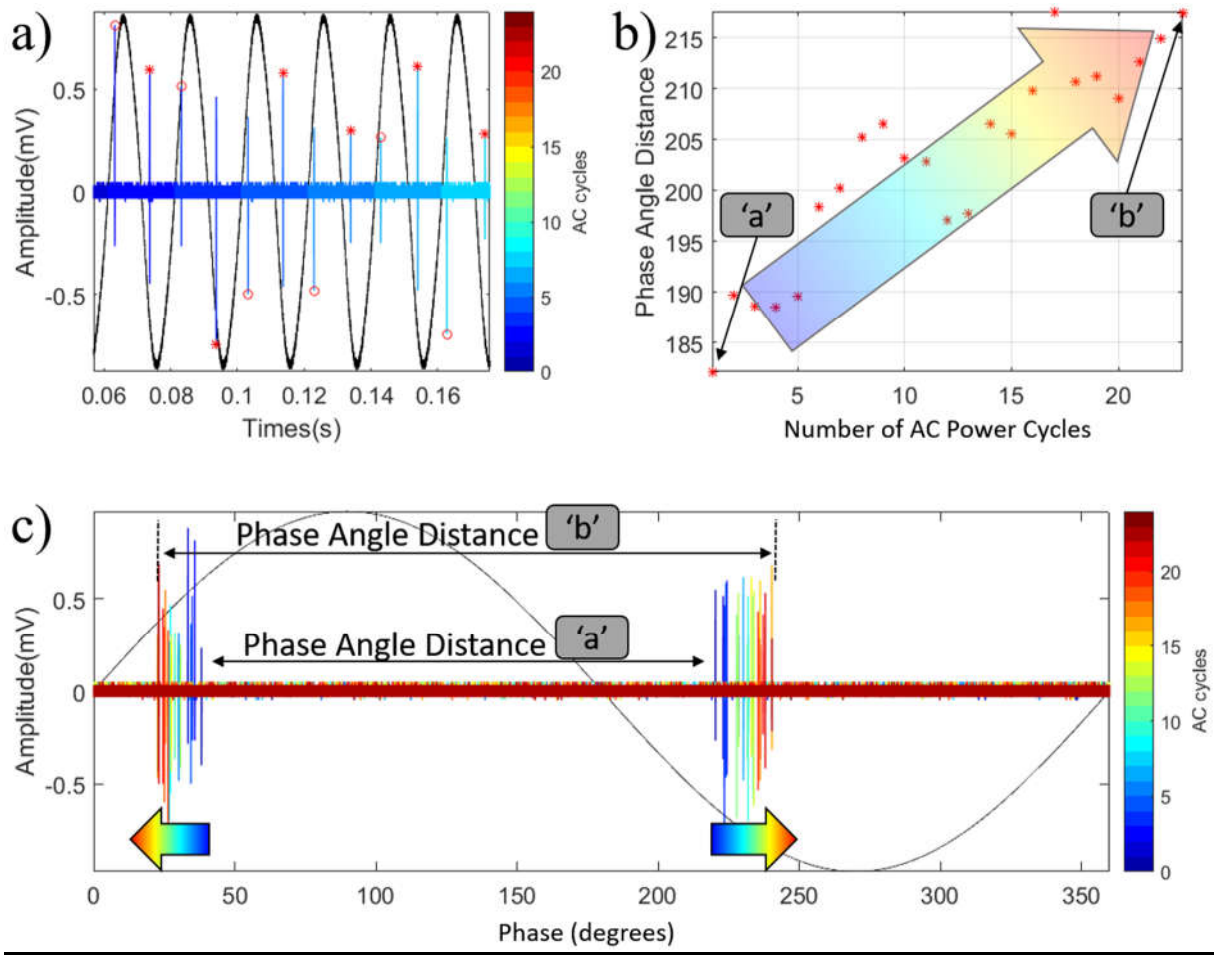

Figure 7.4 Discharge due to metal particles (four metal nuts on a pressboard placed on plane electrode which has a 10 mm gap between the top side electrode and the metal

nuts, tested at 8 kV). (a) PD impulses in five cycles out of 25 AC cycles; (b) phase angle distance between two PD impulses in the positive and negative AC cycles; and (c) PD impulses acquired over 25 AC cycles depicted in a colour scheme to show the evolvement of spatial distance between the impulses in the positive and negative AC cycles.

Figure 7.4(a) shows a pair of PD impulses at positive and negative AC cycles in each AC power cycle. The phase angle distances of all pairs of impulses over 25 AC power cycles are depicted in Figure 4(b). It can be observed from Figures 7.4(b) and 7.4(c) that phase angle distances between impulses at positive and negative AC cycles become larger with the increase of AC cycles. This is the opposite direction from that of internal discharge in Figures 7.2 and 7.3.

Another experiment was conducted, where the test conditions were the same except the distance between the upper electrode and metal particles increased from 10 mm to 20 mm. The corresponding SPPD analysis results are shown in Figure 7.5.

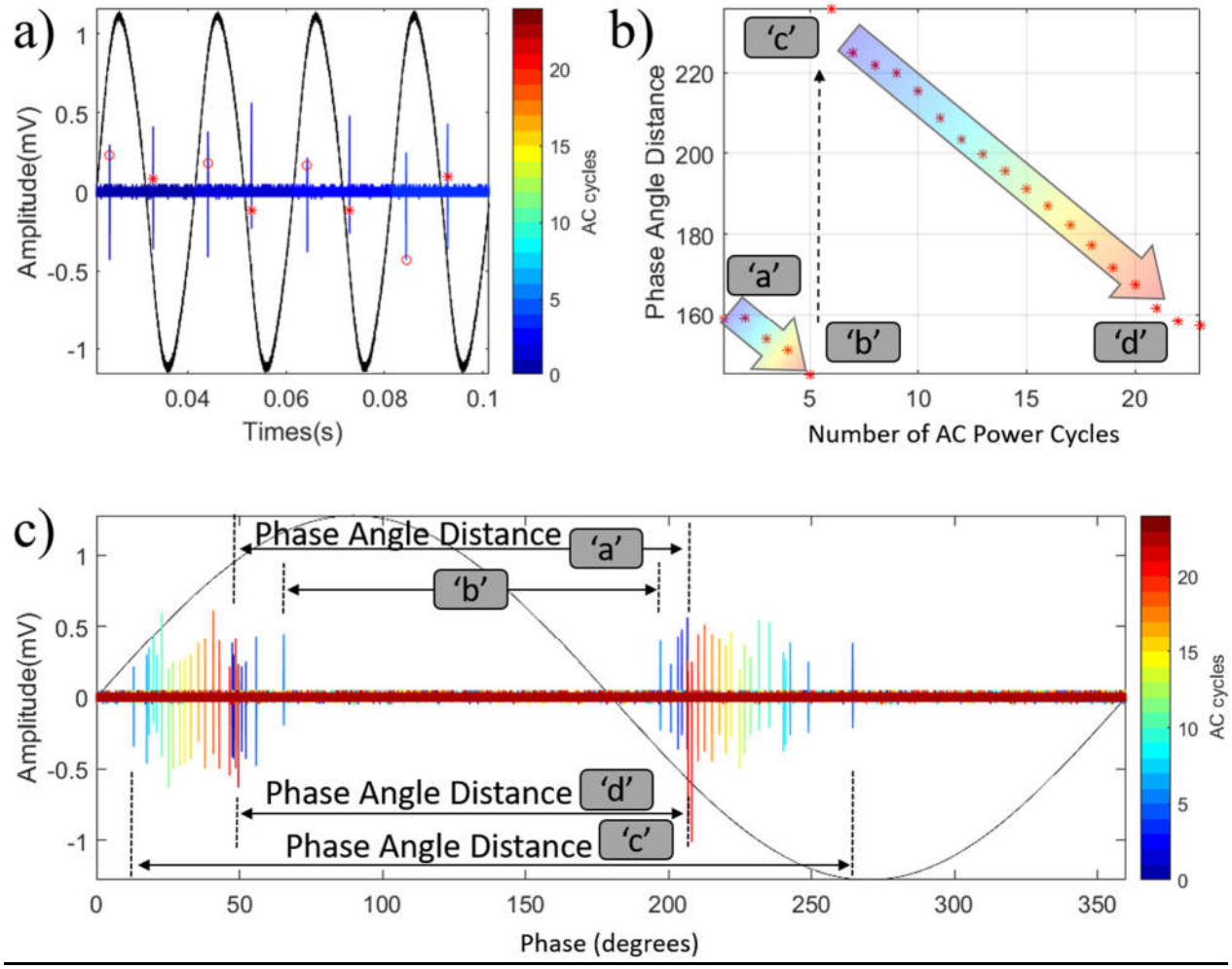

Figure 7.5 Discharge by metal particles in oil (four metal nuts on a pressboard placed on a plane electrode which has a 20 mm gap between the top side plane electrode and metal nuts, tested at 8 kV). (a) PD impulses for the four AC cycles out of 25 AC cycles; (b) phase angle distance between two PD impulses in the positive and negative AC cycles; and (c) PD impulses acquired over 25 AC cycles depicted in a colour scheme to show the evolvement of spatial distance between the impulses in the positive and negative AC cycles.

As it can be seen in Figures 7.5(b) and 7.5(c), the phase angle distance between the positive and negative AC cycle PD impulses is 160° (marked as 'a') in the first AC cycle. It slightly decreases to 140° (marked as 'b') in the 4th AC cycle. It then changes to 240° (marked as 'c') at the 5th AC cycle and then eventually decreases to 155° (marked as 'd') at the 25th AC cycle.

Compared to Figure 7.4, it can be seen that PD impulses are distributed in a wider range and PD impulses in each positive and negative AC cycle propagate towards opposite directions in phase. The above difference may be due to a change in a gap distance between the upper electrode and metal particles of the PD test model. This case study also demonstrates that SPPD analysis method can characterise PD activity more distinctively than using only PRPD analysis.

A third experiment was conducted. The test setup and the conditions were the same as in Figure 7.4 except that the number of metal particles was decreased from four to three. The results of the SPPD analysis is shown in Figure 7.6.

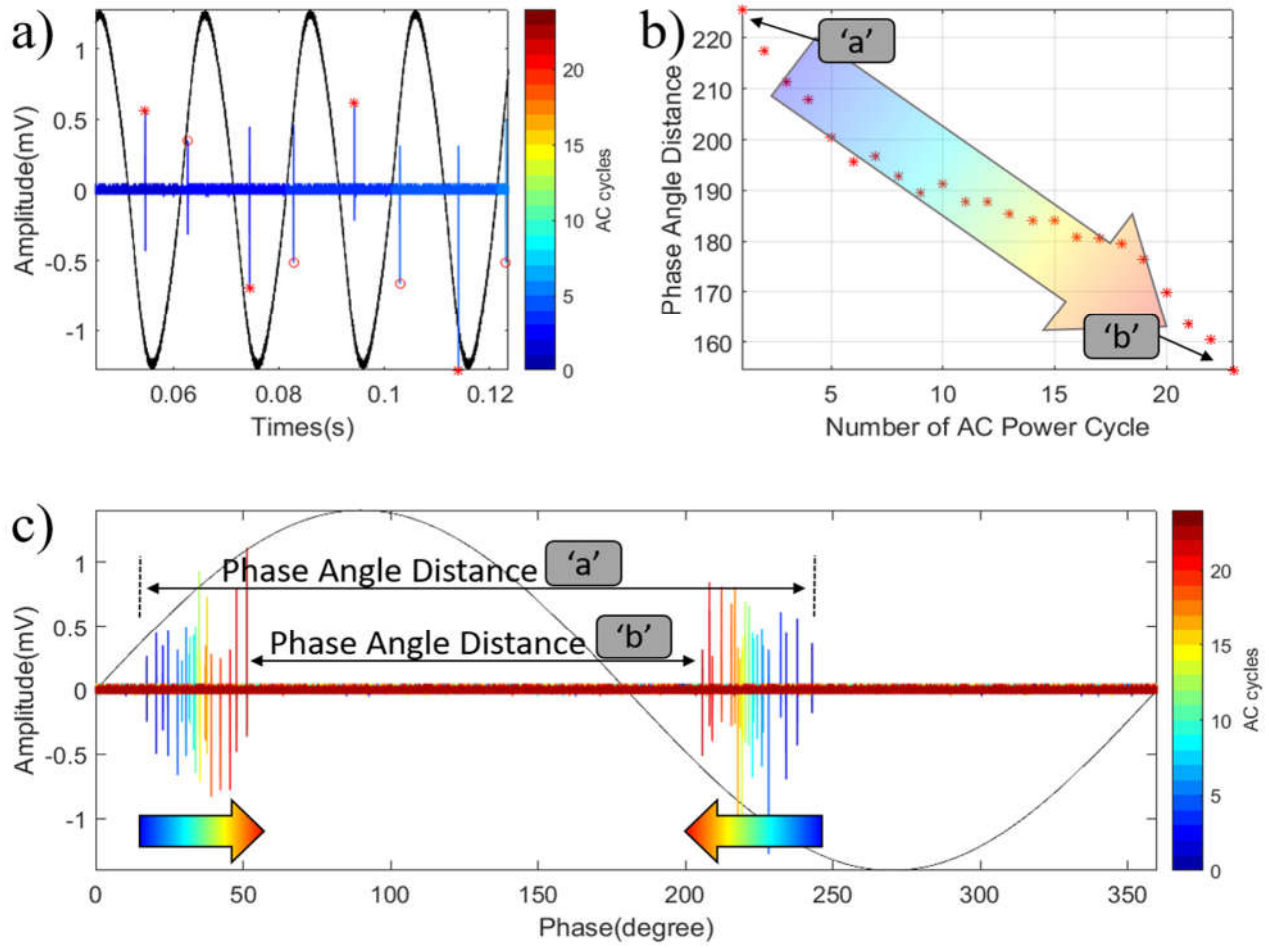

Figure 7.6 Discharge due to metal particles in oil (three metal nuts on a pressboard placed on a plane electrode which has a 10 mm gap between the top side plane electrode and the metal nuts, tested at 8 kV). (a) PD impulses for three AC cycles out of 25 AC cycles; (b) phase angle distance between two PD impulses in the positive and negative AC cycles; and (c) PD impulses acquired over 25 AC cycles depicted in a colour scheme to show the

evolvement of spatial distance between the impulses in the positive and negative AC cycles.

It can be seen that the phase angle distances between PD impulses in the positive and negative AC cycles decreases (two groups of PD impulses head towards each other as indicated by the arrow in Figure 7.6(c)) with respect to AC cycles.

The PD impulses from the above three different configurations of the same type of PD source were exhibited distinctively by the SPPD analysis method. Thus, the SPPD can be complementary to the PRPD analysis method in interpreting PD signals on the same type of PD source with different configurations (e.g., number of metal particles and distance between electrodes).

7.3.3 SPPD Analysis of Surface Discharge and Corona

The SPPD analysis also was conducted for surface discharge, which was generated by placing a steel needle in contact with the surface of two layers of pressboard. A piece of pressboard was placed on top of a flat electrode and tested in air. The result is shown in Figure 7.7.

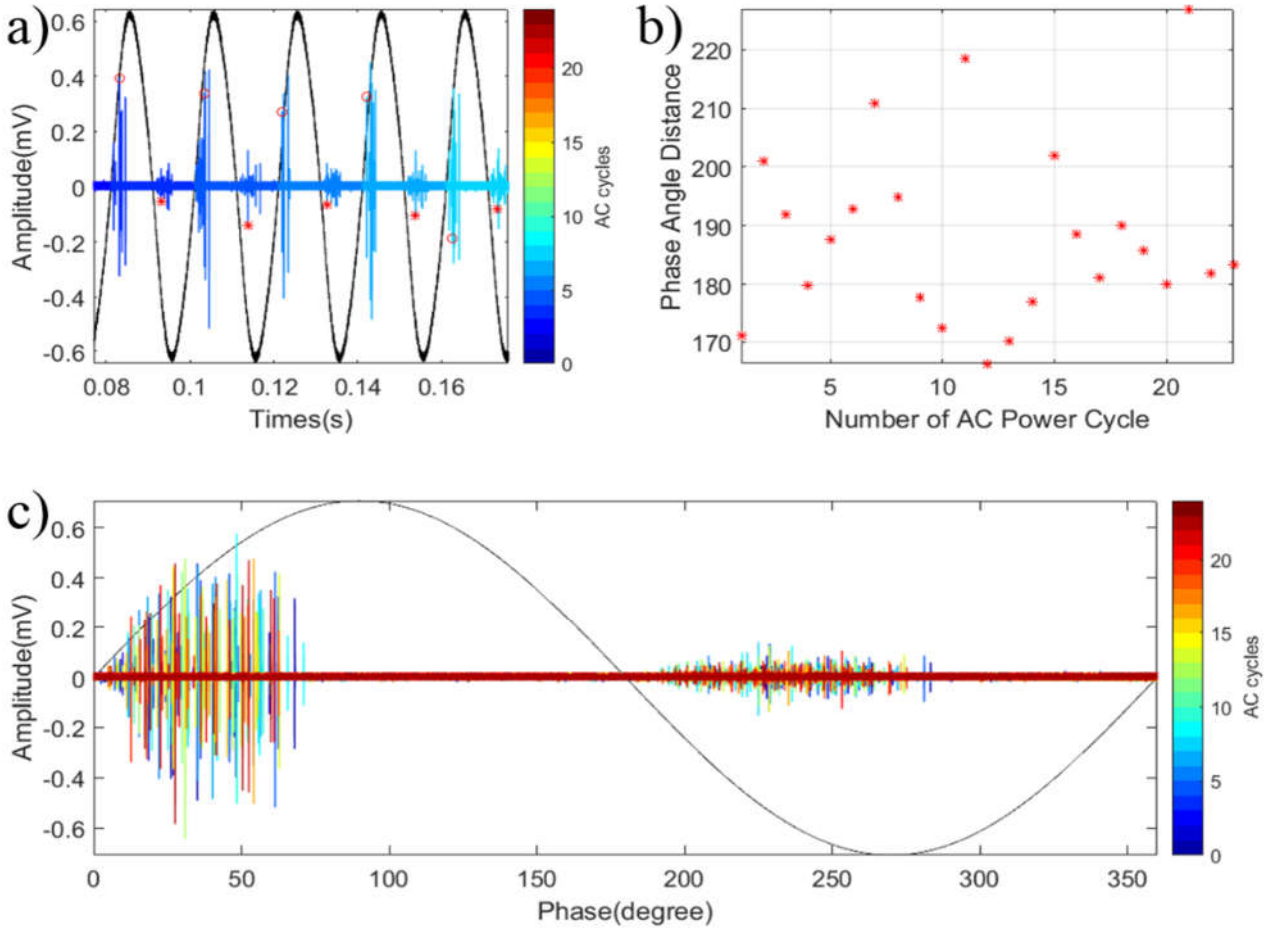

Figure 7.7 Surface discharge in air (pin to plane with two pressboards between the electrodes, tested at 8 kV). (a) PD impulses in four AC cycles out of 25 AC cycles; (b) phase angle distance between two PD impulses in the positive and negative AC cycles; and (c) PD impulses acquired over 25 AC cycles depicted in a colour scheme showing the

evolvement of spatial distance between the impulses in the positive and negative AC cycles.

As shown in Figure 7.7 the PD impulses from the above surface discharge model show an asymmetric pattern in amplitudes, in which high amplitude PD impulses appear in the positive AC cycle and relatively low amplitude PD impulses appear in the negative AC cycle.

Compared to Figures 7.2(b) and 7.3(b) (internal discharge) and Figures 7.4(b), 7.5(b) and 7.6(b) (discharge due to metal particles), the phase angle distances between PD impulses in the positive and negative AC cycles do not show any distinctive pattern in Figure 7.7(b). Such difference is due to the surface discharge being corona type PD whereas the other two are caused by sparking type discharge. By using SPPD analysis, it is thus possible to distinguish the two major types of PD sources.

Corona discharges were obtained by using a point-to-plane electrode configuration. The test voltage was set to 6 kV. The SPPD analysis results are shown in Figure 7.8. Similar to the above surface discharge in Figure 7.7(b), the phase angle distances between PD impulses in the positive and negative AC cycles do not show any distinctive pattern in Figure 7.8(b).

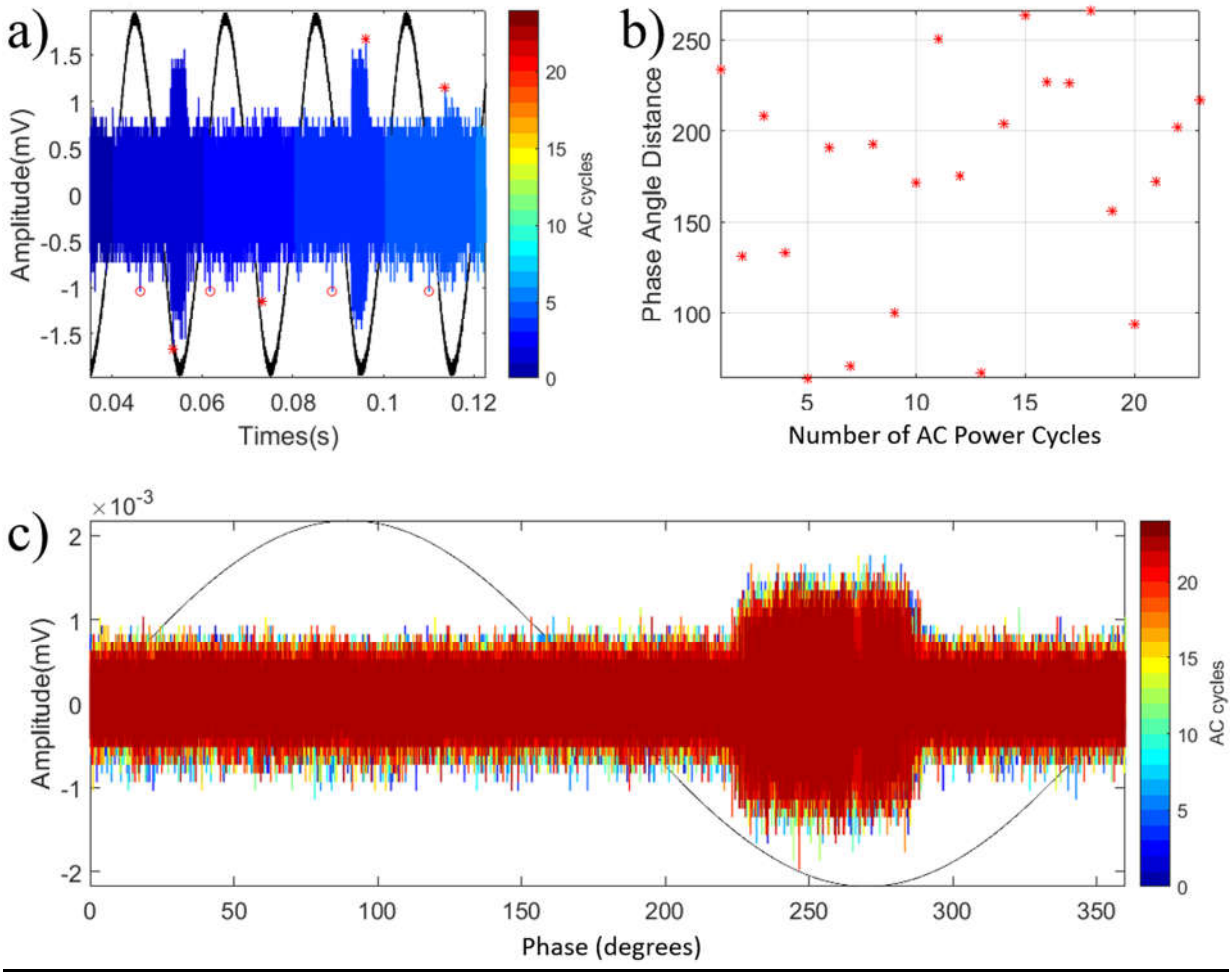

Figure 7.8 Corona in air (pin to plane with a 15 mm gap and without a pressboard between the electrodes, tested at 6 kV): (a) PD impulses in four AC cycles out of 25 AC cycles; (b) phase angle distance between PD impulses in the positive and negative AC cycles and (c)

PD impulses acquired over 25 cycles depicted in a colour scheme showing the evolvement of spatial distance between the impulses in the positive and negative AC cycles.

7.3.4 SPPD Analysis of Multiple PD Sources

In this section, the SPPD analysis method is applied to multiple PD sources to investigate its capability of separating PD impulses from different PD sources. Two types of multiple PD source models are configured as shown in Figure 7.9. The first configuration consists of experimental PD test models of discharge due to metal particles and surface discharge. The second configuration consists of experimental PD test models of internal discharge and surface discharge. By adjusting the geometric configurations of the test models (e.g. distance between electrodes), the discharge inception voltages of different models were controlled to be close to each other during signal measurement.

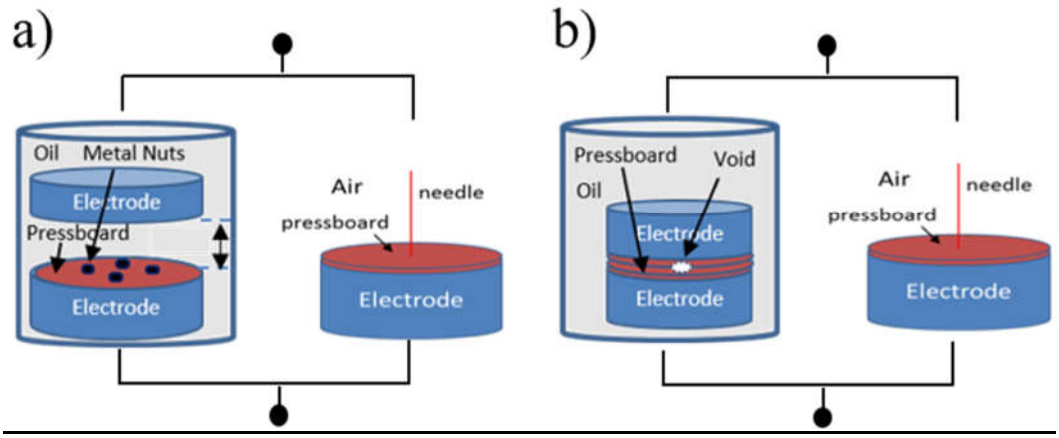

Figure 7.9 Multiple PD source model configurations: (a) multiple PD sources consisting of discharge due to metal particles and surface discharge; (b) multiple PD sources consisting of internal discharge and surface discharge.

The SPPD analysis of the first multiple PD source configuration is presented in Figure 7.10. Three major groups of PD impulses ('A', 'B' and 'C') are formed.

The PD impulses of group 'A' showing sequential propagating PD activities are considered to be generated from the discharge due to metal particles. In this group, the phase angle distances between PD impulses in the positive and negative AC cycles increase with the increase of AC cycles (as indicated by the arrows in Figure 7.10(b)).

PD impulse groups 'B' and 'C' are considered as corona type PD. By referring to the previous SPPD analysis results on single PD sources, they are most probably a surface discharge.

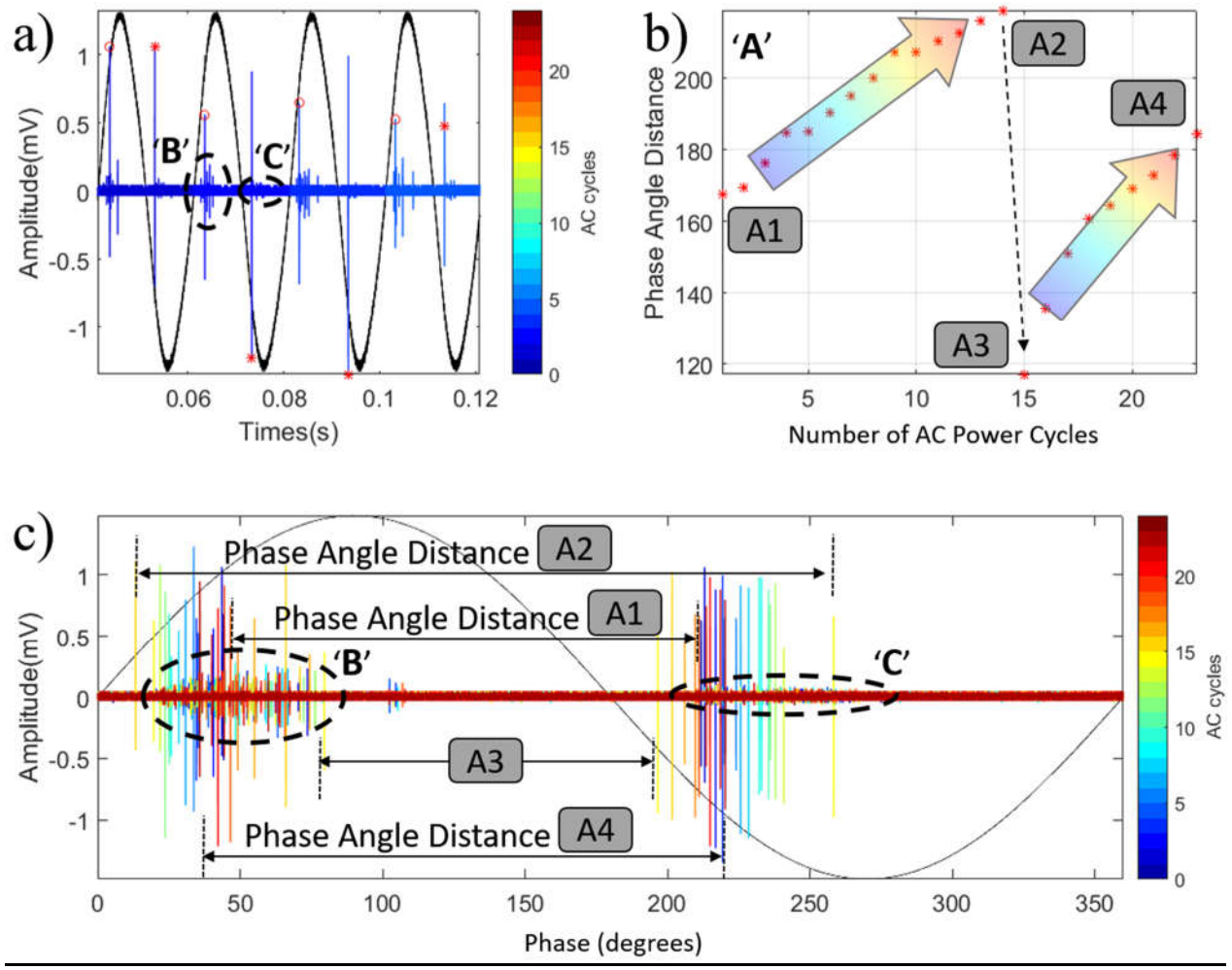

Figure 7.10 PDs from multiple PD sources consisting of floating discharge and surface discharge at 8 kV: (a) detailed PD signal appearance only for four AC power cycles; (b) phase angle distance between PDs (in group 'A') in the positive and negative AC cycles; and (c) SPPD featured diagram showing collective appearance patterns from the multiple PD sources.

The SPPD analysis to the second multiple PD source configuration is presented in Figure 7.11. Two PD impulses (group 'A') are found in each positive and negative cycles as shown in Figure 7.11(a). Phase angle distance between PD impulses in the positive and negative AC cycles is depicted in Figure 7.11(b). These two impulses move towards each other with an increase of AC power cycles. The phase angle distance between PD impulses in the positive and negative AC cycles also show the same trend (as indicated with arrow in Figure 7.11(c)). With reference to Figure 7.2, the sequential propagating PDs in group 'A' are thought to be generated from an internal discharge PD source.

It is noted that the propagation direction of PD impulses can vary under any changed conditions though it is from the same type of insulation defects. Thus, specifying a propagation direction on a specific type of insulation defect may not be practically applicable. As in Figure 7.10, the PD impulses of Group 'B' and 'C' are generated by a surface discharge source. The observations from the above two results of multiple PD sources demonstrate that there are two major categories of PD phenomenon:

sparking type PD and corona type PD. PD test models of internal discharge and discharge due to metal particles results in sequential propagating of PD signals whereas surface discharge results in corona type of PD signals. Additionally, for sparking type PDs, the moving direction of sequential propagating PD signals in phase may vary depending on the type and geometry of the PD source. The observations in SPPD can be utilised as an additional feature for distinguishing PD signals from different insulation defects.

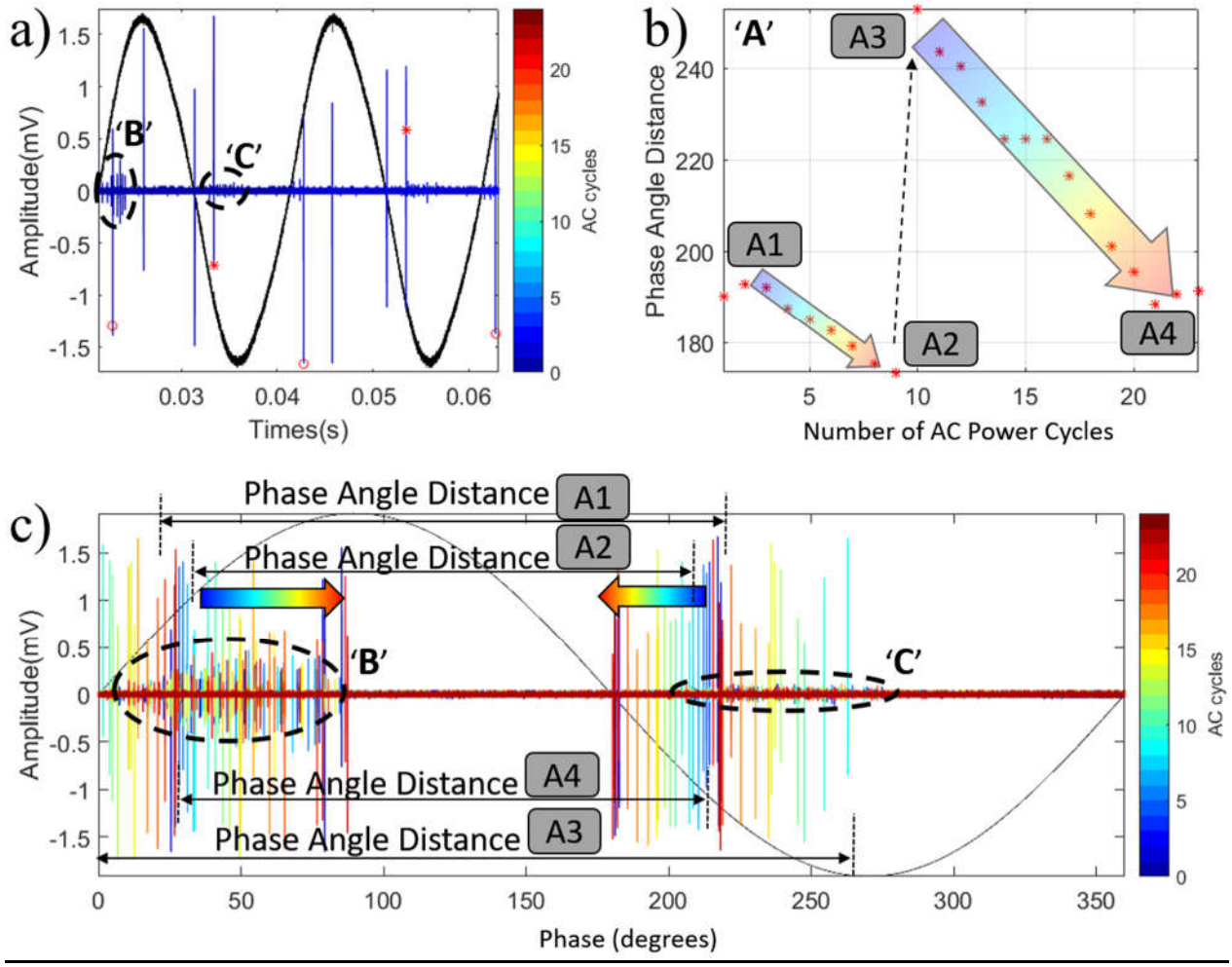

Figure 7.11 PDs from multiple PD sources consisting of internal discharge and surface discharge at 8 kV: (a) detailed PD signals appearance only for two AC power cycles ('B' and 'C' from surface discharge source); (b) phase angle distance for sequential propagating PD signals in group 'A' in the positive and negative AC cycles; and (c) SPPD featured diagram showing collective appearance patterns from the multiple PD sources.

7.4 SPPD Analysis of a Field Transformer

This section presents SPPD analysis results from a Current Transformer (CT), 145 kV, 10 A. The transformer was powered by a PD-free generator and tested using the inductive PD measurement system depicted in Figure 7.1.

During the PD measurement of the transformer, PD signals started to appear at 50 kV. The applying voltage was then raised to 60 kV to maintain the PD activity. The amplitudes of the PD impulses at 60 kV became higher than those at inception, but the phase locations of them were similar to each other. The results and analysis, presented in Figure 7.12 are based on the data obtained at 60 kV.

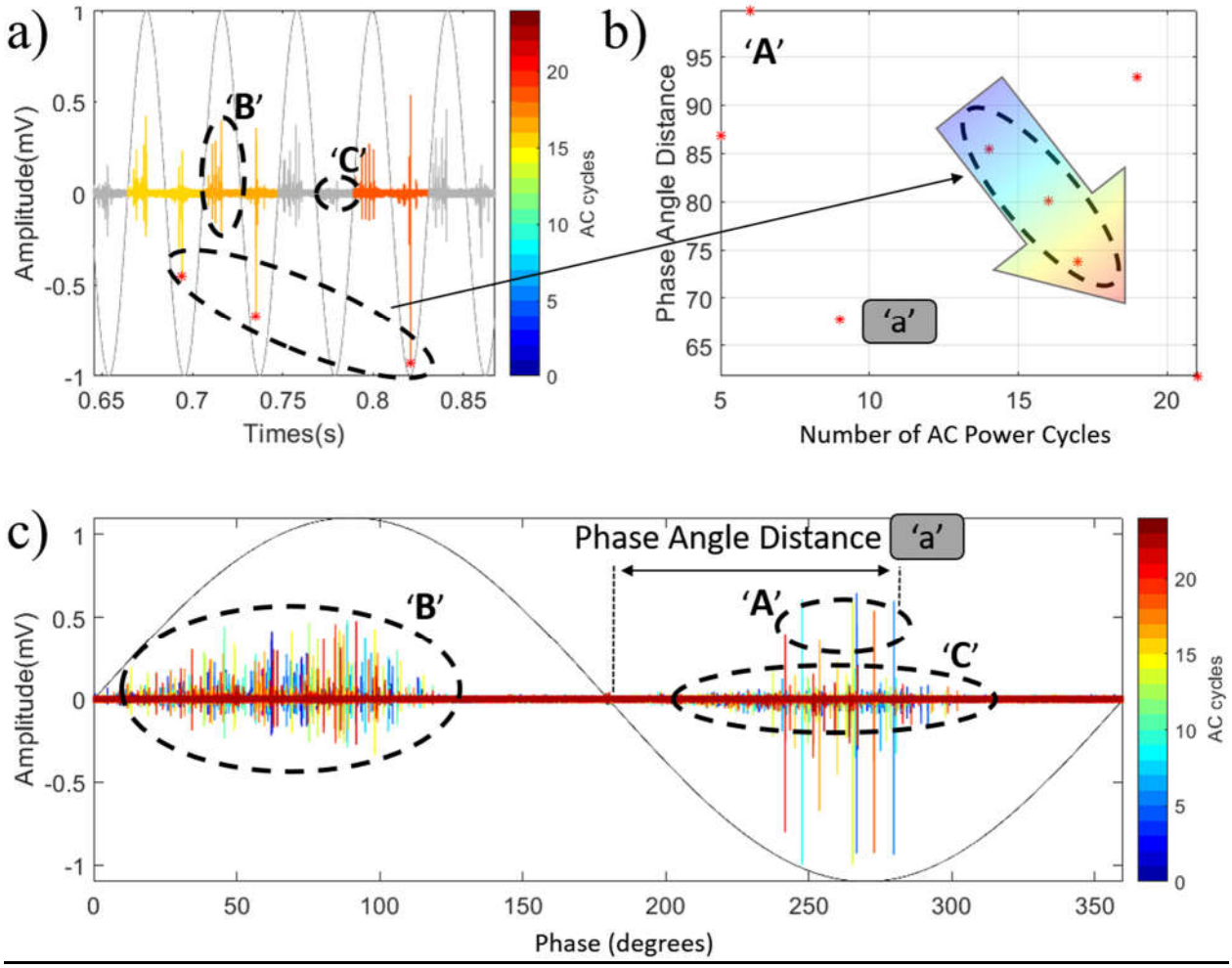

Figure 7.12 PD activity at 60 kV on a field transformer. Sequential propagating PD activity (in 'A' group) and corona type PD (in 'B' and 'C' groups) occur at a time. (a) detailed PD signals appear only for five AC power cycles; (b) phase angle distance for sequential propagating PD signals in group 'A' between negative cycle PD impulses and a mid-point of the AC cycle (180°); and (c) SPPD featured diagram showing collective appearance patterns from data of the field transformer.

As shown in Figure 7.12, three groups of PD impulses were identified by SPPD. These include a sparking type of PD impulse (group 'A') and two corona types of PD impulse (group 'B' and group 'C').

PD impulses in group 'A' have an intermittent appearance in the AC cycle as shown in Figure 7.12(a). Figure 7.12(b) shows a phase angle distance between 180° and PD impulses at the negative cycle of group 'A' since there is only a single impulse per AC cycle.

PD impulses in group ‘A’ do not exhibit a consistent propagation activity throughout all 25 AC cycles, which are different from those in the experimental PD test models. However, amongst the group of impulses, several PD impulses (marked as dashed circles in Figure 7.12(a) and 7.12(b)) move towards the left hand side, causing reduction of the phase angle distance. Thus, the PD impulses in group ‘A’ can be considered induced from an insulation defect causing sparking type PD signals.

The PDs in group ‘B’ and ‘C’ show a corona type of PDs (refer to Section 7.3) which may be due to a discharge in air or a bubble in the oil.

7.5 Summary

In Chapter 6, a transient strength based PD signal extraction method was demonstrated. In this chapter, PD signal analysis was discussed to decide the types of insulation defects and to separate PD signals from different insulation defects. For the purpose, the SPPD analysis method was considered and discussed. The proposed method shows the capability of providing a supportive means to the PRPD method by investigating the sequential propagation characteristics of PD impulses per AC cycle. The SPPD method is focused on the instantaneous feature of a PD signal’s activity whereas PRPD observes the overall picture of PD activities in an AC cycle. This chapter demonstrates that SPPD can be useful and a complementary technical method to the existing PRPD in distinguishing and separating PD impulses originating from different types of discharge sources. To verify the propagating feature of PD signals, SPPD was applied to analyse PD signals acquired from a HFCT-based inductive PD measurement system.

Following inductive PD signal measurement using HFCT, transient-strength based PD signals extraction (demonstrated in Chapter 6) and PD signal analysis using SPPD (demonstrated in Chapter 7), the PD source needs to be located for planning any repair work. In Chapter 8, PD source localisation will be discussed using a vibration sensor for signal measurement and a spatial intersectional method for visualisation.

Chap 8. An Improved Spatial Intersectional Method for Partial Discharge (PD) Source Localisation in a Power Transformer

Contribution of the Chapter

In Chapter 6 and Chapter 7, Partial Discharge (PD) signal extraction using the transient strength of the PD signal and PD source separation and identification using PD signal's sequential propagating property have been presented, respectively. This chapter presents a PD source localisation method using an Acoustic Emission (AE) sensor measurement.

In this chapter, an improved spatial intersectional method is proposed for an effective PD source localisation in a power transformer. To understand the impacts of multiple possible propagation paths of acoustic signals (induced by PD activity) on PD source localisation, the Time of Arrivals (TOAs) of acoustic signals travelling along different paths inside a transformer tank are investigated. Especially, the Savitzky-Golay filter is implemented to determine the TOAs from a number of AE sensor measurements. Based on the acquired TOAs, a three-dimensional (3D) spatial intersectional diagram is constructed. The proposed method can determine the location of a PD source inside a transformer tank. The proposed method is tested on a transformer using three AE sensors and a High Frequency Current Transducer (HFCT).

This chapter has been reproduced from the following paper:

J. Seo, H. Ma and Tapan K. Saha, "An Improved Spatial Intersectional Method for Partial Discharge (PD) Source Localization in Power Transformer," In the Proceedings of the 12th International Conference on the Properties and Applications of Dielectric Materials (ICPADM), 20th - 24th May, 2018, Xi'an, China.

8.1 Introduction

To determine the accurate location of a PD source inside a transformer, a certain number of AE sensors are required [164 - 165]. Each AE sensor is mounted on a known position of a transformer's tank to measure the elapsed travel time of the sound wave (i.e., acoustic signal generated by PD activity) from the PD source to the AE sensors. The elapsed travel time of acoustic signal is known as the TOA, which can be used to calculate the travel distance of an acoustic signal between the PD source and the AE sensor given that the travel velocity of ultrasonic waves in insulation oil or/and a metal tank is known.

However, it is still challenging to coordinate the number of AE sensors for AE signal measurement. The difficulties include extracting acoustic signal from noise, computing the TOAs from the extracted acoustic signal and finally deciding the location of the PD source. To deal with the issues, an improved spatial intersectional visualisation method and a novel signal processing method are developed. An acoustic signal processing method, the Savitzky-Golay filter, is implemented to extract acoustic signals and determine the corresponding TOAs. After the determination of the TOAs, a 3D spatial intersectional diagram is constructed to visualise a possible PD source location within a transformer tank.

In an AE sensor-based PD source localisation, a trigger signal is required as well for stamping the event time of any PD activity, which is essential for computing TOAs of acoustic signals. Thus, a HFCT clamped on the ground cable of a transformer is adopted. The HFCT can be used to decide the time instance at which the electromagnetic PD signal was generated. It can provide an instantaneous time stamp of PD activity since electromagnetic signal travels much faster than an AE signal in insulation oil, windings and the tank. As such, the electromagnetic PD signal captured by a HFCT can be used as a trigger signal to calculate the TOA of acoustic signal.

The obtained acoustic signals consist of clusters of oscillatory damping curves. This introduces difficulties in identifying the exact time instance of an acoustic signal arriving at an AE sensor. Furthermore, the obtained acoustic signal normally has interference from environmental noise. The above two issues pose difficulties in deciding TOA. To address the issues, the Savitzky-Golay filter is adopted. The filter has the unique merit of not causing a time gap between original signal (input) and filtered signal (output). Note that any latency in time for processing an acoustic signal can result in inaccurate TOAs. The proposed Savitzky-Golay filter provides a significant benefit in identifying the TOA of an acoustic signal at an AE sensor.

AE signals (sound waves) generated by PD events may propagate through a number of different travel paths before reaching an AE sensor. The waveform of an acoustic signal is complex in nature

because it may be superimposed with other metamorphosed waveforms due to reflection, refraction, attenuation, diffraction due to different materials and the complicated structure inside a transformer. Additionally, the propagation velocity of acoustic signals in oil can also be influenced by oil conditions of temperature, type and quality inside a transformer tank. To investigate the effect of various propagating paths of acoustic emission signal inside a transformer tank, a computer aided simulation was implemented. It reviews the condition of the latest TOA and the earliest TOA depending on various incident angles of acoustic signal projecting onto the transformer's metal tank from a propagation in oil. Finally, a tangible 3D spatial intersectional diagram is constructed to visualise the possible area in which the PD source may exist.

This chapter is organised as follows. The principle of PD source localisation in a transformer is presented in Section 8.2. A numeric study of sound wave propagation inside a transformer is presented in Section 8.3. In Section 8.4, a case study localising PD source in a transformer is presented. The results from Section 8.2 and Section 8.3 are used in the case study. Section 8.5 concludes this chapter.

8.2 Principles of PD Source Localisation in a Transformer

An AE measurement method can be used to locate a PD source by determining the TOAs of an acoustic signal from a PD source to a number of AE sensors, referred to as acoustic wave propagation velocity. To decide the TOAs, a time instance of a PD event can be detected by using PD signal detector (e.g. HFCT). The TOAs on each AE sensor can be obtained by subtracting the vibration signal's arrival time at AE sensors with a reference time from the PD sensor (HFCT). The acoustic signal travel distance from a PD source to an AE sensor can be calculated as follows [128]:

$$distance(m) = velocity(m/s) \times travel\ time(s) \tag{8.1}$$

The travel time of an acoustic signal denotes the elapsed time that an acoustic signal takes to arrive at an AE sensor from a PD source. However, a number of different sound wave propagation paths can exist for an acoustic signal travelling from a PD source to an AE sensor as shown in Figure 8.1(a) [128]. The acoustic signal at an AE sensor is complex in nature. It is a result of superposition of multiple acoustic sound waves from different propagation paths and metamorphosed waves due to reflection, refraction, attenuation, diffraction in different materials. The complicated winding structure and other constructions inside a transformer tank also impose challenges in acoustic signal measurement for PD source localisation.

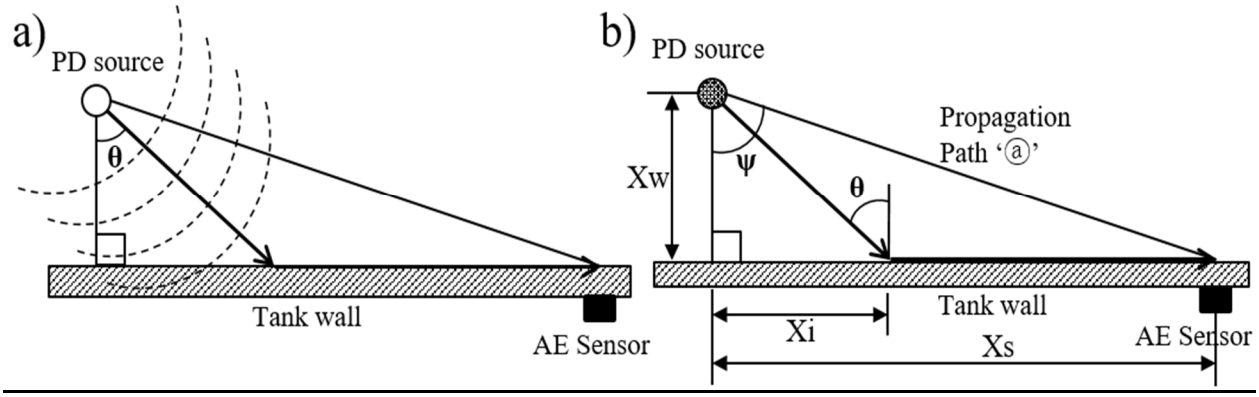

Figure 8.1 (a) Radial acoustic wave propagation patterns; (b) various parameters characterising acoustic wave propagation paths [128].

An acoustic wave originating from a PD source has an omnidirectional or radial propagating property in insulation oil at a speed of v_{oil} and after reaching the transformer's tank wall, it propagates along the metal surface of a transformer tank at a speed of v_{metal}. Note that an acoustic wave travelling through a metal surface is faster than in insulation oil. As such, the shortest path (from a PD source to an AE sensor, path ⓐ in Figure 8.1(b) cannot always guarantee the fastest travel path, which takes the least time for acoustic wave travelling from the PD source to the AE sensor. This will be investigated further in Section 8.3.

Additionally, the propagation speed of an acoustic signal in insulation oil is influenced by temperature and oil viscosity [130]. The carrying frequency of an acoustic signal and the types of gas curtain on top of insulation oil inside a transformer tank can also be factors affecting the propagation speed of an acoustic signal [130]. The ultrasonic wave propagating velocities by oil temperatures in a transformer are shown in Table 8.1 [130].

Table 8.1. Velocity of sound in transformer oil versus temperature [130]

	Oil Temperature (℃)	Propagating Velocity (m/s)
1	50	1300
2	80	1200
3	110	1100

The total travel time of an acoustic signal in combined paths (oil and metal) to an AE sensor can be computed as:

$$t = \frac{\sqrt{Xi^2+Xw^2}}{v_{oil}} + \frac{Xs-Xi}{v_{metal}} \tag{8.2}$$

where *Xw* is a perpendicular distance when an acoustic signal travels from a PD source in insulation oil to a tank's wall as the shortest path, (*Xs – Xi*) is the distance when an acoustic wave only travels through a metal surface (i.e., transformer tank). If *Xi* closes to 'zero' and *Xs* ≫ *Xw*, the acoustic wave can be assumed only to travel along the metal surface (transformer tank) and the elapsed time can be expressed as:

$$t = \frac{Xs}{v_{metal}} \tag{8.3}$$

For the direct path, in which the acoustic wave travels only through insulation oil before reaching an AE sensor, the elapsed wave travel time can be stated as:

$$t = \frac{\sqrt{Xi^2+Xw^2}}{v_{oil}} \tag{8.4}$$

In the above case, an acoustic signal travels a considerable distance '*Xw*' before reaching a transformer's tank wall. Simulation results will be demonstrated in Section 8.3, to show that an acoustic wave travel path in direct and shortest travel distance (travelling only through insulation oil) may take longer time compared to other possible wave propagation paths. This is because wave propagation velocity in oil is slower than that in metal.

The earliest TOA can be achieved when the sound wave strikes a metal tank with a critical incident angle. The critical incident angle (α) can be computed as:

$$\alpha = \sin^{-1}\left(\frac{v_{oil}}{v_{metal}}\right) \tag{8.5}$$

The corresponding wave travel time can be obtained as [129]:

$$t = \frac{Xw}{v_{oil}\cos\alpha} + \frac{Xs-Xw\tan\alpha}{v_{metal}} \tag{8.6}$$

The location of a PD source can be determined by using the sound waves' TOAs (T_i), a wave propagation velocity (v) in a medium and the locations of AE sensors (x_i, y_i, z_i) on a transformer's tank as [8.1] and it can be depicted as shown in Figure 8.2.

$$\begin{aligned}
(\mathrm{x}-x_{s1})^2+(\mathrm{y}-y_{s1})^2+(\mathrm{z}-z_{s1})^2 &= (\mathrm{v}\cdot T_1)^2 \\
(\mathrm{x}-x_{s2})^2+(\mathrm{y}-y_{s2})^2+(\mathrm{z}-z_{s2})^2 &= (\mathrm{v}\cdot T_2)^2 \\
(\mathrm{x}-x_{s3})^2+(\mathrm{y}-y_{s3})^2+(\mathrm{z}-z_{s3})^2 &= (\mathrm{v}\cdot T_3)^2
\end{aligned} \tag{8.7}$$

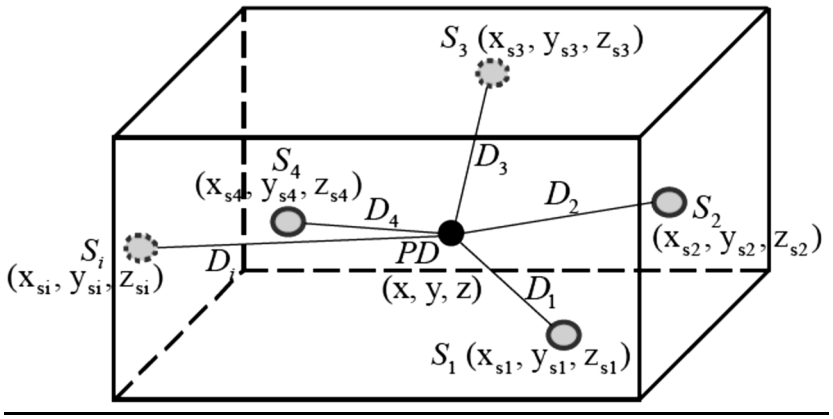

Figure 8.2 PD source localisation in a three-dimensional test object [128].

8.3 Numeric Study of Sound Wave Propagation inside a Transformer

A numeric study was conducted to investigate acoustic signal (sound wave) propagation paths inside a transformer tank, including acoustic signal's travel time and distance with varying incident angles, at which the acoustic signal enters the metal enclosure of a transformer tank. The results of the simulation are shown in Figure 8.3. A transformer tank was modelled as a 3D cubic (two meters on each side) as shown in Figure 8.3(a). Three AE sensors were placed on the middle of respective planes in X-Y, Y-Z and Z-X of the tank. The location of the PD source was randomly decided inside the cube (depicted as a red dot in Figure 8.3(a)). The cube is filled with insulation oil and enclosed within metal material. The temperature of the test was kept constant.

Globally, two extreme propagation paths of acoustic waves travelling from a PD source to an AE sensor are considered: (1) the shortest path (short-dotted lines in Figure 8.3(a)), in which acoustic waves travel only through oil; and (2) the longest path (long-dashed lines in Figure 8.3(a)). The later path consists of two stages; the acoustic wave travels firstly in a perpendicular direction through oil towards a metal wall of the cube and it continues to travel through the tank wall to an AE sensor. In the simulation, acoustic wave propagation paths are altered by varying the incident angles of the acoustic wave to the metal tank from 90° to a possible minimum angle (refer to Figure 8.1(b), 'θ' in the figure). From the results of the simulation, various combinations of travel distance and travel time of acoustic waves are mapped with corresponding acoustic wave propagation paths and incident angles.

The simulation results from Figure 8.3(a) are plotted in Figure 8.3(b). The results demonstrate the travel time and distance of acoustic wave at three sensors (from sensor #1 to #3) according to the acoustic waves' propagation paths. The results include three different propagation paths: (1) the shortest path going through only oil (marked as 'Oil'); (2) the longest path – the perpendicular incident

angle onto the metal tank (marked as 'Metal'); and (3) as the fastest path with the Critical Incident Angle (marked as 'CIA').

Note that the least (or fastest) travel time can be attained when the acoustic wave travels with critical incident angle onto the metal tank. On the other hand, the longest time taken occurs when acoustic wave travels only through oil, though it travels the shortest distance. Moreover, the result shows that the longest travel path (marked as 'Metal') takes less time than the shortest travel path except at sensor #2. This is significant for AE sensors #1 and #3. The above results are due to the fact that the acoustic wave travel time is decided not only by travel distance but also by acoustic wave propagation speed (material type and conditions).

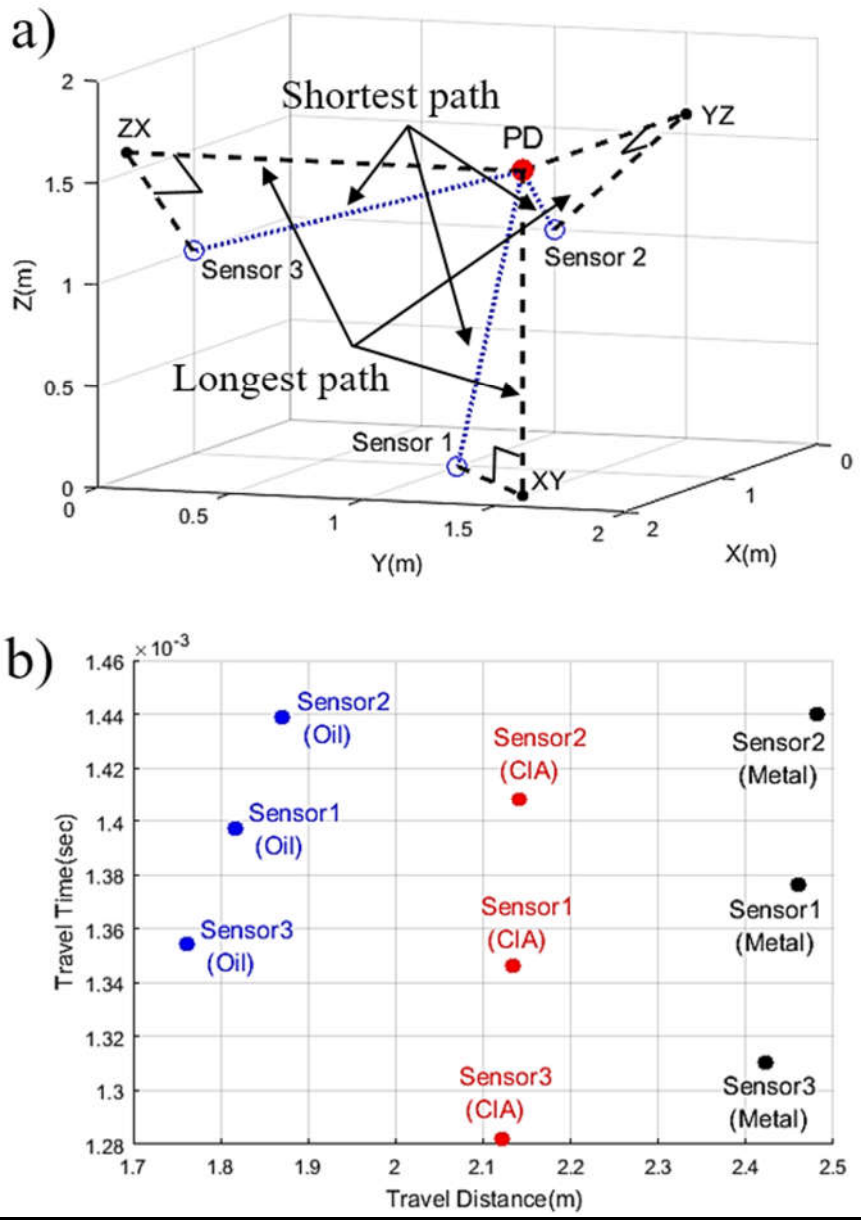

Figure 8.3 Simulation results for three different propagation paths: (a) Acoustic wave propagation paths from a PD source to AE sensors in a simulated tank; (b) simulation results of sound wave travel time and travel distance with different incident angles [167].

'Oil' = the shortest path going through only oil; 'Metal' = the longest path with the perpendicular incident angle onto the metal tank; 'CIA' = the fastest path with the Critical Incident Angle

The relationships between acoustic wave incident angle, travel time and travel distance are depicted in Figure 8.4. The configuration of the AE sensors and cubic dimension is the same as described in Figure 8.3. The relationships prove that the fastest acoustic wave travel path is obtained when it strikes a metal tank at a critical incident angle. For example, for AE sensor #1, acoustic wave travels the fastest, taking 1.35 ms, travelling 2.12 metre and entering at a critical incident angle of 77.3°. Another observation from the results is that the travel time of the acoustic wave (e.g., at 1.37 ms) is the same though the acoustic wave travels at different propagation distances (e.g., 1.9 metre and 2.4 metre). For the obtained critical incident angles at different AE sensors, they are the same due to the constant acoustic wave propagating velocities in oil and metal (refer to Equation 8.5).

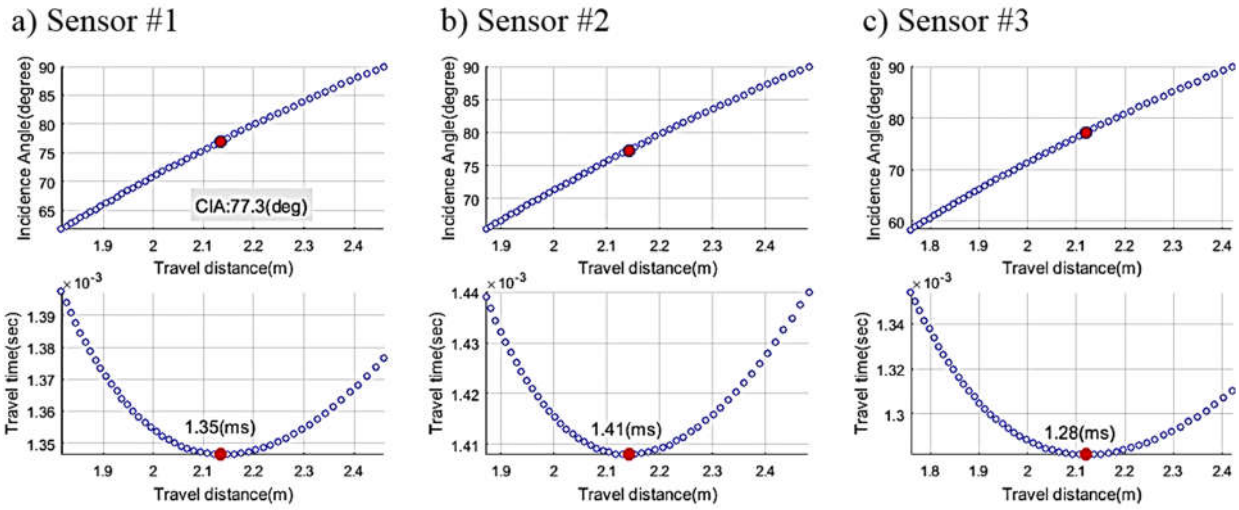

Figure 8.4 Incident angle tracking simulation for investigating the relationship between acoustic wave incident angle, travel time and travel distance: (1) between incident angle and wave travel distance (in top column of the figure); and (2) between wave travel time and distance (in bottom column of the figure) [166].

From the above simulation study, acoustic wave velocity, incident angle and propagation paths are found to be the critical factors affecting PD source localisation. These factors should be carefully considered to minimise any errors in PD source localisation.

8.4 Case Study of PD Localisation in a Transformer

The results presented in the previous sections were verified on a distribution transformer tank with winding removed. The transformer tank is 78 cm along its *X* axis, 36.2 cm along its *Y* axis and height of 119.4 cm (Figure 8.5). AE sensors used in the measurement have an operating frequency range of 50 to 400 kHz. The output signals from the AE sensors are amplified by 60 dB with external pre-

amplifiers. The output signals from three AE sensors and HFCT are integrated with a data acquisition (DAQ) system.

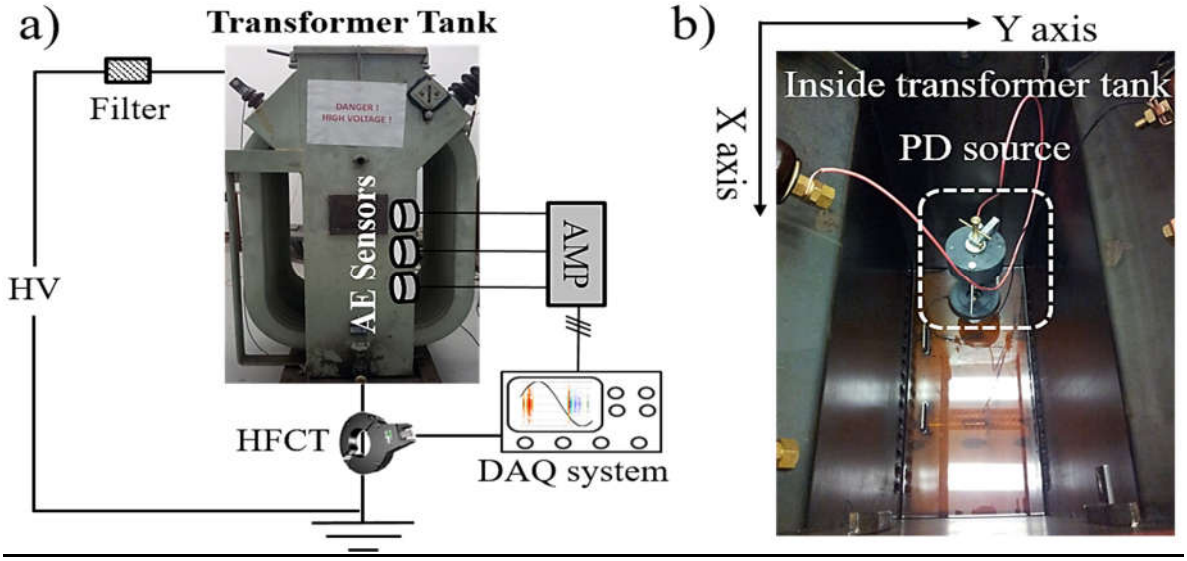

Figure 8.5 (a) AE sensor and HFCT measurement configuration for PD source localisation; (b) experimental PD source model placed inside a transformer tank [167].

A PD experimental model of internal discharge was placed into the transformer tank as a PD source as shown in Figure 8.5(b). It is located inside the tank at *X* axis (7.8 - 15.6 cm) and *Y* axis (14.48 - 21.72 cm). The model was placed 30 cm from the bottom of the transformer tank i.e., *Z* axis (30 cm). Three AE sensors are installed at the centre point of each side of tank (on X side (S2) and both Y sides (S1 and S3) at the same height as the PD source. The experimental PD model was energised to 15 kV for PD signal generation. In the experiment, acoustic signals were acquired by the AE sensors and the electrical PD signal was acquired by a HFCT as shown in Figure 8.5(a). Figure 8.6(a) is a magnification of the acquired PD signal.

A full cycle of the acoustic signal (in grey) acquired by the AE sensor '1' is shown in Figure 8.6(b). Figure 8.6(b) also shows the result of the acoustic signal processed by the Savitzky-Golay filter. Figure 8.6(c) shows the processed acoustic signals acquired from all three AE sensors. It can be seen that the processed acoustic signals clearly depict the original features of acoustic signals without a time delay and distortion.

In reality, for locating PD source, accurate PD location cannot be obtained due to various uncertainties in acoustic signal propagation such as complex propagation paths, inaccurate wave propagation velocity and measurement errors. As a practical approach, indicating a possible area inside a transformer tank satisfies the goal of the measurement.

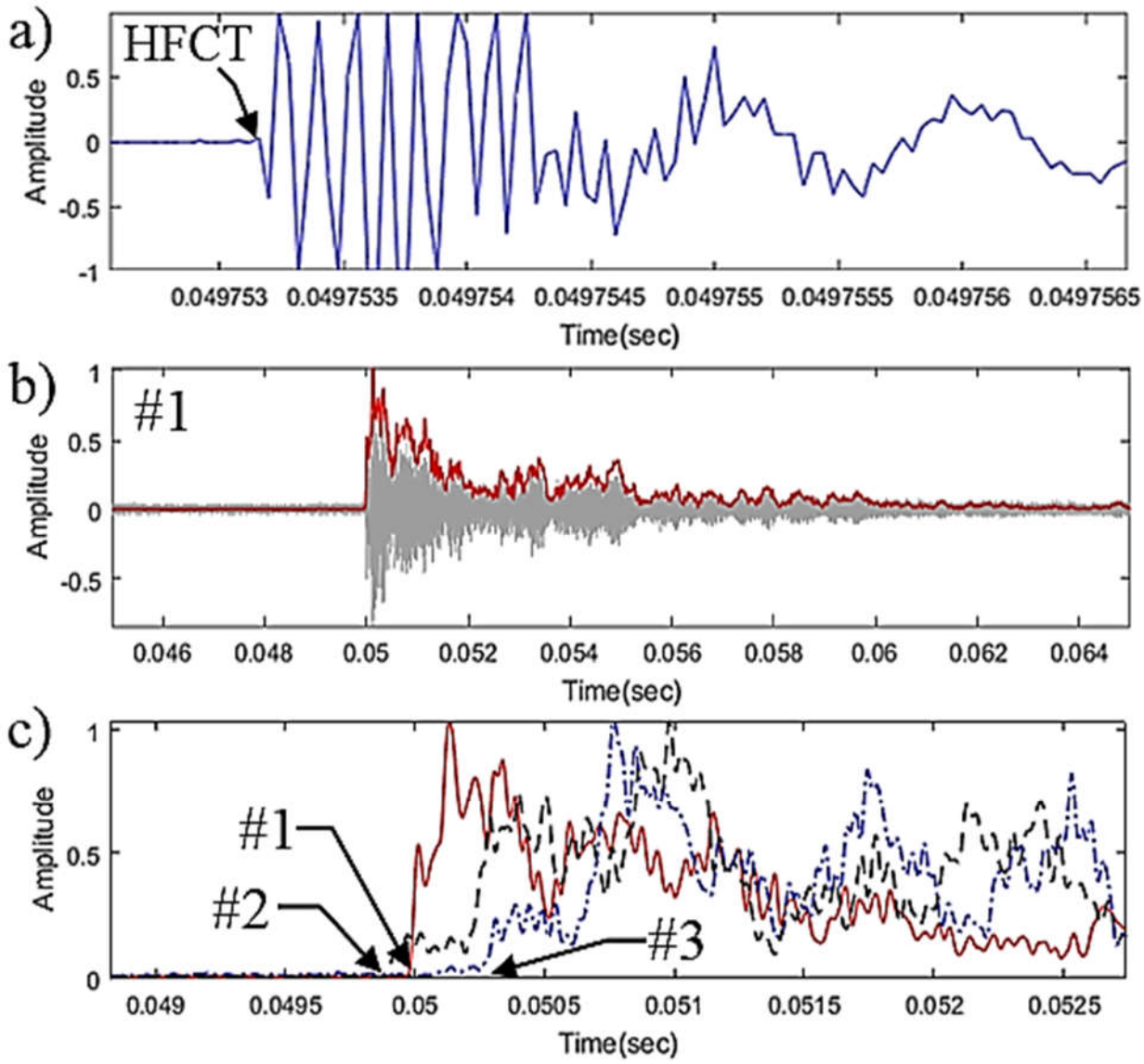

Figure 8.6 (a) PD signals acquired by HFCT; (b) acoustic signal acquired by AE sensor #1 (in grey) and processed acoustic signal by Savitzky-Golay filter (in red); and (c) processed acoustic signals for all three AE sensors [167].

Figure 8.7 shows the possible area of PD source constructed by a spatial intersectional method using the results shown Figure 8.6. The identified PD source is located at the X axis (14 - 22 cm) and Y axis (14 - 21 cm). There is no information regarding Z axis location because of the absence of an AE sensor on Z-X plane. The result shows the proposed method successfully locates the PD source inside the transformer tank.

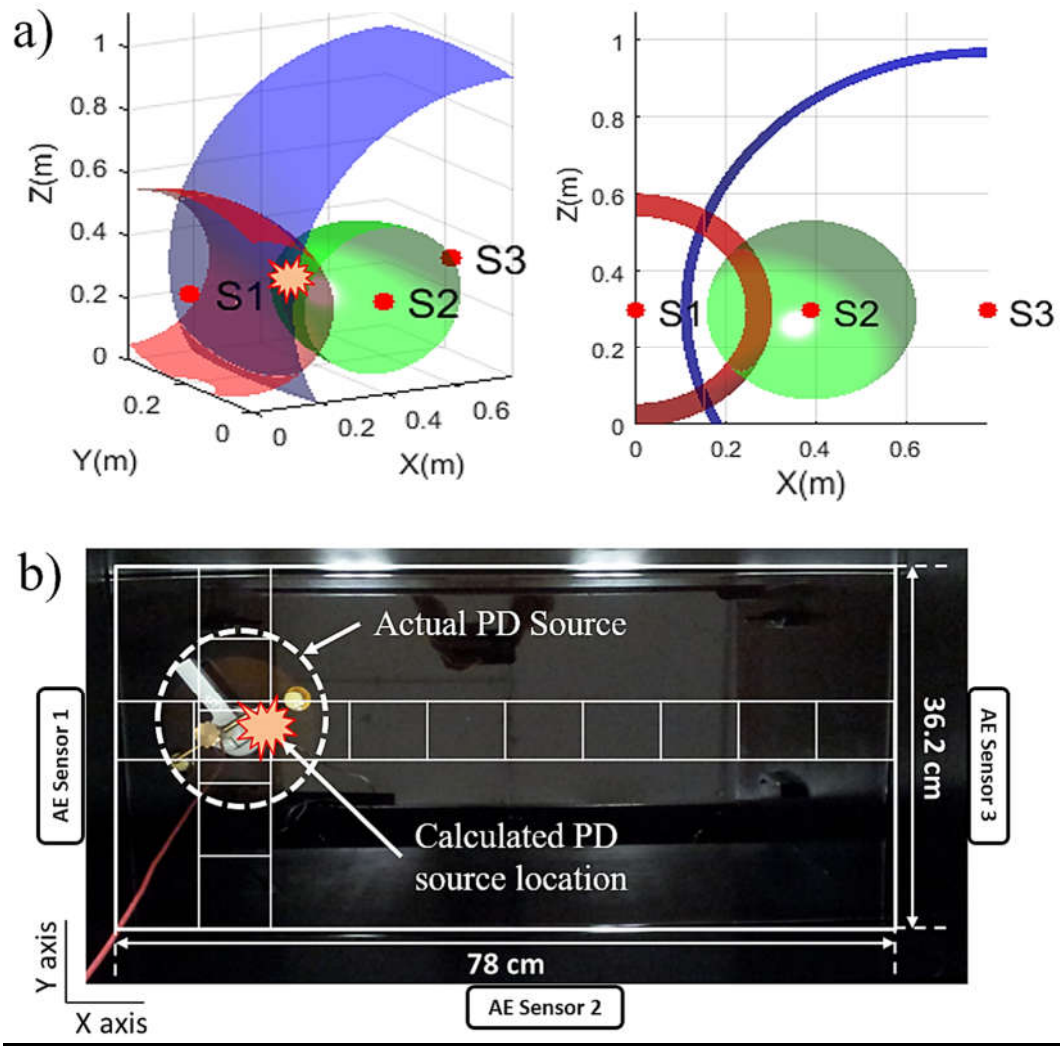

Figure 8.7 (a) PD source localisation by using spatial intersectional representation; (b) PD localisation test result on X-Y plane [167].

8.5 Summary

A PD source localisation method using vibration sensor and visualisation method was discussed in this chapter after investigating the transient strength-based PD signal extraction method in Chapter 6 and the SPPD-based PD signals analysis method to distinguish and separate PD impulses originated from different types of discharge sources in Chapter 7.

This chapter demonstrated that PD source can be localised by calculating TOAs using vibration signal measurement and visualised by a spatial intersectional method. The proposed method was successfully applied to locate a PD source inside a transformer tank. The complex and complicated vibration signals were processed using the previously designed Savitzky-Golay filter, which is proven to be effective in vibration signal extraction and TOA calculation.

Additionally, the effect of various propagating paths of vibration signal to calculation of TOAs was investigated through mathematical simulation. It was found that the shortest TOA can be obtained

when the vibration signal reaches the transformer's tank with an incipient angle decided by permittivity of oil and metal.

Throughout Chapters 6, 7 and 8, important tasks for implementing PD measurement were demonstrated for main winding insulation condition monitoring. Each chapter contributed to develop PD signal extraction using transient strength, PD signal analysis using SPPD and PD source localisation using a spatial intersectional method. The developed methods were verified by online and offline measurement.

In the next Chapter 9, conclusions and future works will be drawn from the two parts of works on OLTC's mechanical condition monitoring (Chapters 3 to 5) and the main winding's insulation condition monitoring (Chapters 6 to 8).

Chap 9. Conclusions and Future Work

9.1 Conclusions

This thesis has been devoted to developing an online sensor-based measurement system and a suite of signal processing algorithms for condition monitoring and diagnosis of a power transformer's OLTC and main winding. The candidate has developed an innovative vibration signal interpretation system and waveform-based vibration comparison method for OLTC condition monitoring. Additionally, a practical and effective PD measurement system has been developed for main winding condition monitoring.

In the first part of this thesis (Chapters 3 to 5), OLTC's mechanical condition monitoring methods were explored. The author has developed a number of innovative and online OLTC mechanical condition monitoring methods:

(1) Vibration interpretation scheme capable of correlating a series of vibration signals generated by OLTC's mechanical operations with corresponding operation of the OLTC's switches; and

(2) Waveform based vibration signal comparison method enabling automated mechanical condition change evaluation.

To interpret the vibration signals of an OLTC, existing methods require complex and time consuming manual manipulation to simulate each fault as well as transformer service interruption. However, the developed novel vibration signal interpretation method could be implemented without complicated manipulation and transformer service interruption. OLTC's vibration signal could be interpreted by analysing arcing and vibration signals obtained from the developed novel joint arcing and vibration signal measurement system. By integrating arcing signals caused by switches' closing events, the mechanical sources of vibration signals could be identified successfully without the time-consuming manual approach.

Additionally, to properly extract important features of arcing signal and vibration signal generated at the same time, advanced signal processing techniques have been developed using the Savitzky-Golay filter. The method is capable of extracting important features of arcing and vibration signals located at different frequencies without causing a time delay between them regardless of the degree of filtration. The signal processing method could improve the accuracy of vibration signal interpretation by maintaining time alignment between the two signals.

To identify a mechanical condition change of OLTC, the candidate has also developed a waveform-based vibration signal comparison method. It could be used for an automated condition monitoring

system that does not require identification of the parameters like event time, amplitude and number of peaks. The waveform-based vibration signal comparison method has shown good sensitivity in identifying a mechanical condition change of OLTC throughout online and offline tests.

In the second part of this thesis (Chapters 6 to 8), PD measurement-based main winding condition monitoring methods were investigated. For establishing a comprehensive online PD measurement system, the candidate has developed a number of important procedures:

(1) Online PD signal measurement system using HFCT;
(2) Transient strength-based PD signal extraction method capable of extracting even low amplitude PD signals;
(3) SPPD analysis method improving PD signal separation effectively; and
(4) Spatial intersectional PD source localisation tool that localises PD source practically.

This thesis has presented effective PD signal extraction and analysis methods to deal with noise immersed PD signals corrupted by an inductive sensor. The developed transient strength-based PD extraction method has demonstrated an efficient, intuitive and fast processing algorithm, which could be used for an online PD monitoring system. Additionally, even the low amplitude of PD signals could be extracted as the method adopts a genuine feature of a PD signal, namely the transient strength of PD signals.

For analysing PD signals effectively, the SPPD analysis method considers the instantaneous propagating feature (moving direction and density) of PD impulses per AC power cycle. The method is capable of distinguishing PD signals from different sources, construction and the types of PD signals sensitively by observing the PD signal's propagating patterns. The method could improve the accuracy of PD analysis with valuable analysis information along with the PRPD analysis method.

The location of a PD source could be localised using an online vibration signal measurement, improved signal processing techniques and a visualisation tool. Especially, it has been found that the critical incident angle of an acoustic signal to a metal tank is important in deciding the shortest travelling time of the wave, which is different from the shortest spatial distance. The consideration of critical angle of an acoustic wave has improved the accuracy of PD source localisation. The previously designed Savitzky-Golay filters could extract acoustic signals of interest and effectively determine the exact TOAs without compromising the accuracy of the time information. Finally, a PD source could be visualised using the developed spatial intersectional PD source localisation.

Detailed description on each chapters of the thesis

Following Chapter 1 introduction, a comprehensive literature review of the various electrical, mechanical and chemical techniques for monitoring and diagnosing problems arising in power transformers has been presented in Chapter 2. Starting with a brief introduction of the construction and operation of a transformer's OLTC and main winding, various condition monitoring methods for each component have been discussed and reviewed. Among them, vibration signal measurement-based OLTC condition monitoring and PD measurement based main winding condition monitoring have been adopted owing to their many benefits, such as, online condition monitoring, competitive sensitivity and the wide range of condition monitoring. However, a number of key challenges were found for successful implementation, such as: (1) lack of a reliable and applicable online vibration (for OLTC) and PD signal (for main winding) measurement system; (2) difficulty with developing effective signal processing methods for each measured signals; and (3) weak interpretation scheme to assess the condition of OLTCs and main winding.

An OLTC is used to regulate the output voltage of a power transformer by changing turns-ratio of the windings mechanically. An OLTC may encounter a number of mechanical issues during its service. These include misalignments between switches and contacts, spring looseness, contaminants on switches and contacts, motor drive system's malfunction and defects in gears and cams. These issues may eventually lead to a malfunction or failure of the OLTC. To provide an online mechanical condition monitoring of an OLTC, this thesis has developed a vibration signal measurement-based condition monitoring system (both hardware and software), which has been successfully applied to two unique types of OLTCs in a substation environment. It has been demonstrated that this system can effectively extract informative characteristics from the measured vibration signals. These characteristics have been correlated to actual events of an OLTC's operations and subsequently used to reveal the mechanical condition change of the OLTC.

Given that OLTCs have complicated configurations and normally lack historic vibration signal measurement data, a novel joint vibration and arcing signal measurement system for OLTC condition monitoring has been developed in this thesis in Chapter 3. It has been demonstrated that by innovatively integrating arcing signal measurement with vibration signal measurement, the joint measurement method is capable of identifying the closing and opening events of an OLTC's switches and subsequently revealing the event sequence of an OLTC's operation. Field experiments have shown that the implementation of the joint measurement system is straightforward and paves the way for online condition assessment of an OLTC.

To jointly analyse the measured vibration and arcing signals for correlating the two different types of signals to mechanical events of an OLTC's operation, it is critical to extract information from both

a vibration signal and an arcing signal in a synchronised manner without any distortions. In Chapter 4 of this thesis, Savitzky-Golay filters have been developed to process and analyse signals acquired from the joint vibration and arcing measurement system installed on two different types of OLTCs. It has been demonstrated that, with the merits of easy implementation and without causing any distortions in its outputs, the Savitzky-Golay filter can be used to extract the envelope curve of the vibration signal, to remove the noise signal in order to extract the arcing signal and to obtain phase information from the measured arcing signal.

The mechanical condition changes of an OLTC can be inferred from time stamps and amplitude of the measured vibration signal. In Chapter 5, a waveform-based vibration signal comparison method using the Savitzky-Golay filter and correlation coefficient has been developed. It has been verified that the waveform comparison method can evaluate the mechanical condition change of an OLTC with considerable sensitivity.

In this thesis, PD measurements have also been applied to monitor the insulation condition of the main winding of a power transformer. Several novel techniques have been developed to address three tasks of PD signal extraction, PD signal analysis and PD source localisation as described in Chapters 6, 7 and 8.

A differential PD signal extraction method has been developed in Chapter 6. Different from conventional methods, the proposed method considers the transient characteristics of measured signals and uses a quantile-based thresholding method to separate the measured signals of interest from noise. The applicability of the proposed method has been verified through case studies using datasets obtained from experimental PD test models in a laboratory and from in-service transformers at substations. It has been demonstrated that the proposed method outperformed a conventional method of wavelet transform in extracting PD signals and identifying the polarity direction of PD signals.

To complement conventional PRPD diagrams, a SPPD signal analysis method was developed in Chapter 7 to analyse PD signals and to recognise the types of PD sources (insulation defects) in a power transformer's insulation system. The SPPD analysis method explored the sequential propagation and occurrence characteristics of PD impulses by observing instantaneous PD activities. It has been demonstrated that the proposed SPPD method has an inherent capability of separating and recognising the types of PD sources, i.e., corona type and sparking type.

In Chapter 8, an improved spatial intersectional method was proposed for an effective PD source localisation in a power transformer. TOAs of acoustic signals travelling along different paths inside a transformer tank have been investigated. A Savitzky-Golay filter has been implemented to determine the TOAs from a number of AE sensor measurements. A 3D spatial intersectional diagram

has been constructed. It has been demonstrated that the proposed method can determine the location of a PD source inside a transformer tank using three AE sensors and a HFCT.

9.2 Future Work

This thesis has developed a number of novel and field applicable techniques to pave the way for reliable condition monitoring and diagnosis of a power transformer. However, as a power transformer is a complicated system, there are still many aspects that need exploration. A number of possible directions for future research works are recommended below.

As discussed in this thesis, OLTCs can encounter various types of faults. These may include motor drive system defects, spring looseness, misalignment of switches and contacts and coking on switches and contacts, etc. These faults can be identified using the measured vibration and arcing signals. Additionally, the arcing signal can also be used to reflect the condition of transition impedance. The amplitude of the arcing signals can be compared to see an impedance change of the component as before-and-after method. It is necessary to investigate the correlations between these OLTC's faults and the measured vibration and arcing signals. The investigation could suggest how the different types of OLTC mechanical faults can affect vibration and arcing signals. A database can then be constructed and used to train machine-learning algorithms to identify the fault type of an OLTC.

The ultimate aim of the online PD measurement of a transformer is to provide a means for automatic identification of the PD sources either inside the transformer's tank, i.e., establishing whether the PD signals are generated by voids/cavities in pressboard/insulation paper (internal discharge) or by protrusions (corona) or significant electric fields tangential to the surface of pressboard's surface (surface discharge) or by bubbles in the oil insulation (discharge in oil); or by drifting metal particles (discharge due to floating particles). In the past three decades, a variety of artificial intelligence (AI) techniques has been proposed for automatic PD source classification. Some representative algorithms include artificial neural networks (ANNs), Support Vector Machines (SVMs), clustering analysis and knowledge systems. However, it remains a challenging task for PD source identification when multiple PD sources co-exist in a transformer. The approaches reported in the literature for multiple PD source classification include the mixed Weibull model, an auto-correlation function, a time-frequency (TF) map and density-based spatial clustering and blind source separation.

The above approaches assume the PD impulses from different PD sources exhibit different waveforms. Thus, the characteristics of PD impulse waveforms are used in multiple PD source classification, which involves a two-step approach: (1) PD signals separation, i.e., the obtained PD impulses are transformed and then separated into different groups; and (2) PD source classification, i.e., the PD source associated to each individual group is identified. However, PD impulses originating

from different sources can be overlapped and merged together, which may pose difficulties in separating these PD impulses. Moreover, the waveform of PD impulses can be distorted and high frequency components can be attenuated before they reach the PD measurement system. This causes more ambiguity in separating PD signals. Furthermore, the clustering method for grouping PD impulses requires some prior knowledge regarding the PD source, which may not be available. The convergence of the clustering methods cannot always be guaranteed. Considering the above limitations of the separation-then-identification approach for multiple PD sources classification, further investigation is much needed.

To verify and refine the condition monitoring techniques and software algorithms developed in this thesis, more extensive onsite measurements need to be performed.

References

[1] Australian CIGRE Panel for Transformers, “Australian/New Zealand Transformer Reliability Survey,” Western Power Australia, 1996.

[2] A. Petersen and P. Austin, “Impact of recent transformer failures and fires: Australian and New Zealand experiences,” CIGRE, 2004.

[3] CIGRE Working Group A2.37, “Transformer reliability survey,” Brochure 642. Paris, France: CIGRE, 2015.

[4] J. Jagers and S. Tenbohlen, “Evaluation of transformer reliability data based on national and utility statistics,” presented at 16th Int. Symp. High Volt. Eng., Cape Town, South Africa, 2009.

[5] D. Martin, J. Marks and Tapan K. Saha, "Survey of Australian power transformer failures and retirements," in IEEE Electrical Insulation Magazine, vol. 33, no. 5, pp. 16-22, September-October 2017.

[6] IEC 60214, Tap-changers – Performance requirements, test methods and application guide.

[7] Dieter Dohnal, “On-load tap changers for power transformers”, Reinhausen.

[8] “On-load tap changers, type UZ,” ABB 1ZSE 5492-104 en, Rev. 9.

[9] “On-load tap changer VACUTAP VV operation instructions,” Reinhausen, 164/08 EN.

[10] J.J. Erbrink, E. Gulski, P.P. Seitz, R. Leich, “Advanced on-site diagnosis of transformer on-load tap changer”, IEEE International Symposium on Electrical Insulation, Vancouver, Canada, pp. 252-256, June 2008.

[11] IEEE Standard Requirements for Tap Changers," in IEEE Std C57.131-2012 (Revision of IEEE Std C57.131-1995), 2012.

[12] Reinhausen, “On-load tap changer VACUTAP VV Technical Data,” TD 203/04.

[13] T. Bengtsson, H. Kols, L. Martinsson, B.O. Stenestam, M. Foata, F. Leonard, C. Rajotte, J. Aubin, "Acoustic diagnosis of tap changers," CIGRE SC 12, 1996.

[14] H. U. Schellhase, R. G. Pollock, A. S. Rao, E. C. Korolenko, B. Ward, "Load tap changers: investigations of contacts, contact wear and contact coking," in Electrical Contacts, 2002. Proceedings of the Forty-Eighth IEEE Holm Conference, pp. 259-272, 2002.

[15] S. Schoft, J. Kindersberger, H. Löbl, “Joint resistance of busbar-joints with randomly rough surfaces”, Proceedings of the 21th International Conference on Electric Contact Phenomena, Zurich, Switzerland, pp. 230-237, September 2002.

[16] R. Holm, “Electric contacts: theory and application”, 4th edition, Springer Verlag, New York, 1967.

[17] K. Lemelson, “About the failure of closed heavy current contact pieces in insulating oil at high temperature”, IEEE transactions on parts, hybrids, and packaging, vol. Php-9, No.1, pp. 50-52, March 1973.
[18] W. M. S. C. Samarasinghe, D. Martin, H. Ma and Tapan K. Saha, "A review on influencing factors of sulphur corrosion and metal passivation in power transformers," 2017 Australasian Universities Power Engineering Conference (AUPEC), Melbourne, VIC, pp. 1-5, 2017.
[19] P. J. Hopkinson, “Electrical contacts for off-circuit tap changers for oil immersed transformers”, IEEE/PES Transformers Committee, DETC working group, October 2005.
[20] ANSI/IEEE C57.12.90-1987: American national standard / IEEE Standard Test Code for Liquid-Immersed Distribution, Power, and Regulating Transformers.
[21] IEC 60076-1: Power Transformers – Part 1: General.
[22] IEEE Std 4-1995, IEEE Standard Techniques for High-Voltage Testing.
[23] IEEE Std 62-1995: IEEE Guide for Diagnostic Field Testing of Electric Power Apparatus. Part 1: Oil Filled Power Transformers, Regulators, and Reactors.
[24] IEEE Std C57.140-2006: IEEE Guide for the Evaluation and Reconditioning of Liquid-Immersed Power Transformers.
[25] IEEE Std C57.131-1995: IEEE Standard Requirements for Load Tap Changers.
[26] “CPC 100”, Multifunctional Primary Test System for Substation Commissioning and Maintenance, Omicron.
[27] “MTO210 Transformer Ohmmeter”, Transformer Winding Resistance and Tap-changer Test Set, Megger.
[28] J. J. Erbrink, E. Gulski, J. J. Smit, P. P. Seitz, B. Quak, R. Leich, et al., "Diagnosis of Onload Tap Changer Contact Degradation by Dynamic Resistance Measurements," IEEE Transactions on Power Delivery, vol. 25, pp. 2121-2131, 2010.
[29] J. J. Erbrink, “Tap changer diagnostics on high voltage power transformers using dynamic resistance measurement”, Graduate thesis Delft University of Technology, Delft, the Netherlands, 2007.
[30] M. Landry, O. Turcotte, F. Brikci, “A complete strategy for conducting dynamic contact resistance measurements on HV circuit breakers,” IEEE Transactions on Power Delivery, vol. 23, No. 2, pp. 710-716, April 2008.
[31] Y. Cui, H. Ma and T. Saha, "Improvement of power transformer insulation diagnosis using oil characteristics data preprocessed by SMOTEBoost technique," in IEEE Transactions on Dielectrics and Electrical Insulation, vol. 21, no. 5, pp. 2363-2373, October 2014.
[32] CIGRE WG D1.32, "DGA in Non-Mineral Oils and Load Tap Changers and Improved DGA Diagnosis Criteria," 2010.

[33] M. Duval, "The duval triangle for load tap changers, non-mineral oils and low temperature faults in transformers," IEEE Electrical Insulation Magazine, vol. 24, pp. 22-29, 2008.
[34] M. Duval and A. DePablo, "Interpretation of gas-in-oil analysis using new IEC publication 60599 and IEC TC 10 databases," IEEE Electr. Insul. Mag., vol. 17, Issue 2, pp. 31-41, 2001.
[35] M. Duval, "A review of faults detectable by GAS-in-Oil analysis in transformers," IEEE Electrical Insulation Magazine, vol. 18, Issue 3, pp. 8-17, 2002.
[36] V. Sokolov, V. Mayakov, G. Kuchinsky, A. Golubev, "On-site partial discharge measurements in power transformers," Doble Conferences, 2000.
[37] L. E. Lundgaard, "Partial discharges in transformer insulation," Report of TF 15.01.04, CIGRE, Paris, 2000.
[38] B. Fallou, I. Davies, R. R. Rogers, E. H. Reynolds, F. Viale, A. Devaux, R. Fournie, J. Galand, P. Vuarchex, E. Dornenburg, "Application of physico-chemical methods of analysis to the study of deterioration in the insulation of electrical apparatus," CIGRE, Paris, pp. 15-07, 1970.
[39] E. Rivas, J. C. Burgos, J. C. Garcia-Prada, "Condition assessment of power OLTC by vibration analysis using wavelet transform," IEEE Transac tions on Power Delivery, vol. 24, pp. 687-694, April 2009.
[40] E. Rivas, J. C. Burgos, J. C. Garcia-Prada, "Vibration analysis using envelope wavelet for detecting faults in the OLTC tap selector," IEEE Transactions on Power Delivery, vol. 25, pp. 1629-1636, 2010.
[41] H. K. M. F. T. Bengtsson, F. Leonard, "Monitoring tap changer operations," CIGRE SC 12, 1998.
[42] P. L. L. Allard, M. Foata, S. Prajescu, C. Landry, C. Rajotte, "Vibro-acoustic diagnostic: contributing to an optimized On-Load Tap Changer (OLTC) maintenance strategy," CIGRE SC A2, 2010.
[43] P. Kang and D. Birtwhistle, "Condition monitoring of power transformer on-load tap-changers. Part 1: Automatic condition diagnostics," IEE Proceedings: Generation, Transmission and Distribution, vol. 148, pp. 301-306, 2001.
[44] P. Kang and D. Birtwhistle, "Condition monitoring of power transformer on-load tap-changers. II. Detection of ageing from vibration signatures," in IEE Proceedings - Generation, Transmission and Distribution, vol. 148, no. 4, pp. 307-311, July 2001.
[45] J. Seo, H. Ma and Tapan K. Saha, "Vibration measurement and signal processing for condition assessment of OLTC of transformer," 2015 IEEE PES Asia-Pacific Power and Energy Engineering Conference (APPEEC), Brisbane, QLD, pp. 1-5, 2015.
[46] J. Seo, H. Ma and Tapan K. Saha, "Analysis of Vibration Signal for Power Transformer On-Load Tap Changer (OLTC) Condition Monitoring," IEEE Power and Energy Society General Meeting 2018, Portland, OR USA, August 2018.

[47] J. Seo, H. Ma and Tapan K. Saha, "A Joint Vibration and Arcing Measurement System for Online Condition Monitoring of Onload Tap Changer of the Power Transformer," in IEEE Transactions on Power Delivery, vol. 32, no. 2, pp. 1031-1038, April 2017.
[48] T. A. Prevost and T. Oommen, “Cellulose insulation in oil-filled power transformers: Part I history and development,” Electrical Insulation Magazine, IEEE, vol. 22, no. 1, pp. 28-35, 2006.
[49] H. P. Moser, “Transformerboard. Birkhäuser Verlag,” 1979.
[50] Tapan K. Saha, "Review of modern diagnostic techniques for assessing insulation condition in aged transformers," IEEE Trans. Dielectr. Electr. Insul., vol. 10, pp. 903-917, 2003.
[51] M. Wang, A. J. Vandermaar and K.D. Srivastava, "Review of condition assessment of power transformers in service," IEEE Electr. Insul. Mag., vol. 18, pp. 12-25, 2002.
[52] Hamaguchi, Marcelo & Cardoso, Marcelo & Vakkilainen, Esa, “Alternative Technologies for Biofuels Production in Kraft Pulp Mills - Potential and Prospects,” Energies. 53390, vol. 5, no. 7, pp. 2288-2309, December 2012.
[53] L. Cheim, D. Platts, T. Prevost and S. Z. Xu, "Furan Analysis for Liquid Power Transformers," IEEE Electr. Insul. Mag., vol. 28, Issue 2, pp. 8-21, 2012.
[54] K. B. Shaban, A. H. El-Hag and K. Benhmed, "Prediction of Transformer Furan Levels," in IEEE Transactions on Power Delivery, vol. 31, no. 4, pp. 1778-1779, August 2016.
[55] IEEE Guide for the Interpretation of Gases Generated in Oil-Immersed Transformers, C57.104, 2008.
[56] P. S. Pugh and H. H. Wagner, "Detection of incipient faults in transformers by gas analysis," Power Apparatus and Systems, Part III. Transactions of the American Institute of Electrical Engineers, vol. 80, Issue 3, pp. 189-193, 1961.
[57] Mineral Oil-impregnated Electrical Equipment in Service – Guide to the Interpretation of Dissolved and Free Gases Analysis, IEC60599, 2007.
[58] A. Mollmann and B. Pahlavanpour, "New guidelines for interpretation of dissolved gas analysis in oil-filled transformers," Electra, CIGRE France, vol. 186, Issue 30-51, 1999.
[59] “Insulated bushings - Guide for the interpretation of dissolved gas analysis (DGA) in bushings where oil is the impregnating medium of the main insulation (generally paper),” IEC TS 61464:1998.
[60] S. A. Ward, "Evaluating Transformer Condition Using DGA Oil Analysis," in Proceedings of 2003 Annual Report Conference on Electrical Insulation and Dielectric Phenomena, 19-22 October, 2003, Albuquerque, NM, USA, pp. 463-468, 2003.
[61] S. Corporation, "Serveron White Paper: DGA Diagnostic Methods,", 2007.
[62] R. R. Rogers, "IEEE and IEC Codes to Interpret Incipient Faults in Transformers, Using Gas in Oil Analysis," IEEE Transactions on Electrical Insulation, vol. 13, Issue 5, pp. 349-354, 1978.

[63] IEEE Guide for the Detection and Determination of Generated Gases in Oil-Immersed Transformers and Their Relation to the Serviceability of the Equipment, ANSI/IEEE Std. C57.104, 1978.
[64] A. Abu-Siada and S. Islam, "A New Approach to Identify Power Transformer Criticality and Asset Management Decision Based on Dissolved Gas-in-Oil Analysis," IEEE Trans. Dielectr. Electr. Insul., vol. 19, Issue 3, pp. 1007-1012, 2012.
[65] H. Sun, Y. Huang and C. Huang, "A Review of Dissolved Gas Analysis in Power Transformers," Energy Procedia, vol. 14, Issue 1, pp. 1220-1225, 2012.
[66] V. Miranda and A. Castro, "Improving the IEC table for transformer failure diagnosis with knowledge extraction from neural networks," IEEE Trans. Power Delivery, vol. 20, Issue 4, pp. 2509-2516, 2005.
[67] N. Bakar, A. Abu-Siada and S. Islam, "A review of dissolved gas analysis measurement and interpretation techniques," IEEE Electr. Insul. Mag., vol. 30, Issue 3, pp. 39-49, 2014.
[68] M. Duval and L. Lamarre, "The duval pentagon-a new complementary tool for the interpretation of dissolved gas analysis in transformers," IEEE Electr. Insul. Mag., vol. 30, Issue 6, pp. 9-12, 2014.
[69] B. Pahlavanpour and I. A. Roberts, "Transformer Oil Condition Monitoring," in Proceedings of Proceedings of the 1998 IEE Colloquium on Transformer Life Management, October 22, London, UK, pp. 1-6, 1998
[70] S. Forouhari and A. Abu-Siada, "Remnant life estimation of power transformer based on IFT and acidity number of transformer oil," 2015 IEEE 11th International Conference on the Properties and Applications of Dielectric Materials (ICPADM), Sydney, NSW, pp. 552-555, 2015.
[71] H. Gumilang, "Hydrolysis Process in PLN P3BJB Transformers as an Effect of Oil Insulation Oxidation," in Proceedings of IEEE International Conference on Condition Monitoring and Diagnosis (CMD), September 23-27, 2012, Bali, Indonesia, pp. 1147-1150, 2012.
[72] S. Okabe, S. Kaneko, M. Kohtoh and T. Amimoto, "Analysis Results for Insulating Oil Components in Field Transformers," IEEE Trans. Dielectr. Electr. Insul., vol. 17, Issue 1, pp. 302-311, 2010.
[73] "IEEE Guide for Installation of Oil-Immersed Transformers (10 MVA and Larger 69-287 kV Rating)," in ANSI/IEEE Std. C57.12.11, 1980.
[74] M. Koch and S. Tenbohlen, "Evolution of bubbles in oil-insulation paper influenced by material quality and ageing," IET Electr. Power Appl., vol. 5, Issue 1, pp. 168-174, 2011.
[75] D. Martin, T. Saha, O. Krause, G. Buckley, S. Chinnarajan, R. Dee and G. Russell, "Improving the determination of water content of power transformer insulation paper near the end of its functional life," 2016 Australasian Universities Power Engineering Conference (AUPEC), Brisbane, QLD, pp. 1-6, 2016.

[76] D. Martin, T. Saha, J. Hockey, G. Caldwell, G. Buckley and S. Chinnarajan, "An investigation into improving the measurement of the water content of transformer electrical insulation," 2017 IEEE Innovative Smart Grid Technologies - Asia (ISGT-Asia), Auckland, 2017, pp. 1-4.
[77] D. Martin and T. Saha, "A review of the techniques used by utilities to measure the water content of transformer insulation paper," in IEEE Electrical Insulation Magazine, vol. 33, no. 3, pp. 8-16, May-June 2017.
[78] R. B. Keey, T. A. G. Langrish and J. C. F. Walker, "Kiln-Drying of Lumber," Berlin Heidelberg: Springer Verlag, 2000.
[79] A. F. Howe, "Diffusion of moisture through power-transformer insulation," Proc. Inst. Electr. Eng., vol. 125, Issue 10, pp. 978-986, 1978.
[80] T. V. Oommen, "Moisture equilibrium charts for transformer insulation drying practice," IEEE Transactions on Power Apparatus and Systems, vol. 103, Issue 10, pp. 3062-3067, 1984.
[81] S. D. Foss and L. Savio, "Mathematical and experimental-analysis of the field drying of power transformer insulation," IEEE Trans. Power Delivery, vol. 8, Issue 4, pp. 1820-1828, 1993.
[82] A. M. Emsley and G. C. Stevens, "Kinetics and mechanisms of the low-temperature degradation of cellulose," Cellulose, vol. 1, Issue 1, pp. 26-56, 1994.
[83] R. Jeffries, "The Sorption of Water by Cellulose and Eight Other Textile Polymers," Journal of the Textile Institute Transactions, vol. 51, Issue 9, pp. T339-T340, 1960.
[84] IEEE Guide for Acceptance and Maintenance of Insulating Oil in Equipment, IEEE C57.106, 2002.
[85] Y. Du, M. Zahn, B. C. Lesieutre, A. V. Mamishev and S. R. Lindgren, "Moisture equilibrium in transformer paper-oil systems," IEEE Electr. Insul. Mag., vol. 15, Issue 1, pp. 11-20, 1999.
[86] D. F. Garcia, B. Garcia and J. Burgos, "A review of moisture diffusion coefficients in transformer solid insulation-part 1: Coefficients for paper and pressboard," IEEE Electr. Insul. Mag., vol. 29, Issue 1, pp. 46-54, 2013.
[87] Y. Du, "Measurements and modelling of moisture diffusion processes in transformer insulation using interdigital dielectrometry sensors," PhD dissertation, Dept. Electr. Eng. Comp. Sci, Mass. Inst. Tech., Cambridge, MA, 1999.
[88] Tapan K. Saha, M. Darveniza, D. J. T. Hill and T. T. Le, "Electrical and chemical diagnostics of transformer insulation - Part B: Accelerated aged insulation samples," IEEE Trans. Power Delivery, vol. 12, Issue 4, pp. 1555-1561, 1997.
[89] J. Antonio Almendros-Ibanez, J. Carlos Burgos and B. Garcia, "Transformer Field Drying Procedures: A Theoretical Analysis," IEEE Trans. Power Delivery, vol. 24, Issue 4, pp. 1978-1986, 2009.

[90] J. Fabre and A. Pichon, "Deteriorating processes and products of paper in oil. Application to transformers," CIGRÉ paper 137, Issue 1, pp. 1-18, 1960.
[91] CIGRE, “Furanic compounds analysis : a tool for predictive maintenance of oil-filled electrical equipment,” TF 15.01.03, 1997.
[92] D. Allan, "Recent advances in the analysis and interpretation of aged insulation from operating power transformers," in Proceedings of The 5th International Conference on Properties and Applications of Dielectric Materials(ICPADM), Seoul, Korea, pp. 202-205, 25-30 May, 1997.
[93] R. Blue, D. Uttamchandani and O. Farish, "A novel solid-state material for furfuraldehyde detection," IEEE Trans. Dielectr. Electr. Insul., vol. 4, Issue 3, pp. 341-343, 1997.
[94] Tapan K. Saha and P. Purkait, "Investigation of polarization and depolarization current measurements for the assessment of oil-insulation paper of aged transformers," IEEE Trans. Dielectr. Electr. Insul., vol. 11, Issue 1, pp. 144-154, 2004.
[95] Tapan K. Saha and P. Purkait, "Investigation of an expert system for the condition assessment of transformer insulation based on dielectric response measurements," IEEE Trans. Power Delivery, vol. 19, Issue 3, pp. 1127-1134, 2004.
[96] Tapan K. Saha, M. Darveniza, Z. T. Yao, D. J. T. Hill and G. Young, "Investigating the effects of oxidation and thermal degradation on electrical and chemical properties of power transformers insulation," IEEE Trans. Power Delivery, vol. 14, Issue 4, pp. 1359-1367, 1999.
[97] Tapan K. Saha, M. Darveniza, D. J. T. Hill and T. T. Le, "Electrical and chemical diagnostics of transformer insulation - Part A: Aged transformer samples," IEEE Trans. Power Delivery, vol. 12, Issue 4, pp. 1547-1554, 1997.
[98] D. Urquiza, B. García and J. C. Burgos, "Statistical Study on the Reference Values of Furanic Compounds in Power Transformers," IEEE Electr. Insul. Mag., vol. 31, Issue 4, pp. 15-23, 2015.
[99] A. M. Emsley, X. Xiao, R. J. Heywood and M. Ali, "Degradation of cellulosic insulation in power transformers. Part 2: Formation of furan products in insulating oil," IEE Proceedings-Science Measurement and Technology, vol. 147, Issue 3, pp. 110-114, 2000.
[100] X. Chendong, "Monitoring Insulation Paper Ageing by measuring Furfural Contents in Oil," in Proceedings of 7th International Symposium on High Voltage Engineering (ISH), Dresden, Germany, pp. 139-142, 1991.
[101] T. Leibfried, M. Jaya, N. Majer, M. Schafer, M. Stach and S. Voss, "Postmortem Investigation of Power Transformers — Profile of Degree of Polymerization and Correlation with Furan Concentration in the Oil," IEEE Trans. Power Delivery, vol. 28, Issue 2, pp. 886-893, 2013.
[102] A. B. Shkolnik and R. T. Rasor, "Statistical insights into furan interpretation using a large dielectric fluid testing database," in Proceedings of IEEE PES Transmission and Distribution Conference and Exposition (T&D), May 7-10, Orlando, FL, USA, pp. 1-8, 2012.

[103] C. Ekanayake, S. M. Gubanski, A. Graczkowski and K. Walczak, "Frequency response of oil impregnated pressboard and paper samples for estimating moisture in transformer insulation," IEEE Trans. Power Delivery, vol. 21, pp. 1309-1317, 2006.
[104] W. S. Zaengl, "Dielectric spectroscopy in time and frequency domain for HV power equipment. I. Theoretical considerations," in IEEE Electrical Insulation Magazine, vol. 19, no. 5, pp. 5-19, September - October 2003.
[105] U. Gafvert, L. Adeen, M. Tapper, P. Ghasemi, and B. Jonsson, "Dielectric Spectroscopy in Time and Frequency Domain Applied to Diagnostics of Power Transformers," presented at The 6th International Conference on Properties and Applications of Dielectric Materials, Xi'an, China, 2000.
[106] M. Ohlen, P. Werelius, "Bushing insulation diagnostics based on dielectric response" Megger.
[107] K. Ibrahim, R. M. Sharkawy, M. M. A. Salama and R. Bartnikas, "Realization of partial discharge signals in transformer oils utilizing advanced computational techniques," in IEEE Transactions on Dielectrics and Electrical Insulation, vol. 19, no. 6, pp. 1971-1981, December 2012.
[108] K. Wang et al., "A new image-oriented feature extraction method for partial discharges," in IEEE Transactions on Dielectrics and Electrical Insulation, vol. 22, no. 2, pp. 1015-1024, April. 2015.
[109] M. Homaei, S. M. Moosavian and H. A. Illias, "Partial Discharge Localization in Power Transformers Using Neuro-Fuzzy Technique," in IEEE Transactions on Power Delivery, vol. 29, no. 5, pp. 2066-2076, October 2014.
[110] R. Ghosh, B. Chatterjee and S. Dalai, "A method for the localization of partial discharge sources using partial discharge pulse information from acoustic emissions," in IEEE Transactions on Dielectrics and Electrical Insulation, vol. 24, no. 1, pp. 237-245, February 2017.
[111] R. Liao, L. Yang, J. Li and S. Grzybowski, "Aging condition assessment of transformer oil-insulation paper model based on partial discharge analysis," in IEEE Transactions on Dielectrics and Electrical Insulation, vol. 18, no. 1, pp. 303-311, February 2011.
[112] M. Zhu et al., "Partial discharge signals separation using cumulative energy function and mathematical morphology gradient," in IEEE Transactions on Dielectrics and Electrical Insulation, vol. 23, no. 1, pp. 482-493, February 2016.
[113] M. H. Wang, "Partial discharge pattern recognition of current transformers using an ENN," in IEEE Transactions on Power Delivery, vol. 20, no. 3, pp. 1984-1990, July 2005.
[114] IEC 60270-2000, "High voltage test techniques – Partial discharge measurements," 2000.
[115] F. H. Kreuger, "Partial discharge detection in HV equipment," London Butterworth, UK, 1989.
[116] A. Cavallini, G. C. Montanari and M. Tozzi, "PD apparent charge estimation and calibration: A critical review," Dielectrics and Electrical Insulation, IEEE Transactions, vol. 17, Issue 1, pp. 198-205, 2010.

[117] IEC 62478/Ed1: “High voltage test techniques - measurement of Partial discharges by electromagnetic and acoustic methods,” 2012.
[118] D. Evagorou, A. Kyprianou, P. L. Lewin and A. Stavrou, “Feature extraction of Partial discharge signals using the wavelet packet transform and classification with a probabilistic neural network,” vol. 4, Issue 3, pp. 177-192, 2010.
[119] M. J. Foxall, A. P. Duffy, J. Gow, M. Seltzer-Grant and L. Renforth, “Development of a new high current, hybrid ‘Ferrite-Rogowski’, high frequency current transformer for Partial discharge sensing in medium and high voltage cabling,” 59th International Wire & Cable Symposium - November 7th - 10th 2010 - Rhode Island Convention Centre, Providence, RI, USA, 2010.
[120] X. Zhao, Z. Sun, Z. Guo and Y. Li, “Identification of parameters in a high-frequency current transducer using for partial discharge measurements,” Electronic Measurement & Instruments, 2009. ICEMI '09. 9th International Conference, pp. 1.413 – 1.416, August 2009.
[121] M. Florkowski and B. Florkowska, “Wavelet-based partial discharge image denoising,” Generation, Transmission & Distribution, IET, vol. 1, Issue 2, pp. 340-347, March 2007.
[122] Shie Qian, “Introduction to Time-Frequency and Wavelet Transforms”, Prentice Hall PTR, ISBN-10: 0130303607, 2002.
[123] G. Luo, D. Zhang, Y. Koh, K. Ng and W. Leong, “Time-frequency entropy-based partial discharge extraction for nonintrusive measurement,” IEEE Trans. Power Delivery, vol. 27, No. 4, pp. 1919-1927, October 2012.
[124] J. Ramirez-Nino, S. Rivera-Castaneda, V.R. Garcia-Colon and V.M. Castano, “Analysis of Partial discharges in insulating materials through the wavelet transform,” Comput. Mater. Sci., 9, pp. 379-388, 1998.
[125] X. Ma, C. Zhou and I. Kemp, "Automated wavelet selection and thresholding for PD detection,” IEEE Electrical Insulation Magazine, vol. 18, pp. 37-45, 2002.
[126] I. Shim, J. J. Soraghan and W. H. Siew, “Detection of PD utilizing digital signal processing methods. Part 3: Open-loop noise reduction,” Electrical Insulation Magazine, IEEE, vol. 17, Issue 1, pp. 6-13, January - February 2001.
[127] I. Shim, J. J. Soraghan and W. H. Siew, “Digital signal processing applied to the detection of partial discharge: An overview,” Electrical Insulation Magazine, IEEE, vol. 16, Issue 3, pp. 6-12, May - June 2000.
[128] IEEE C57.127-2007, “IEEE Guide for the Detection and Location of Acoustic Emissions from Partial Discharges in Oil-Immersed Power Transformers and Reactors,” IEEE Standard, August 2007.
[129] B. T. Phung, T. R. Blackburn and Z. Liu, “Acoustic Measurements of Partial Discharge Signals,” Journal of Electrical & Electronics Engineering, Australia, vol. 21, No. 1, pp. 41-47, 2001.

[130] E. Howells and E. T. Norton, “Parameters Affecting the Velocity of Sound in Transformer Oil,” IEEE Transactions on Power Apparatus and Systems, vol. PAS-103, Issue 5, May 1984.
[131] R. Jongen, P. Morshuis, J. Smit, A. Janssen, and E. Gulski, "A statistical approach to processing power transformer failure data," in Proceedings of the 19th International conference on electricity distribution; CIRED, 2007.
[132] CIGRE-WG 12.05, "An international survey on failures in large power transformers," ELECTRA, vol. 88, pp. 21-48, 1983.
[133] J. J. Erbrink, E. Gulski, J. J. Smit, P. P. Seitz, B. Quak, R. Leich, et al., "On-load tap changer diagnosis - an off-line method for detecting degradation and defects: Part 1," IEEE Electrical Insulation Magazine, vol. 26, pp. 49-59, 2010.
[134] P. Kang and D. Birtwhistle, "Condition assessment of power transformer onload tap changers using wavelet analysis and self-organizing map: field evaluation," in IEEE Transactions on Power Delivery, vol. 18, no. 1, pp. 78-84, January 2003.
[135] J. Seo, H. Ma and Tapan K. Saha, “Probabilistic wavelet transform for partial discharge measurement of power transformer,” IEEE Transactions on Dielectrics and Electrical Insulation, vol. 22, no. 2, pp. 1105-1117, April 2015.
[136] ABB, "On-load tap-changers, type UZ Technical guide," 2003.
[137] REINHAUSEN, “REINHAUSEN OLTC VACUTAP VV Operating Instructions,” 164/08 EN.
[138] P. Kang and D. Birtwhistle, "Condition assessment of power transformer on-load tap-changers using wavelet analysis," IEEE Transactions on Power Delivery, vol. 16, pp. 394-400, 2001.
[139] J. Seo, H. Ma and Tapan K. Saha, "On Savitzky-Golay Filtering for Online Condition Monitoring of Transformer On-Load Tap Changer," in IEEE Transactions on Power Delivery, vol. 33, no. 4, pp. 1689-1698, August 2018.
[140] A. Savitzky and M. J. E. Golay, “Soothing and Differentiation of Data by Simplified Least Squares Procedures,” Analytical Chemistry, vol. 36, pp. 1627-1639, 1964.
[141] R. Schafer, “What is a Savitzky-Golay filter?” IEEE Signal Processing Magazine, vol. 28, issue 4, pp. 111-117, 2011.
[142] R. Schafer, “On the frequency-domain properties of Savitzky-Golay filters,” 2011 Digital Signal Processing and Signal Processing Education Meeting, DSP/SPE, pp. 54-59, 2011.
[143] N. Domonelli, A. Rao, and P. Kundur, "Life extension and condition assessment - techniques for ageing utility infrastructure," IEEE Power and Energy Mag., vol. 4, No. 3, pp. 24-35, 2006.
[144] R. Bartnikas, “Partial discharges: their mechanism, detection and measurement”, IEEE Trans. Dielectr. Electr. Insul., vol. 9, No.5, pp. 763-808, October 2002.

[145] C. Chang, J. Jin, C. Chang, T. Hoshino, M. Hanai, and N. Kobayashi, "Separation of corona using wavelet packet transform and neural network for detection of partial discharge in gas-insulated substations," IEEE Trans. Power Del., vol. 20, pp. 1363-1369, April 2005.
[146] L. Chen, W. Lin, T. Tsao, and Y. Lin, "Study of partial discharge measurement in power equipment using acoustic technique and wavelet transform," IEEE Trans. Power Del., vol. 22, pp. 1575-1580, July 2007.
[147] H. Zhang, T. Blackburn, B. Phung, and D. Sen, "A novel wavelet transform technique for on-line partial discharge measurements part 1: WT de-noising algorithm," IEEE Trans. Dielectr. Electr. Insul., vol. 14, pp. 3-14, February 2007.
[148] X. Zhou, C. Zhou, and I. Kemp, "An improved methodology for application of wavelet transform to partial discharge measurement denoising," IEEE Trans. Dielectr. Electr. Insul., vol. 12, pp. 586-594, June 2005.
[149] X. Ma, C. Zhou, and I. Kemp, "Interpretation of wavelet analysis and its application in partial discharge detection," IEEE Trans. Dielectr. Electr. Insul., vol. 9, pp. 446-457, 2002.
[150] L. Satish and B. Nazneen, "Wavelet-based denoising of partial discharge signals buried in excessive noise and interference," IEEE Trans. Dielectr. Electr. Insul., vol. 10, pp. 354-367, 2003.
[151] J. Seo, H. Ma and Tapan K. Saha, "A Novel Signal Extraction Technique for Online Partial Discharge (PD) Measurement of Transformers," Int. Trans. Electr. Energ. Syst., 26: 1032-1048, 2016.
[152] S. Sriram, S. Nitin, K. Prabhu, and M. Bastiaans, "Signal denoising techniques for partial discharge measurements," IEEE Trans. Dielectr. Electr. Insul., vol. 12, pp. 1182-1191, 2005.
[153] R. K. Young, "Wavelet Theory and Its Application," Kluwer Academic Publishers, 1993.
[154] S. G. Mallat, "A Wavelet Tour of Signal Processing," London, U.K.: Academic Press, 1998.
[155] R. Wilcox, "Introduction to Robust Estimation and Hypothesis Testing," Academic Press, 2012.
[156] A. Najafipour, A. Babaee, and S. M. Shahrtash, "Comparing the trustworthiness of signal-to-noise ratio and peak signal-to-noise ratio in processing noisy partial discharge signals," Science, Measurement & Technology, IET, vol. 7, No.2, pp. 112-118, 2013.
[157] CIGRE, "Partial Discharges in Transformers," Working Group D1.29, February 2017.
[158] D. Aschenbrenner and H. G. Kranz, "On line PD measurements and diagnosis on power transformers," IEEE Transactions on Dielectrics and Electrical Insulation, vol. 12, issue 2, pp. 216-222, April 2005.
[159] G. C. Stone, "Partial Discharge Diagnostics and Electrical Equipment Insulation Condition Assessment," IEEE Transactions on Dielectrics and Electrical Insulation, vol. 12, no. 5, pp. 891-903, 2005.

[160] J. Seo, H. Ma, and Tapan K. Saha, “Differential Partial Discharge Extraction Technique for Online Power Transformer Insulation Assessment,” In the Proceedings of Proceedings of IEEE Power and Energy Society General Meeting, 2014.
[161] A. Cavallini, X. Chen, G. Montanari, and F. Ciani, "Diagnosis of EHV and HV transformers through an innovative partial-discharge-based technique," IEEE Trans. Power Del., vol. 25, pp. 814-824, 2010.
[162] A. Contin, A. Cavallini, G. Montanari, G. Pasini, and F. Puletti, "Digital detection and fuzzy classification of partial discharge signals," IEEE Trans. Dielectr. Electr. Insul., vol. 9, pp. 335-348, 2002.
[163] IEC Standard, 60599 (1999), “Mineral oil – impregnated equipment in service - Guide to the interpretation of dissolved and free gases analysis”, International Electrotechnical Commission (IEC).
[164] S. Markalous, S. Tenbohlen, and K. Feser, “Detection and location of partial discharges in power transformers using acoustic and electromagnetic signals,” IEEE Dielectrics and Electrical Insulation Society, pp. 1576-1583, December 2008.
[165] I. Maeda, T. Kaneko, O. Takenouchi, and T. Miyake, “Characteristics of on-line and off-line partial discharge for hydrogenerator stator windings with AE sensor and CT sensor,” Electrical Insulating Materials, 2008. (ISEIM 2008). International Symposium, pp. 577-580, September 2008.
[166] J. Seo, H. Ma and Tapan K. Saha, "An Improved Spatial Intersectional Method for Partial Discharge (PD) Source Localization in Power Transformer," In the Proceedings of the 12th International Conference on the Properties and Applications of Dielectric Materials (ICPADM), Xi’an, China, 20th - 24th May, 2018.